

# Inspection of nuclear intermediate level waste LW packaging and assets in situ



**Omer Elnasaney**

**Department of Electronic and Electrical  
Engineering**

**University of Strathclyde**

A thesis submitted for the degree of  
Doctor of Philosophy

## Abstract

The UK generates 15 % of its annual electric energy from nuclear power plants, and half of the nuclear power plants in the UK are expected to be retired by the year 2025 [1]. Physical containment of all **Intermediate Level Waste (ILW)** produced by the decommissioning processes are cement-encapsulated and enclosed in corrosion resistant waste containers stored in above ground interim storage vaults until they are deemed safe for geological disposal [2]. The current **Generic Waste Package Specification (GWPS)** calls for a target total container lifetime of 500 years [3]. To ensure that the containers' structural integrity remains within safe conditions during its time in operation, regular **Condition Monitoring, and Inspection (CM&I)** is required. This is challenged by the large quantity [4] and tight storage arrangement of the ILW vaults [5]. To overcome these challenges and cost associated with removing the ILW containers for regular inspection, this project proposes robotic inspection systems that can inspect 500 L ILW drums while in-situ using non-contact sensors deployed by mobile robotic system. The robotic systems are designed to operate in legacy vaults environments without modifying the vaults or the containers or their arrangement.

The theoretical assessment of CM&I sensors indicates that only less than 42% of the facets of interest can inspected using direct line of sight sensors. The sensors and techniques used to inspect and monitor the containers proposed, should allow the operators to inspect the drums' structural changes and degradation using the sensor fusion of data from laser scanner, photogrammetry and non-contact air coupled ultrasonics. This should provide a screening tool to identify damaged ILW drums' structures and provide a starting point to create digital twins of the individual drums for long term damage prediction and end of service life estimation.

## List of abbreviations

3D	Three dimensional
LLW	Low Level Waste
ILW	Intermediate Level Waste
HLW	High Level Waste
UILW	Unshielded Intermediate Level Waste
SILW	Shielded Intermediate Level Waste
GDF	Geological Disposal Facility
RWM	Radioactive Waste Management Ltd
NIREX	Nuclear Industry Radioactive Waste Executive
EPS1	Encapsulated Products Store 1
B.N.F.L	British Nuclear Fuels Limited
CMM	Coordinate Measuring Machine
CMS	Coordinate Measuring System
T.O.F	Time Of Flight
IMU	Inertial Measurement Unit
BLDC	Brush-Less Direct Current
MAV	Micro Aerial Vehicle
ESC	Electronic speed controller
HMI	Human Machine Interface
CM&I	Condition Monitoring and Inspection
SNR	Signal to Noise Ratio
NDT	Non-Destructive Testing
NNL	National Nuclear Laboratory UK
TX	Transmitter
RX	Receiver
TRL	Technology Readiness Level
NDE	Non-Destructive Evaluation
NDA	Nuclear Decommissioning Authority
RC	Radio control
PID	Proportional integral derivative

# Table of Content

## Contents

<b>Abstract .....</b>	<b>ii</b>
<b>List of abbreviations.....</b>	<b>iii</b>
<b>Table of Content .....</b>	<b>iv</b>
<b>Table of Figure .....</b>	<b>vii</b>
<b>Disclaimer .....</b>	<b>xxvi</b>
<b>Acknowledgement .....</b>	<b>xxvi</b>
<b>Chapter 1 : Introduction .....</b>	<b>1</b>
1.1 <i>Problem Statement.....</i>	<i>1</i>
1.2 <i>Research Objectives and Questions.....</i>	<i>1</i>
1.3 <i>Contributions to knowledge.....</i>	<i>2</i>
1.4 <i>Thesis layout.....</i>	<i>3</i>
<b>Chapter 2 : Nuclear decommissioning products storage environment.....</b>	<b>5</b>
2.1 <i>Introduction.....</i>	<i>5</i>
2.2 <i>Nuclear decommissioning containers.....</i>	<i>7</i>
2.3 <i>ILW 500 L drums.....</i>	<i>9</i>
2.4 <i>ILW 500 L drum stillages.....</i>	<i>11</i>
2.5 <i>The vault .....</i>	<i>12</i>
2.6 <i>In-situ CM&amp;I challenges.....</i>	<i>18</i>
2.7 <i>Containers ageing.....</i>	<i>23</i>
2.8 <i>Modelling the environment .....</i>	<i>26</i>
2.9 <i>Summary.....</i>	<i>29</i>
<b>Chapter 3 : Robotics and coordinate measuring systems challenges.....</b>	<b>31</b>
3.1 <i>Introduction.....</i>	<i>31</i>
3.2 <i>CMS uncertainty.....</i>	<i>31</i>
3.2.1 <i>CMS hardware errors.....</i>	<i>33</i>
3.2.2 <i>Workpiece errors.....</i>	<i>35</i>
3.2.3 <i>Sampling strategy .....</i>	<i>37</i>
3.2.4 <i>Fitting and scanning algorithm.....</i>	<i>39</i>
3.2.5 <i>Extrinsic factors .....</i>	<i>40</i>
3.3 <i>Geometrical scanning tools .....</i>	<i>41</i>
3.3.1 <i>Tactile probing.....</i>	<i>41</i>

3.3.2	Optical scanning .....	42
3.3.3	Scanning beyond obstacles .....	45
3.3.4	Ultrasonic inspection .....	49
3.3.5	Geometrical scanning tools evaluation .....	57
3.4	<i>Proposed scanning tools for in-situ inspection of ILW containers</i> .....	58
3.4.1	1 <sup>st</sup> data set: Video imagery .....	58
3.4.2	2 <sup>nd</sup> data set: 3D Laser point cloud scans.....	59
3.4.3	3 <sup>rd</sup> data set: Ultrasonic inspections/scans .....	60
3.4.4	Data fusion .....	61
3.5	<i>Quantifying surfaces accessible via direct line of sight</i> .....	63
3.6	<i>Summary</i> .....	71
<b>Chapter 4 : Proposed Mobile robotic inspection systems</b> .....		<b>72</b>
4.1	<i>Introduction</i> .....	72
4.2	<i>Existing robotics technology</i> .....	72
4.2.1	Manipulators .....	73
4.2.2	Locomotion .....	76
4.2.3	Soft Robotics .....	78
4.2.4	Aerial approach .....	81
4.3	<i>Position tracking and navigation</i> .....	82
4.4	<i>Available robotic technology summary</i> .....	85
4.5	<i>Rapid visual inspection using UAVs</i> .....	88
4.5.1	Proposed airframe.....	88
4.5.2	Prototype .....	91
4.5.3	Endurance .....	94
4.5.4	Control model.....	96
4.5.5	Compromises and future work .....	99
4.6	<i>Passive ILW inspection robot</i> .....	99
4.6.1	Anchoring .....	101
4.6.2	<b>XYplane</b> sensor motion.....	103
4.6.3	Z axis .....	105
4.6.4	Stillage hopping .....	107
4.6.5	Power source and drives.....	111
4.6.6	Navigation and sensor localisation.....	113
4.6.7	Sensor module.....	114
4.6.8	Automation and swarming .....	114
4.6.9	Digital simulation.....	117
4.6.10	Mechanical Prototype.....	121
4.6.11	Compromises and future work .....	126
4.7	<i>Summary</i> .....	127
<b>Chapter 5 : Ultrasonic inspection of ILW 500 L drums</b> .....		<b>128</b>
5.1	<i>Introduction</i> .....	128
5.2	<i>Transducer selection</i> .....	128
5.2.1	EMATs .....	128

5.2.2	Air(gas)-coupled piezoelectric ultrasonic transducers .....	130
5.3	Wave detection optimisation.....	145
5.4	Numerical validation .....	150
5.5	Measuring <b>V<sub>gr</sub></b> .....	157
5.6	Real-life inconsistencies.....	174
5.6.1	Manufacturing work hardening .....	174
5.6.2	Manufacturing tolerances.....	175
5.6.3	Radiation embrittlement .....	178
5.6.4	Cementitious immobilisation.....	179
5.7	The average drum .....	182
5.8	Summary.....	184
<b>Chapter 6</b>	<b>: Ultrasonic Lamb wave inspection of varying samples .....</b>	<b>185</b>
6.1	Introduction.....	185
6.2	Remote transducers angle control and sweeping.....	185
6.3	Signal acquisition optimisation.....	192
6.3.1	Signal averaging and data acquisition time .....	192
6.3.2	Aliasing .....	198
6.3.3	Noise and Electromagnetic interference .....	212
6.3.4	Optimisation summary .....	215
6.4	Cementitious encapsulation effects on Lamb waves propagation. ....	216
6.4.1	Cementitious contents expansion simulation.....	216
6.4.2	Practical limitations .....	220
6.4.3	Observations .....	229
6.4.4	Predictions and future improvements .....	242
6.5	Defect and discontinuity detection.....	244
6.5.1	Scenario 1: Defect after the first RX detection point .....	244
6.5.2	Scenario 2: Defect in the path from TX to RX .....	254
6.5.3	Scenario 3: Multiple defects presence after the first RX detection point.....	261
6.5.4	Scenario 4: Multiple defects surrounding the RX detection point .....	265
6.5.5	Processing detection patterns .....	266
6.5.6	Reflected wave validation.....	273
6.6	Transducers performance over time .....	280
6.7	Summary.....	280
<b>Chapter 7</b>	<b>: Future work and conclusion .....</b>	<b>282</b>
7.1	Future developments.....	282
7.2	Future research .....	283
7.3	Final conclusions.....	284
<b>Chapter 8</b>	<b>: Appendix .....</b>	<b>287</b>
8.1	Java code.....	287

Table of Figure

Figure 1: Multi barrier containment concept [11]. ..... 6

Figure 2: Nuclear Industry Radioactive Waste Executive (NIREX) LLW containers[11]. ..... 8

Figure 3: NIREX ILW standard containers[11]. ..... 8

Figure 4: Different designs of ILW 500 L drums[16]. ..... 9

Figure 5: ILW 500 L drum waste package encapsulating a mixed cement matrix (waste-form) [17]. ..... 9

Figure 6: (Left) Standard ILW 500 L drum overall external dimensions and identifier [15]. Centre- Standard RWM 500 L drum lifting features layouts [10]. (Right) Dounreay drum lifting crane assembly [21]. ..... 10

Figure 7: Isometric view of typical ILW stillage [3]. ..... 11

Figure 8: Section of the manufacturing drawing of a typical 500 L drum stillages created by Graham Engineering Ltd. .... 12

Figure 9: (Left) 3D visualisation of vault stacking [24]. (Right) Hunderson A ILW storage facility [27]. ..... 12

Figure 10: Dounreay storage facility mock-up with 500 L drums highlighted in orange [21][26]. ..... 13

Figure 11: Generic Nirex repository design [5]. ..... 14

Figure 12: Emplacement in the UILW Vault (Longitudinal-section) [24]. ..... 14

Figure 13: (Left) ILW containers’ ISO Standard RWM twistlock geometry and dimensions [23]. (Right) ILW containers’ ISO Standard RWM twistlock aperture geometry and dimensions [19]. ..... 15

Figure 14: ILW containers' ISO Standard RWM twistlock lifting arrangement layouts and geometry [20].	16
Figure 15: Gallery cross section showing typical UILW package array [11].	17
Figure 16: Gallery cross section (6.35m ID) showing typical UILW package array [11].	17
Figure 17: Staggered ILW containers arrangement.	18
Figure 18: WR-SGS, Model G3250-200) machine used to inspect medium size nuclear waste containers for external damage and radiation levels [29].	19
Figure 19: (Left) Example of waste drum in concrete package in front of an X-ray detector [31].	19
Figure 20: (Left) Geometrical laser scanner mounted in a wall inside EPS1, facing a transport rail on which the ILW are transported. (Right) The transport platform used to deliver the 500 L ILW drums to the laser scanner, the platform incorporated a turn table to rotate the drums and expose all their facets to the laser scanner field of vision [28].	20
Figure 21: Shadow/silhouette of an ILW 500 L drum mounted onto a turntable and exposed to SL beam for metrological scanning [6].	21
Figure 22: Measurements from the drum silhouette shadow metrology [6].	21
Figure 23: ILW immobilising cementitious matrix [16].	24
Figure 24: (Left) Section view of manufacturing drawing of 500 L drum acquired from B.N.F.L. (Right) 3D rendered model of 500 L drum created from B.N.F.L manufacturing drawing.	26



Figure 25: (Left) Top view of a of 500 L stillage from Serco report [3]. (Right) 3D rendered model of 4 x 500 L in a holding stillage created from available manufacturing drawings of a typical stillages. .... 27

Figure 26: Isometric view of a 7x7 staggered stacking of 500 L ILW drum stillages. .... 28

Figure 27: 3D rendering of the densely packed ILW 500 L drum stillage stacks inside an ILW vault..... 29

Figure 28: Error components that lead to CMM uncertainty [36]..... 32

Figure 29: Factors influencing selection of mobile CMS [37]. .... 32

Figure 30: (Left) CMM calibration blocks and probing stylus [40]. (Right) CMM Calibration sphere and probing stylus [40]. .... 34

Figure 31: Part form error wavelength in relation to sampling points [45]. .... 36

Figure 32: Obstructions limiting the direct line of sight access to 500 L ILW drums in a stillage highlighted in **red**. (**Note:** This only applies to this model of stillage and obstructions in other models may differ.) ..... 36

Figure 33: Profile data acquisition by a stylus-type profilometer [46]. . 37

Figure 34: Circularity runout measured from the difference between two circles centred on a datum. One circle coincides with the furthest point on the profile and the other coincides with the nearest point on the profile..... 39

Figure 35: General tactile probing system. (Left) single axis probing. (Right) 3 dimensional probing [42]. .... 42

Figure 36: Optical scanner setup used by Sellafield plant to test optical scanners ability to scan ILW 500 L drums inside a radioactive

environment [28] (See Section 2.6 Figure 20 for an image of a scanner inside EPS1).....	44
Figure 37: (Left) 3 AR.Drones flying in the testbed. (Right) Testbed setup with frame supporting 6 Vicon T160 positioning cameras [61].....	44
Figure 38: (Left) Fusion of 18 radiographies of a medium-sized nuclear decommissioning drum taken at different drum positions. (Right) two tomography slices extracted from cone-beam computerized X-ray tomography acquisitions [30].....	46
Figure 39: Tangential tomosynthesis, geometry (left) and example of tomosynthesis result (right). [31] .....	46
Figure 40: (Left) Linac Mini-Linatron Varian. Electrons are accelerated from the left (electron gun side) to the right (target side). The length of accelerating cavity is 1.2 m [30]. (Right) Example of waste drum in concrete package in front of an X-ray detector [31].....	47
Figure 41: (Left) The Lynkeos Muon static Imaging System installed at the Lynkeos Technology fabrication facility, used to scan ILW containers [64]. (Right) MURAY mobile muon telescope [63]. .....	48
Figure 42: (a) Detection of uranium metal (red region) inside an ILW 500 L drum replica using a muon imaging system at Sellafield UK. (b) cross section of the ILW 500 L drum replica in which the Uranium was placed [64].....	49
Figure 43: Acoustic wave travelling between a transducer and a workpiece.....	51
Figure 44: Mechanism in which an EMAT generates an ultrasonic shear wave into a workpiece, magnetic field ( $B_m$ ), Lorentz force ( $Fl$ ) and Eddy current ( $Ie$ ).....	55

Figure 45: Three-dimensional surface-mesh of a 500 L ILW drum created using from UAV deployed camera photogrammetry [83]..... 59

Figure 46: Cross section of an ILW drum point cloud and the different possible perimeter scenarios based on estimated lines of best fit from ultrasonic circumferential measurements. .... 62

Figure 47: (Left) Illustration of an incomplete point cloud image with circumference measurement larger than expected. (Right) Illustration of the expected estimation of a stretched point cloud image based on circumference measurement. .... 62

Figure 48: Expected data from fusion of different inspection/scanning methods. .... 63

Figure 49: (Left) Side view of a drum highlighted in blue inside a stillage. (Right) highlighted drum view extracted from the rest of the complete stillage view..... 64

Figure 50: (Left) View of a drum highlighted in blue, from the corner of the stillage. (Right) highlighted view extracted from the rest of the complete stillage view..... 64

Figure 51: Reconstruction of the 3D view expected from stitching the individual drum’s surfaces highlighted in blue in Figure 49 and Figure 50. .... 65

Figure 52: (Left) Cross section of an ILW stillage with the surfaces of a drum accessible from the centre hole highlighted in blue. (Right) highlighted view extracted from the rest of the complete stillage view. .... 66

Figure 53: Reconstruction of the 3D view expected from stitching the individual drum’s surfaces highlighted in Figure 52 to the 3D reconstruction previously created in Section 3.4.2..... 66

Figure 54: (Left) Point cloud of an incomplete ILW 500 L drum from direct line of sight scan simulation. (Right) percentage of point present in 1.0 mm layer of the complete point cloud. .... 68

Figure 55: ILW drum circumference divided into 4 quadrants, the distribution of points from the point cloud in n Figure 54 that lies in each of these quadrants is presented Figure 56. .... 69

Figure 56: Percentage of points per quadrant in a point cloud of an incomplete ILW 500 L drum from direct line of sight scan simulation .. 70

Figure 57: Human operator controlling a Brokk robot for pick and place operations inside a radiologically active environment. The operator is viewing the robot through a 1.2m thick lead-glass window, and controlling each joint with a separate lever, while estimating the inverse kinematics from experience [88]. .... 73

Figure 58: (Left) AARM robot passing through a small gap into a nuclear reactor cavity.(Right) AIA robot assembled, CEA-LIST Laboratory, June 2007 [89]. .... 74

Figure 59: (Left) OCRobotics snake like arm anchored onto a tractor transport system [91]. (Right) OCRobotics robot arm anchored onto a KUKA robot arm, accessing a point of interest through a small gap [91]. .... 75

Figure 60: RoMeLa STriDER [96]. .... 78

Figure 61: Earthworm-inspired burrowing soft robot rectilinear locomotion actuation sequence. Green represents inflation and grey represents deflation [100].	79
Figure 62: (Left) Inflatable robot manoeuvring under and around obstacles to turn a valve [101]. (Right) inflatable soft robot travelling vertically into the air to act as a radio antenna [101].	80
Figure 63: Plant inspired robot growth mechanism [101].	80
Figure 64: Dexterous Hexrotor with sampling arm for physical samples from inside a cylindrical grain silo in a mock-up of the WIPP exhaust shaft [83].	81
Figure 65: Design feedback loop caused by changes in UAV propeller or endurance parameters.	82
Figure 66: Marvelmind acoustic positioning system beacons and receivers [108].	83
Figure 67: 3D render describing the monotony of the densely packed ILW 500 L drum stillage stacks inside an ILW vault.	84
Figure 68: Predicted quadrotor layout required to fit in a 0.23 m gap between stillage stacks.	88
Figure 69: Top view of the proposed UAV layout to fit a 7" propeller in the 0.23 m (9") gap between stillage stacks.	89
Figure 70: Principle of coaxial helicopter swashplate mechanism[111].	89
Figure 71: Side view of the proposed UAV layout, forces, and attitude axis.	90
Figure 72: (Right) Front view of the proposed airframe with propellers at the roll/pan position. (Left) Front view of the airframe with propellers at the yaw position.	91

Figure 73: CAD model of the proposed UAV layout. ....	92
Figure 74: 3D virtual view of the proposed UAV manoeuvring between ILW stillages. ....	92
Figure 75: Prototype of the proposed UAV design. ....	93
Figure 76: Internal arrangement of the EDF axle and roller bearing housing.....	94
Figure 77: IBT power Lithium polymer batteries cells weight vs capacity trend line [112].....	95
Figure 78: iNav UAV controller position estimation flowchart [113].....	96
Figure 79: Gyro stability control modules setup used to stabilise the proposed UAV prototype. ....	97
Figure 80: Hackflight controller bare minimum PID controllers necessary for stable a UAV flight [113]. ....	98
Figure 81: 3D model of the passive robot proposed locked on to top of an ILW 500 L stillage stack, while deploying a sensor down to reach the lower stillage tiers. ....	100
Figure 82: Isometric view of steps taken by a twist-lock mechanisms to anchor the robot onto a stillage top corner.....	102
Figure 83: Illustration of the pivot and extension points of the arm carrying the Z-axis module. ....	103
Figure 84: Illustration of a rack and pinion arrangement to extend and retrieve the Z-axis module along the linear axis (B). ....	104
Figure 85: Z-axis module moving the sensor module along the Z axis by rolling and unfolding a slit tube.....	105
Figure 86: Magnetometer deployment using roll out tube for a NASA cube satellite [115].....	105

Figure 87: (Left) Slit tube boom deployment stages. (Right) slit tube deployment mechanism designed by Rocco [117].	106
Figure 88: Helical bi-stable slit tube unwrapping around a beam [119].	107
Figure 89: Step 1 in the stillage hop process.	108
Figure 90: Step 2 in the stillage hop process.	109
Figure 91: Step 3 in the stillage hop process.	109
Figure 92: Step 4 in the stillage hop process.	110
Figure 93: Radiation shielding tether power sources in radioactive environment [87].	112
Figure 94: Highlighted in blue is the area surrounding the stillage stacks that will always be clear of obstacles, where a path for the sensor module to travel through can be created.	116
Figure 95: Virtual Simulation illustrating the proposed robot mounted on a stillage and performing a visual scan. The view on the bottom right is the sensor module POV at this robot state.	117
Figure 96: Simulation of POV of optical sensor/camera observing the container from the Sensor module.	120
Figure 97: Isometric views of the latest CAD model of the 15 % scale robot prototype.	121
Figure 98: 15 % scale model of the proposed robot anchored onto a 15 % scale mock 500 L ILW stillage and drums.	122
Figure 99: 15 % scale model of the proposed robot connected to its controller and motor drivers.	123
Figure 100: (Left) First iteration of clearance mechanism used to create a gap between the mock stillage and the scale robot. (Right) final linear	

mechanism used to create a gap between the mock stillage and the scale robot. ....	124
Figure 101: Cable management and D-Sub connectors used to power and interact with the scale robot. ....	125
Figure 102: Views of the 3D printed 15 % ILW drum models from a video camera deployed by the 15 % scale robot. ....	126
Figure 103: (A) EMAT transducer monitor showing no readings of waves or reflections detected from the setup in picture (B). (B) INNERSPEC Technologies testing a commercially available EMAT transducer to generate acoustic waves across the ILW drum circumference. (C) setup of an EMAT transducer with a ferromagnetic plate on the inner side of the drum. ....	129
Figure 104: Mode conversion at fluid/solid boundary [81]. ....	131
Figure 105: Rayleigh wave propagation along matter surface. ....	132
Figure 106: (Left) Compressional waves in a plate symmetric Longitudinal mode “S” and antisymmetric Flexural mode “A”. (Right) Dispersion curves of Lamb waves in an aluminium plate: phase velocity Vs frequency [124]. ....	132
Figure 107: Illustration of how Rayleigh waves caused by induced waves refraction create multiple longitudinal waves sources along its route along a workpiece surface. ....	133
Figure 108: Dispersion curve created using ‘Disperse’ software showing different wave modes and their group velocity ( $V_{gr}$ ) in relation to the wave mode frequencies ( $f$ ) while travelling through a 2.33 mm thick stainless-steel plate. ....	135



Figure 109: Dispersion curve created using ‘Disperse’ software showing different wave modes and their angle of incident in relation to the excitation frequencies ( $f$ ) while travelling through a 2.33 mm thick plate. .... 135

Figure 110: Air couple transmitter (TX) and receiver (RX) setup generating and receiving a wave on/through the surface of an empty ILW 500 L drum sample and an oscilloscope view of the acoustic waves detected by the receiver during the successful wave generation/detection. .... 136

Figure 111: Schematic of the equipment used to generate and detect an A0 wave along the circumference of an ILW 500 L drum..... 137

Figure 112: (Top) Oscilloscope readings from the signal generator before amplification. (Bottom) Oscilloscope readings of signal detected by the receiver (Blue), and wave envelope (red) ..... 139

Figure 113: Predicted ultrasonic wave path to, along and from drum surface. .... 141

Figure 114: CAD of wedge used to align the transducers  $8.15^\circ$  tangent to the drum/sample circumference..... 146

Figure 115: Raw signal in Blue and wave envelope in red, and wave envelope and peak points detected by the MATLAB code in red..... 147

Figure 116: MATLAB signal analyser, showing the amplitudes of the normalised frequencies spectrums along the sample..... 148

Figure 117: Filtered signal with a  $0.95\pi$  rads/sample highpass signal filter in blue, and wave envelope and peak points detected by the MATLAB code in red. .... 149

Figure 118: Illustration of waves paths to, from and around the drum circumference. .... 151

Figure 119: Sample reading from Figure 117 with T.O.F from Figure 118 highlighted. ....	152
Figure 120: Illustration of wave path while being detected by RX at different detection points off the drum circumference. ....	159
Figure 121: MATLAB signal analyser, showing the frequencies at $0.2 \pi$ rads/sample having the highest energy levels of -20 dB in line with the raw signal above. ....	162
Figure 122: (Top) Raw data with a 30 samples peak envelope detection. (Bottom) Filtered reading with a $0.18$ to $0.22 \pi$ rads/sample bandpass signal filter and a 30 samples peak envelope. ....	163
Figure 123: Peak detection samples of a Lamb wave being detected from the setup described in Figure 120 at different locations on the drum circumference. ....	164
Figure 124: Manufacturing drawing of 5 different diameter test sample .....	167
Figure 125: Lamb wave dispersion curve created using 'Disperse' software showing different wave modes and their wave group velocity ( $V_{gr}$ ) change in relation to induced wave frequencies ( $f$ ) while travelling through a 2.5 mm thick plate. ....	167
Figure 126: Lamb wave dispersion curve created using 'Disperse' software showing different wave modes and their angle of incident in relation to induced wave frequencies ( $f$ ) while travelling through a 2.5 mm thick plate. ....	168
Figure 127: Setup used to validate the accuracy of the circumferential measurement using Lamb waves .....	169

Figure 128: Filtered oscilloscope readings of signals detected by the receiver from 5 different drum cross section samples identical in every way except for the overall 5mm difference in diameters as shown in Figure 124. .... 170

Figure 129: Antisymmetric A0 Lamb wave group velocity  $V_{gr}$  vs  $f$  of different stainless-steel plate thicknesses. This data is generated using ‘Disperse’ with the same settings described in Section 5.2.2 with the plate thickness as the variable. .... 176

Figure 130: Antisymmetric A0 Lamb wave  $V_{gr}$  vs  $f$  of different plate thicknesses at  $f$  range between 0 and 0.2MHz. .... 177

Figure 131: Left-Cut views of nuclear waste drums containing different types and layouts and of nuclear decommissioning products [132]. Right-Metallic scrap material embedded in immobilising cementitious matrix inside an ILW 500 L drum [132] ..... 179

Figure 132: (Top) Lamb wave dispersion curve created using ‘Disperse’ software showing different wave modes and their wave group velocity ( $V_{gr}$ ) change in relation to induced wave frequencies ( $f$ ) while travelling through a 316 stainless-steel sheet with air on one layer and concrete/cement on the other layer to represent an immobilised drum. (Bottom) Lamb wave dispersion curve created using ‘Disperse’ software showing different wave modes and their wave group velocity ( $V_{gr}$ ) change in relation to induced wave frequencies ( $f$ ) while travelling through a 316 stainless-steel sheet with air on both layers of the sheet to represent an airgap between the concrete/ cement and the drum’s wall. .... 180

Figure 133: Showing potential gap between cement and the wall due to air bubbles [64]. .....	182
Figure 134: CAD of the proposed gimbal mechanism required to align and control the air-coupled transducers TX and RX angles to achieve the desired Lamb wave refraction and detection. ....	186
Figure 135: Prototype of the proposed gimbal mechanism required to align and control the air-coupled transducers TX and RX angles to achieve the desired Lamb wave refraction and detection. ....	187
Figure 136: CAD of the gimbal mechanism created to compensate for the missing axis required to align and control the ultrasonic transducers TX and RX angles to achieve the desired Lamb wave refraction and detection.....	188
Figure 137: Gimbal mechanism created to compensate for the missing axis required to align and control the air-coupled transducers TX and RX angles to achieve the desired Lamb wave refraction and detection. ...	189
Figure 138: Gimbal mechanism aligning the transducer mounts with a cylindrical stainless-steel sample.....	189
Figure 139: Software algorithm for gimbal alignment. ....	190
Figure 140: Effects of oscilloscope averaging of 16, 64, 256 and 1024 on the SNR of amplified Lamb waves detected by the RX off an 800 mm diameter 2.5 mm thick 316 stainless steel circular sample.....	193
Figure 141: Effects of oscilloscope averaging of 2000, 3000, 4086 and 5000 on the SNR of amplified Lamb waves detected by the RX off an 800 mm diameter 2.5 mm thick 316 stainless steel circular sample.....	194
Figure 142: Detection of the Lamb wave for the 8 <sup>th</sup> time from the a 3000 averages signal reading. ....	196

Figure 143: Plot of the peak number against the location peak sample number from Figure 142, and line of best fit that joins all sample numbers. ....	197
Figure 144: Detection of the Lamb wave for the 12 <sup>th</sup> time from the a 3000 averages signal reading, and the observation of phases shifted synchronous peaks near the start of the signal. ....	199
Figure 145: Small phase shifted peaks with <i>T.O.F Circumference</i> synchronicity near the initial Lamb wave detection peaks in the 4068 averages reading. ....	200
Figure 146: (Top) Lamb wave detection pattern using a 10 ms oscilloscope sampling period and 10 ms excitation burst period. (Bottom) The same Lamb wave detection pattern using a 20 ms oscilloscope sampling period and 10 ms excitation burst period.....	203
Figure 147: (Left) Lamb wave detection patterns detected while using different excitation burst periods. (Right) Lamb wave detection patterns of two successive excitations using different burst periods.....	205
Figure 148: Lamb wave detection paterns aquired using different excitation burst periods and a constant osciliscpe sapling period of 20 ms. ....	206
Figure 149: 3D plot of the signals detected (Volts vs Time) at different distances between TX and RX.....	208
Figure 150: 2D representation of the 3D plot of the signal detected (Volts vs Time) at different distance between the TX incidence point and RX detection point.....	209
Figure 151: Lamb wave peak detections using different BNC cable length between the RX and the transimpedance amplifier. ....	211

Figure 152: Top view of equipment layout on the experiment bench (components sizes and spacing not to scale).....	212
Figure 153: Trigger pulse EMI with the RX and RX signal amplification components placed in different angle to the TX signal amplification components. ....	213
Figure 154: Simulated expansion of immobilisation cement using parting sections. ....	217
Figure 155: Manufacturing drawing of tapered 316 Stainless-steel sample used to simulate ILW 500 L drum in pressured state. ....	218
Figure 156: Mechanical clamping force to hoop stress conversion (Taper angle and space between the stainless steel and cement exaggerated for clarity) .....	219
Figure 157: (Left) 3D CAD model of cement moulding being pressed into a Stainless-steel tapered sample using an M12 threaded bar cross section view of the setup. (Right) Cross-sectional view of the clamping arrangement. (The circular disc used for clamping are replaced with a rectangular plate in image for visual clarity).....	219
Figure 158: (Left) CAD of 7 piece cement mould designed to be made from wood and machined on a lathe. (Right) Maximum cement moulding size expected from the mould. ....	220
Figure 159: 7 piece wooden mould and cement moulding release.....	221
Figure 160: 8.15 ° degree hanging wedge for a 5 ° tapered sample....	222
Figure 161: (Left) Cement moulding being pressed into the Stainless-steel tapered sample using an M12 threaded bar. (Right) TX and RX mounted onto the tapered sample using the 3D printed mounting wedge. ....	222
Figure 162: Truncated cone dimension [140]. ....	224

Figure 163: Free body diagram representing the transformation of the clamping force into hoop force. $R1$ and $R2$ are the angled component of $F_c$ , while $R2$ and $R3$ are the component of $F_{radial}$ as demonstrated on the force component diagrams on right. ....	225
Figure 164: (Left) SOLIDWORKS FEA simulation results presenting the mechanical stresses experienced by an 800 mm diameter ILW 500 L drum with a 2.33 mm wall expanded to 804 mm (URES=2mm) due to uniform pressure of $5.3 \times 10^6 Nm^2$ on its internal shell wall. (Right) Resultant displacement (URES) of the drum shell due to the pressure loading from the simulation. ....	227
Figure 165: Lamb waves detection patterns from the tapered stainless-steel sample. ....	229
Figure 166: Lamb waves detection patterns from the tapered stainless-steel sample with the cement moulding resting inside it. ....	230
Figure 167: Lamb waves detection patterns from the tapered stainless-steel sample with the cement moulding pressed into it using an M12 threaded bar torqued to 20N. ....	231
Figure 168: Lamb waves detection patterns from the tapered stainless-steel sample with the cement moulding pressed into it using an M12 threaded bar torqued to 30N. ....	232
Figure 169: Lamb waves detection patterns from the tapered stainless-steel sample with the cement moulding pressed into it using an M12 threaded bar torqued to 40N. ....	233
Figure 170: 3D representation of the Lamb waves detection patterns from the tapered stainless-steel sample with different setting for comparison. ....	234

Figure 171: 2D visual representation of the data from Figure 170 with readings from each scenario grouped together based on the distance from TX and RX in which the data is acquired. (Vertical axis in this plot refers to groups of signals and not exact values. Refer to previous plots for true data values.).....	236
Figure 172: Lamb wave detections with TX and RX spaced at 70 cm. .	238
Figure 173: Lamb wave detections with TX and RX spaced at 70 cm. .	239
Figure 174: Lamb wave detections with TX and RX spaced at 20 cm. .	240
Figure 175: Lamb wave detections with TX and RX spaced at 20 cm. .	241
Figure 176: Illustration of wave paths to, from and around the circumference of a cylindrical sample with a discontinuity/defect at the largest distance between TX and RX.....	245
Figure 177: Longitudinal waves travelling at $171.85^\circ$ caused by Lamb waves travelling in the anticlockwise direction. ....	247
Figure 178: Illustration of wave paths to, from and around the circumference with a defect present in the shortest distance between TX and RX. ....	254
Figure 179: Illustration of wave paths to, from and around the circumference of a cracked/defected drum with 2 or more defects on one side between the TX an RX.....	261
Figure 180: Illustration of wave paths to, and around the circumference of a cracked drum with cracks on both side between the TX an RX....	265
Figure 181: First stage of a flow chart to identify defects along the circumference of an ILW 500 L drum.....	266



Figure 182: Scenario 3 clockwise wave patten from the initial wave (red) and wave pattern from the <i>timenth escaped detection</i> waves (green). .....	269
Figure 183: Second stage of a flow chart to identify the defect scenario along the circumference of an ILW 500 L drum. ....	270
Figure 184: Identifying if the Lamb wave is able to bypasses(escape) through or around the defect.....	271
Figure 185: Identifying the difference between Scenario 1 and 2 based on the <i>distance</i> $D \cup$ crack polarity. ....	272
Figure 186: Flow chart to identify the defect scenario along the circumference of an ILW 500 L drum.....	273
Figure 187: Manufacturing drawing used to fabricate the intentionally defected sample. (Figure is not scale) .....	274
Figure 188: Layout of the ultrasonic transducers TX and RX in relation to the defect.....	275
Figure 189: Defected 800m diameter 316L stainless-steel sample being inspected using a pair of air-coupled ultrasonic transducers.....	275
Figure 190: (Top) Lamb wave detections with the transducer RX pointing towards the TX at 8.15 °. (Bottom) Lamb wave detections with the transducer RX pointing towards the reflections at 171.15 °. ....	276

## Disclaimer

The identification of any commercial products or trade names does not imply endorsement or recommendation by the authors or their institutes.

## Acknowledgement

This research has been funded by the UK Nuclear Decommissioning Authority (NDA) and supervised by the National Nuclear Laboratory (NNL).

I am very thankful to Professor Charles Macleod for his patience, help and moral support during my struggles in the Covid-19 pandemic, Morteza Tabatabaeipour for teaching me the foundation of my knowledge of ultrasonic waves, and Walter Galbraith for helping me achieve the milestones of my experiments.

I would also like to thank Gary Bolton, John-Patrick Richardson, Darren Potter, Rick Short and Ed Butcher for their belief in my ideas and introducing me to the nuclear industry.

# Chapter 1: Introduction

## 1.1 Problem Statement

The UK generates 20% of its annual electric energy from nuclear power plants, and half of the nuclear power plants in the UK are expected to be retired by the year 2025 [1]. The physical containment of all nuclear Intermediate Level Waste (ILW) produced by the decommissioning processes of active and retiring plants, are cement-encapsulated and enclosed in corrosion resistant containers and stored in interim storage vaults until they are deemed safe for geological disposal [2]. Some of these nuclear ILW containers have shown signs of structural deformation during their long-term storage in above ground vaults [6]. Thus, to ensure that the structural integrity of the ILW containers is maintained during its contents aging process, regular condition monitoring and inspection (CM&I) of the containers is required. This is challenged by the large quantity [4] and tight storage arrangement of the ILW vaults [5]. To overcome this challenge and eliminate any risks associated with moving the ILW containers out of their resting place, an in-situ inspection method is required.

## 1.2 Research Objectives and Questions

The project aims to identify possible means of deploying CM&I tools into nuclear ILW vaults, to assess the ILW containers' structural health during their long-term storage while in-situ. This includes,

- Assessing automated means to deploy CM&I sensors into the vaults that can access all areas of interest.
- Identifying and evaluating the optimum sensor technologies to use for the CM&I task.
- Ensuring that any systems proposed are able to operate in retrofit environment without have to modify the existing containers or containers' stacking arrangements.

### 1.3 Contributions to knowledge

This project presents a number of unique and novel, industry focused contributions to the fields of nuclear decommissioning and remote CM&I in the form of,

- Quantitatively identifying the direct line of sight access limitation and locations to an ILW 500 L drums, while stored inside a typical four drum stillage stacked inside an ILW vault. Studies in **Section 3.5** revealed that the direct line of sight CM&I tools are limited to 30 % of the drum surfaces of interest and can possibly be extended to 42 % if the sensors are able to access the stillages central backfill holes.
- A data fusion-based solution is proposed in **Section 3.4** to create the desired full scan of ILW containers using incomplete sets of data from multiple non-contact sensor technologies that compensate and complement each other using both direct and indirect line of sight sensors' data.
- A low-profile aerial vehicle able to travel in the 0.23 m gap between the ILW containers to deploy small sensors for rapid CM&I of ILW containers while in-situ is proposed in **Section 4.5**.
- A novel robotic mechanism proposed in **Section 4.6** that relies on existing nuclear storage containers' designs and standards, to anchor and manoeuvre itself across them to deploy CM&I tools into the small gaps between the containers. The robot relies on slit tube boom technology to accurately deploy and locate sensors into far and hard to reach points of interest.
- A non-contact and non-destructive inspection technique to measure the circumference of 500 L ILW drums ultrasonic transducers is described and verified in **Section 5.2.2**. The

technique uses Lamb waves time of flight (T.O.F) to measure the drums' circumference from a small access point without the need to access the entire drum circumference.

- The effects of pressure applied by changes in solid cementitious contents inside an ILW 500 L drum, on the propagation of Lamb waves traveling around its circumference, is experimentally verified in **Section 6.4**.
- A pattern-based algorithm to detect discontinuities in 500 L ILW drums using Lamb waves is proposed in **Section 6.5.5**. The algorithm utilises wave detection patterns from Lamb wave travelling around the drum shell multiple times to detect and locate defects in the drum shell.

## 1.4 Thesis layout

- Chapter 1 of this this thesis introduces the problem statement of the project and the main objectives and contributions to science achieved by the research.
- Chapter 2 describes the nuclear waste storage environments and the challenges the nuclear industry face in maintaining and inspecting the waste containment containers.
- Chapter 3 is a literature review of inspection tools and their suitability for remote and robotic inspection, and reviews research and industrial robotic systems suitability for the task of CM&I ILW containers.
- Chapter 4 proposes a UAV design to suit the flying conditions inside the ILW vaults for rapid inspection, and a passive robotic system for long term sensor deployment for precise in-situ inspection inside the ILW vaults.
- Chapter 5 describes the challenges and suitability of non-contact ultrasonic inspection in the task of non-contact circumferential measurements via restricted access, and validates its suitability for defect screening.

- Chapter 6 investigates the uncertainty factors associated with the non-contact air coupled ultrasonic inspection with the aged ILW drums as the subject of focus.
- Chapter 7 is the final conclusion of the project and a summary of the research and development required in future to further develop the systems proposed in the thesis.
- Chapter 8 is an appendix of the software code used in the project.

## Chapter 2: Nuclear decommissioning products storage environment.

### 2.1 Introduction

The UK generates 15 % of its annual electric energy from nuclear power plants, and half of the nuclear power plants in the UK are expected to be retired by the year 2025 [1]. The increase in capacity of new nuclear facilities combined with the retirement of a large number of power plants [7], makes the maintenance and decommissioning of nuclear facilities an important aspect in the evolution of the nuclear industry. Condition monitoring and inspection of nuclear facilities and decommissioning products is crucial, for the safety of the assets and the environment. This includes both operational facilities and decommissioning products [8].

The UK **Nuclear Decommissioning Authority (NDA)** concept for the disposal of nuclear decommissioning products involves:

- **Physical containment:** At this stage, all decommissioning products waste-forms are cement-encapsulated and enclosed in corrosion resistant waste-form containers. These containers are then stored in a above ground interim storage vaults [2]. The UK will store the waste-form containers for a minimum of 100 years and can potentially increase that to 300 years [9].
- **Geological isolation:** After the interim storage period, the waste-form containers are transferred to underground **Geological Disposal Facility (GDF)**, where the decommissioning products will be stored for decades, until the depositories are full, and all the containers are deemed stable.
- **Chemical conditioning:** At that point, the facility operators in consultation with society may decide to backfill the GDF by filling the gaps between the containers with cementitious backfill, sealing the underground openings and backfilling access ways, to protect the facility from any human intrusions, and the environment from any form of radioactive leaks [10].

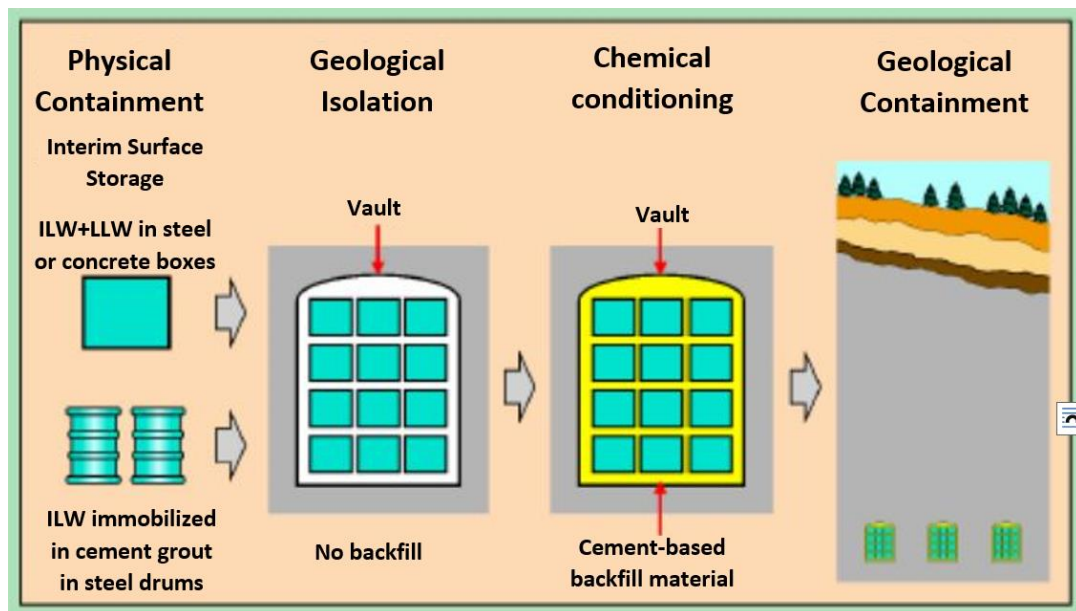


Figure 1: Multi barrier containment concept [11].

During the interim storage phase of the decommissioning product containers, **Condition Monitoring and Inspection (CM&I)** of the **Intermediate Level Waste (ILW)** containments from the nuclear power plants is required, to assess the current and future structural integrity of the containers during the long-term storage stage of their decommissioning [12]. As part of this assessment, geometrical scans of the containers are required and undertaken, to screen and quantify the containers deformation or damage, during their long storage time [12]. The current **Generic Waste Package Specification (GWPS)** calls for a target total container lifetime of 500 years [3].

This project focuses on the potential use of robotic systems to CM&I ILW containers in-situ during their interim storage phase, in the above ground storage vaults and GDFs prior to the backfill phase. This encompasses eliminating the need for moving the containers from their resting place in the stores to the inspection zones and increasing the scanning efficiency of CM&I to all the containers, instead of a small number of accessible samples.



## 2.2 Nuclear decommissioning containers

The UK National Radioactive Waste Inventory (DETR 1999a) categorises nuclear decommissioning products into 3 types [13]:

- **H**igh **L**evel **W**aste (HLW).
- **I**ntermediate **L**evel **W**aste (ILW).
- **L**ow **L**evel **W**aste (LLW)

HLW mainly consists of spent fuels, that are subject to increase in temperature due to their radioactivity [13]. LLW and ILW are mainly metals, organics, glass, ceramics, concrete, cement, rubble and graphite[13]. Other miscellaneous inorganics such as, sludges, flocs, liquid concentrates and soil can also fall under LLW and ILW [13].

LLW packaging require containment only and no radiation shielding, whereas ILW packages are categorised as **U**nshielded **I**ntermediate **L**evel **W**aste (UILW) Packages and **S**hielded **I**ntermediate **L**evel **W**aste (SILW) Packages [11]. The unshielded packages require remote handling due to their radiation levels or containment requirements, and shielded containers either have built-in shielding or contain low-activity material, that allows conventional handling techniques [11].

In the UK, the LLW and ILW decommissioning products are stored in six standard waste packages.

<b>Waste Container</b>	<b>Typical Contents</b>
500 Litre drums	The normal container for most operational ILW
3m <sup>3</sup> box	A larger container for solid wastes
3m <sup>3</sup> drum	A larger container for 'in-drum mixing and solidification of liquid and sludge type wastes
4-meter box	Large items of waste, especially from decommissioning operations
4-meter LLW box	For LLW
2-meter LLW box	For LLW

Table 1:Types of waste containers used in the UK [14].

The UK LLW and ILW containers are typically made from thin stainless steel sheet, and some are internally shielded using cementitious encapsulation up to 300mm thick [14]. Other proposed shielded

containers are expected to be constructed from reinforced concrete between 150 mm and 240 mm thick [14]. The majority of UILW packages are assumed to be 500 Litre drums, packed in groups of four within a disposal stillage, shown in Figure 3 [11]. The ILW 500 L drums will be the main target of the CM&I system developed by the project because of their packaging complexity and quantum.



Figure 2: Nuclear Industry Radioactive Waste Executive (NIREX) LLW containers[11].



Figure 3: NIREX ILW standard containers[11].

## 2.3 ILW 500 L drums

Over the years, different design iterations of the ILW 500 L drums have been created and filled to accommodate the process requirements for treating a diverse range of radioactive wastes, namely solid, liquor and annular grouted [15]. Some of these iteration can be seen in Figure 4. All the iterations are fabricated from corrosion resistant austenitic stainless steels [2], which are then filled with decommissioning products mixed with immobilising cementitious matrix [16] seen in Figure 5.



Figure 4: Different designs of ILW 500 L drums[16].

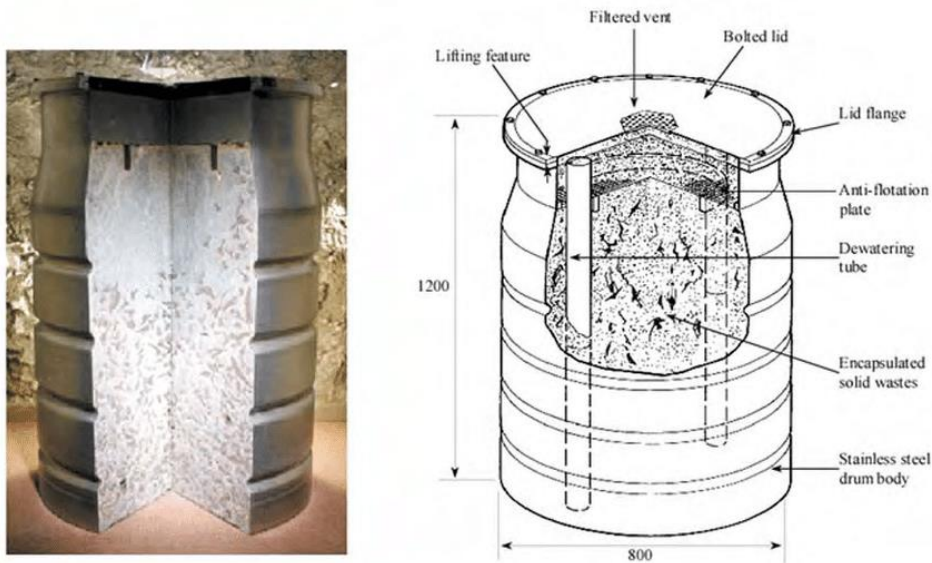


Figure 5: ILW 500 L drum waste package encapsulating a mixed cement matrix (waste-form) [17].

The drums are manufactured using 7 French gauge (2.33 mm or 13 B.S.W.G) 316L [15] or 2.5 mm 316S11 [18] austenitic stainless steel sheets rolled into the drums' cylindrical shape and autogenously seam welded along the vertical joint using plasma welding [15]. The body is then swaged in order to provide extra body strength and to tailor the container to interface with plant specific handling capabilities [15]. The drums' base is made of slightly thicker bottom base sheet of 2.93 mm [15]. As a standard all drums are 800 mm in diameter with maximum height of 1230 mm [19]. The lids are connected using a 15 mm to 30 mm thick lid flange, from which the drums can be lifted according to **Radioactive Waste Management (RWM) standards** [15][20].

A full ILW 500 L drum gross mass is limited to a maximum weight of 2000 Kg [15] with maximum external surface radiation level of 10 micro Sievert per hour (mSv/h) [20]. The maximum permitted payloads' heat is 6 W/m<sup>3</sup> [20], this equates to 2.82 W output for a typical ILW 500 L drum payload of 0.47 m<sup>3</sup> [19] . All ILW packaging and drums must have a defined alpha-numerical identifier format and location, that must remain identifiable by automated systems for a minimum period of 150 years following manufacture [10].

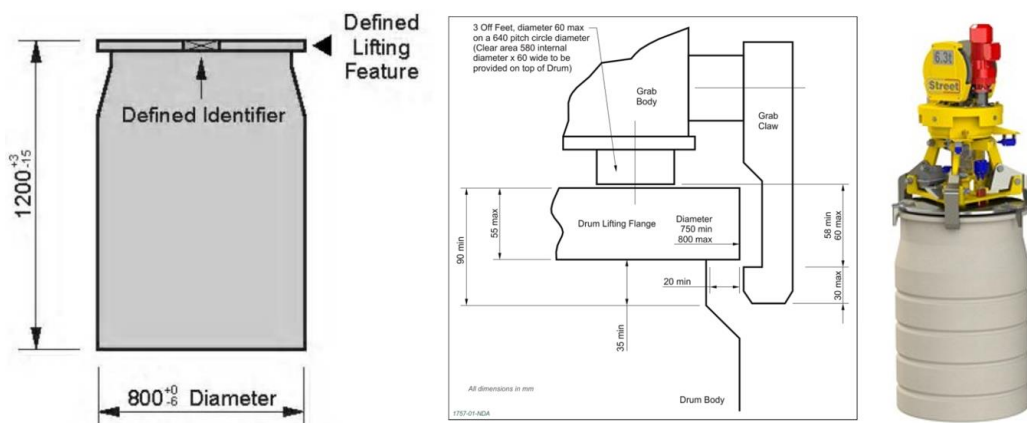


Figure 6: (Left) Standard ILW 500 L drum overall external dimensions and identifier [15]. Centre- Standard RWM 500 L drum lifting features layouts [10]. (Right) Dounreay drum lifting crane assembly [21].

## 2.4 ILW 500 L drum stillages

The ILW 500 L drums are packed in sets of four on disposal stillages fabricated from 316L austenitic stainless steel plates [3]. The stillages lifting points are designed to handle a stillage gross mass up to 9 tons [22] and support total load of 540 kN [23]. They can be stacked in columns up to 7 tiers high, using the twistlock lifting mechanism [23][24]. Each unit is stacked with maximum offset of **25 mm** in each orthogonal direction for cuboidal packages or a **25 mm** radial offset for cylindrical packages from the disposal units above and below [19].

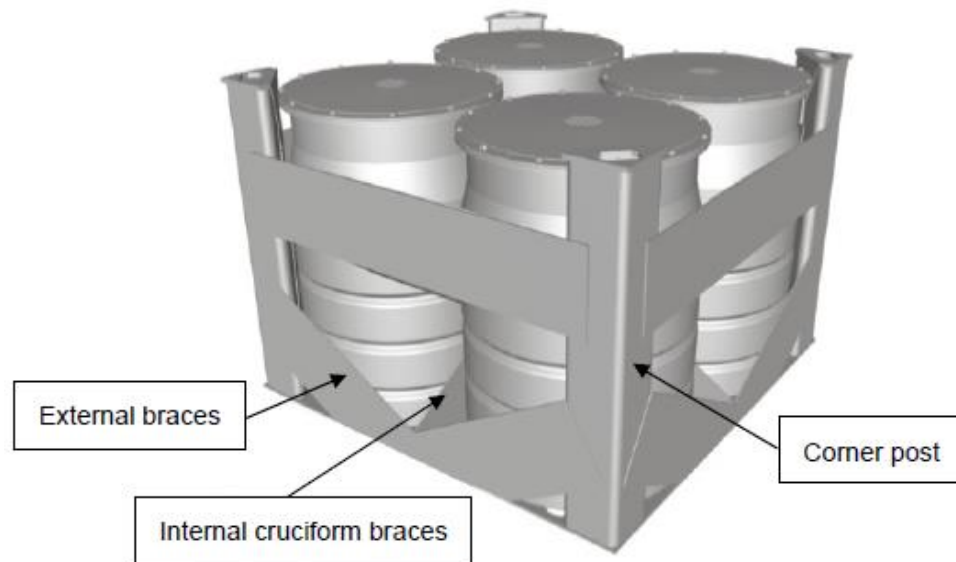


Figure 7: Isometric view of typical ILW stillage [3].

The stillages have circumferential stiffeners separating the drums, and a **0.25 m** circular hole in the centre of the base plate, surrounded by a set of **100 mm** holes under each drum [3]. These holes are cut to allow flow of concrete between the containers, once they reach their final backfill stage [25].

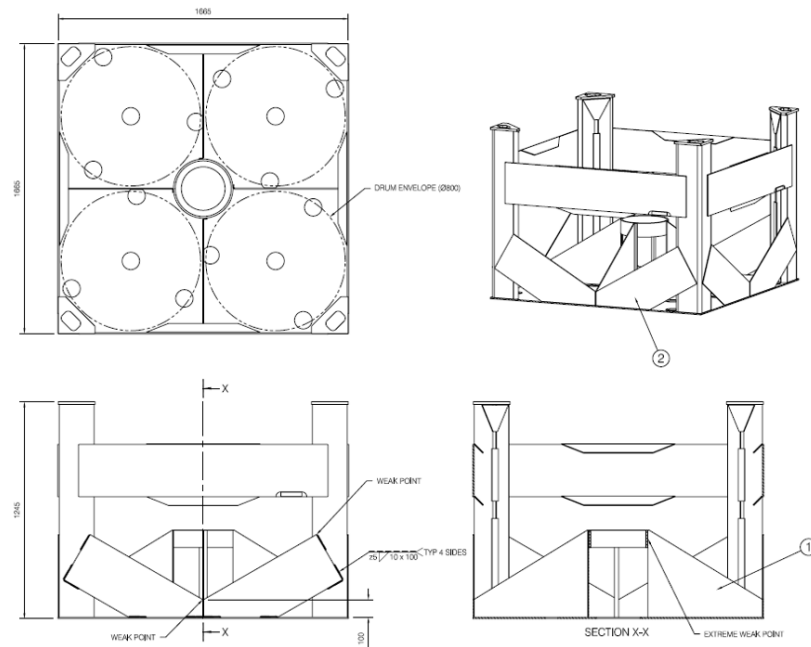


Figure 8: Section of the manufacturing drawing of a typical 500 L drum stillages created by Graham Engineering Ltd.

## 2.5 The vault

Typically, the ILW and LLW storage vaults would be 16 m wide, 16 m high, and up to 300 m in length. In these vaults, 500 L drum stillages, 3 m<sup>3</sup> drums and 3 m<sup>3</sup> boxes are stacked into 7 rows of columns, each column is 7 stillages high [24]. The stacking starts from the far end of the vault, making its way to the hatch door [24]. If the 500 L drums are stored without stillages, different stacking arrangement would be expected, such as that used at Dounreay storage facility in the UK [21][26].



Figure 9: (Left) 3D visualisation of vault stacking [24]. (Right) Hunderson A ILW storage facility [27].

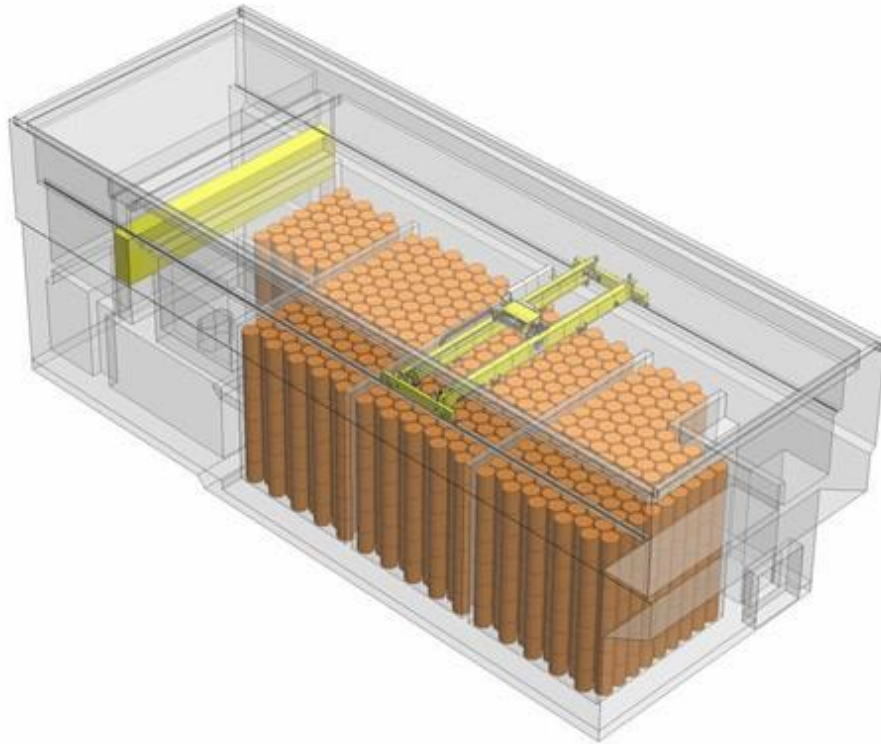


Figure 10: Dounreay storage facility mock-up with 500 L drums highlighted in orange [21][26].

The stillages, 3 m<sup>3</sup> drums and boxes are **1.245 m** in height and **1.665 m** in width and length [25] making a full 7 stack column approximately **8.715 m** high [5]. The columns are stacked linearly with a minimum gap distance of **0.23 m** gap between the columns [5]. The temperature in the vaults is assumed to vary between **25 °C** and **35 °C**, and the relative humidity of **70 %** to **85 %** and air velocity up to 10 Km/h [25].

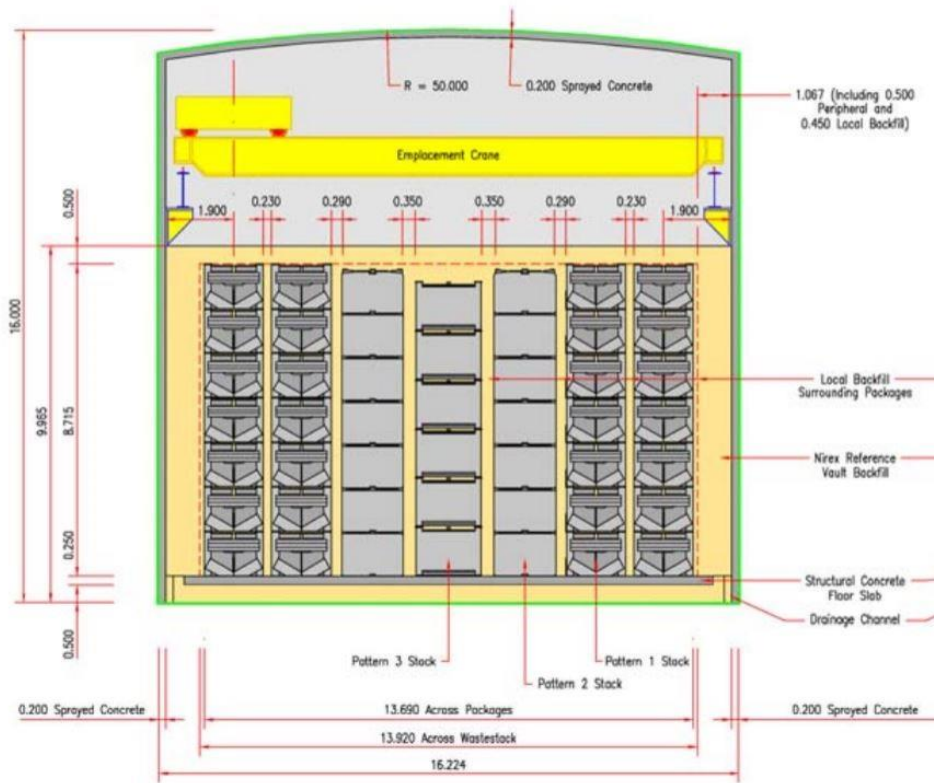


Figure 11: Generic Nirex repository design [5].

In large above ground GDFs, overhead cranes are used for stillages and container placement. The containers, stillages, and overhead crane enters the vault via a set of shielded doors [24]. Therefore, any robotic systems that are to enter the vault, must be able to pass through the shielded doors. Equipment larger than the shielded door area could be assembled inside the vault, provided that all the individual components can pass through the shielded doors.

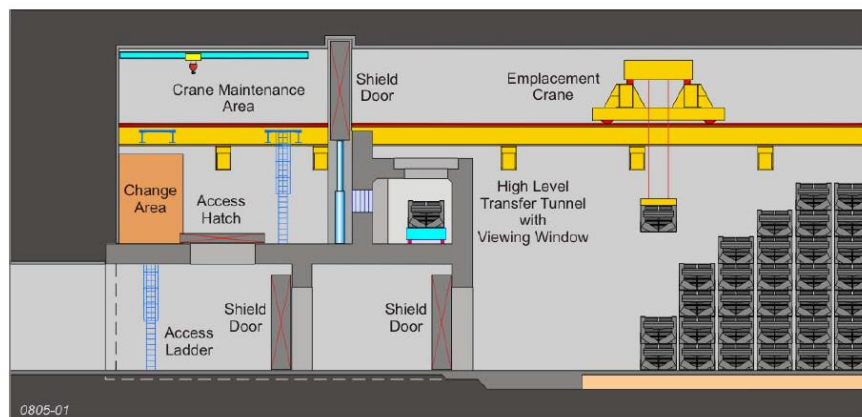


Figure 12: Emplacement in the UILW Vault (Longitudinal-section) [24].



Inside the vault, overhead cranes use standardised spreader ‘twistlock’ lifting arrangement demonstrated in Figure 13 and layouts to meet WPS/604 [22] and RWM TSCS 1079 [19] described in Figure 14. This standardised design is defined by the **R**adioactive **W**aste **M**anagement Ltd (RWM), to enhance the stores operational efficiency and safety. This makes the lifting arrangement a common feature between all types of ILW and LLW containers in all stores [20].

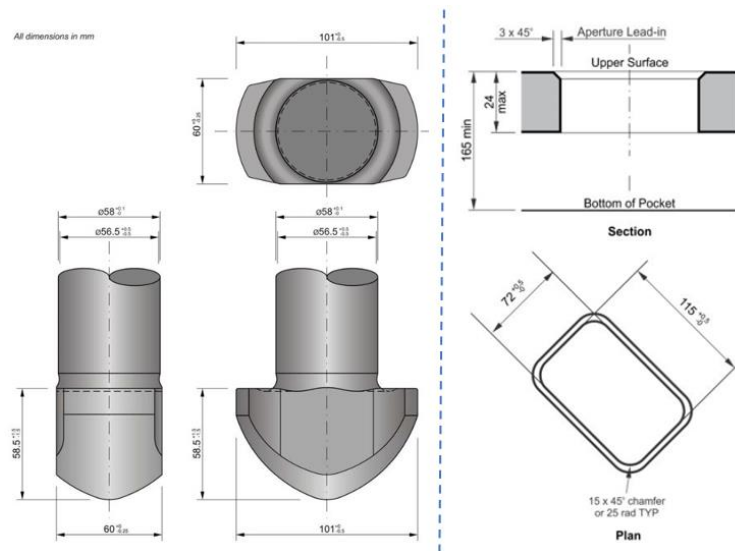


Figure 13: (Left) ILW containers’ ISO Standard RWM twistlock geometry and dimensions [23]. (Right) ILW containers’ ISO Standard RWM twistlock aperture geometry and dimensions [19].

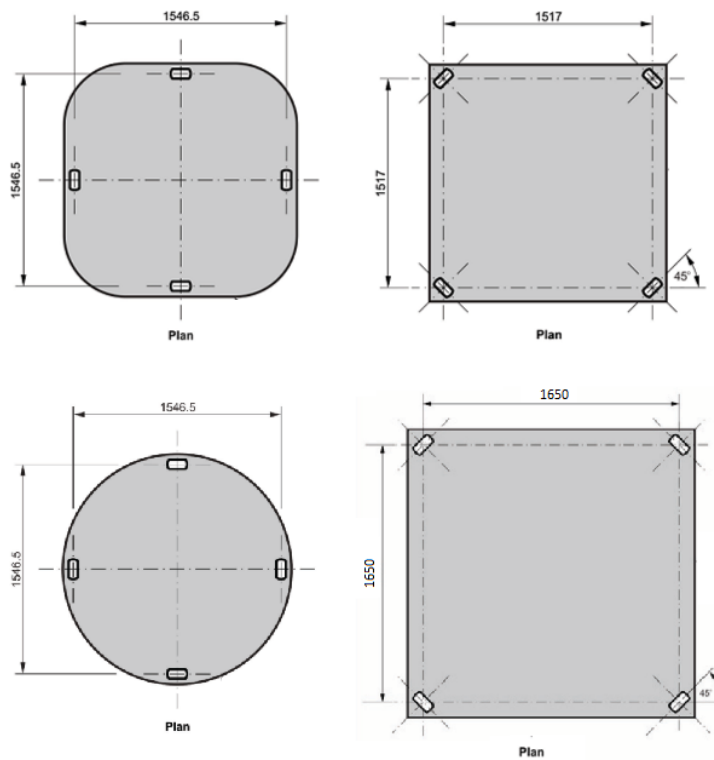


Figure 14: ILW containers' ISO Standard RWM twistlock lifting arrangement layouts and geometry [20].

Vault cranes can be a great asset in the emplacement of sensors, to monitor the state of the ILW while in-situ, however not all vaults are expected to have overhead cranes. Underground stores and GDFs are expected to use stacker trucks instead of overhead cranes [11], while still adhering to the same WPS/604 [22] lifting arrangement standards. These underground stores and GDFs will be excavations in the form of tunnels ranging between **300 m** to **800 m** long and **9m** high, in medium strength rock mass such as clay rock, and are expected to have a 'D' profile or horseshoe shape [11]. These tunnels (vaults) will accommodate UILW packages in arrays of **3** packages wide, stacked up to **6** packages high or **7.47 m**, leaving a small clearance gap between the stacks and the tunnel wall, due to the tunnel cross sectional profile [11] as described in Figure 15.

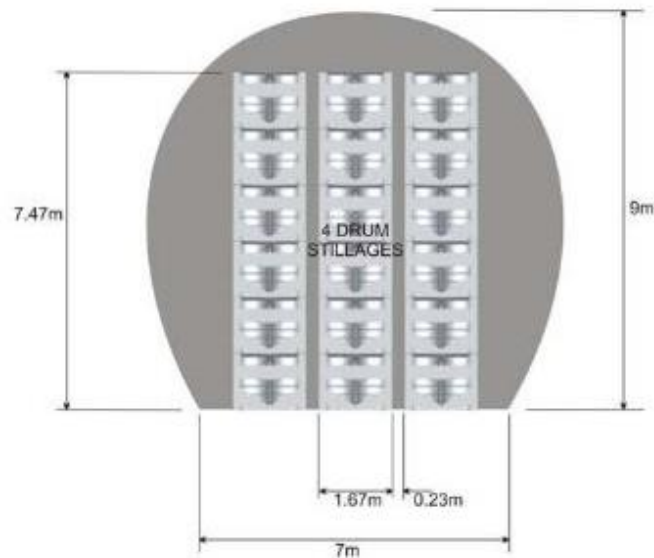


Figure 15: Gallery cross section showing typical UILW package array [11].

The smallest practical underground tunnel with 'D' profile cross sectional area presented in Figure 16 is expected to have an inner diameter of **6.35 m** and house a stillage arrays of 2 stillages wide by 6 high, with the minimum gap distance of **0.23 m** [11]. Therefore, the ideal CM&I system should be able to fit in the smallest expected constrains, and not be reliant on the overhead cranes.

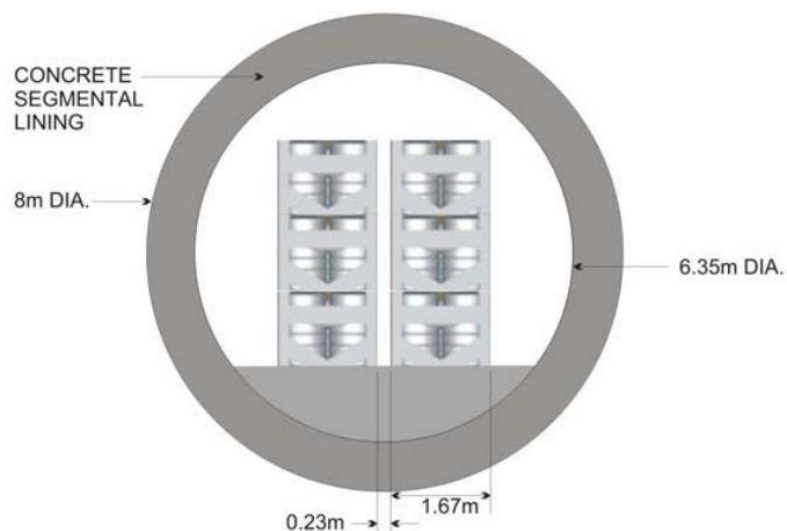


Figure 16: Gallery cross section (6.35m ID) showing typical UILW package array [11].

Published studies investigated offsetting the stillage stacking columns as demonstrated in Figure 17 to minimise the crack propagation in the backfilling concrete [25], have been considered in this project. Thus the arrangement presented by Figure 17 will be assumed throughout the project, because it provides the worst-case scenario for paths between the stacked package columns.

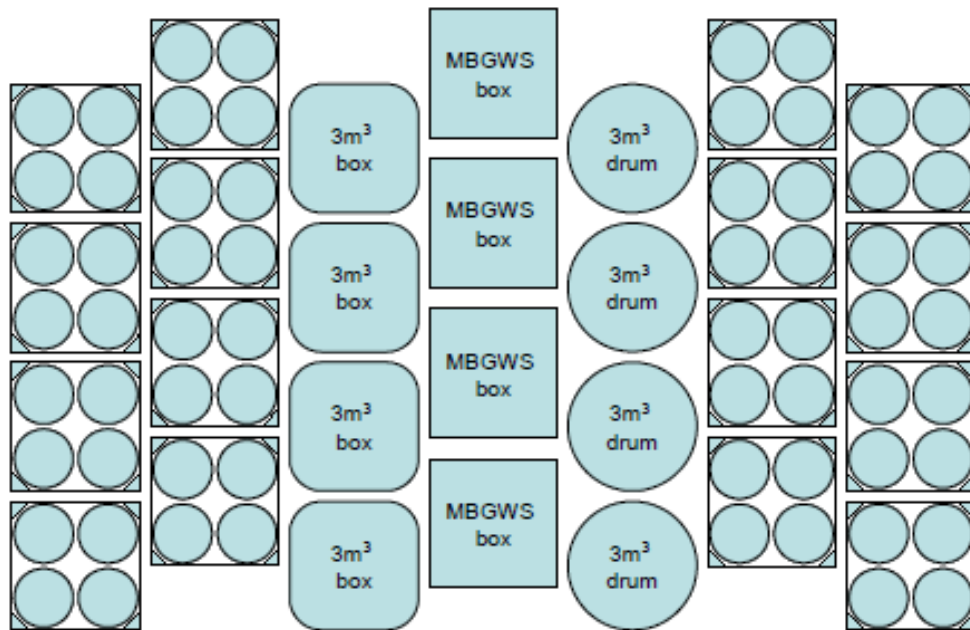


Figure 17: Staggered ILW containers arrangement.

## 2.6 In-situ CM&I challenges

Metrological scans for CM&I of medium sized nuclear waste-form containers is currently performed by moving the containers out of their storage place and mounting them onto assays that manoeuvre them and exposes them to non-contact scanners to captures all the external dimensions and parameters [28]. An example of such scanning assays is the ANTECH **Wide Range Segmented Gamma Scanner** (WR-SGS, Model G3250-200) shown in Figure 18, that inspects medium nuclear waste containers for external damage and radiation levels [29]. The WR-SGS assay system works by rotating the containers along its cylindrical axis, while a set of sensors mounted on a linear axis parallel to the cylindrical axis move in synch with the container's rotation to expose the scanning sensors to all the external facets of the container's cylindrical shell [29].



Figure 18: WR-SGS, Model G3250-200) machine used to inspect medium size nuclear waste containers for external damage and radiation levels [29].

Similarly high-energy X-ray radiography and X-ray tomography have been used in similar manner to scan through medium sized nuclear waste drums for internal inspection [30] as seen in Figure 19. X-ray provided an extra view of the state of the internal contents, and structure of the container. (See Figure 38 for an example of the internal scan of a medium sided ILW drum using X-ray)

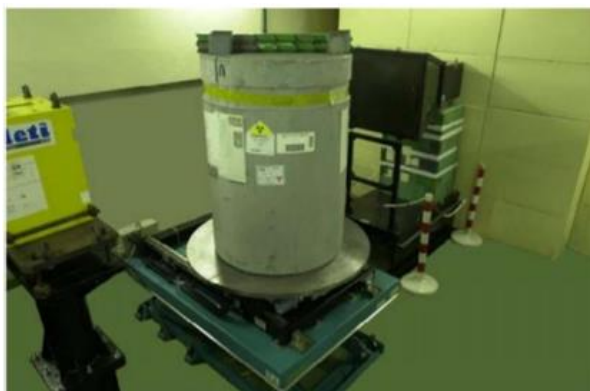


Figure 19: (Left) Example of waste drum in concrete package in front of an X-ray detector [31].

To avoid removing the ILW 500 L drums from the UK Encapsulated Products Store 1 (EPS1) for CM&I, geometrical phase vision laser scanners were tested by mounting them inside the store's radiation zones [28] as seen Figure 20 (Left), and craning the drums out of their resting place onto the turntable seen in Figure 20 (Right), to expose all the drums' facets to the laser scanners [28]. The laser scanners require radiation shielding and to be kept at a reasonable distance away from the drums to minimise electronics damage caused by the gamma radiation from the drums [28]. A minimum of 400 mm standoff from the drum was also necessary to maximise the scanners coverage of the drums' surfaces[28].



Figure 20: (Left) Geometrical laser scanner mounted in a wall inside EPS1, facing a transport rail on which the ILW are transported. (Right) The transport platform used to deliver the 500 L ILW drums to the laser scanner, the platform incorporated a turn table to rotate the drums and expose all their facets to the laser scanner field of vision [28].

To avoid exposing the dimensional scanners to the ionising radiation, "Nexia Solutions" used structured light (SL) and beamed it through a 0.75m thick lead glass observation window in the store [6], to perform dimensional scans of the drums. The drums were craned out of their resting place and mounted individually onto a turntable where they were rotated while being exposed to the SL beam as seen in Figure 21. The shadow/silhouettes of the SL beam was then used to measure the drums dimensions as seen in Figure 22, to overcome the optical noise caused by the reflectivity of the drums surfaces [6].

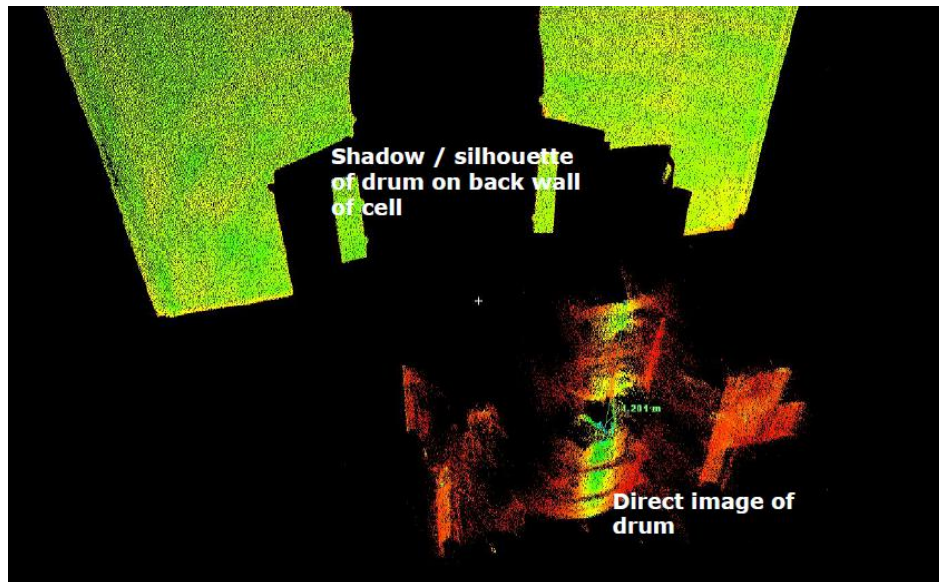


Figure 21: Shadow/silhouette of an ILW 500 L drum mounted onto an turntable and exposed to SL beam for metrological scanning [6].



Figure 22: Measurements from the drum silhouette shadow metrology [6].

Using SL beams through the shielded observation window allowed the operators to dimensionally scan 12 ILW drums [6], without inserting or removing anything into or out of the shielded zone. This reduced the

financial cost and human exposure to ionising radiation dose during the process, but increased the scan post processing to compensate for the surface reflections and high refraction caused by the thick shielding glass [6]. This also limited the scans accuracy to the region of **3 to 5 mm**, due to light scattering and reflections from the drum surfaces and the thick shielding glass.

Although the laser and SL scanning methods described can offer reliable and accurate means of dimensionally scanning the ILW containers without removing them out of the radiation zones, they still require taking the drums out of their resting place inside the long-term stores to be placed on the inspection platforms. This is a challenging process due to the large quantity and compact stacking arrangements describe in Section 2.5. For example, moving a container placed at the low tiers far end of the vault for inspection, will require moving all the containers stacked above it first out of the way to access its lifting points, and may also require moving containers in other stacks to clear the route for the crane to access and displace the container of interest out to the inspection point. This will cause frequent lifting and displacement of the top tier containers to clear the way for the bottom ones, which can fatigue and damage their structure and lifting arrangement due to the mechanical stresses caused by the frequent loading and handling of them [13]. Therefore the ideal CM&I method would be one that can enter the storage repository to perform the scans in-situ [32], without moving any of the containers from of their resting place.

Based on the information published by Sellafield Ltd. on the environment in which the containers are stored in, the facilities are expected to have [32]:

- Poor access due to the compact stacking of the waste packages.
- Dark or poorly lit facilities.
- A life span of many decades.
- Radiation dose rates that require remote handling.
- No power supply points.
- Variable package designs, shapes, sizes, and storage configurations.



In this environment, the nuclear industry is looking to monitor the ILW containers for [32]:

- Deformation of packages.
- Corrosion of package material both inside and outside
- Temperature of the package and its contents
- Pressure inside the package
- Chemical analysis of gases and their evolution change rate

## 2.7 Containers ageing

The ILW interim storage repositories in the UK are currently stored in both coastal and rural areas [2], close to power plants. This increases the probability of their exposure to sea-salt aerosol, which can create a thin film of salt on to the containers' surfaces, that will act as an electrolyte in humid environments, and cause Stress Corrosion Cracking (SCC) [2]. This type of SCC is a phenomenon referred to as Atmospheric Chloride-Induced Stress Corrosion Cracking (AISCC).

AISCC risks the structural integrity of ILW containers, during both interim storage and the operational phase of geological disposal. Very little data regarding parameters such as induction times and crack growth rates and their dependence on various environmental variables are available [33].

Stresses exhibited by ILW containers are not limited to loading and handling, stresses can also be caused by the increase in content volume when confined by the containers' walls. Increases in the volume of the immobilising cementitious matrix inside the container can happen at reduced rates for hundreds to thousands of years due to the hydration of the cements, or the formation of solid and/or colloidal oxidation products and hydrogen gas, from the corrosion of metals embedded in the cementitious materials [13].

Even if the container walls are designed to handle large stresses from its content load and expanding content volume, over time these stresses will cause the material structure to creep and plastically deform even at room temperature [34]. The creep effect on the material can occur at stresses below the material yield strength. Plastic deformation from

creep in austenitic stainless-steel metals can be detectable after 20 to 30 years of operation [35].



Figure 23:ILW immobilising cementitious matrix [16].

Plastic deformation along with the corrosion of the container wall material, will change the wall thickness of the container. Therefore, it is important to monitor such changes in the wall thickness, to compute the true life-expectancy of every container. Based on the individual container's changes throughout its service. This can be achieved using regular dimensional metrology, for CM&I.

Given that some of the effects discussed can take tens to hundreds of years to show any visible or significant changes to the containers [13] (See Table 2 and Table 3 for numeric details). It is important that the CM&I methods used, allow for a **Non-Destructive Evaluation (NDE)** that is both precise and accurate enough to generate reliable sets of data. That intention is that such techniques can identify any changes in the containers' structures, in the early stages of their expected long storage time.

Item	Corroded thickness ( $\mu\text{m}$ )	
	150 years time frame	500 years time frame
Metal surface in contact with grout/waste-form	6	20
Metal surface exposed to atmosphere	256	870
Metal plate with one surface in contact with grout/waste-form and one exposed to atmosphere	262	890
Metal plate with both surfaces exposed to atmosphere	512	1740

Table 2: Total corrosion of 304L and 316L grade stainless steels over the 150 year and 500 year time frames [3].

Period	Environment	Duration	Corrosion rate ( $\mu\text{m yr}^{-1}$ )	
			Uniform	Pitting
Interim surface storage	Storage building up to 100 % RH, -5 to 35°C	Up to 150 years	0.04	1
GDF during operations	Underground up to 90 % RH, 10 to 30°C	Up to 300 years	0.04	2 <sup>4</sup>

Table 3: Stainless steel corrosion data used in the assessment of container integrity [3].

Based on an external dimensional examination of a number of aged 500 L drums currently stored in the UK EPS1 stores using the structural light scanning method described in Section 2.6, one of the drums scanned displayed [6]:

- Two surface bulges which were **8 mm** and **8.5 mm** proud of the normal drum surface.
- Oversized diameter of **804 mm**.
- The drum's lid was **1.3** degrees out of parallel compared to the rolling rings, with an overall tilt between **0.9°** and **1.6°**.

The tilt was observed in multiple drum samples when rotated on the inspection assays turn table. The other drum sample also showed [6]:

- Slight under height of approximately **10 mm**.
- Some showed out-of-round of up to **11 mm**.

## 2.8 Modelling the environment

A detailed 3D model of the ILW storage environment was created in Solidworks **Computer Aided Design (CAD)** software, to get a true visualisation of the space limitations inside the store. The drum in the CAD models were driven from manufacture drawings from British Nuclear Fuels Limited (B.N.F.L) and Sellafield Ltd, and the Nirex ILW standards detailed in Sections 2.2 , 2.3 and 2.4.

A section of the drums in the workspace include bulging, expansion and warping deformations matching the findings of the Nexia Solution report described in Section 2.7.

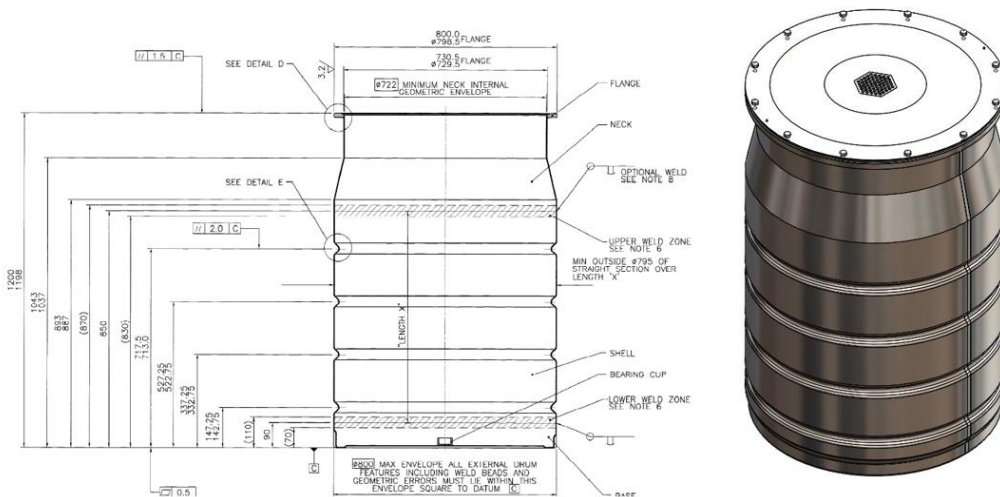


Figure 24: (Left) Section view of manufacturing drawing of 500 L drum acquired from B.N.F.L. (Right) 3D rendered model of 500 L drum created from B.N.F.L manufacturing drawing.

Similar to the drums, the stillages were also modelled alongside the drums, based on manufacturer drawings from Graham Engineering LTD, Serco reports [3] and the Nirex ILW standards detailed in Section 2.3, 2.4 and 2.5. The stillages modelled were assumed to have no deformations associated with age.

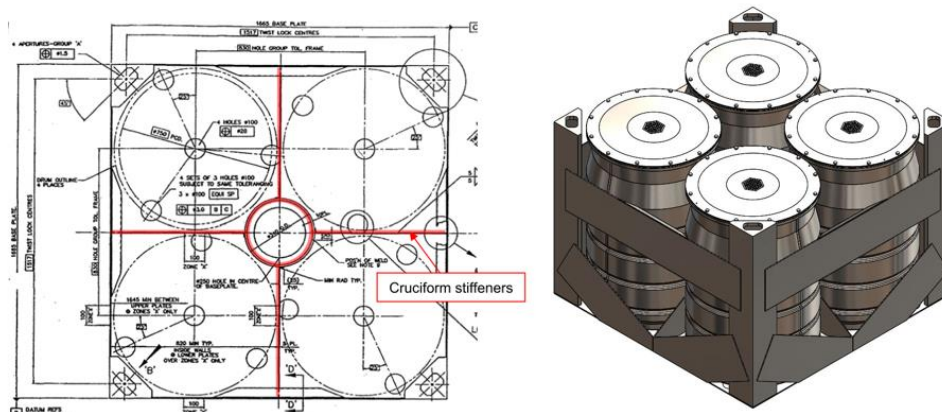


Figure 25: (Left) Top view of a of 500 L stillage from Serco report [3]. (Right) 3D rendered model of 4 x 500 L in a holding stillage created from available manufacturing drawings of a typical stillages.

Once the models of the drums and stillages were complete, an overall model was created to represent the stacked stillages 7 tiers high and 7 tiers wide, as per the expected arrangement in the storage vaults described in Section 2.5. Figure 26 demonstrates a 2D isometric view of the 3D model of the stillage stacks. The 3D model provides a clear view of the spatial constraints and physical limitations between the stillage stacks, and visually highlight possible paths for sensors between the containers. This enables us to highlight the available surfaces for inspection and the challenges to reach them.

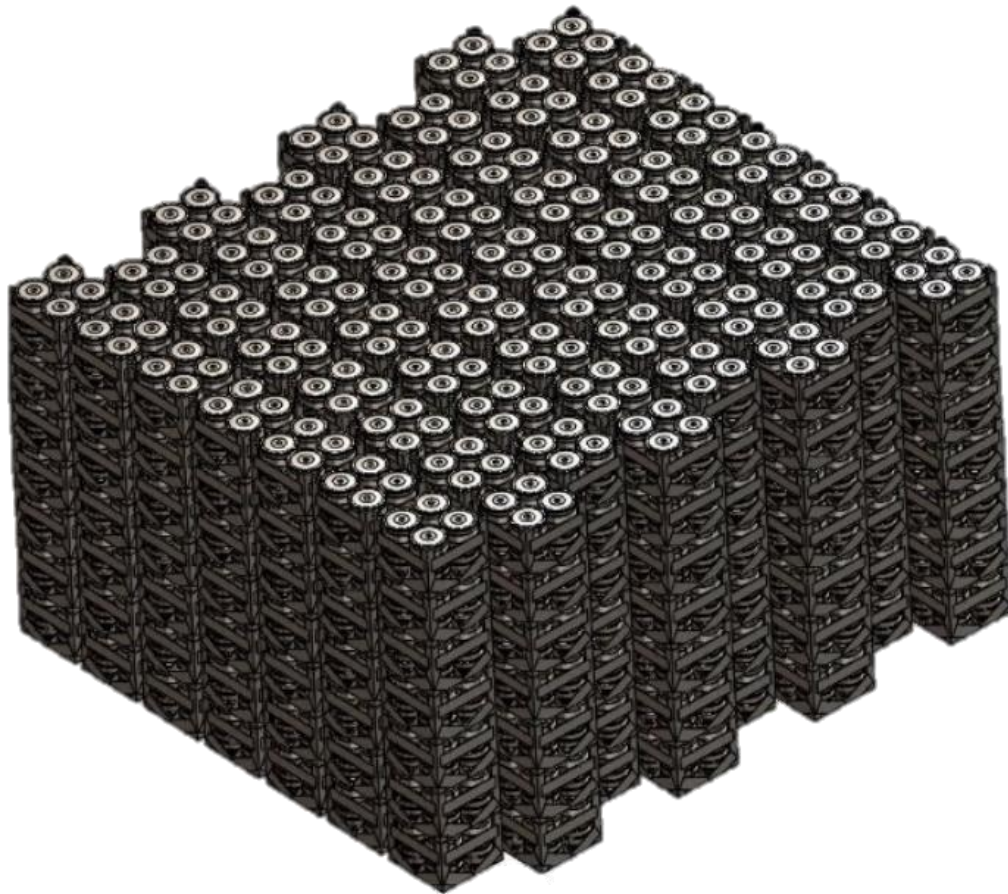


Figure 26: Isometric view of a 7x7 staggered stacking of 500 L ILW drum stillages.

The high-quality rendering of the sensor's point of view captured from different angles of the 3D model, can potentially be used to investigate the possible use of computer visual recognition to detect some of the expected anomalies that may occur in the drum surfaces. These renderings can be distorted, and their quality reduced to simulate the less-than-ideal view expected from the real environment challenges described in Section 2.6 to further verify the suitability of computer visual recognition methods in the restricted real-life scenarios.

A complete investigation on which drum surfaces would be accessible by in an ideal scenario will be discussed in Chapter 3 and proposed methods to access and probe these surfaces will be proposed in 3.3.4.2.3.

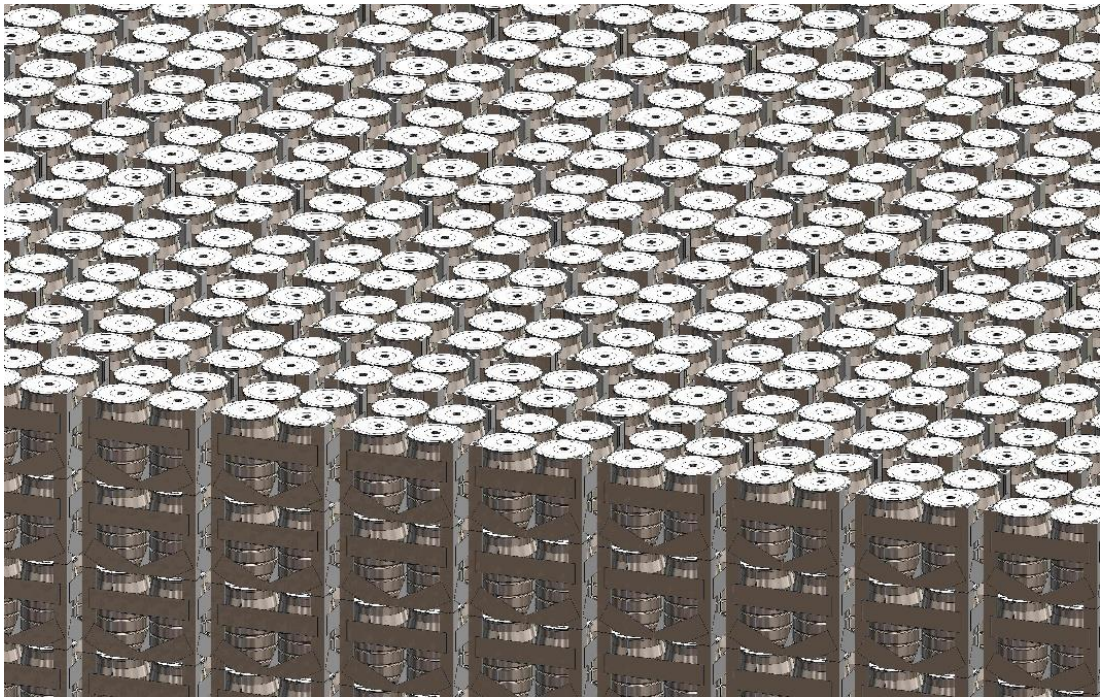


Figure 27: 3D rendering of the densely packed ILW 500 L drum stillage stacks inside an ILW vault.

## 2.9 Summary

A mobile system is required for CM&I of the decommissioning product from retired nuclear power plants and other nuclear facilities while in-situ. The CM&I processes must be able to screen and detect any potential damage that can compromise the 500 years of operation expected from the 500 L ILW drum. The ideal system should be able to detect the 500 L drums' structural **deformation**, external and internal material **corrosion**, **temperature**, internal **pressure** and released **gases**. The CM&I process must be executable while the drums are stacked in their stillages (in-situ) to eliminate the need of handling or moving the drums from their resting place.

To dimensionally represent the spatial constraints and visual limitations expected to be faced by the required mobile CM&I system, a literature review of the nuclear 500 L ILW drums and their environment was conducted and used to create a detailed 3D model of the ILW vault environment.

Any proposed mobile CM&I systems should ideally operate in the already existing retro storage vaults without the need to modify the current vault's structure or storage arrangement. Therefore, the system sensors must be deployable in the **0.23 m** gap between the stillage columns and reach all **4** drums in every tier of the **7** tiers of stillage stacks, with an expected over all stillage stack high of **8.715 m**. The system would ideally be able to reach the far end of the stores that **do not have** built in **overhead cranes**.

The geometrical inspection of the system needs to detect warping and tilting in the 500 L drums in the range of **0.9°** and **1.6°**, diameters with accuracy of at least **3 to 5 mm**, surface bulges in the region of 8 mm and surface rust, to match the current inspection methods reliability.

The system and sensors must operate reliably and achieve the required accuracies in a poorly lit environment with temperature variant of **25 °C** and **35 °C**, and the relative humidity of **70 %** to **85 %**. The sensor location and accuracy must not be compromised by the ventilation air velocity of **10 Km/h**, drum radiated heat output of **2.82 W** and external surface radiation level of **10 mSv/h**.



## Chapter 3: Robotics and coordinate measuring systems challenges

### 3.1 Introduction

This project proposes a novel robotic system that can enter the vaults described in Chapter 2 and perform the CM&I of ILW 500 L drums in-situ. This aims to eliminate the possibility of human exposure or contact with the ILW containers during handling or moving. As well as increase the frequency and quantity of containers being monitored, by also eliminating the need for unstacking and moving them for inspection.

One of the main criteria in the CM&I of ILW 500 L drums, is the observation and detection of any physical structural deformations or anomalies on the drum, caused by the aging process of the drum or its waste form expansion [13] and/or corrosion described in Section 2.7. This can be performed using a **Coordinate Measuring Machine (CMM)**.

CMMs are used in manufacturing industries to measure irregular shapes that cannot be measured easily using basic tools such as callipers and machinist gauges. CMMs operate by probing multiple points on an object surface and calculating the 3D metrological distances between these points. Some CMMs can store multiple points to digitally display and process them in what is commonly known as a 3D-scan or point cloud.

This Chapter will discuss the theory and challenges that may face a mobile CMM in the CM&I of the ILW drums in-situ, and the expected errors associated with a mobile CMM and any supporting equipment required to complement it to create a complete **Coordinate Measuring System (CMS)**. It will focus on the theory and suitability of different types of CMM probing technologies, followed by a review on the existing robotic technologies that can aid in the deployment of task specific mobile CMS.

### 3.2 CMS uncertainty

To create the perfect CMS for a specific task, it is important to understand the challenges and factors that will affect the accuracy and reliability of the tools used to collect the required measurements. There

are 21 main error factors in every CMM that can affect their measurements accuracy [36].

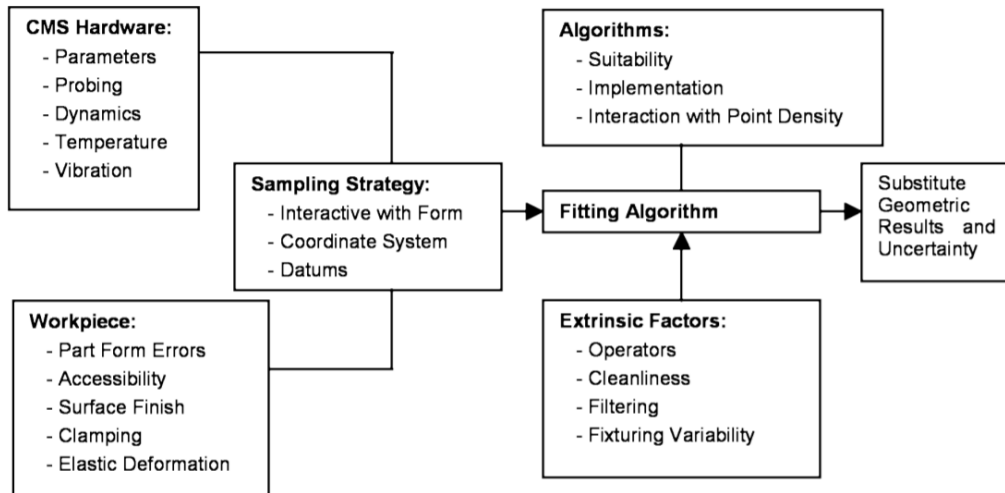


Figure 28: Error components that lead to CMM uncertainty [36].

These factors cannot always be fully eliminated, but the CMS can be designed to limit the CMM error to an acceptable level [36]. Figure 28 illustrates the distribution of the error factors and how they are grouped and Figure 29 lists the factors that can influence the selection of a mobile CMS.

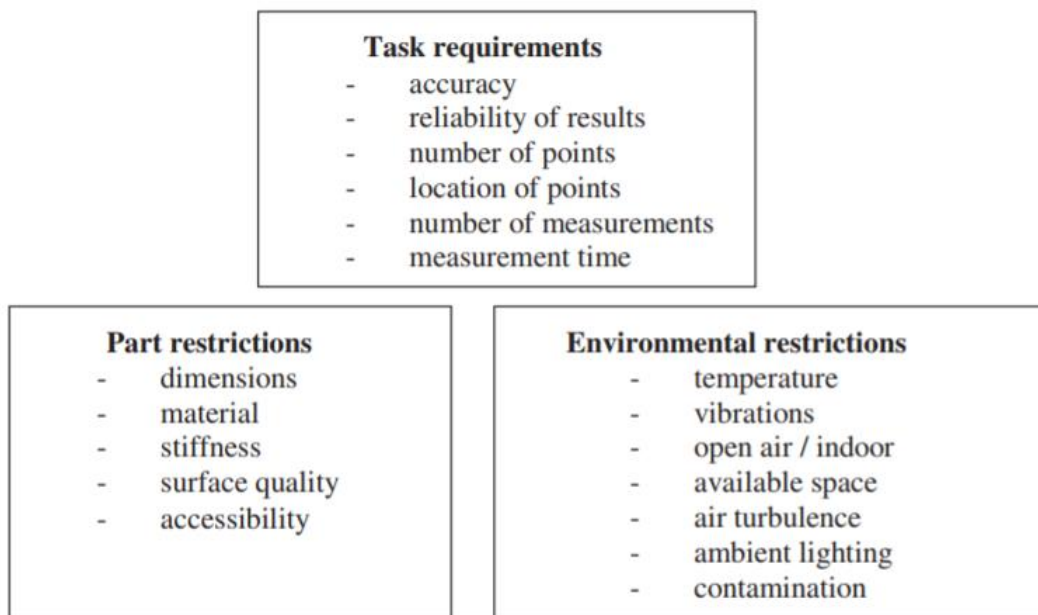


Figure 29: Factors influencing selection of mobile CMS [37].

### 3.2.1 CMS hardware errors

The CMS hardware used in inspecting nuclear assets not only have to adhere to the general CMS requirements, but it must also be able to cope with the ambiguity and harshness of the ILW vault environment. The main CMS hardware errors are due to parameters, probing, dynamics, temperature and vibrations [36].

**Parameters** or parametric error is the difference in the length between two 1-meter measurements, commonly known as calibration. In 1799 a rectangular platinum polished bar was used by the Academy of Sciences in Paris to embody the metric length standard of 1 meter and calibrate measuring tools to. This was redefined in 1983 as the length of the path travelled by light in vacuum during a time interval of  $1/299,792,458$  of a second[38]. In the modern day where neither of these definitions can realistically be used to calibrate every CMM, international defined metric standard calibration methods are used instead. Industrial standards such as ISO10360-2 “E” for length, are used to verify the performance of a CMM when measuring linear dimensions [39]. To determine the CMM calibration to ISO10360-2 “E”, a set of 5 gauges (calibration blocks) with known reference length are measured by the CMM 3 times at 7 different positions. Giving a total of 105 separate length results that are to be used in specifying the system’s calibration error [40]. Similarly, ISO10360-2 “P” test is used to calibrate the CMM volumetric probing, this is done using a reference sphere that is to be probed at 25 evenly distributed points, to calibrate the CMM probes [40].

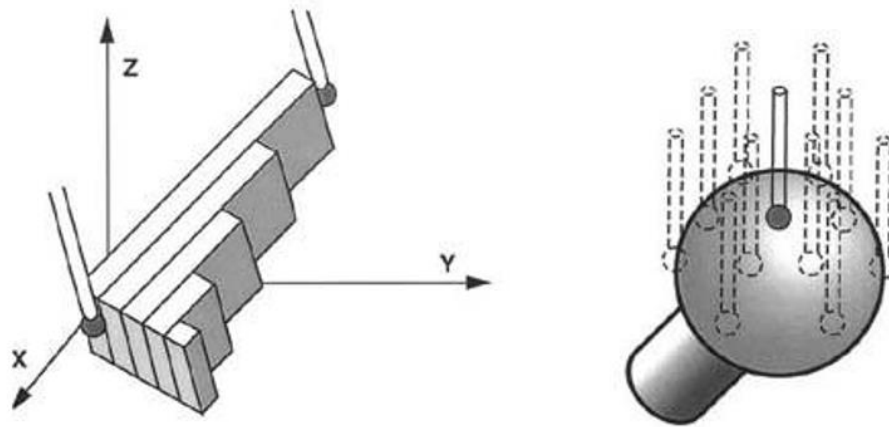


Figure 30: (Left) CMM calibration blocks and probing stylus [40]. (Right) CMM Calibration sphere and probing stylus [40].

By applying such ISO tests on any proposed CMS, the difference between the measured dimensions and the calibration piece dimensions will quantify the parametric errors of the final system. This will minimise the on-field testing of the proposed system and increase its efficacy before deployment into the vaults.

**Probing errors** are uncorrected systematic and apparently random errors caused by the inspection probe itself [36], thus Probing errors will vary depending on the probing technology and mechanism. This will be considered in Section 3.3.

**Dynamic** errors in CMM readings, are caused by the structural dynamics of the machine movement and trajectory, causing the dynamic errors to vary rapidly in time [41]. This means that at a stationary state, the dynamic errors will be localised, and would not affect the overall workpiece dimensional measurement [41]. This can be minimised by dampening and/or pausing the machine movement for a time period, to allow the dynamic vibrations caused by the system movement to attenuate and reach a steady state [41].

Once a CMS reaches a stationary steady state, the dynamic effects in probing caused by the environmental **vibrations** can lead to accidental deviations in discrete-point measurements, or cause an apparent waviness in the measured surface in scanning mode [36][42]. These vibrations can be caused by anything from nearby operating machinery, air movement, seismic activity, or even the CMS own components. The

significance of the vibration errors will depend on the proximity and intensity of the vibration source in relation to the probing accuracy and location.

Finally, the CMS hardware errors caused by **temperature**, are a result changes in the equipment calibration due to temperature fluctuation [36]. This change in calibration is a result of the measuring equipment itself expanding or contracting due to the changes of their temperatures caused by the external environment or the work piece it is scanning. This can possibly be overcome by calibrating the equipment at their expected operation temperature or by compensating for the known changes in the final readings. Consequently, it will be important to have a temperature measurement associated with all the metrological measurements in the ILW vaults to validate or compensate for the temperature error in the metrological measurements.

### 3.2.2 Workpiece errors

The ILW 500 L drums like any workpiece being metrologically scanned by a CMM/CMS, can influence several error factors in the measurements, due to its own characteristics, therefore it is important to understand the ILW drum properties and characteristics to minimise the workpiece errors. **Workpiece** errors are caused by the physical characteristics of the workpiece itself, this includes part form, accessibility, surface finish, clamping and elastic deformation errors [36].

CMM/CMS work by recoding the coordinates of sample points on a workpiece, these points can then be computationally linked to represent the workpiece surface. If the gap between the sample points is larger enough for a defect to exist between the sample points, the defect could be missed by the system resulting in an inaccurate evaluation [43][44]. **Part form errors** are a function of the ratio between the sampling interval and the form error wavelength, and the total number of samples collected [45]. If Fourier transforms are used to compute a wave that interlinks all the sampling points as seen in Figure 31, the wave computed can be used to identify the error magnitude based on the wave's amplitude [45]. Minimising the gaps between the samples can reduce such errors, at the cost of increasing the sampling time.

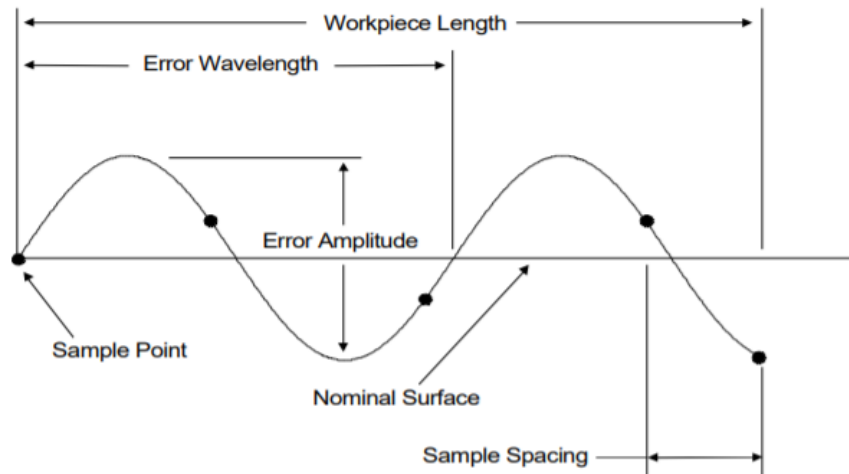


Figure 31: Part form error wavelength in relation to sampling points [45].

Increasing the sampling points density to minimise the **part form errors** during the in-situ inspection of ILW 500 L drums, will be limited by the accessibility to the drums due to the holding stillage structure.

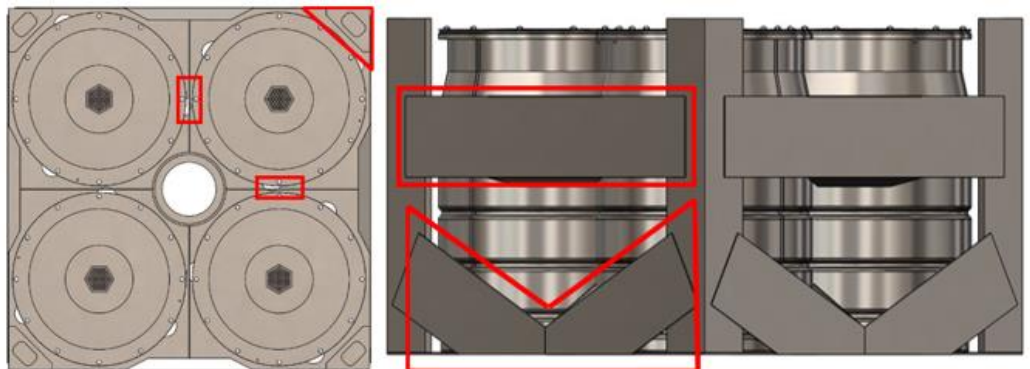


Figure 32: Obstructions limiting the direct line of sight access to 500 L ILW drums in a stillage highlighted in **red**. (**Note:** This only applies to this model of stillage and obstructions in other models may differ.)

The restricted access to the surfaces of interest on the drums will significantly increase the risk of **accessibility** errors where the computationally linked points miss localised dents or deformations hidden behind the stillage structure. Therefore, the probing technology used by the CMS must be able to scan beyond the line of sight to reach these hidden surfaces.

The work piece errors caused by **clamping** and **elastic deformation** are generally a result of the distortion caused by the clamping forces on the workpiece [36]. Given that this project is focused on in-situ inspection, the ILW drums are not expected to be clamped in assays such as described in Section 2.6 Figure 20, thus no workpiece clamping errors are expected.

Finally, the **surface finish** errors can be caused by the surface roughness in relation to the probe size as shown in Figure 33 [36], or the reflectiveness of a shiny surface when using optical probes as will be described in Section 3.3.2.

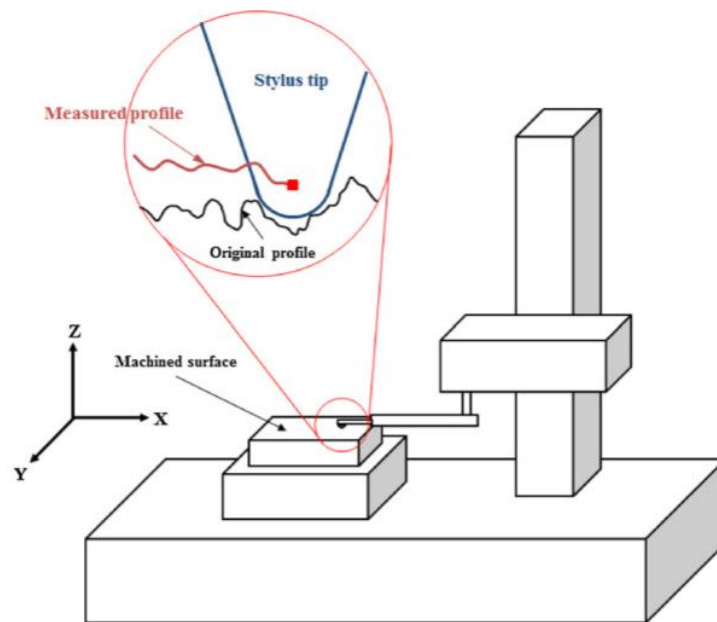


Figure 33: Profile data acquisition by a stylus-type profilometer [46].

### 3.2.3 Sampling strategy

Sampling strategy errors are mainly due to inadequate sampling of complex forms and the uncertainties magnification due to inadequate datums [36].

**Coordinate system** errors can result from incomplete exactness of transferred measurement results between Calibration artifacts and real parts[36]. Computers cannot calculate in real numbers and must convert real numbers into binary values for subsequent processing. This conversion process and the length of the binary value used in the

calculation, is limited by the computing processor architecture and floating points handling methods [47]. This results in some decimal points of irrational numbers to be rounded off, in what is commonly known as the floating-point error[48]. Therefore, any computer processors used on a CMS must have a computational architecture, that can handle the minimum number of decimal places expected from the system [48] in order to achieve .

The datum is a reference point, surface, or axis on an object against which measurements are made. This makes CMM **datum errors** depend on both the measuring mechanism as well as the workpiece [49]. In the case of the CMS that will be proposed to CM&I the ILW 500 L drums, the holding stillage anchor points will be used as the datum points, this will be explained in detail in Section 4.6.1.

For example, the true characteristics of a circular profile are defined by a continuous form [50]. In practice, the radius of nominally round workpieces (ILW 500 L drums) tends to vary from point to point around the periphery [49] [51]. Out of roundness (OOR) or circularity runout, quantifies these variations, this can be a result of manufacturing inaccuracies, deformities, bulges or dents in the round objects. The most accurate way of measuring OOR of a component is by measuring the variations in the radii (runout) of a component from an accurate rotating datum [52], with the difference between the largest and smallest radii being the OOR runout [51] (See Figure 34 for visual clarification). Using different numbers of discrete points, will create different reference runout circles due to the lobe positions [49] which will move the datum and result in different OOR [52].



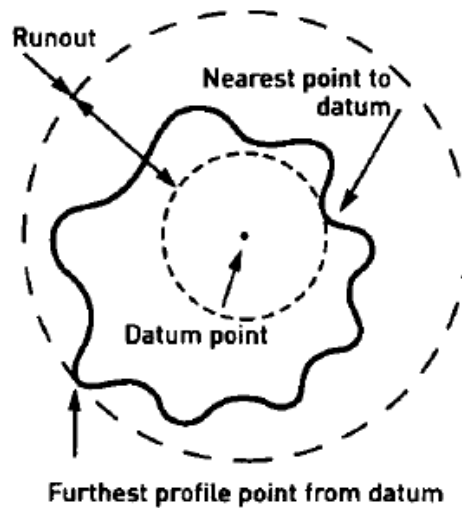


Figure 34: Circularity runout measured from the difference between two circles centred on a datum. One circle coincides with the furthest point on the profile and the other coincides with the nearest point on the profile.

The sampling strategy **interaction with form** (interaction between CMM and ILW containers) generally use a relatively small number of points and extrapolate them to determine the part geometry, these points are either collected at random or equidistant sampling [53]. The use of random sampling can often result in unrealistic representation of the geometric features [53], because it can miss small feature that lay between the random samples such as dents or keyholes and not include them in the extrapolations. Equidistant sampling does not have that problem if the spacings between the samples are smaller than any features that needs to be detected, to ensure that these features are not missed out between the samples. However, it will still be challenged by the CMM access to all the points of interest required to create a true representative geometry, as described in Section 3.3.1.

### 3.2.4 Fitting and scanning algorithm

The algorithm suitability and selection, implementation and interaction with point density, dominate the **algorithms** error categories[36].

Continuing with the example of ILW 500 L drums OOR described in Section 3.2.3, the four main methods to quantify the OOR of an object from CMM readings are [54],

- I. The minimal-radial-separation (MRS)
- II. The least-squares centre (LSC)
- III. The maximum-inscribed circle (MIC)
- IV. Minimum-circumscribed circle (MCC)

Where the reference circle used to determine the out of roundness is determined by the CMM rotating axis or coordinate axis datum point. Linear and non-linear fitting algorithms with varying computational complexity can be used to determine the reference circles used to quantifying the OOR using any of the methods given, with varying results depending on the fitting algorithms **implementation** [54]. This will also be influenced by the **point density** constraints caused by access restriction and limited interaction with form will skew the OOR results as described in Section 3.2.3.

The **suitability** of the fitting algorithm will depend on the type and quantity of data acquirable by the proposed CMS. This will depend on the type of probing technology used by the CMS and its limitations. This will be the subject of Section 3.3 and the possibility/suitability of fitting data from different probing technologies will be evaluated in Section 3.3.5.

### 3.2.5 Extrinsic factors

**Operators** errors are generally a result of variations in the operator to machine interactions and operators' selectable options [36]. Thus, this may be reduced by simply reducing the human machine interaction and automating as much of the scanning process as possible. **Filtering** Errors are a result of the differences in filtering parameters used by the different operators to achieve smooth readings that they can comprehend based on their individual skill level [36]. This can be reduced by reducing the human machine interaction and automating the filtering process to use uniform filtering parameters/settings for consistencies. It is also important to note that **filtering** errors can be associated with the **fitting** and evaluation **algorithms** errors even in the absence of human-machine interaction, because the fitting parameters can change depending on the data and scenarios being processed.

**Fixture variability** is very similar to the clamping errors discussed earlier in Section 3.2.2 from the ILW 500 L drum point view, thus can potentially

be ignored given that the scans are expected to be performed in-situ without having to move or clamp the drums using any fixtures. However, the errors caused by fixturing and clamping of the mobile CMM itself into the place from which it will perform the scans must be considered.

**Cleanliness** errors are caused by contaminants between the scanning probe and the workpiece [36]. In the case of an ILW 500 L drum in an ILW storage facility, contaminants can include dust and aerosol particle from the constant ventilation [55]. The composition and quantity of dust particles in an ILW storage facility varies between vertical and horizontal surface. A study at Treated Radwaste Store (TRS) located at Winfrith in the UK, detected chloride aerosol particles concentrations range from 0.75 to 11.4  $\mu\text{g}/\text{cm}^2$  on the vertical surfaces and 13  $\mu\text{g}/\text{cm}^2$  on the horizontal drum surfaces [55]. Other contaminants include oxalate, sulphates, nitrates and carbon [55]. The presence of such a minute amount of contaminant particle between the probes and workpieces may be insignificant in the range of measurements accuracies expected by the proposed CMS, however this facility is not as close to the coast as some other stores, and higher levels of aerosol salt deposits may be expected in other storage facilities [55].

### 3.3 Geometrical scanning tools

This Section will describe the different industrial CMM probing technologies currently available and review their suitability and sources of measurement errors specific to in-situ CM&I of the ILW 500 L drums in accordance with Section 3.2.

CMMs can utilise different types of sensing probes and techniques to measure and calculate the overall shape of a given item. The sensing probe is one of the most important elements of a CMM, and is responsible for the overall accuracy of the dimensional measurements [56]. Industrial CMM probing systems must ensure reproducibility of the sensing sub-process in the sub-micro-meter range [42] [57].

#### 3.3.1 Tactile probing

Most industrial CMMs rely on tactile probing because of its high accuracy and reliability [58].

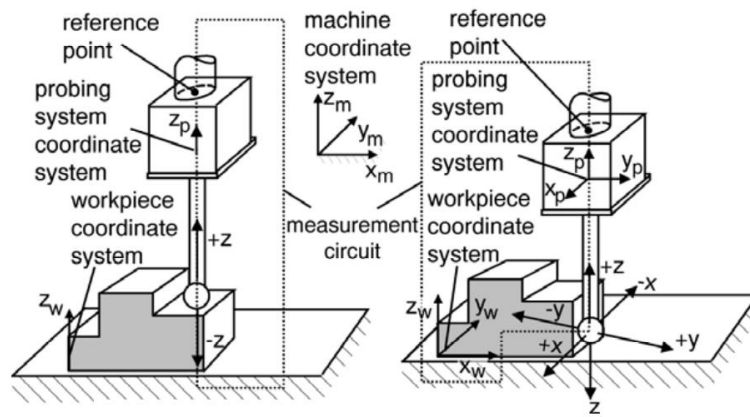


Figure 35: General tactile probing system. (Left) single axis probing. (Right) 3 dimensional probing [42].

Tactile based probing relies on mechanical contact of the stylus tip with the object of measurement [58]. The physical force from the contact between the stylus and the workpiece, triggers limit switches or other mechanisms to register the stylus contact event [58]. The position of the stylus itself is then measured using path measuring systems, generally in all three coordinate axes, to establish the stylus contact point, relative to a predetermined datum or origin [58].

Although Tactile probing techniques can provide reliable industry proven means to metrologically inspect the ILW 500 L drums geometry, they will be challenged by the access space limitation, caused by the compact drum stacking arrangements described in Section 2.4, 2.5 and 3.2.2. The tight gaps between the stillages and drums may inhibit the tactile sensor arm from reaching the points of interest on a given drum while in-situ. This could be overcome using non-contact probing techniques.

### 3.3.2 Optical scanning

CMM probes are not limited to tactile sensing probes, optical and magnetic probes can be used where physical contact with a system is not possible. Camera triangulation and photogrammetry, Laser Range Finders (LRF) , Structured Light (SL) are some of the many tools/probes used in non-contact metrological scans of complex components [37].

Visual structural inspection using video cameras deployed by robots is commonly used in the nuclear industry to detect cracks, pitting or

corrosion [7]. Visual inspections can be expanded to photogrammetry, where still images or videos of three-dimensional objects can be used to compute the true dimensions of these objects from their images. Photogrammetry uses angle measurements of trackers/features from different two-dimensional images of captured from different angles and location, to create a three-dimensional surface-meshes of the objects in the images [37].

3D LRFs can be robotically deployed to locations of interest to gain direct line of sight where they can acquire point cloud scans of the surfaces of interest. Different point cloud scans can then be stitched/fused together using distinctive features in the point clouds of the scans. Alternatively if there is no distinctive features in the point clouds to use in the stitching/fusing algorithms, the location information of the scanner itself could be obtained from the deployment robot's inertial measurement unit (IMU), and used as a datum or reference point in the data stitching/fusing algorithms [59].

LRFs emit a laser beam towards a target and calculate the distance between it and the target using the reflected beam's Time of flight (T.O.F). T.O.F is the time for the signal (laser light) to travel from the LRF sensor source to a target and back [59]. LRFs only needs 1 % signal reflectivity to operate [37], however highly reflective (shiny) stainless steel surfaces and close-range inspections can also be problematic and negatively affect the accuracy of the measurements [60].

A number of commercially available optical based dimensional scanners such as "Cloud Compare", "ATOS", "Geomagic" and "GOM" have been tested by the NNL and Sellafielld in the UK, and provided very promising and reliable results [12][28][6].

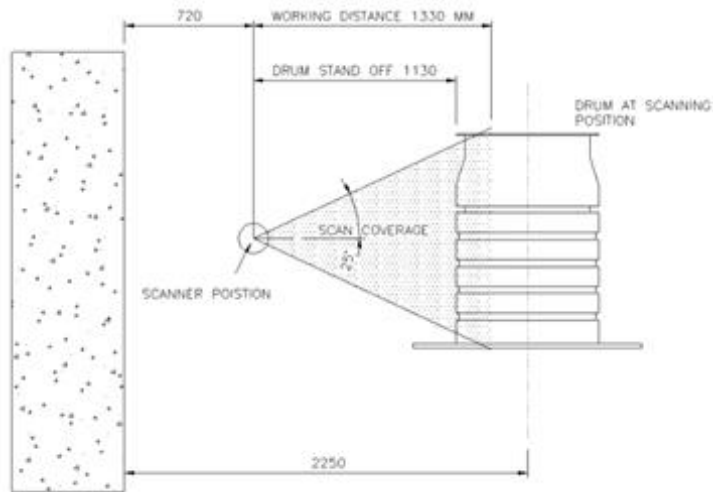


Figure 36: Optical scanner setup used by Sellafield plant to test optical scanners ability to scan ILW 500 L drums inside a radioactive environment [28] (See Section 2.6 Figure 20 for an image of a scanner inside EPS1).

NNL research concluded that to have a stationary optical/laser scanning system, 2 or 3 fixed scanners will need to be placed 2.5 to 3.0 meters from ground, with a tilt angle up and down of about 60 °, to scan the drums sides, top and bottom [28]. Each scanner will be expected to require calibration and will degrade overtime due to exposure to nuclear radiation [28].

Unmanned Aerial Vehicles (UAV) have been previously used to deploy video cameras to perform experimental metrological inspection of ILW 500 L drums, to detect waste form expansion in a lab environment [61].

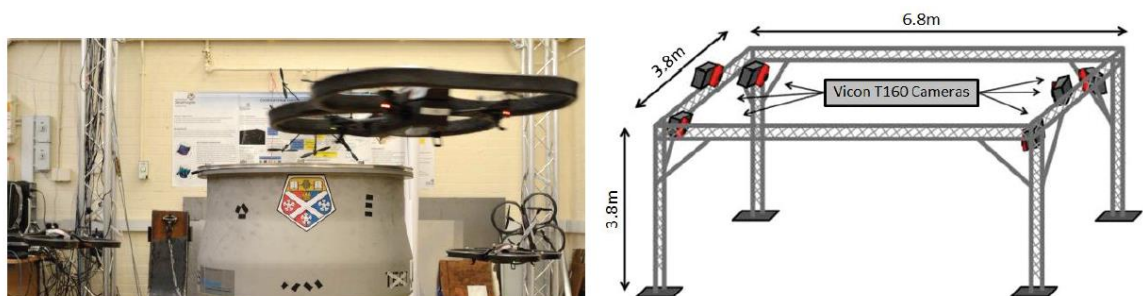


Figure 37: (Left) 3 AR.Drones flying in the testbed. (Right) Testbed setup with frame supporting 6 Vicon T160 positioning cameras [61].

The setup used quadrotor UAVs to fly around an empty ILW 500 L drum sample to capture images of the drum from different locations and angles, which were then used to create a three-dimensional surface-mesh of the drum [61]. The drum was placed in the middle of a testbed setup (Figure 37) where the UAVs used Vicon positioning cameras for attitude control and navigation around the point of interest (the ILW 500 L drum) [61].

If an optical sensor is to be placed in the gaps (0.23 m) between the stillage stacks for in-situ inspection, it will likely be less than 100 mm away from the containers to account for the sensor size, deployment mechanism and clearances. This is significantly less than the 400 mm spacing recommended [28] in Section 2.6. Moreover, even though optical scanning does not require the probe (camera lens/optical sensor) to be able to physically reach and touch every point of interest to perform a geometrical scan, optical scanners still require a direct line of sight from the sensor to the point of interest. This will limit the applicability of optical scanners in the in-situ scanning of ILW 500 L drums due to the blind areas caused by holding stillage structure (areas not in direct line of sight cause by obstacle described in Figure 32).

### 3.3.3 Scanning beyond obstacles

High-energy imaging radiography and tomography can provide a solution to overcome the blind spot challenge faced by optical scanners. High-power X-rays beams have been used to scan through medium sized nuclear waste drums and were able to penetrate through drum material and content to create 2D slices of points of interest as seen in Figure 38 [30].

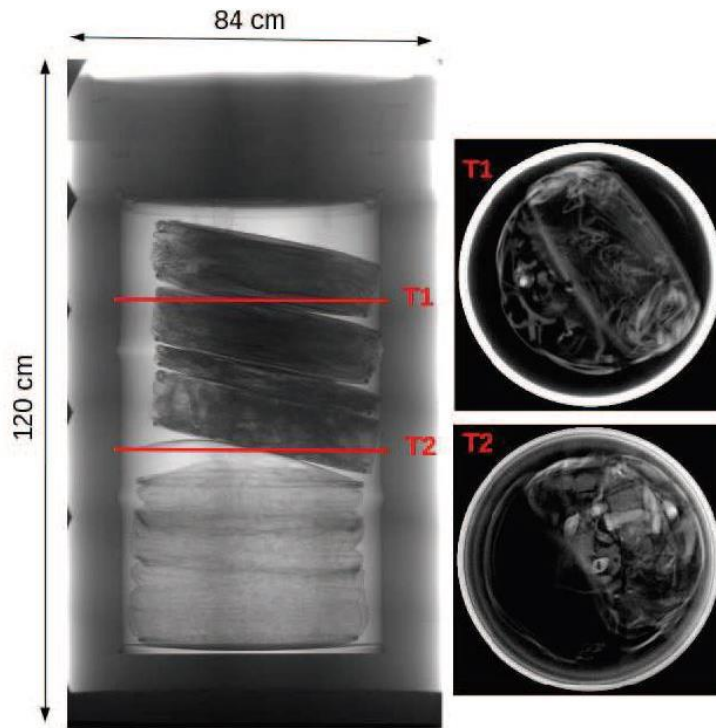


Figure 38: (Left) Fusion of 18 radiographies of a medium-sized nuclear decommissioning drum taken at different drum positions. (Right) two tomography slices extracted from cone-beam computerized X-ray tomography acquisitions [30].

Instead of the 2D tomography slices, X-ray tomosynthesis can directly create 3D representations of the volumes of interest, which are particularly suitable for delamination defects detection between external envelope and internal binding concrete [31] seen in Figure 39 , and allows thorough control of the periphery of the larger drums in a few tens of minutes [31].

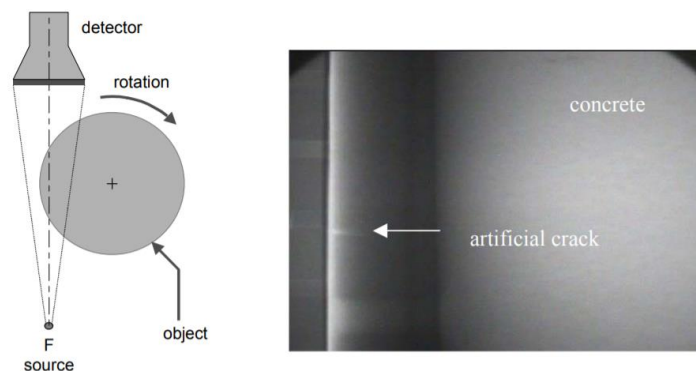


Figure 39: Tangential tomosynthesis, geometry (left) and example of tomosynthesis result (right). [31]



Industrial tomographs are generally not suitable for inspecting large parts/structures, because the tomographs equipment themselves will have to be equally large to provide a large enough scanning volume for parts/structures to fit in [58]. This eliminates its use in scanning a large object such as a complete ILW vault or an individual ILW stillage stack and removing individual drums to a tomograph scanning volume defeats the in-situ inspection target.

Given that the X-ray can penetrate through the ILW 500 L drums' surfaces, they should also be able to penetrate through stillages structure (made from the same materials as the drums [3]) and directly access the drums surfaces. However this will be challenged by, the large size of the equipment required to generate the high energy X-ray beams [30][31] which will need to fit between the stillage stacks.

Moreover, the X-ray detector will have to be positioned between the inside the stillages between the drums which will be challenged by the spatial constraints. If the X-ray is positioned outside the stillage the X-ray will have to penetrate through both sides of the stillage, 2 drums and their contents which will all be superimposed on a single scan image. This would complicate the defect identification due to the clutter in the scans.



Figure 40: (Left) Linac Mini-Linatron Varian. Electrons are accelerated from the left (electron gun side) to the right (target side). The length of accelerating cavity is 1.2 m [30]. (Right) Example of waste drum in concrete package in front of an X-ray detector [31].

Muographs on the other hand are capable of non-invasive scanning massive structures without the need of large equipment. This was demonstrated in the scanning of the King Khufu pyramid in Giza, which allowed scientist to detect a previously unknown void inside the pyramid

[62] [63]. Muon radiography is capable of scanning area ranges from tens of centimetres to hundreds of metre square, and muon tomography is capable of scanning areas in the centimetre to tens of centimetres range [63].

Muons are unstable subatomic particle created when cosmic rays interact with the earth's atmosphere. Once the muons are created, they travel with high energy in a straight line towards the ground but are slowed or deflected by electrons and proton in matter. Muon particles average energy is approximately four orders of magnitude that of a typical X-rays, allowing them to penetrate through thick materials, lead, and the radiation shielding of nuclear waste containers [64].

Muon telescopes (Figure 41) are used to detect the cosmic muon trajectory before and after it is deflected by matter (element in an object), these trajectories are then used to compute the location and size of different elements in the object. Such a technique was able to detect uranium elements locations inside a heavily shielded nuclear waste container in Sellafield [64] as demonstrated in Figure 42.



Figure 41: (Left) The Lynkeos Muon static Imaging System installed at the Lynkeos Technology fabrication facility, used to scan ILW containers [64]. (Right) MURAY mobile muon telescope [63].

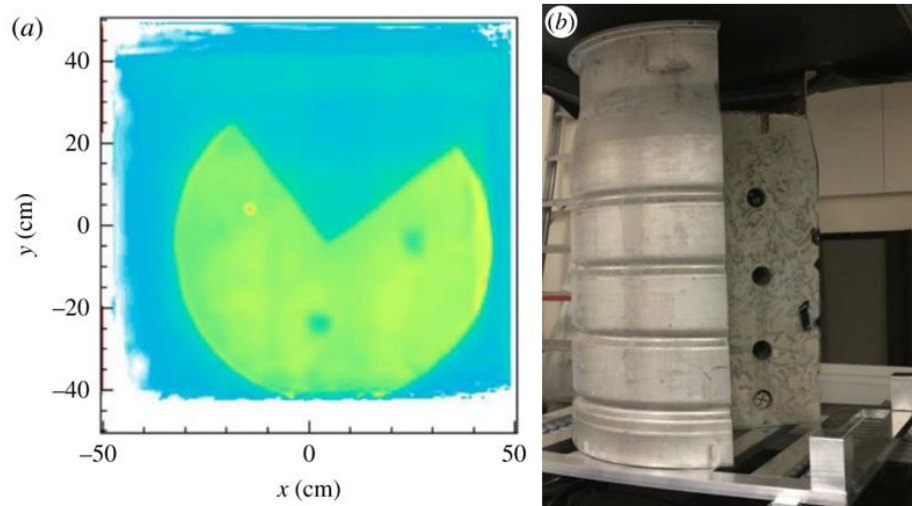


Figure 42: (a) Detection of uranium metal (red region) inside an ILW 500 L drum replica using a muon imaging system at Sellafield UK. (b) cross section of the ILW 500 L drum replica in which the Uranium was placed [64].

The extreme penetration capability of muography comes at the cost of time. A single muograph image can take many days and in some case month to develop, because it is a passive system that relies on muons generated by cosmic activities and not a controlled muon source [63] [64] [62]. This makes muography unsuitable for moving objects and time sensitive applications [63]. In the ILW vault scenario, it will be challenged by the space limitation available to fit the detectors in the ideal places for individual drums' scans.

### 3.3.4 Ultrasonic inspection

Unlike vision-based inspection methods, ultrasonic wave can reach parts of a structure that are not in direct line of sight of the sensor. Ultrasonic waves can be directed to travel into, on, or along a material surface to follow a structure's bends and reach hidden locations away from the sensor line of sight [65]. This is often done during the inspection of pipework where the bottom side is resting on the ground or partially buried, and not accessible [66]. Most commercially available ultrasonic transmitters and receivers use piezoelectric transducers for the wave generation and receiving. Piezoelectric transducers convert electrical

signal oscillations into mechanical oscillations (vibrations/acoustic waves) and vice versa to generate and receive acoustic signals.

Ultrasonic waves of a known velocity ( $V_{wave}$ ) can be generated on or through a material using transducers, and the time it takes the wave to travel from the transmission point to the receiving/detection point, commonly known as **Time Of Flight (T.O.F)**, can be used to calculate the distance the wave travelled. This distance measurement from T.O.F can be performed in different directions to create a complete map of the item being inspected [67].

#### 3.3.4.1 Ultrasonic transducers coupling

When a piezoelectric ultrasonic transducer is placed on a workpiece for inspection, the significant difference between the acoustic impedances of the air gap lying between the transducer and the workpiece, causes a significant portion of the acoustic energy from the transducer to be reflected back to its source, instead of travelling towards the test subject, via that air gap [68]. The specific acoustic impedance of a material is calculated using,

$$Z = \rho c \quad \text{Equation 1}$$

Where (Z) is the acoustic impedance ( $Kg\ m^{-2}s^{-1}$ ),  $\rho$  = the density of the material ( $Kg\ m^{-3}$ ), and  $c$  = the speed of sound in the material ( $ms^{-1}$ ). The reflection coefficient (R) of an acoustic wave travelling from one medium of a given acoustic impedance  $Z_1$  to another of impedance  $Z_2$  is

$$R = \frac{Z_1 - Z_2}{Z_1 + Z_2} \quad \text{Equation 2}$$

According to Equation 2 the reflection coefficient (R) will be closer to 1 if  $Z_2$  is many magnitudes smaller than  $Z_1$ , causing most of the wave to be reflected back to its source. This loss of energy is avoided in most commercially available piezoelectric transducers by filling the gap between the transducer and the workpiece with acoustically matching **coupling** mediums such as oil, grease or water [69], that have an acoustic impedance ( $Z_2$ ) that matches the source ( $Z_1$ ) to reduce (R) closer to zero. Water has an acoustic impedance of  $1.476 \times 10^6\ Kg\ m^{-2}s^{-1}$  [70], which

will significantly reduce the reflection coefficient ( $R$ ) of a wave travelling into it according to Equation 2, compared to air that has an acoustic impedance of  $3.850 \times 10^2 \text{ Kg m}^{-2} \text{ s}^{-1}$  [70]. The insertion of a wave transmitted from a ceramic transmitter to air is typically around -90 dB [71] due to the wave reflection. The ideal coupling medium would (See Figure 43) have an acoustic impedance that is close to matching both the ceramic piezoelectric transmitter and the material to be inspected to reduce the reflections at every stage to the waves journey and maximise efficiency of the acoustic wave energy transfer.

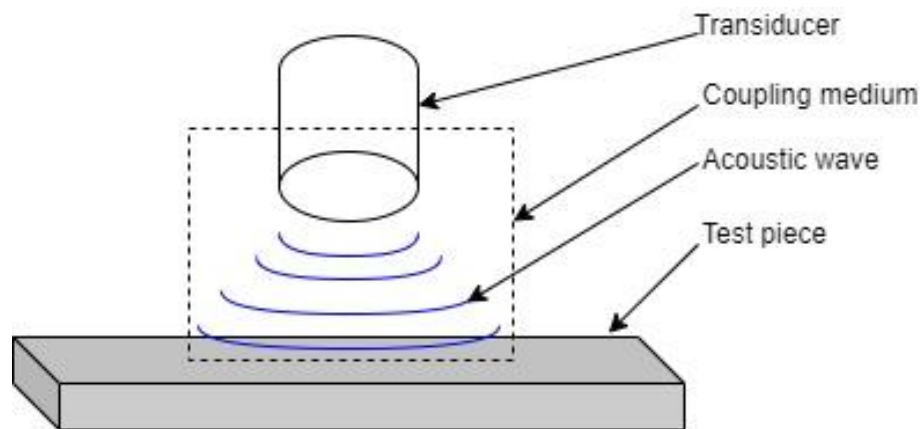


Figure 43: Acoustic wave travelling between a transducer and a workpiece.

If an ultrasonic wave travelling through air interacts with the stainless-steel surface of an ILW drum with impedance of  $44.66 \times 10^6 \text{ Kg m}^{-2} \text{ s}^{-1}$  [70],

$$\begin{aligned}
 R &= \frac{Z_{air} - Z_{stainless\ steel}}{Z_{air} + Z_{stainless\ steel}} \\
 &= \frac{3.850 \times 10^2 - 44.66 \times 10^6}{3.850 \times 10^2 + 44.66 \times 10^6} \quad \text{Equation 3} \\
 &= -0.99998
 \end{aligned}$$

This means that 0.99998 (99.998 %) of the waves will be reflected and only  $2 \times 10^{-5}$  (0.002 %) of it will travel into the stainless steel. The negative sign indicates that the reflected wave is  $180^\circ$  out of phase with the incident wave. On the other hand, if water coupling was used,

$$\begin{aligned}
 R &= \frac{Z_{water} - Z_{stainless\ steel}}{Z_{water} + Z_{stainless\ steel}} \\
 &= \frac{1.476 \times 10^6 - 44.66 \times 10^6}{1.476 \times 10^6 + 44.66 \times 10^6} \\
 &= -0.93602
 \end{aligned}
 \tag{Equation 4}$$

0.936 (93.6 %) of the waves will be reflected and 0.06398 (6.4 %) would travel into the stainless steel.

Water or liquid content in coupling fluids can act as a nuclear moderator and increase the rate of fast neutrons thermalization, a 1 % increase in the moisture of radiation shielding cement increases the effectiveness of fast neutron thermalization by 15 % [72]. Thermalized neutrons have a higher probability of being absorbed by neighbouring radioactive isotopes and sustain a thermal chain reaction [73]. Therefore, the use of any ultrasonic transducers that rely on a liquid-based acoustic coupling must not be considered. Alternatively, dry Acoustic coupling mediums made from soft materials can be an option to bridge the air gap between the transducer and the workpiece [74].

Dry acoustic coupling mediums are placed in the gap between the transducer and the workpiece, and clamping force is applied to sandwich it in place to expel out all air gaps/bubble to create a suitable matching coupling medium for the wave to travel in [74]. This makes the surface quality of the workpiece an important factor in the coupling efficiency because rough surfaces can trap air between them and the dry coupling medium causing insertion losses as the waves travel through the air bubbles. Moreover, the required forced contact between the dry coupling material and the ILW containers may contaminate the dry coupling material with radiated particles, or the salt deposits described in Section 2.7 [55]. This may transfer the contaminant particles from one drum surface to another drum and increase the chances of cross contamination between the drums and/or stress corrosion cracking [2]. This can be avoided by regularly cleaning or replacing the dry coupling materials, however that will slow the inspection process and increase its complexity, especially in terms of recycling or decommissioning the contaminated dry coupling materials. This leaves non-contact ultrasonic transduction methods as the most viable method for the inspection of the ILW containers.

### 3.3.4.2 Non-contact ultrasonic wave generation

Contact free generation and detection of acoustic waves into and from a workpiece can be achieved in four main ways, Pulsed laser generation, optical holographic or interferometric detection, **Electro-Magnetic Acoustic Transducers (EMATs)**, and Piezoelectric transducers with air(gas)-coupling [69].

#### 3.3.4.2.1 *Optical ultrasound generation*

Laser beam ultrasound generation and detection permits non-contact ultrasonic measurements in both electrically conducting and non-conducting materials in difficult to reach and hostile locations, using three different mechanisms, radiation pressure, thermo-elasticity, and ablation [69].

Out of these three mechanisms, radiation pressure is the least efficient and is not used in practical application [69]. Laser thermoelastic acoustic wave generation works by inducing a thermal energy into a finite depth of a material using lasers. This causes volumetric changes to the material at the locations of laser exposure due to thermal expansion, which consequently create an elastic wave (acoustic wave) in the material [69]. To optically produce high amplitude/energy waves that would be capable of travelling long distances and/or be easier to detect by the receivers laser ablation may be required [69].

When a workpiece material absorbs the laser energy during the laser ablation process, a very thin layer of the material can evaporate causing slight surface damage to the workpiece [69]. This makes laser ablation not suitable for long term repetitive inspection of the same test surfaces due to the regular long-term damage to these surfaces. Periodical long term inspection of the ILW drums is one of the project aims, which makes the thermoelastic process the only optical method that is truly non-destructive and still capable of generating an ultrasonic wave for non-destructive evaluation purposes [69].

#### 3.3.4.2.2 *Electro-Magnetic Acoustic Transducers (EMAT)*

EMAT Transducers eliminate the need of acoustic coupling fluids by generating the wave within the material itself using two methods. Using

the Lorentz force when the workpiece material is electrically conductive or by magnetostriction when the workpiece material is ferromagnetic [75][76].

Both methods of generating the ultrasonic wave using EMATs in the inspection of the ILW 500 L drums are challenged by the austenitic 316L stainless steel from which the ILW drums are made [15] [18]. 316L stainless steel is non-ferromagnetic [77], and have a high electrical resistance ( $74\mu\Omega/\text{cm}$ ) compared to common mild steels and aluminium alloys. For comparison 316L stainless is almost 10 times more electrically resistive than aluminium and about 5 times more than mild steel [78].

In paramagnetic/ non-ferromagnetic materials, EMATs induce ultrasonic waves into a workpiece using two interacting magnetic fields. A relatively high frequency (RF) electromagnetic field in the range of 0.5 Mhz to 10 Mhz is generated by the EMAT's electrical coils, and a low frequency or static field generated by the EMAT's magnets [79]. Alternating current coils inside the EMATs are used to generate eddy currents in paramagnetic material's surfaces [75]. The interaction between the magnetic fields and the eddy currents generate a Lorentz force in a manner similar to an electric motor, which generate the vibrations/waves into the workpiece [79]. This reduces the EMAT effectiveness due to the practicality of the size of magnets required in their design to react effectively with the eddy currents generated by the EMAT's electromagnetic coil [80]. Figure 44 demonstrates the mechanism in which an EMAT generates an ultrasonic shear wave in a workpiece using Lorentz forces and the direction of the waves in relation to the magnetic fields and eddy currents.



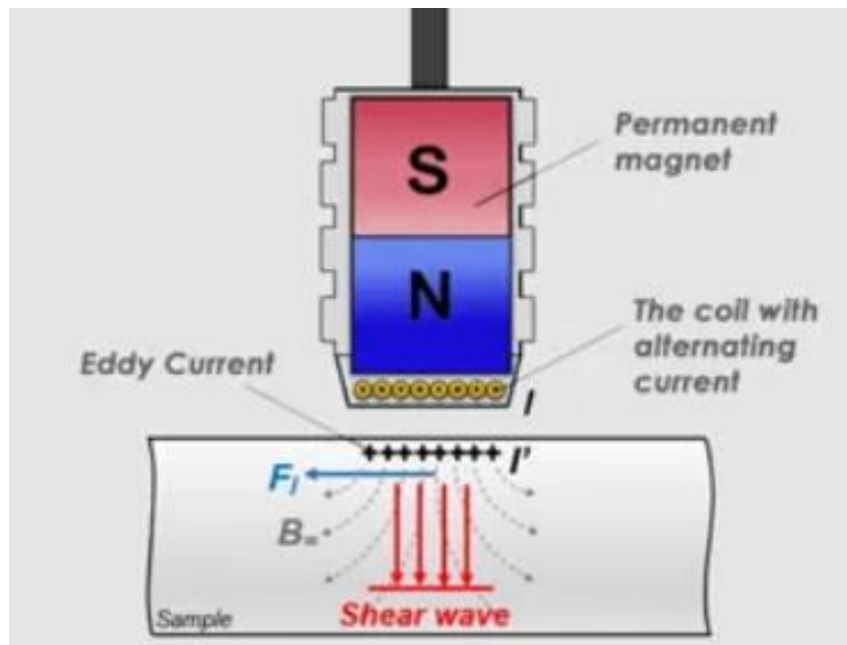


Figure 44: Mechanism in which an EMAT generates an ultrasonic shear wave into a workpiece, magnetic field ( $B_m$ ), Lorentz force ( $F_l$ ) and Eddy current ( $I^e$ ).

The ringing effects in the EMAT's magnets limits them to pitch-catch arrangement where the transmitter and receivers are different elements separated physically [80], thus different access points for the transmitter and receiver will be required to inspect the ILW drum effectively while in-situ.

#### 3.3.4.2.3 Gas(air)-coupled piezoelectric transducers

Gas(air)-coupled piezoelectric transducers operate in the same manner as a typical liquid coupled piezoelectric transducer (explained in Section 3.3.4). Air-coupled piezoelectric transducers simply output high enough energy to induce a detectable ultrasonic wave into a workpiece after all wave energy losses caused by,

- 1- The insertion losses as the signal is transmitted from a ceramic piezoelectric transmitter to air as described in Section 3.3.4.1 (typically -90 dB) [71].
- 2- Kinetic losses as the wave travels through the air as a longitudinal wave from the transmitter to the workpiece (attenuation).
- 3- Portions of the longitudinal wave missing their target (workpiece) due to the non-matching surface profile of the transducer and the

sample [81] (Irregularities in the surface curvature in the case of deformed ILW 500 L drums).

- 4- The majority of the wave being reflected away by the target material acoustic impedance mismatch with air (more than 99%) before the rest is refracted at different angles and speeds into the workpiece according to Snell's law [82] [81] (refer to Section 3.3.4.1 and Section 5.2.2 for details).
- 5- Kinetic losses as the wave travels through or along the workpiece surface as Rayleigh or Lamb waves [82] [81].
- 6- Kinetic losses as the wave travels through the air as a longitudinal wave from the workpiece to the receiver.
- 7- Portions of the wave travelling from the workpiece towards the receiver missing their target (receiver).
- 8- Portions of the wave being reflected away by the receiver ceramic piezoelectric surface due acoustic mismatch.

The refraction of the longitudinal waves into Rayleigh or Lamb waves as they contact the target follows Snell's law [82] [81], and will depend on the longitudinal wave's properties and environment, as well as the target's mechanical properties. This will be explained in detail in Section 5.2.2.

The ultrasonic wave mode and frequency will determine the ultrasonic wave's velocity, making the wave velocity a variable rather than a constant, which complicates the calibration and distance measurements using the T.O.F. The relations between the wave modes, wave frequencies and wave velocity are obtained using dispersion curves, Section 5.2.2 will explain dispersion curves in details, and 5.6 will explain the real life inconsistencies that will cause the ultrasonic waves velocities to vary as they travel around the drums' shells.

### 3.3.5 Geometrical scanning tools evaluation

Based on the literature presented in Section 3.3 the following can be presumed.

Sensor	Advantage	Challenges
<b>Tactile</b>	Accurate, dependable and industry proven method of metrology.	Requires access and contact with the ILW containers' surfaces.
<b>Optical</b>	Proven in the inspection of the 500 L ILW.	Requires direct line of sight. May be affected by containers' surfaces reflectivity.
<b>X-ray</b>	Can penetrate through the stillage structures to inspect the ILW drums beyond line of sight.	Bulky equipment that requires access to opposing sides of the workpiece.
<b>Muography</b>	Completely noninvasive and can even inspect the content of containers while in-situ.	Too slow (requires many weeks for a single image).
<b>Contact ultrasonic</b>	Accurate, dependable and industry proven method of metrology/inspection. Commercially available in compact hand-held forms.	Coupling fluids contaminate the containers surfaces and risk radiation neutrons thermalization.
<b>Optical ultrasonics</b>	True non-contact metrological inspection.	May require ablation which will be damaging in repetitive inspection.
<b>EMAT ultrasonics</b>	True non-contact metrological inspection. Commercially available in compact hand-held forms.	Challenged by the non-ferromagnetic and low electric conductivity of the ILW containers.
<b>Air-coupled ultrasonics</b>	True non-contact metrological inspection. Commercially available in compact forms.	Accuracy is challenged by the environment and workpiece characteristics.

### 3.4 Proposed scanning tools for in-situ inspection of ILW containers

To overcome some of the probing technologies challenges described in Section 3.3 and evaluated in Section 3.3.5, multiple probing systems may be required to compensate for each other's shortcomings. This can be in the form of three data sets that complement each other.

1. Video imagery
2. 3D Laser point cloud scans
3. Ultrasonic inspection/scans

#### 3.4.1 1<sup>st</sup> data set: Video imagery

Video cameras deployed using a mobile robot is proposed to collect the first data set. This will offer the detection of surface cracks and corrosion or pitting as commonly done in nuclear assets inspection [7].

Although the precursor research work described in Section 3.3.2 successfully used camera images in metrological photogrammetry of ILW 500 L drums cameras [61], it used large number of tracker points and features (stickers) for the image processing algorithms to use as references (datums) as seen in Figure 45. These visual features are required for the image stitching and photogrammetry software algorithms to use as references/datums during the image stitching process [37]. The addition of visual feature (stickers) will not be practical in ILW in-situ inspection, leaving the image processing algorithm challenged by the monotony and lack of distinctive features around the drum shell and its environment. This is further exacerbated by the limited field of vision described and represented in Figure 27.



Figure 45: Three-dimensional surface-mesh of a 500 L ILW drum created using from UAV deployed camera photogrammetry [83].

### 3.4.2 2<sup>nd</sup> data set: 3D Laser point cloud scans

A 3D laser scanner on a mobile platform is proposed to create a point cloud map of every dimension of every item in the store. 3D LRF scanners have been previously used successfully to metrologically inspect ILW 500 L drum ex-situ as described in Section 2.6, making them a more trusted option in metrological scans than photogrammetry. Mobile robots can move the 3D laser scanners to different locations of interest to increase their direct line of sight accessibility. 3D point cloud scans from different locations can be stitched/fused together using the robot IMU data as reference [59], the IMU can provide the sensors' location and 3D orientation relative to a datum using gyros, magnetometers and compasses. The IMU references from which the scans and/or images were acquired, can be then used as datums in the image stitching algorithms [37][84], to reduce the fitting algorithms reliance on distinctive features in the scans stitching process. This makes the accuracy of the stitch process in the scenarios that lack distinctive features, dependent on the accuracy of the IMU readings as well as the fitting algorithms. A detailed study will be conducted in Section 3.5 to determine the ILW 500 L drums' surfaces accessible via direct line of sight while they are in their stillage stack (in-situ inside the vault).

### 3.4.3 3<sup>rd</sup> data set: Ultrasonic inspections/scans





Due to the access limitation challenges and contamination risks, non-contact ultrasonic inspection techniques are proposed for ILW 500 L drums' circumferential measurements and inspection.





Ultrasonic inspection is commonly used to detect cracks and pitting corrosion in pipes at hidden places such as between pipes and pipe mounts [85], which can be similar to inspecting of the drum surfaces hidden by the stillage structure. **Electro-Magnetic Acoustic Transducers (EMATs)** and Gas(air)-coupled piezo electric transducers show the most potential for inspection beyond direct line of sight access, based on their commercial availability and proven technology readiness level in different industries. Moreover, their compactness compared to the other non-contact tool described in Section 3.3 makes them an ideal candidate for robotic deployment.

Ultrasonic waves can be directed to travel along a surface instead of through it, to map the structure's surfaces using the T.O.F of the ultrasonic wave reflections from the surface edges [86]. It may not be possible to directly use such a technique to map the external surface shell of ILW 500 L drums, due to their cylindrical and curved structure, that lacks the sharp edges needed to reflect the ultrasonic waves for the map construction. However, if an ultrasonic wave is induced and detected along the circumference of an ILW 500 L drum from a narrow access point in the stillage, ultrasonic waves could provide a 1D distance measurement of a drums' complete circumference and/or detect discontinuities/cracks along the circumference blind spots. An overall distance measurement longer than the expected drum circumference would indicate an extension in the perimeter, which can be a result of drum swelling, or a dent (inner or outer) (visually described in Figure 46). Similarly, wave reflections or measurement shorter than the expected, may indicate and locate cracks along the drum circumference. This concept will be investigated and discussed and investigated in detail in Chapter 5.

### 3.4.4 Data fusion

Fusing ultrasonic circumferential measurements from different cross-sectional layers along the drum's heights with the drums' incomplete point cloud from a 3D laser scanner, could potentially provide a mean to locate dents in the hidden surfaces of the drums.

Cross-sections of the drum circumference can potentially be obtained from a laser scan point cloud. Some of these cross-sections will be incomplete circles due to the blind spots in the laser scan, however the available points in the cross section can potentially be used as contours to indicate the circumference location and margins as seen in in Figure 46 in . A shape of the same external perimeter length as an ultrasonic circumference measurement of that cross section, can then be overlaid onto the point cloud contours to achieve the best fit as indicated in Figure 46 in . If the overlaid shape is too long to create a round circle onto the point cloud contours, different circle iterations with higher out of roundness values can be estimated until a reasonable fit can be achieved as indicated in Figure 46 in  and . These iteration can then be compared with the different iteration of the cross sections above and below them until a matching set of iterations converge into a realistic 3D form to indicate a possible internal or external 3D dent in the blind spots as seen in Figure 46. These dents will always be estimates and their position and steepness will depend on the iterations fitting algorithms. Applying this principle to all the cross-sectional layers of the drums can be the solution to creating a complete estimated point cloud of the drums' shells to act as digital twins, for long term monitoring of expansions or defect progressions.

	Drum contours from a cross-section of a laser scan point cloud
	Perimeter estimated by creating line of best fit joining contours from the point cloud only
	Possible perimeter variations estimated by creating line of best fit that match the ultrasonic circumferential measurements.
	

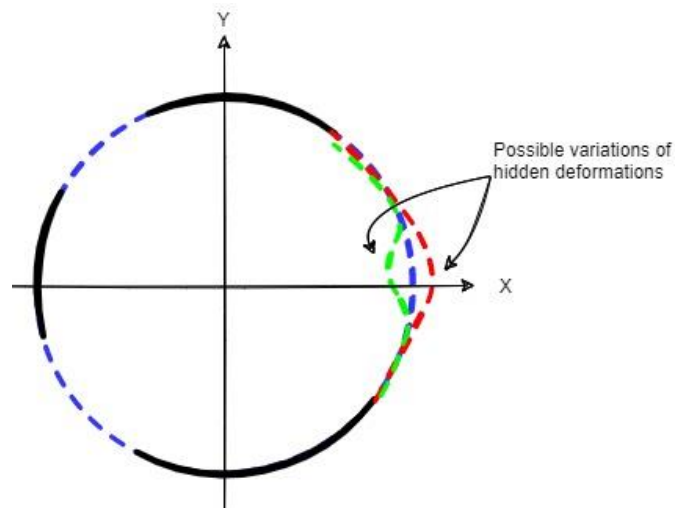


Figure 46: Cross section of an ILW drum point cloud and the different possible perimeter scenarios based on estimated lines of best fit from ultrasonic circumferential measurements.

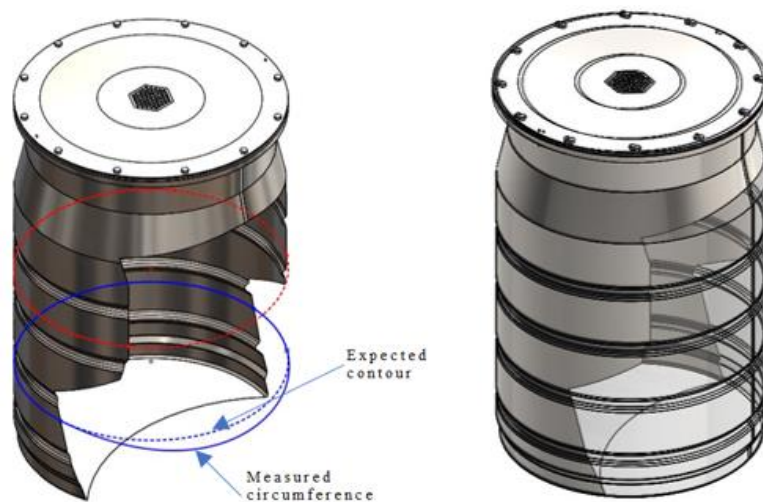


Figure 47: (Left) Illustration of an incomplete point cloud image with circumference measurement larger than expected. (Right) Illustration of the expected estimation of a stretched point cloud image based on circumference measurement.



After creating an estimate of a ILW 500 L drum surface mesh using the fusion of the point cloud and the ultrasonic measurements, images from cameras can potentially be overlaid onto the mesh to create a partial surface reference of the model. The surface feature added from camera images will still be limited to direct line of sight surfaces only.

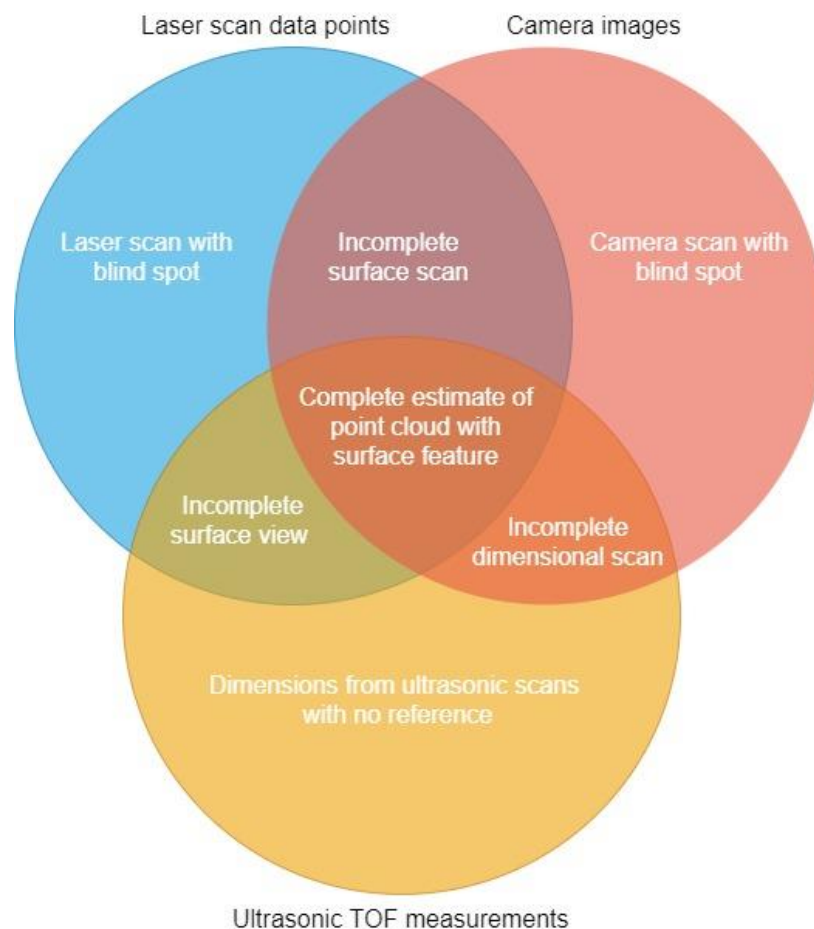


Figure 48: Expected data from fusion of different inspection/scanning methods.

### 3.5 Quantifying surfaces accessible via direct line of sight

A study has been conducted to equate the overall ILW 500 L drum facets surface area accessible from direct line of sight, using probing system such as tactile, optical or laser scanners. This study assumed that the probe could fit in the tiny gap between the stillages and move freely in that gap, but not enter the perimeter of the stillage (area between the drums inside a single stillage). The CAD models of the ILW drum holding stillages created in Section 2.8 were used to represent the scenario.

The stillage models were aligned at different angles and all the non-visible surfaces from the possible viewing angles were cut out of the 3D model, to create a representation of the best-case scenario 3D scan, that could be generated from probes/sensors that can only access the drum using direct line of sight.

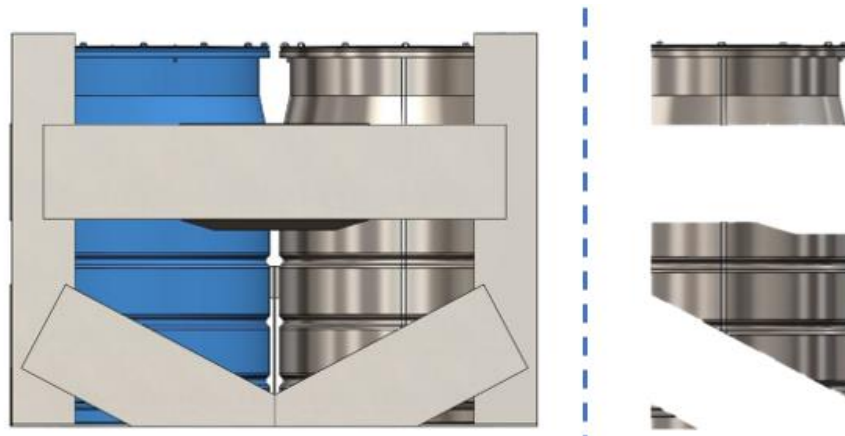


Figure 49: (Left) Side view of a drum highlighted in blue inside a stillage. (Right) highlighted drum view extracted from the rest of the complete stillage view.

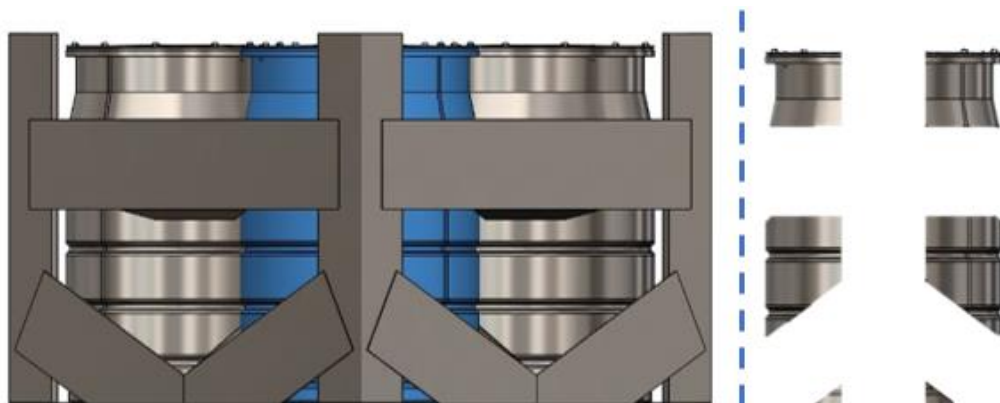


Figure 50: (Left) View of a drum highlighted in blue, from the corner of the stillage. (Right) highlighted view extracted from the rest of the complete stillage view.

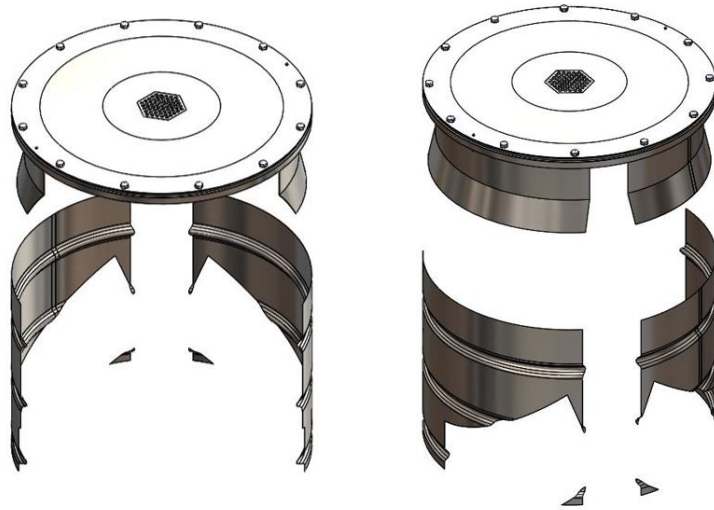


Figure 51: Reconstruction of the 3D view expected from stitching the individual drum's surfaces highlighted in blue in Figure 49 and Figure 50.

This concluded that direct line of sight probes/sensors can only access approximately 0.92 m<sup>2</sup> out of the 3.02 m<sup>2</sup> of the external surface area of a given drum, equating to only **30 %** of the surface required to be inspected. This excludes the surface of the lid, lid mounting flange and the bottom surface in contact with the stillage floor. No literature have been found indicating any potential long term aging effects on the drum lids during the time of this research, however more research in future will be required to assess the possibility of accessing the bottom surfaces on which the drum sits on using the 100mm holes at the bottom of the stillages seen in Figure 25 or other innovative means.

If the probe access is extended to the centre of the stillages via the 250 mm holes the in the centre of stillages base plates, the surfaces highlighted in Figure 52 will be observable, which will increase the accessible surface area via direct line of sight to **42 %**.

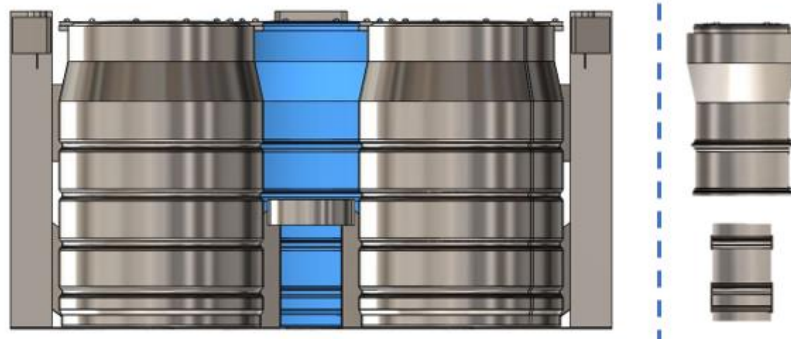


Figure 52: (Left) Cross section of an ILW stillage with the surfaces of a drum accessible from the centre hole highlighted in blue. (Right) highlighted view extracted from the rest of the complete stillage view.

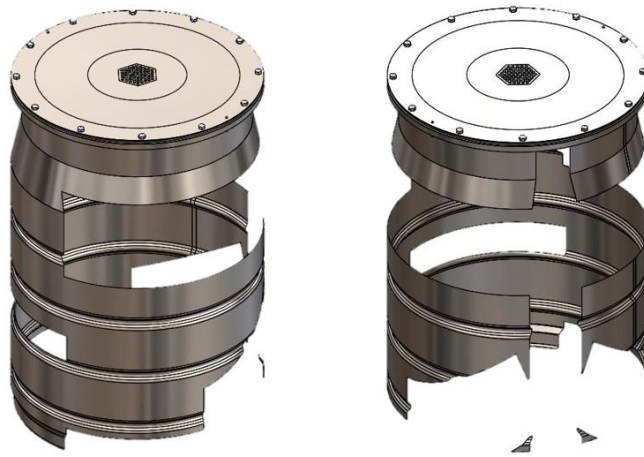


Figure 53: Reconstruction of the 3D view expected from stitching the individual drum's surfaces highlighted in Figure 52 to the 3D reconstruction previously created in Section 3.4.2.

Consequently, inspection probes capable of accessing surfaces beyond direct line of sight will be necessary to inspect the majority of the drums' surfaces.

Like the real scenario, these surface areas results are subject to part form errors, because the CAD model uses individual single points to perform its area calculations and the density and layout of the points creating the 3D CAD model shell along with the computer architecture used will influence the calculations results. The results will also vary depending on the stillage and drum iteration used (Figure 4 presents some of the

different drum designs currently in operation). Therefore the 30 % and 42 % access should be used as a guide and not an exact value.

The CAD models of the incomplete drums were processed using a java script developed to convert the 3D CAD model into a 3D point cloud shell data set. The shell data set was split into cross-sectional layers of 1.0 mm and the percentage of points per layer was calculated. Figure 54 shows that if the 42 % surfaces access was achievable using the holes at the centre of the stillage, there will always be a percentage of the drum surface accessible along the height of the drum, based on the presence of point cloud data in every 1.0 mm thick cross-sectional layer. These small surfaces along the height of the drum, can then be used to measure the drum's circumference using the ultrasonic probes. As well as provide extra point cloud data for potentially contour recognition to use in the data fusion process described in Section 3.4.4 Figure 47.

Splitting the point cloud into 4 quadrants as seen in Figure 55 indicates that not all the surfaces need to provide access to the ultrasonic probes will be present on the same side/quadrant of the drum as demonstrated by the plots in Figure 56. Therefore, the direct line of sight scans and ultrasonic measurements will have to be performed from different sides of the stillages.

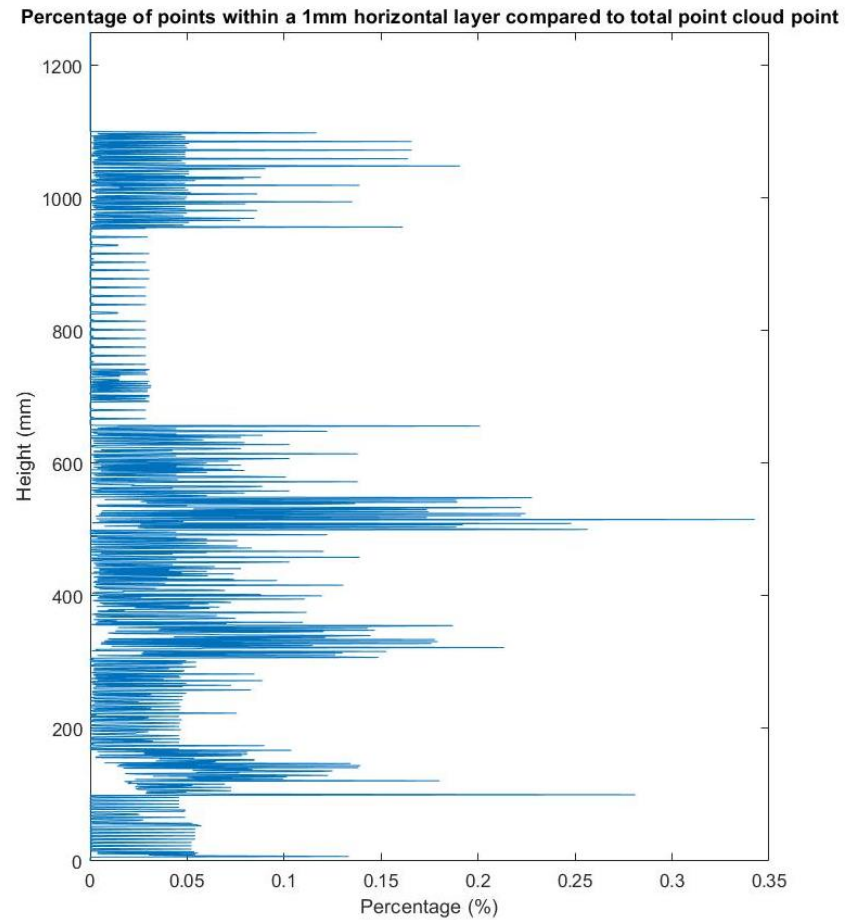
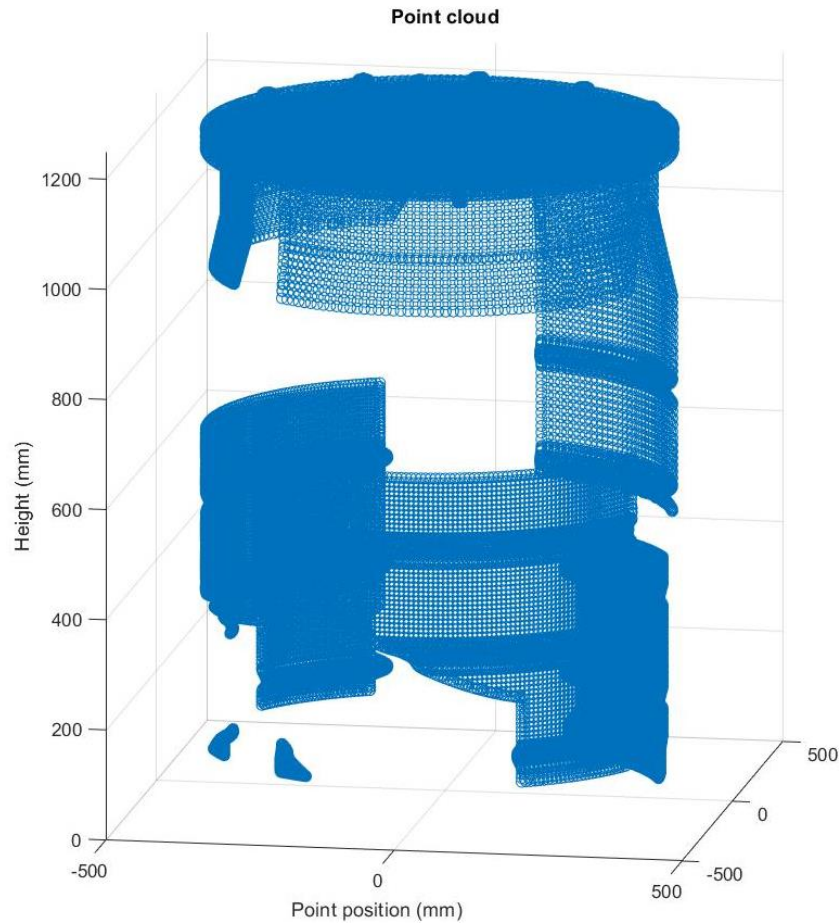


Figure 54: (Left) Point cloud of an incomplete ILW 500 L drum from direct line of sight scan simulation. (Right) percentage of point present in 1.0 mm layer of the complete point cloud.

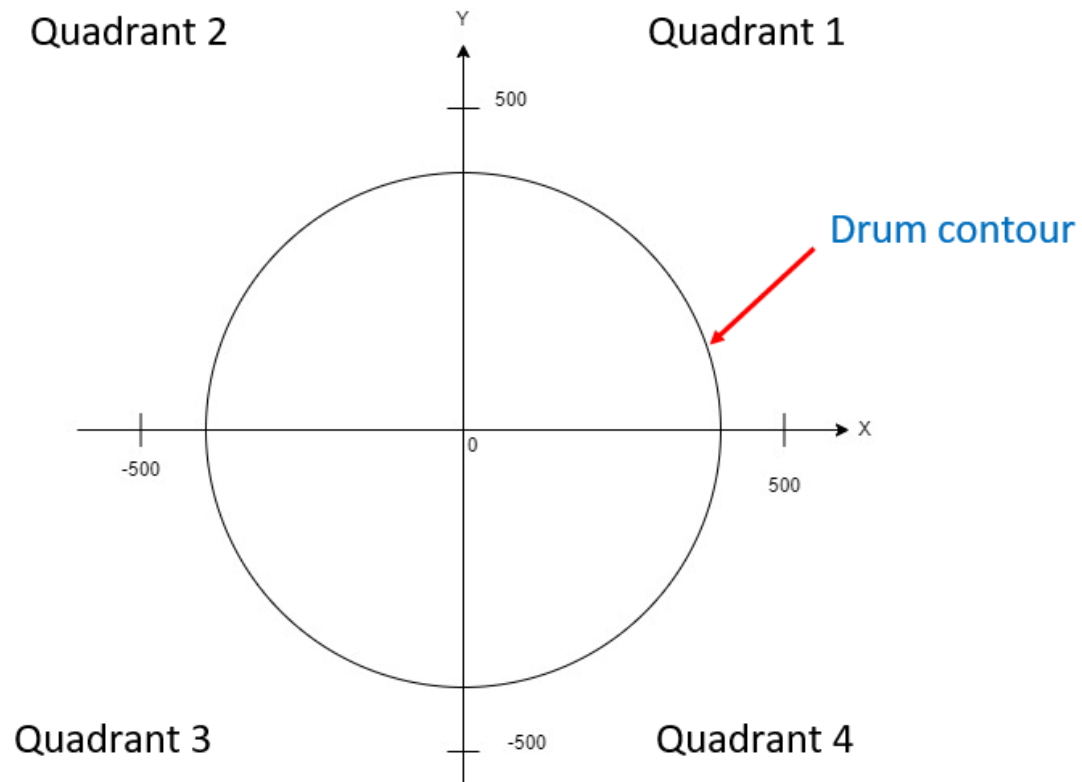


Figure 55: ILW drum circumference divided into 4 quadrants, the distribution of points from the point cloud in n Figure 54 that lies is in each of these quadrants is presented Figure 56.

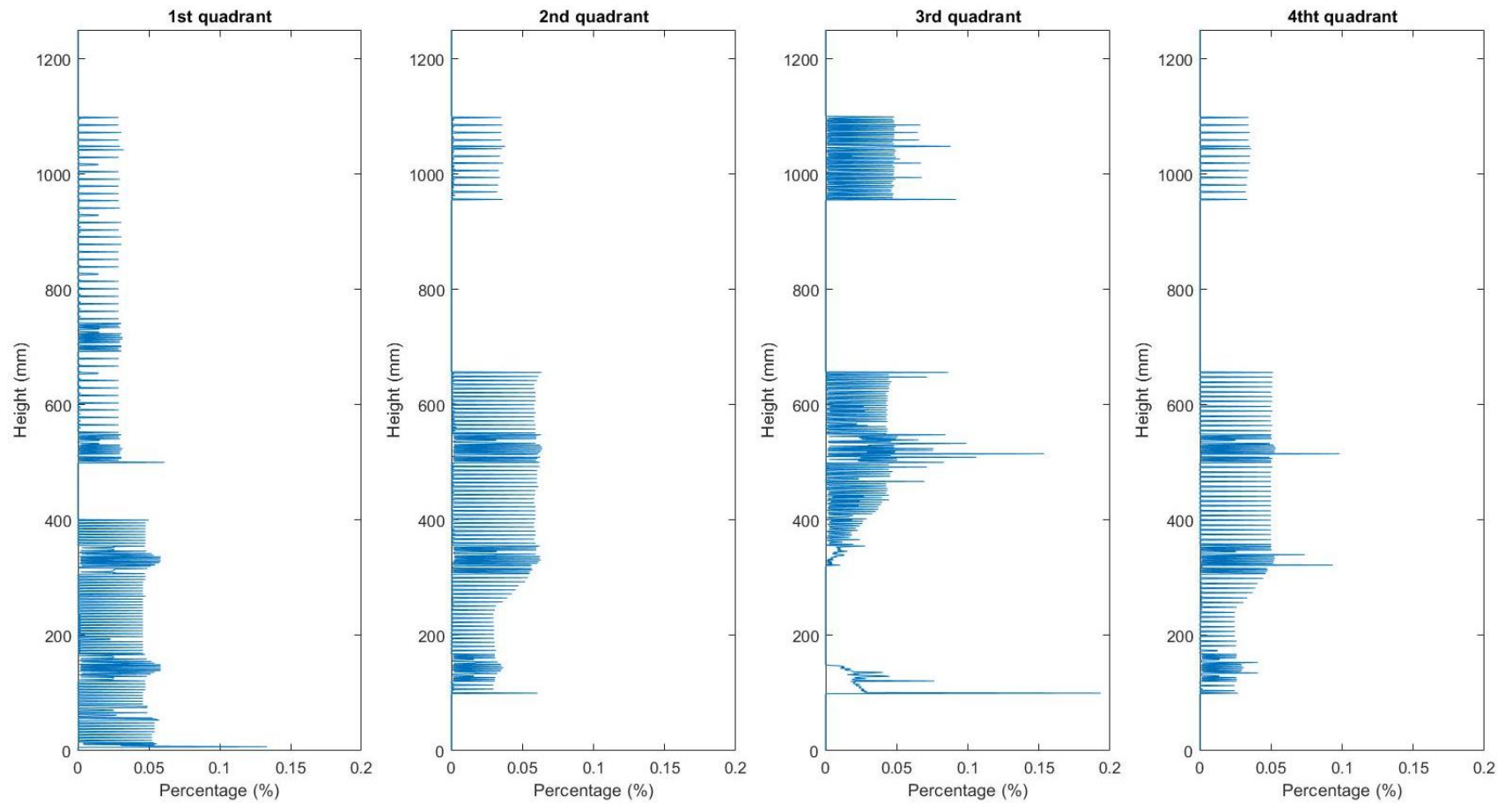


Figure 56: Percentage of points per quadrant in a point cloud of an incomplete ILW 500 L drum from direct line of sight scan simulation



### 3.6 Summary

A set of recommendation to any proposed robotic CMS can be decided at this stage to minimise the uncertainties caused by the error factors described in Section 3.2 in the specific task of ILW 500 L drums inspection in-situ.

From a **hardware** perspective, the CMM **probes** chosen must be able to reliably gather the **parameters** required to metrologically inspect the ILW drums' including facets that are not in direct line of sight. The probe and probe deployment mechanism must maintain a low profile to fit in the **0.23 m** gap between the stillage stacks [5], to maximise the CMS **accessibility** and minimise **part form errors**.

All the ILW 500 L drums (**workpiece**) in stores adhere to WPS/604 [22] and RWM TSCS 1079 [19] standards and have defined alpha-numerical identifiers as described in Section 2.3 and 2.4. This will guarantee certain aspects of commonality in all types and iterations of the containers, such as overall size **access** gaps and **surface finish**. These standards can be used as a guide to design the CMS to identify and use for essential tasks such as **clamping**, **datum** identifications and **fitting algorithms**.

Once a CMS concept is designed, the hardware and software required to bring the concept to life will be chosen, to minimise the **sampling strategy** and **fitting algorithms** errors. The CMS data acquisition **algorithms** must be able to cope/compensate for the expected fluctuations in **temperatures** inside the vaults during dimensional scanning operations and fuse data from different types of probes/inspection tools to overcome some **access** limitations. Mobile CMS and probes physical mechanisms must cause minimal **dynamic** errors during motion and dampen natural and environmental **vibrations**.

The fusion of multiple sensors' data using different probing technologies capable of complementing each other's missing data, will be required to expand the inspection scope. This will require the implementation of different scanning and post processing algorithms to **suit** the different sensors' technologies while operating in synch, to provide adequate data for the **fitting Algorithms**.

## Chapter 4: Proposed Mobile robotic inspection systems

### 4.1 Introduction

After reviewing the spatial restrictions and environmental challenges of accessing nuclear ILW storage vaults in Chapter 2, and the challenges this present to the metrological and structural inspection technologies described in Chapter 3. It became clear that a bespoke robotic CMS will be required, to access and deploy the inspection sensors into the tight and hostile environment of the nuclear waste storage facilities.

The main aim of this Chapter will be to propose and design a robotic CMS system to CM&I ILW containers in-situ, capable of:

- Deploying metrological scanning tool reliably and accurately into an ILW vault to perform CM&I tasks on ILW 500 L drums in-situ.
- Operating in an existing environment without the need of modifying the existing vaults structures or storage arrangements.
- Deploying the CMS probes/sensors to locations that would provide the maximum amount of data from the drums.
- Mechanically stabilise or anchor the CMS to the existing structures, for stable metrological scanning.
- Provide a reliable power source for prolonged scanning operations.
- Handling temperature changes and prolonged exposure to radio-nuclide radiation.
- Providing a retrieving plan for failure/damaged scenarios.
- Convenient decommissioning at end of its operational life.

### 4.2 Existing robotics technology

Research in the general area of robotics for hazardous environments is driven by specific design requirements and type of applications [87]. The deployment of sensors into the 0.23 m access gap between the ILW stillages stacks [5], or scanning a 9.0 m height range [23] to access all the tiers of a stillage stack, may be possible using a number of already existing statically mounted robotic arms/manipulators. However combining this with a reach requirement of hundreds of meters to cover the depth of the vaults [24], creates a challenge to statically mounted

robotic arms. This creates a need for a mobile system that can manoeuvre into the far ends of the vaults using already existing structures and operating in the legacy environment without modifying it.

#### 4.2.1 Manipulators

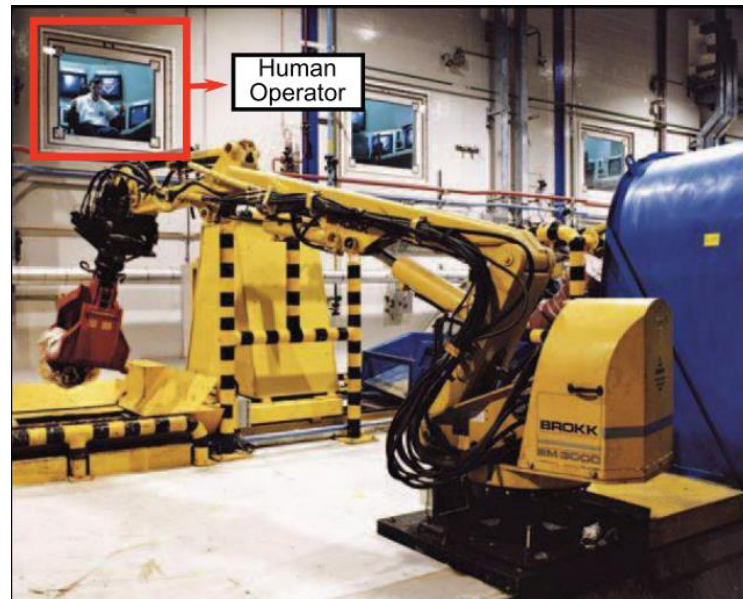


Figure 57: Human operator controlling a Brokk robot for pick and place operations inside a radiologically active environment. The operator is viewing the robot through a 1.2m thick lead-glass window, and controlling each joint with a separate lever, while estimating the inverse kinematics from experience [88].

Robotic and manual manipulator arms have been used and proven in the nuclear industries for many decades reliably, with very little changes in their designs since the 1960s [88]. Tele-operating hydraulic Brokk robot arms (Figure 57) have been widely trusted in the industry due to their ruggedness and reliability for many decades [88]. These robots operate with no joint-encoders or inverse-kinematics algorithms, and rely on the operator skills to control the arms using viewing windows or CCTV cameras for feedback [88].

Modern robotic arms such as the AARM shown in Figure 58 have been radiation hardened and used in nuclear reactors for various inspection and service operations [87]. The AARM robotic manipulators has 4 degrees-of-freedom: linear boom, boom roll, shoulder pitch, elbow

pitch; and a gripper [87]. The AARM robot is able to fold itself into a small compact shape to access areas through tight gaps, where it unfolds to reach the points of interest, while providing actuator compliance and electronic feedback for collision detection [87]. Longer reach robotic arms such as **Articulated Inspection Arm (AIA)**, were developed to operate inside the Tore Supra tokamak thermonuclear experimental reactor [89]. The AIA has an 8 meters long cantilever arm, consisting of five 0.16 m diameter titanium joints [89].

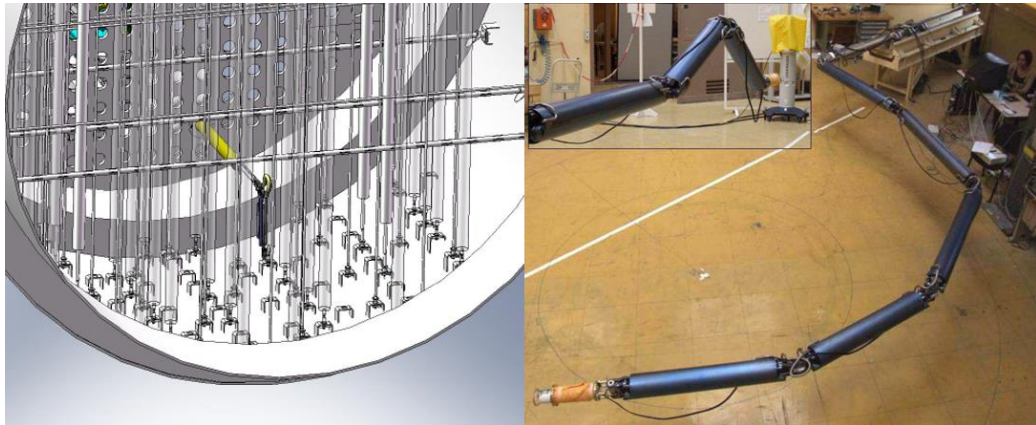


Figure 58: (Left) AARM robot passing through a small gap into a nuclear reactor cavity.(Right) AIA robot assembled, CEA-LIST Laboratory, June 2007 [89].

This design layout allows the AIA manipulator to fit in the 0.23 m gap between the ILW stillages and cover the height of stillage stacks. However, as its joints length will have a large swing arm radius, it will be difficult to control when reaching points close to the robot base, because of the limited space available for its joint to fold in. This problem can be overcome by adding a larger number of joints as seen on the OCRobotics snake arms demonstrated in Figure 59 [90]. Snake or trunk like robotic manipulators have been used in the inspections and repairs of Ringhals AB, CANDU nuclear reactors and during Sellafield nuclear plant decommissioning [91]. This makes them an industry proven candidate to be used in the spatially challenging inspections if they can achieve the long reach required for in-situ CM&I of ILW containers.



Figure 59: (Left) OCRobotics snake like arm anchored onto a tractor transport system [91]. (Right) OCRobotics robot arm anchored onto a KUKA robot arm, accessing a point of interest through a small gap [91].

Most present-day industrial robots use a semi-closed-loop method for position control, where feedback signals from position sensors (rotary or linear encoders) attached to the robots' joints drives (axial or linear actuators) are used, to reduce the robots' end effector and joints position errors [92]. Consequently, when a snake/trunk like manipulator is used as a CMM, the uncertainty in its end effector (stylus or scanning probe) location will increase with the number of degrees of freedom of the robot, because of the uncertainty error in the individual joint position feedback. Moreover, the elastic deformations on the cantilever arms caused by the arms own weight or its payload, will change the curvature of the joints causing a change in its endpoint location [92], making the weight of the cantilever arm (arm joints weight and payload combined) the key factor that limits the manipulator arm length [93].

The end effector position uncertainty could be overcome using external sensors that can track the end effector location directly, while being independent from the robot's mechanical structure, however this will be challenged by any external tracking systems access limitations in the ILW vaults. This concept will be explored further and reviewed in Section 4.3.

Therefore, it is recommended that any robotic manipulator proposed to deploy sensors for the specific task of ILW containers inspection in-situ, be designed as short and light as possible, while still maintaining the minimum reach requirements to access a full stillage/container stack (up to 8.715m high[5]). From there, a mobile platform is recommended to carry this light and short (relative to the vault length) manipulator towards the containers at the far end of the vault (up 300m away [24]).

#### 4.2.2 Locomotion

Since it is not desired to create a stationary CMS robotic manipulator that can reach the far ends of the vaults as described in Section 4.2.1, it becomes necessary to find a method to move the manipulator arm as close as possible to the points of interest. Overhead cranes will not be available at all ILW vaults as described in Section 2.5, thus the manipulator needs to move independently using the available space and existing structures only.

Mobile bases such as the KUKA KMP 1500 or the tracked OCRobotics platform previously described in Figure 59, are capable of transporting robotic manipulators to different locations to increase their reach. A mobile robot base has to be large and/or heavy enough to act as a ballast and keep the centre of gravity of the robot within the base area, to stop it from toppling when the manipulator is extended away from the base. Alternatively, the base can anchor itself mechanically or magnetically to a different structure that would then act as the base/ballast.

The 0.23 m gap between the stillage stacks [5] is not ample space for a large base area to fit in given the required manipulator reach, and floor anchoring requires modifications to the ILW vaults. This makes the volume above the containers the only reasonably sized space to accommodate a mobile manipulator and base (See Figure 9, Figure 11, Figure 15 and Figure 16). In that volume, the vaults' ceilings and the top surface of the containers are the only surfaces available for a robotic base to travel on and anchor to, unless it can fly in the available volume without the need for any surfaces.

If a robot is to be designed to climb and travel on the ceiling or walls of the vault, it will need to adhere (anchor) itself to their surfaces securely,

to minimise the CMS dynamic errors [Section 3.2.1]. Generally electro or permanent magnets and vacuum suction pads are the two methods used by industrial climbing robots to adhere to walls and surfaces [94]. Other animal inspired techniques that mimic gecko feet adhesion principal for climbing have shown good potential, but still require development to improve their stability and surface type dependency [94].

The vault walls/ceiling will be either made of hard rock or cement [25], thus eliminate the choice of using of magnetic adhesion due to nonferrous surfaces. The rocks or cement roughness/porosity and chances of cracks reduces the reliability of a vacuum adhesion [95]. Fans can be used to exert forces on the robot itself to push it against the wall/ceiling for adhesion, instead of negative pressure between the robot and wall. This will require continuous power supply to maintain the adhesion, creating a risk of falling in the event of faults or power loss. Thus, a passive method that do not require continuous power or active adhesion to stay in place is more desirable.

Research in novel biologically inspired robotic locomotion at the **Robotics and Mechanisms Laboratory (RoMeLa)** at Virginia Tech, have inspiring new mechanisms that can be applied on climbing and scanning robots to travel and climb the ILW stillages [96]. The passive-dynamic locomotion of robots such as **STriDER (Self-excited Tripedal Dynamic Experimental Robot)**, provides an example of a dynamic walk with high energy efficiency and minimal control [96]. By applying a similar mechanism, a robot can locomote on top of the top tier of the stillages, without the constant need for power to maintain its position/state.

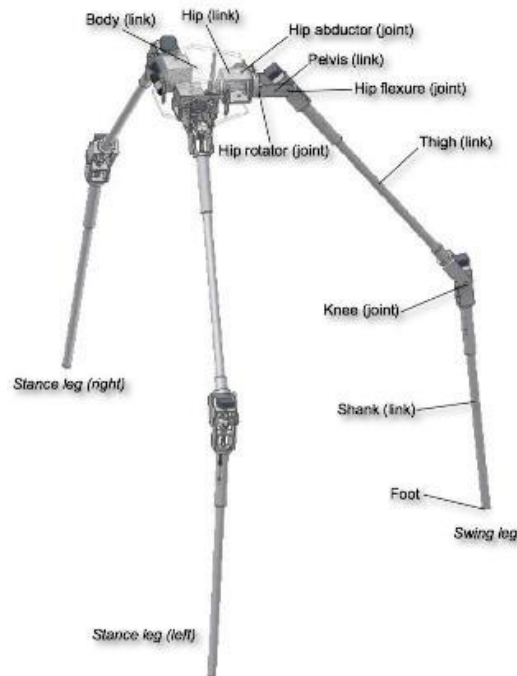


Figure 60: RoMeLa STRiDER [96].

All the ILW 500 L drums (**workpiece**) in stores adhere to WPS/604 [22] and RWM TSCS 1079 [19] , which means that they have a common twistlock lifting mechanism (anchor point) with known layout for handling as described in Section 2.5. Thus, it is proposed to use the twistlock lifting points to latch the robots' limbs onto, to use the stillage size and weight as a ballast. This idea will be exploited in more detail in Section 4.6.1.

#### 4.2.3 Soft Robotics

All the snake like robotic manipulators described in Section 4.2.1 are limited to concertina locomotion, where the manipulators push against a fixed point (its own base) to move forward [97]. In nature limbless animals can use four different main modes of locomotion to move forward, concertina, rectilinear, lateral undulation, and sidewinding [98]. Some of these modes of motions are made possible by exploiting the soft structures of the animal bodies to move in complex natural environments [99]. This inspired robotic engineers to incorporate soft structures and technologies into their designs and develop new adaptive and malleable robots [99].



Limbless animals in the wild only use concertina or rectilinear modes to move in tight spaces, and correspondingly these 2 modes of locomotion are the only modes suitable for snake like robots to move in tight space and narrow pipes or channels [97]. Unlike the concertina mode described earlier, limbless animals perform rectilinear motion by shortening and lengthening their body periodically along its length to travel in a straight line (single dimensional motion) [98][100]. This is mode of motion requires a soft flexing structure which is challenged by traditional rigid structured robots [100].

To overcome the structural rigidity limitations, novel robots such as the earthworm-inspired burrowing robot in Figure 61, are made from soft bodies that allows the use of rectilinear motion in single straight line through narrow gaps [100]. This robot is designed to clean pipes and it moves in them by expanding and contracting its body without the need of wheels or legs [100].

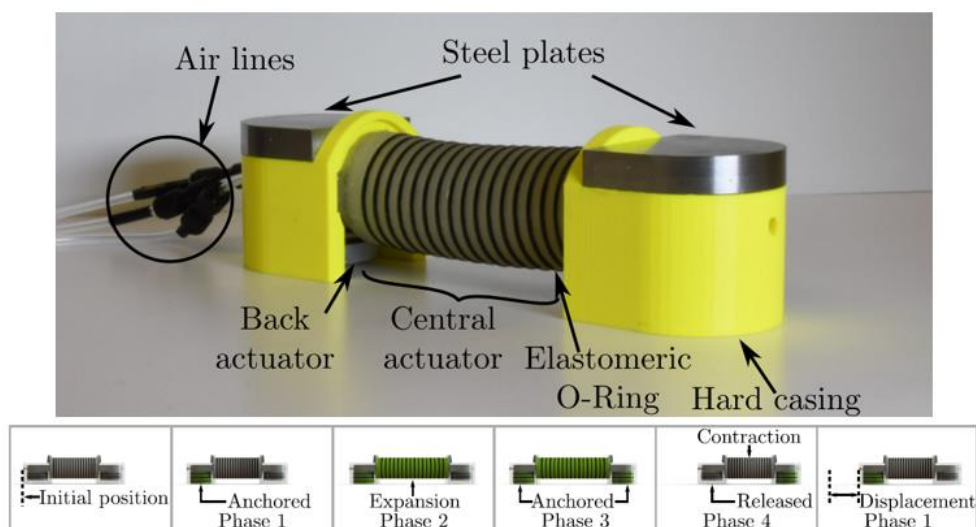


Figure 61: Earthworm-inspired burrowing soft robot rectilinear locomotion actuation sequence. Green represents inflation and grey represents deflation [100].

Although this earthworm robot concept will be ideal to manoeuvre within the small gaps between the containers in the ILW vaults, its reach will be limited by its climbing abilities. Next generation soft robotics to achieve long reach inspired by plants have been created using soft

inflatable robots, and are able to extend thousands of percents in length from their base [101].

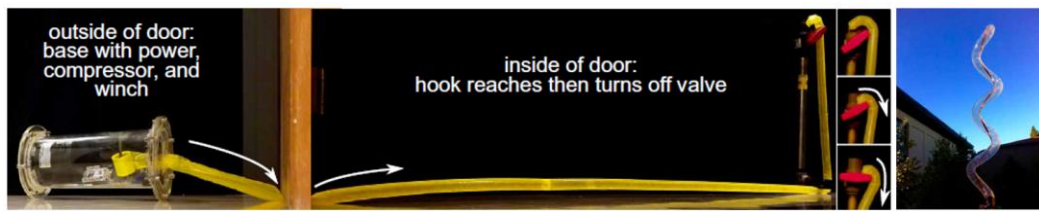


Figure 62: (Left) Inflatable robot manoeuvring under and around obstacles to turn a valve [101]. (Right) inflatable soft robot travelling vertically into the air to act as a radio antenna [101].

The plant inspired robot in Figure 62 operate by inflating a tube like structure as seen in Figure 63 to simulate plant growth to reach long distances, and asymmetric lengthening of its tube to enables active steering [101]. This can be a great tool for navigating all the complex and tight gaps within the ILW vaults for optical inspection of hard-to-reach points of interest.

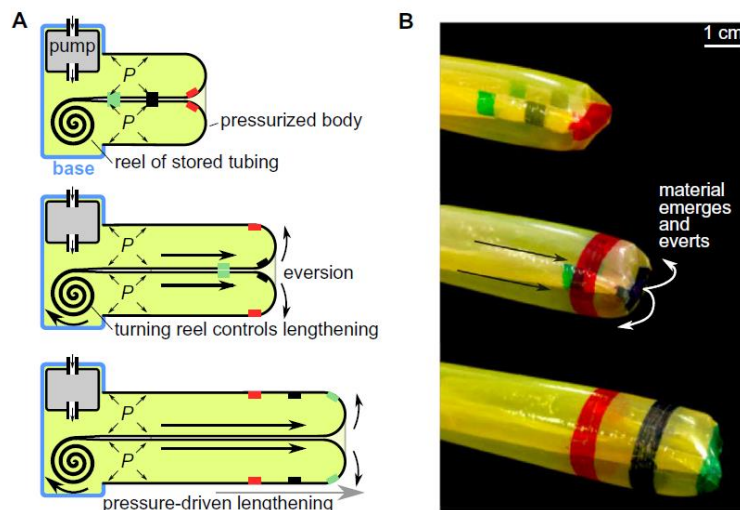


Figure 63: Plant inspired robot growth mechanism [101].

Soft growing robots can deploy sensors into the points of interest in the ILW, and its intentionally soft (elastic) structure will compress and stretch into the required shapes to allow it to reach the desired points of interest. The elasticity that allows soft robots to achieve their reach, is also the main reason to impair their use in metrology. Soft robots have an almost infinite number of shapes and/or configurations due to the

absence of rigid beams and/or straight lines in their structure [102]. This will impair the use of their actuators' position sensors feedback in reverse kinematics to position the end effectors/probes [92], unless external end effector locating methods that are independent of the robot structure are used. Tools such as laser trackers, stereo cameras, IMUs or GPS can independently detect the end effector position without actuators' position sensors feedback [103], however they too may also be challenged by the access limitations as will be described in Section 4.3.

#### 4.2.4 Aerial approach

If there is no suitable terrain for a mobile manipulator or a soft robot to travel or climb, an aerial approach could be a solution.

The interest in the use of **Unmanned Aerial Vehicles (UAV)** for asset surveying and inspection have surged in the recent years [104]. Most indoor aerial vehicles use multirotor platforms due to their hovering abilities and superiority in manoeuvring at low speeds in small spaces with minimal moving parts [104]. UAVs can offer a very agile aerial robotic platforms to access the tight spaces in the ILW storage facilities, and have been previously used to deploy optical sensors (cameras) to perform metrological inspection of ILW 500 L drums, to detect waste form expansion [61] as previously described in 3.3.2.



Figure 64: Dexterous Hexrotor with sampling arm for physical samples from inside a cylindrical grain silo in a mock-up of the WIPP exhaust shaft [83].

Most multi-rotors require multiple propellers on the same axis to counterbalance and stabilise their platform. To fit two counter balancing propellers in the 0.23 m gap between the stillages, the propellers diameter must be less than half the gap size (<0.125 m). The efficiency and thrust of propellers is exponentially proportional to their diameter [105], and adequate vehicle endurance in the CM&I of ILW container is a major requirement to cope with the thousands of containers [88] that need to be inspected.

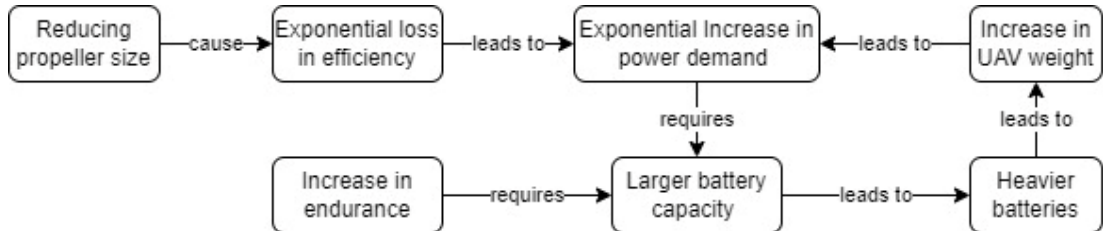


Figure 65: Design feedback loop caused by changes in UAV propeller or endurance parameters.

To escape this design feedback loop, either the endurance or the propeller size must be compromised, or the power source weight compromise is removed from the loop completely by replacing it with a tethered power source. A power source on the ground can be tethered to the UAV to provide unlimited endurance to the UAV via a power cable at the cost of manoeuvrability and range [106].

Assuming that all the power and endurance problems can be overcome at the design phase of the UAV, the UAV will also require external end effector location tracking because of the absence of stationary reference/datum points in its floating/flying body.

### 4.3 Position tracking and navigation

External tracking of robots' location and end effectors position is a common practice in many industries, **Global Positioning System (GPS)** radio signals are commonly used onboard rovers and aerial vehicles for tracking and navigation. In airtight vaults or tunnels (environments similar to ILW vaults) where direct contact between the GPS receivers and satellite signals are inhibited [107], alternative acoustic positioning systems such as Marvelmind positioning system can be an alternative to

GPS. Marvelmind acoustic positioning systems use an array of stationary acoustic beacons such as those demonstrated in Figure 66, which would be placed in different locations in the GPS denied environment, while an acoustic receiver is placed on a mobile robot.

The beacons and the receiver interconnect using radio networks to trigger acoustic signals from the beacons, which would then be detected by the Marvelmind acoustic receiver onboard the mobile robot. The T.O.F of the acoustic signals from the beacons to the receiver is then used to triangulate the receiver positions in relation to the different beacons in 3 dimensional space, to an accuracy of  $\pm 20$  mm [108].



Figure 66: Marvelmind acoustic positioning system beacons and receivers [108].

For the signals triangulation algorithm to work effectively, the acoustic signal from the beacons needs to be detected directly by the receiver to calculate the direct line of sight T.O.F. Consequently, the ability of acoustic signals to diverge and reflect off solid obstacles such as the ILW containers shells, before being detected by the receiver, can result in non-direct line of sight signals T.O.F to be computed, which will skew the triangulation location [108]. This reduces the confidence in acoustic signal location triangulation inside crowded ILW vault environments, where the acoustic signals have plenty of surfaces to bounce off before reaching the signal receivers.

Alternatively **Wireless Sensor Networks (WSN)** systems similar to those used in tracking mining personnel in tunnels [107], do not require direct line of sight between the reference signal sources and the receivers for location triangulation. WSN systems use radio wave strength instead of

T.O.F to calculate the distance between a signal source and the mobile receiver [107]. Radio signals strength attenuates non-linearly in relation to the distance from its source, and can be affected by the presence of metals [107]. This will also challenge the accuracy of such a system in the ILW vaults, due to the metallic radio shielding of the ILW containers.

In environments where no localisation reference nodes/beacons are present, modern experimental robots use Simultaneous Localisation And Mapping (SLAM). SLAM can utilise 2D or 3D scans from laser range-finders, sonars and/or optical sensors, to create a real-time dynamic map of its environment as it moves through it [109][110].

Just like the photogrammetry and image/point cloud stitching algorithms described in Section 3.3.2, SLAM uses geometrical and visual features of the different objects in the environment as reference points for the map building [109]. This makes SLAM ideal for chaotic environments where large number of geometrically varied object exists to use as reference [109][110], but that is not the case in the synchronous and monotonous ILW vault shown in Figure 67.

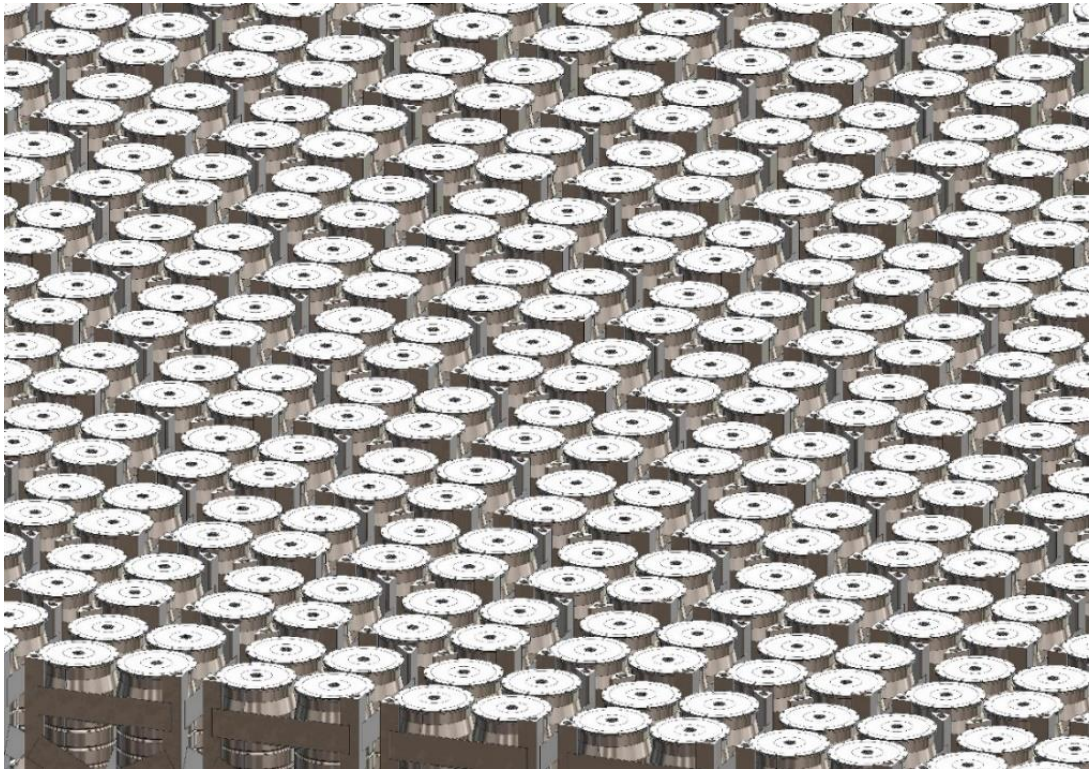


Figure 67: 3D render describing the monotony of the densely packed ILW 500 L drum stillage stacks inside an ILW vault.

#### 4.4 Available robotic technology summary

A unique robotic CMS platform is required to deploy inspection sensors to CM&I ILW containers in-situ. The robot must be designed with CMS requirements as priority to optimise its efficacy in performing the required metrological and inspection tasks. Any proposed CMS must be able to cope with the,

- Restricted spatial access and navigation.
- Variations in workpieces/inspection subjects.
- Probing sensors and sampling strategies.
- ILW vaults radiation levels, temperature variations and natural vibrations.

To achieve this, a summary of the current robotic technologies described in Section 4.2 was created to exhibit what each technology can offer to the CM&I of the ILW 500 L drums in-situ, and the challenges and compromises these technologies may face. All the positive attributes from this summary will then be used to inspire new hybrid robots that benefit from the existing proven technologies to create a CMS with minimal compromise.

	<b>Advantages</b>	<b>Disadvantages</b>	<b>Inspiration</b>
<b>Industrial robotic arms /manipulators</b>	<p>Already used and proofed by the nuclear industries.</p> <p>System accuracy have been enhanced by many specialists over decades for use in CMS.</p>	<p>Limited reach in relation to the ILW store depth.</p> <p>Requires large volume to bend the manipulators which may not fit in the gap between stillages.</p>	<p>Ability to calculate XYZ position of end effector or target based on the reverse kinematics of the manipulator state.</p>
<b>Snake/trunk robots</b>	<p>These manipulators can move easily between the stillages and drums to reach inside the stillages and collect the required measurements.</p>	<p>Inspection of faraway targets is inhibited by the bulk body of their base that cannot pass in the tight gaps between the stillages.</p> <p>To increase agility and reach both far and close targets without a moving base, more segments/joints will be required which will increase the metrological errors.</p>	<p>Thin and flexible manipulators can be created to fit in the tight gaps by moving all the bulky components and drivers needed to power the manipulator out of the arm body/length and into a base, away in an open volume.</p>



<b>Robotic manipulator mobile platform</b>	Increases the range of a robotic manipulator without increasing the arm size or complexity.	Requires a large area and weight to act as ballast/base to stop the manipulator from toppling. Requires a mean of climbing and anchoring on the stillages or the vault structure securely to reach locations of interest. Industrial suction and magnetic base techniques will be challenged by the vault surfaces.	Having a mobile platform that can operate/maneuver in the empty volume above the stillages will increase the inspection manipulator reach. The anchoring of the mobile platform used must be passive and not require constant power for safe deployment.
<b>Soft robotic</b>	Can be folded, compacted, or deflated to pass through small gaps. Can compress and stretch to fit in complex environment.	The absence of rigidity in a soft robot gives it an almost infinite number possible arrangements, making reverse kinematics of its parts complicated and unreliable as CMM.	If a soft robot manipulator can become rigid at points of interest, it could then be used in CMS.
<b>UAV</b>	Can reach locations of interest with no physical contact with any objects in the store.	If battery powered; operation time will be limited by battery life.	Offers a completely contact free platform to deploy the sensor quickly to the points of interest.

The proposed hybrid robots will be split into two directions, an industrial robust/proven technology approach and a novel futuristic approach using aerial vehicles.

## 4.5 Rapid visual inspection using UAVs

The first proposed CMS is a novel photogrammetry UAV that is a continuation of the existing research work described in 3.3.2. To take this existing photogrammetry concept and apply it to in-situ inspection, the quadrotor will have to be scaled down in size to fit in the 0.23 m ( $\approx 9''$ ) gap between the stillage stacks. This means that the quadrotor's propellers must be less than 3'' in diameter to allow a reasonable safety margin of at least 1'' clearance between the blades and the stillages.

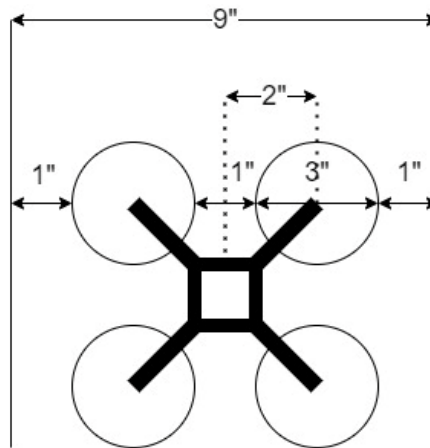


Figure 68: Predicted quadrotor layout required to fit in a 0.23 m gap between stillage stacks.

The reduction in propellers diameter affects its coefficient of thrust ( $C_t$ ) because of the reduction in the propellers' Reynolds number at a given air density ( $\rho$ ), and the exponential reduction in their reference velocity ( $nD$ ) and reference area ( $D^2$ ) [105].

$$Thrust = C_t \rho n^2 D^4 \quad \text{Equation 5}$$

The propellers' reference area and velocity are used in this context instead of absolute area and velocity, because the propeller surface area and velocity change along the propeller's cord [105].

### 4.5.1 Proposed airframe

To reduce the exponential losses in efficiency associated with the reduced propeller size, and increase the thrust of the UAV, a bi-copter

system was proposed and designed to use a single pair of propellers along the roll axis of the UAV.

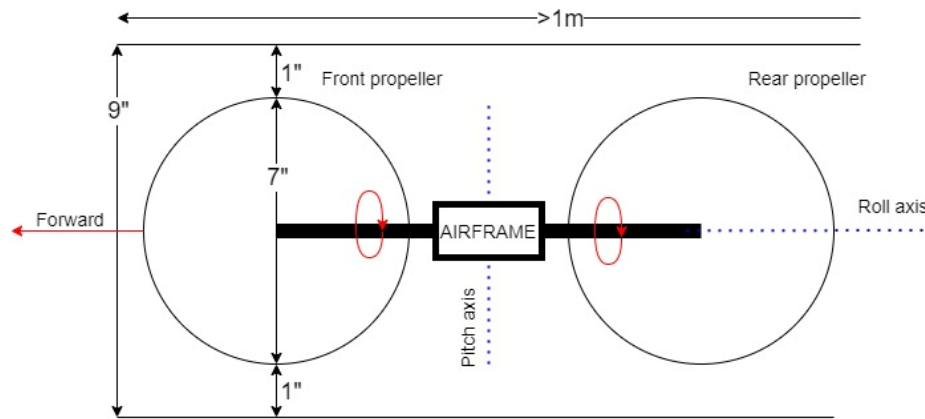


Figure 69: Top view of the proposed UAV layout to fit a 7" propeller in the 0.23 m (9") gap between stillage stacks.

This bi-copter design allows the propeller diameter to be increased up to 7" (2.33 times larger than 3" propeller) using the same clearance and constraints. This will increase the thrust by a factor of at least  $2.33^4 = 29.5$ , as well as increase the  $C_t$  and  $nD$  due to the larger Reynolds number associated with the larger propellers.

Helicopter and coaxial propeller setups would have the same 7" propeller diameter. Helicopter and coaxial propeller control their thrust vector using a swash plate as demonstrated in Figure 70.

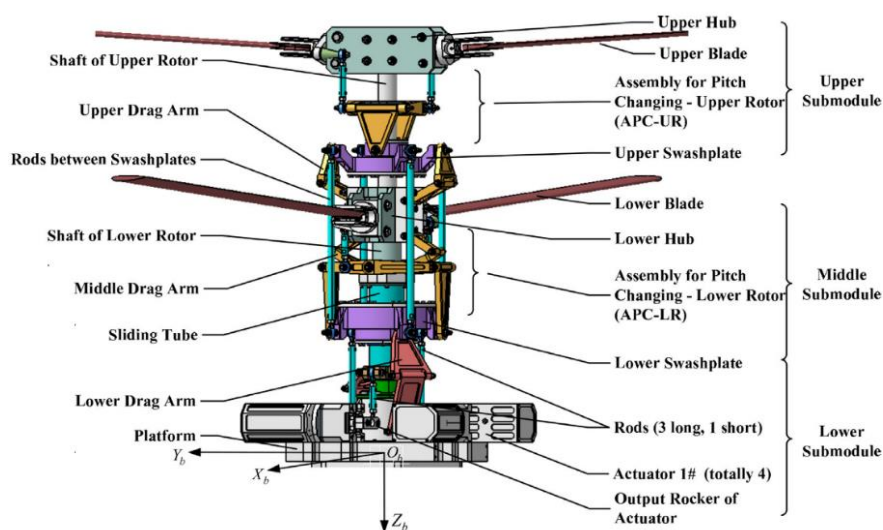


Figure 70: Principle of coaxial helicopter swashplate mechanism[111].

Swash plates control the rotors thrust vector by synchronising the movement of the large number of linkage arms and pivots demonstrated in Figure 70, as they rotate around the rotor shaft to tilt the individual rotor's angles while the rotors revolve around the shaft. The tilting of the rotor during their revolution around the shaft creates different thrusts in different locations of their rotation. This differences in thrusts causes the entire mechanism to apply the thrust vector in different directions to control the helicopter attitude and trajectory [111].

The dependence of the swash plates thrust vectoring mechanism on a large number of moving parts to operate in synch at high speed as they move multiple times per rotor revolution, exponentially increases the chance of the mechanism failure, because the failure of a single components will cause the failure of the entire mechanism. This makes swash plate thrust vectoring an undesirable UAV control mechanism in the presence of simpler mechanisms such as those used in multi-rotor platforms such as quadrotors that only use 4 at moving components in the form of electric motors.

The UAV layout proposed in Figure 69 on the other hand creates a hybrid between swash plate thrust vectoring and multirotor UAVs, by using differential thrust between the front and rear propellers for pitch control like a basic multi-rotor, and the rotation of the propeller mounting arm around the airframe weight for Yaw and roll control as described in Figure 71.

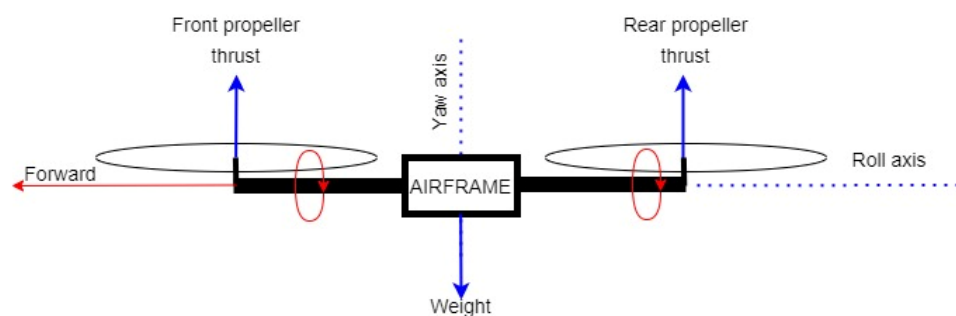


Figure 71: Side view of the proposed UAV layout, forces, and attitude axis.

By rotating the propeller mounting arms in the same direction, the thrust force vector will have a side component to roll and/or pan the airframe.

Whereas rotating the arms in opposite directions will yaw the airframe around the yaw axis.

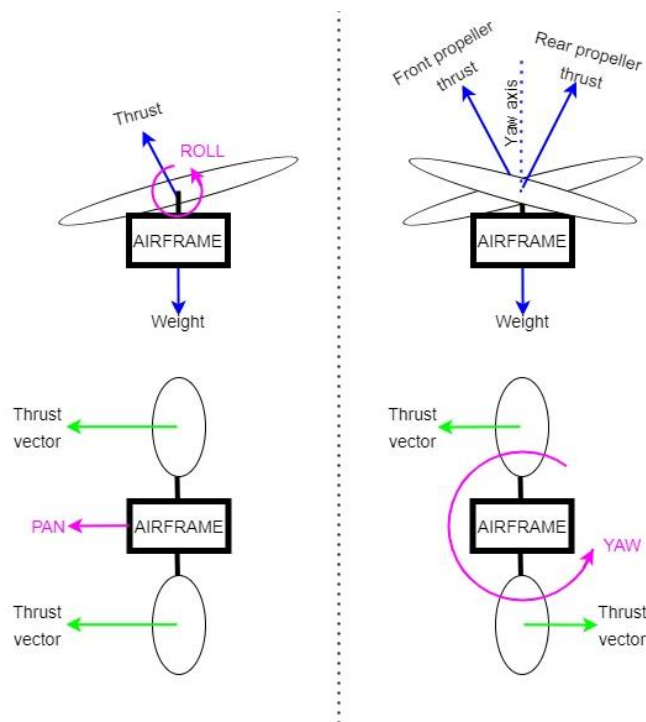


Figure 72: (Right) Front view of the proposed airframe with propellers at the roll/pan position. (Left) Front view of the airframe with propellers at the yaw position.

#### 4.5.2 Prototype

A prototype of the proposed airframe was modelled in CAD to ascertain how the airframe would fit between the stillages from a 3D perspective. The model used a propeller smaller than 7", to match commercially available propellers at the time for prototyping.

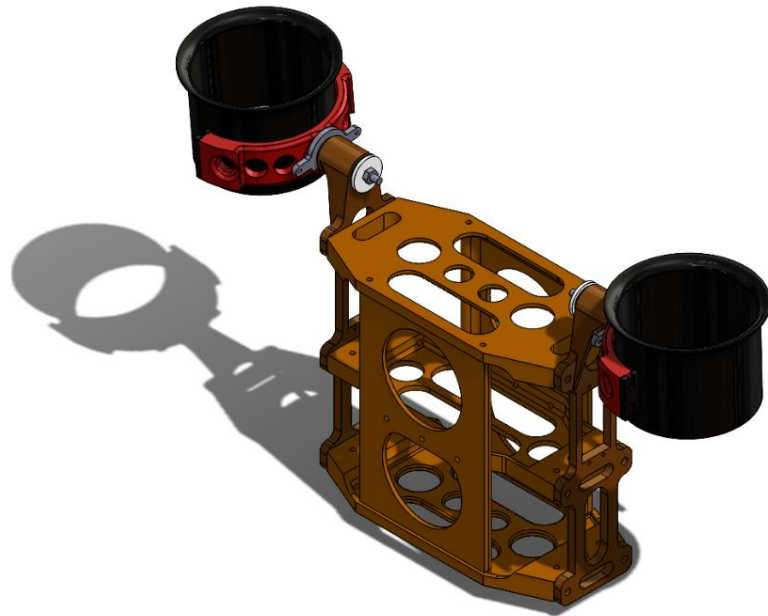


Figure 73: CAD model of the proposed UAV layout.

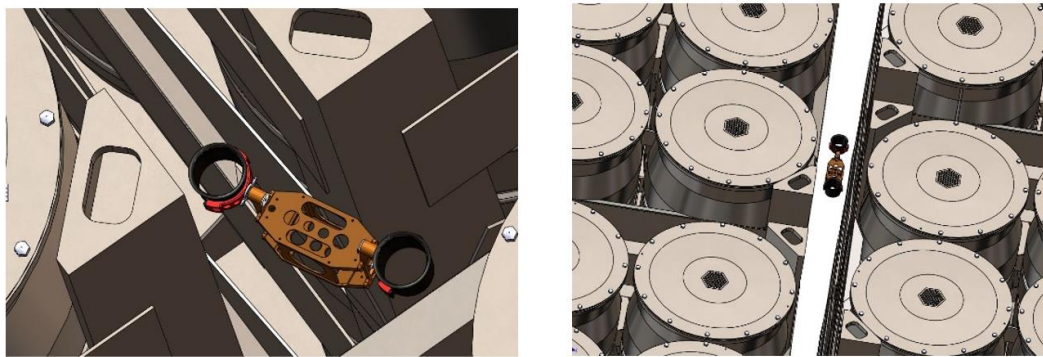


Figure 74: 3D virtual view of the proposed UAV manoeuvring between ILW stillages.

The proposed design has fewer moving parts than a coaxial thrust setup and would theoretically allow the UAV to manoeuvre between the stillages, with an estimated take-off weight up to 2.0 Kg using off the shelf components. The UAV can be built using 3D printed parts and off the shelf components only. **Electric Ducted Fans (EDF)** were used instead of conventional propellers to protect the blades from damage if the UAV physically contact obstacles (stillage or drums) during proximity flight testing. A prototype of the proposed UAV is presented in Figure 75.

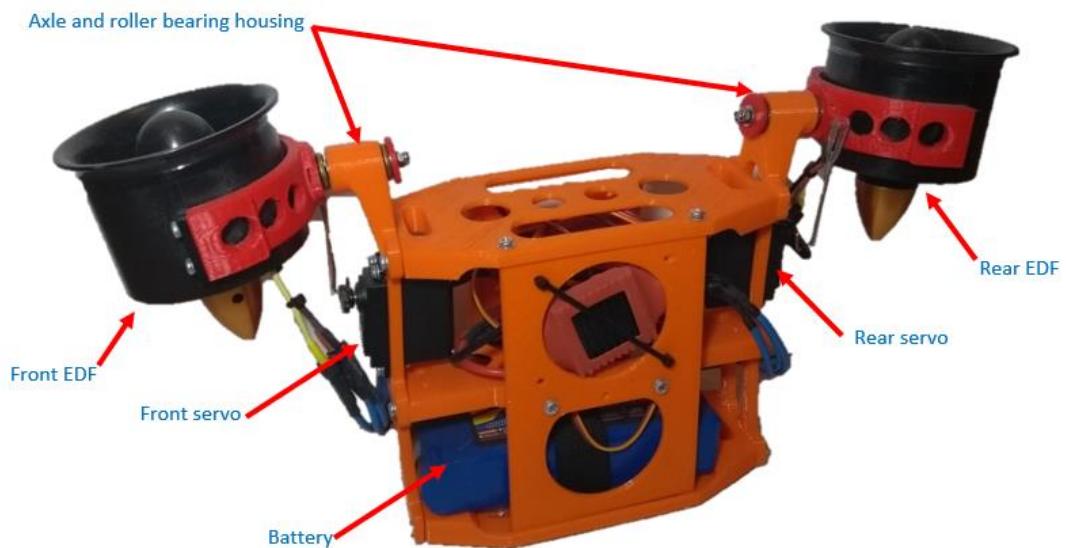


Figure 75: Prototype of the proposed UAV design.

The prototype used a lithium polymer battery as a power source, and electronic speed controllers (ESC) coupled to a set of 3 gyros and 2 servos to remotely control the UAV. The control system philosophy used to control the EDFs' thrusts and angles will be explained and evaluated in Section 4.5.4.

The prototype used a set of ball bearings press fitted into the frame through which the axle holding the EDFs was located. A set of thrust bearings were fitted between the shaft mount and the shaft locking nut as seen in Figure 76 to reduce friction on the shaft and allow it to rotate freely while locked firmly along its axis. This reduces the forces on the control servo by directing the thrust force onto the frame instead of the control servo and allow it to rotate the EDF smoothly.

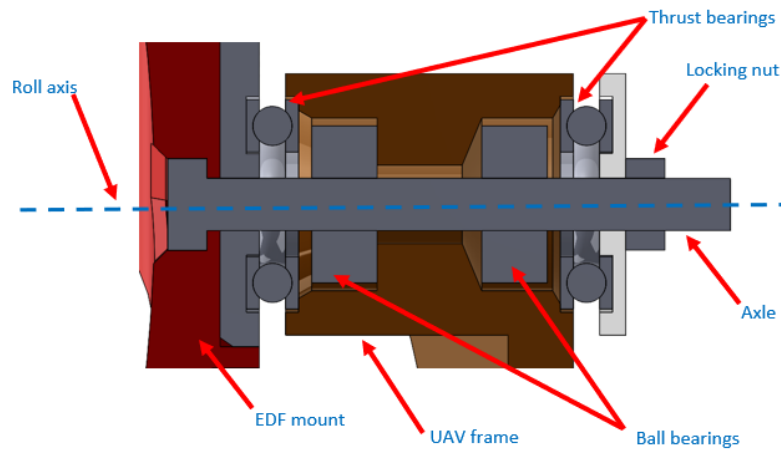


Figure 76: Internal arrangement of the EDF axle and roller bearing housing.

### 4.5.3 Endurance

Inspecting a large number of points and samples accurately could take a long time, making the endurance of the UAV a determining factor in its suitability for CM&I tasks.

The EDF used in the prototype was capable of producing 1.25 Kg of thrust at 14.8 volts and 43 Amp, therefore the maximum take-off weight must be less than 2.5 Kg (1.25 x 2). If the UAV weight is not significantly less than the maximum thrust, the UAV may be able to take off only, but will not be able to manoeuvre easily, because of the components of thrust lost in the lateral directions during manoeuvring causing a reduction in the upward thrust used for lift/take-off.

If we assume that it is operating at maximum power to fly at a weight of 2.0 Kg. The lithium polymer batter capacity needed to achieve a 30 minute of endurance will require 4 battery cells to produce the 14.8 volts (3.7 V per lithium polymer cell) and have capacity of,

$$\begin{aligned}
 \text{capacity} &= \text{number of motor} \\
 &\quad \times \text{current rating} \times \text{time} \\
 &= 2 \times 43 \text{ A} \times 0.5 \text{ h} = 43 \text{ Ah}
 \end{aligned}
 \tag{Equation 6}$$



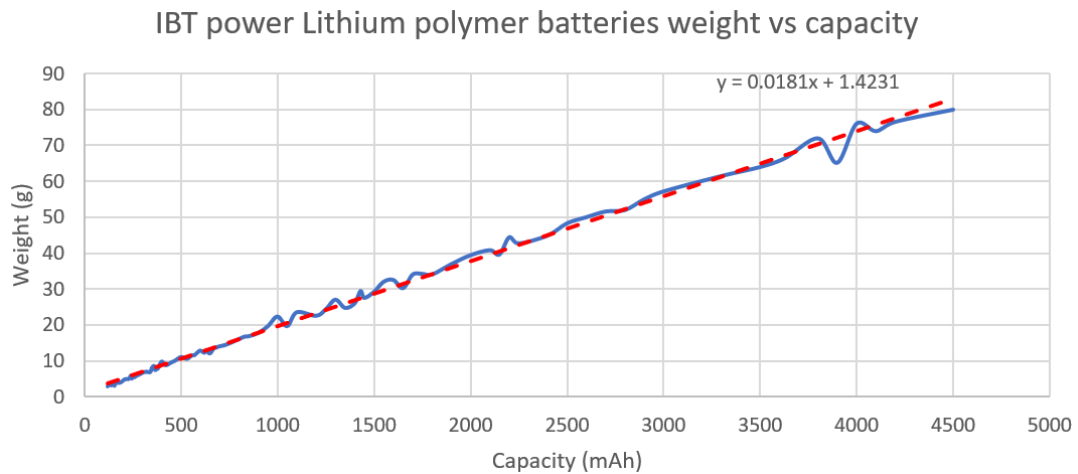


Figure 77: IBT power Lithium polymer batteries cells weight vs capacity trend line [112].

Based on the equation of the trend line of battery weight vs capacity from Figure 77, the weight of a 43Ah capacity battery is,

$$\begin{aligned} \text{weight}_y &= 1.423 + (0.018 \times \text{Capacity}_x) = && \text{Equation 7} \\ 1.423 + (0.018 \times 43000) &= 780\text{g per cell} \end{aligned}$$

This equates to a 4-cell battery weight of 3.12 Kg. This is more than 1.5 times the expected total flight weight of the UAV.

If the thrust motors and EDF are changed to ones that are capable of providing the required thrust to lift this 3.12 Kg battery along with the rest of the airframe, the efficiency and power consumption will change non-linearly as described in Equation 5. Consequently, the results of Equation 6 and Equation 7 will change, which in return will change Equation 5 values again as previously described in Figure 65. Therefore, either the thrust (flying weight) or the endurance must be chosen as a priority to avoid a design scope creep.

If the 2.0 Kg thrust power setup is used and the battery weigh is limited to 1.0 Kg to allow 1.0 Kg for the UAV structure and sensors. The battery capacity will be limited to approximately 3.4 Ah, which will provide a fight time of 0.08 hours or 4.8 minutes only.

These endurance restrictions can potentially be solved by connecting a power cable (tether) directly to the UAV as a continuous fixed weight power source. This will however complicate the control dynamics and

stabilisation of the UAV due to the oscillating weight and dragging forces of that tether, as well as limit its agility and access into complex environments [106].

**Note:** The battery versus capacity and power rating data in this section should be used for reference only, because it is from individual manufacturers. Values will differ between manufacturers but should remain within the same order of magnitude, and other battery types will have different weigh capacity ratio.

#### 4.5.4 Control model

Generally, UAVs achieve control using multiple sensors to identify the UAV attitude and location, and compensate for environmental factors and instabilities caused by the UAV dynamics [113].

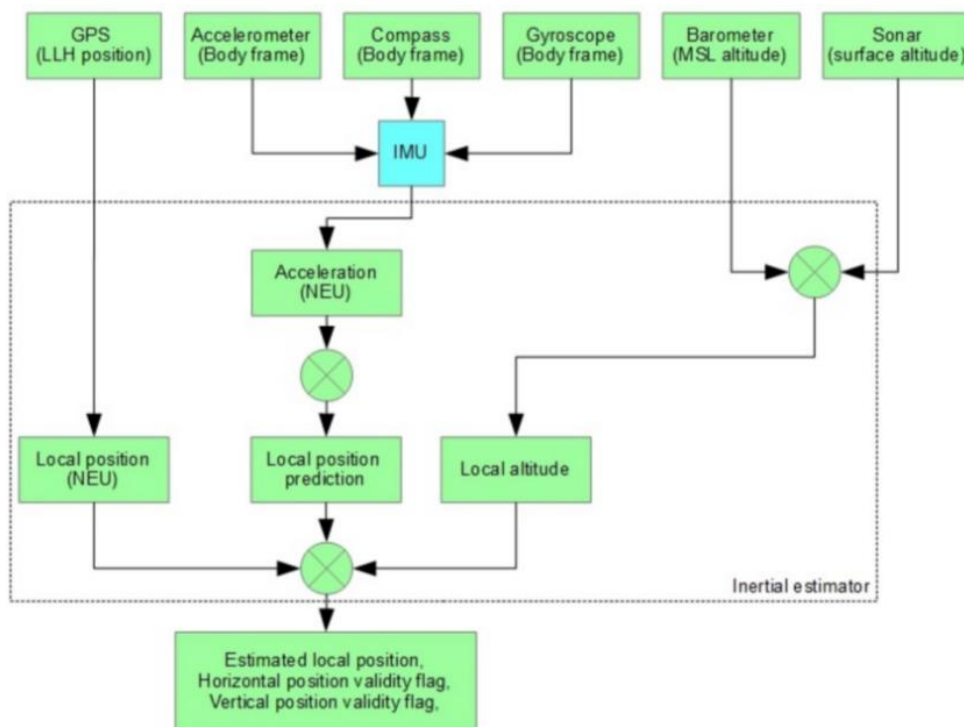


Figure 78: iNav UAV controller position estimation flowchart [113].

The previous research work described in Section 3.3.2 used direct line of sight sensors (Vicon testbed) for attitude, stability and location control [61], this will not be possible in the in-situ inspection scenario as described in Section 4.3.

There was no off the shelf electronic stabilising systems available to control the proposed UAV layout at the time of experimentation. To overcome this and avoid creating a bespoke complex stability system, off the shelf modular electronic stabilisation components from remote controlled (RC) model aeroplane were used to perform the attitude and stability controls. Gyro modules are commonly used to stabilise RC model aeroplanes and helicopters along their rotation axis. 3 of these gyros were used to create the signals required to drive the servos and motors to stabilise the UAV, and their signals were mixed using signal mixing modules to get the desired control layout in Figure 79.

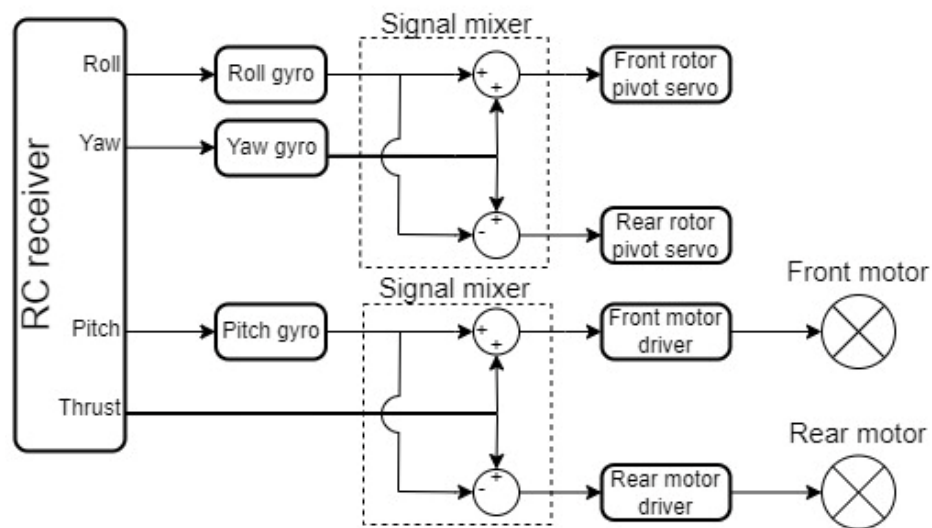


Figure 79: Gyro stability control modules setup used to stabilise the proposed UAV prototype.

During bench testing, the setup reacted and moved the servos and thrust the motors as expected to counteract rotations/movements induced into the model by hand. However, the first few tests flight showed that the setup was not adequately stabilised and very difficult to control, due to the axis coupling caused by the setup dynamics. The coupling of the axis of rotation is caused by the inertias and forces exerted on a given axis as a byproduct of controlling a different axis [114].

For example, if a disturbance causes the UAV to pitch up, the pitch gyro will trigger a signal to increase the speed of the rear motor to increase its thrust to lift up the rear of the UAV to relevel it. This increase in the rear rotor speed will cause an increase the inertia of the rear motor resulting

in a disturbance in the yaw of the UAV. The disturbance in the yaw will then be compensated by the yaw gyro, triggering a signal to change the thrust angles of the EDF to turn the UAV to the desired orientation. The change in the thrust angle caused by the yawing mechanism will in return cause a disturbance in the altitude and pitch of the UAV which will then be compensated by different gyros and result in other disturbances in return.

For the UAV to overcome this coupling and disturbances cycle to achieve stability, the gyros feedback must be coupled and a proportional integral derivative (PID) functions introduced to the control loop, to account and compensate for the expected axis coupling [113]. Moreover, if the battery is replace with a tether to increase the UAV's endurance, the tether will significantly change the stability and control dynamics of the system [114][106]. This should be part of the future work required to raise the technology readiness level of this idea.

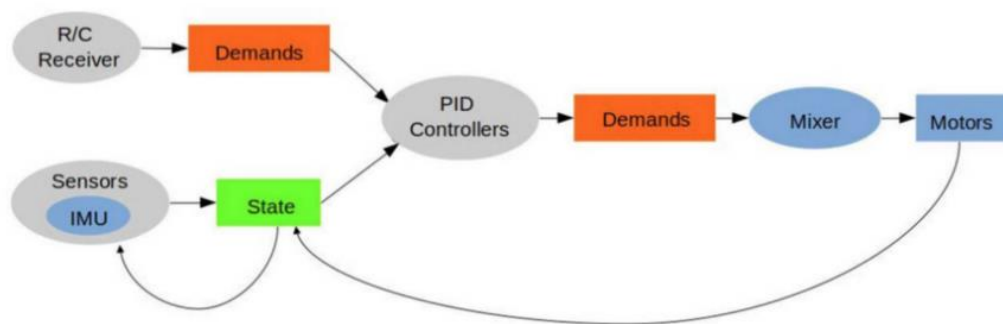


Figure 80: Hackflight controller bare minimum PID controllers necessary for stable a UAV flight [113].

From a mechanical perspective the system natural stability can also be improved using counter rotating propellers that counter act each other's inertia and momentum, as well as lowering the systems centre of gravity to allow it to naturally seek an upright state.

Once the stability and attitude are perfected, the UAV will need to navigate its way in the vault without external localisation tools, as described in Section 4.3. The empty volume above the containers (see Figure 11, Figure 15 and Figure 16) can potentially be used by the UAV to navigate above stillage stacks instead of the spaces between them. This would allow the UAV to use the vault's walls and structural features as

references for navigation using dead reckoning or SLAM, instead to the monotonous volumes between the stillage stacks.

#### 4.5.5 Compromises and future work

In summary this proposed UAV will benefit the inspection of ILW 500 L drum in-situ by offering a quick access tool to inspect/detect visual damage using lightweight cameras that do not require long inspection/data collection time.

The bi-copter platform proposed requires more work to achieve stability and can benefit from design changes to enhance the natural mechanical stability of the platform using the pendulum effect of its body weight. It would benefit from a bi-copter specific stability/control system, or a modified open source stabilisation systems to achieve the Gyro coupling and PID controls desired [113].

The use of UAVs will complicate the use of contact-based inspection tools due to the changes in the UAV stability dynamics during contact [83]. The vibration and dynamic motion of an unstable (not anchored) platform can easily lead to misalignment and drift in visual 3D data stitching [84].

The use of UAVs limits inspection time due to their endurance limitations, and consequently limits the system to fast inspection probes and minimise the quantity of data collected. This in return reduces the confidence in the collected data as described in Section 3.2.

Although using a tethered power source removes the endurance time constrains. The use of a tether will limit the platform range and agility. As well as increase the risk of failure due to cable entanglement.

#### 4.6 Passive ILW inspection robot

This section introduces the idea of a semi-autonomous passive crane like robot to deploy the metrological scanning sensors, into the small gap between the ILW 500 L drums stillages in the ILW vaults. This robot is presented in Figure 81, it is inspired by the satellite industry approach of deploying large arms and solar arrays in space, after being packaged inside very small volumes in launching rockets.

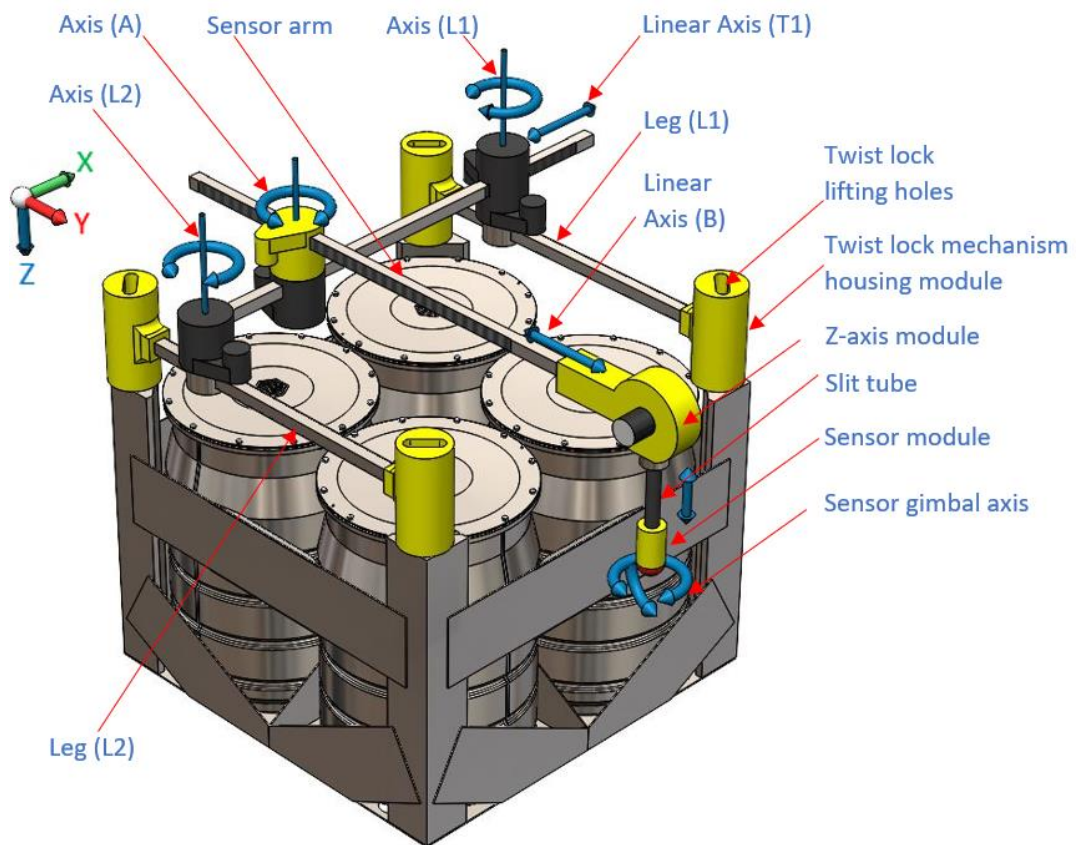


Figure 81: 3D model of the passive robot proposed locked on to top of an ILW 500 L stillage stack, while deploying a sensor down to reach the lower stillage tiers.

The robot is equipped with an extendable arm made from a slit tube, to deploy a sensor module into the bottom tiers of stillages, while anchored on top of a stillage stack using twistlocks. The sensor module will contain a 2-axis gimbal to orient the onboard metrological sensors to view all possible angles and faces of a given stillage. The robot structure is made from modular components to ease on site assembly, reconfiguration, and decommissioning.

The robot is designed to be lifted onto the first accessible complete stack of stillages using stacking trucks or a crane if available, where it will then manoeuvre independently across stillage stacks without the constant need of a crane or a stacking truck, to reach all the completes stillage stacks in the vaults. It uses hydraulic or electromechanical axial motors to rotate and extend its axis and limbs, powered via an umbilical tether

for endurance, and to keep electronics out of the vaults and radiation zones for operational longevity.

#### 4.6.1 Anchoring

Most nuclear decommissioning products are housed in containers and stillages, made from austenitic stainless steels, because of its high resistance to corrosion [2]. The iron in austenitic stainless steels such as 316 and 304 that are used in the ILW packaging [2], remains in the form of austenite (gamma iron) which is a non-ferromagnetic phase of iron [77]. This eliminates the use of standard industrial magnetic based fixtures and clamps used in machinery metrology.

Over the years many iterations, shapes, types and sizes of ILW containers have been created and stored in the existing ILW vaults. Regardless of all the variabilities in the containers, all the containers have entered and/or will enter the vaults using the same vault cranes and/or lifting trucks that use the same spreader twistlock lifting arrangement layouts to meet WPS/604 [22] and RWM TSCS 1079 [19] as per Figure 13 and Figure 14. Making the twistlock lifting apertures the key feature to use as a consistent anchor point for the robot to lock onto in both legacy and future containers.

The robot can be deployed using the crane or the lifting truck used to stack the stillages in the vault, by lifting the robot from its own twistlock lifting apertures shown in Figure 82, and placing it on top of a stillages stack as per Figure 81.

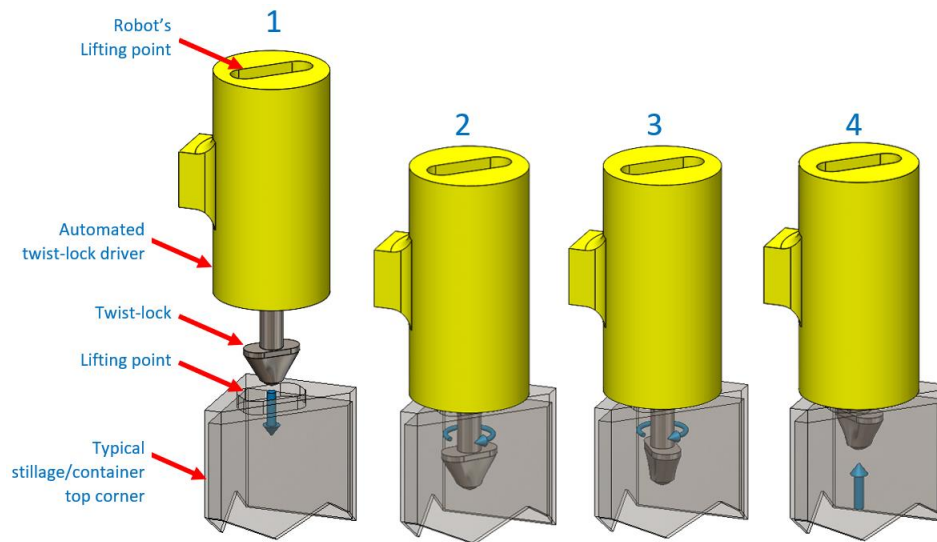


Figure 82: Isometric view of steps taken by a twist-lock mechanisms to anchor the robot onto a stillage top corner.

Once the robot is on top of a stillage, it will:

1. Align the twistlock module with the container's Twistlock aperture.
2. Lower down the twistlock module to fit the twistlock Key into the aperture.
3. Rotate the twistlock key to trap it in the aperture.
4. Retract the twistlock key up to latch the robot secure onto the container.

The twistlock lifting arrangement on the ILW 500 L drum stillages' is designed to lift gross mass up to 9 tons [22] and support a total load of 540 kN [23]. This will be a hard limit to the accepted weight of the final robot depending on the full stillage stack overall weight, and the robot's swing arm moments when extended or moving. The centre of gravity of the robot + stillage/container must always remain within the surface area of the stillage/container described in Figure 14 for stability, assuming a rigid lock between the robot and the stillage lifting points (except during the process of moving from one stillage stack to another).

By anchoring the robot to the ILW 500 L drum stillages twistlock, the following will be achieved:



- The anchoring of the robot to a stillages full of heavy encapsulated 500 L drums with gross weights of hundreds of kilograms, gives the robot a large and heavy stable base, to minimise any dynamic and vibration forces on the robot to improve its stability during metrological scans.
- The presence of identically laid out anchor points can be used as datum points by the robot during metrological scanning and inspection of the ILW containers.
- Mechanically locking the robot onto the stillages saves operation power and energy, because the robot does not have to constantly supply power for its drives to balance or hold the robot in position like most legged robots or aerial vehicles.
- The arrangement of the stillage stack and anchor points will aid in the dead reckoning processes for navigating the robot in the vaults (This will be detailed in Section 4.6.6).
- The anchoring mechanism should be strong enough to operate using 3 or even 2 locks only for redundancy, to ensure that the robot is not crippled if one or two twistlocks mechanically fail.
- The robot anchoring mechanism module should be designed to fit in a ILW drum directly to ease its end-of-life decommissioning process.

#### 4.6.2 $XY_{plane}$ sensor motion

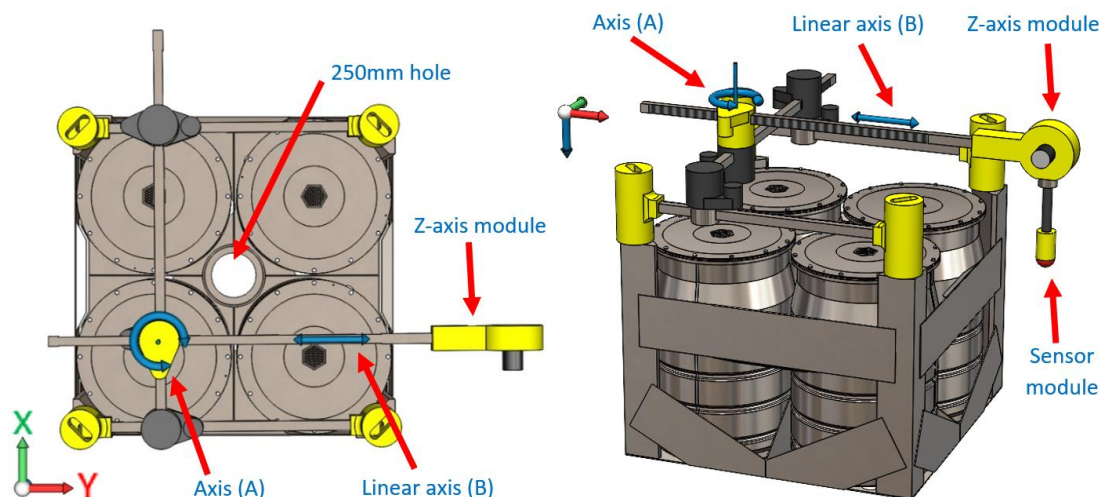


Figure 83: Illustration of the pivot and extension points of the arm carrying the Z-axis module.

Once the robot is locked on top of a stillage stack, the robot will use a 2-axis arm to move the Z-axis module across the  $XY_{plane}$ . This is performed by rotating axis (A) module and extending/retrieving linear axis (B) arm. The X and Y coordinates of the robot's end effector (sensor module) can be defined as,

$$\begin{aligned} X &= \Delta B \cos(A_{\theta}) + K_X & Y &= \Delta B \sin(A_{\theta}) + K_Y & Z &= \Delta Tube + K_Z \end{aligned} \quad \text{Equation 8}$$

$K_{XYZ}$  is the sensor origin point offset from datum point at zero(origin) state of the robot. The extending/retrieving of the linear axis (B) will be performed using a rack and pinion mechanism.

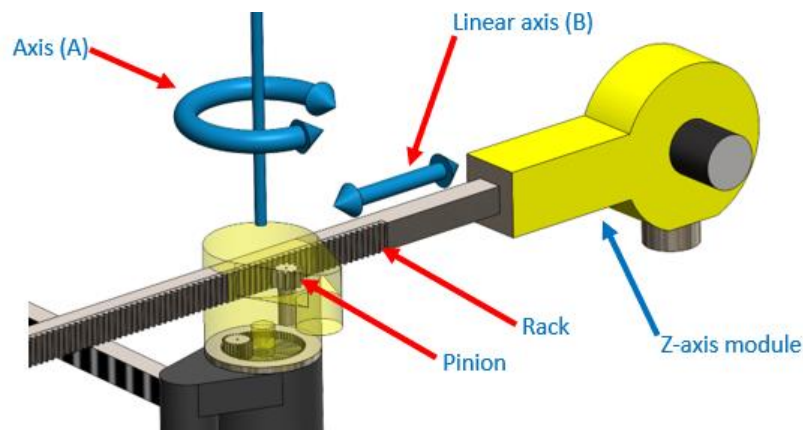


Figure 84: Illustration of a rack and pinion arrangement to extend and retrieve the Z-axis module along the linear axis (B).

The Axis (A) module is offset from the centre of the robot's body (see Figure 83), to give the Z-axis module access to the centre of the stillage, to allow the Z-axis module to lower the sensors module into the 250mm hole in the centre of the stillages. This will increase the direct line of access of the sensors from **30 %** to **42 %** as described in Section 3.5. (Note: these percentages still do not include the drums' lid or bottom surface it is sitting on.)

### 4.6.3 Z axis

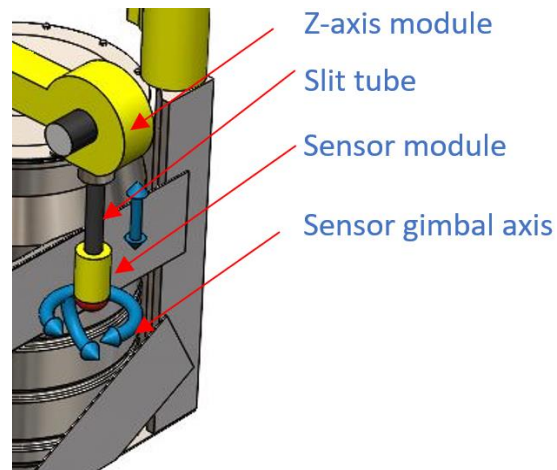


Figure 85: Z-axis module moving the sensor module along the Z axis by rolling and unfolding a slit tube.

The Z axis motion of the sensor module will be performed using a compact slit tube mechanism. These mechanisms are currently used in nuclear and nano satellites technologies to deploy long range arms from compact housing [115]. A rigid 10 m boom can be folded and stored in a box as small as 100 X 100 X 50 mm [115], and will be sufficient to cover the maximum stillage stacking height of 9.0 m [23] without the need for any of the complex multi-joint manipulator arm mechanisms described in Section 4.2, or a soft body for rectilinear motion.

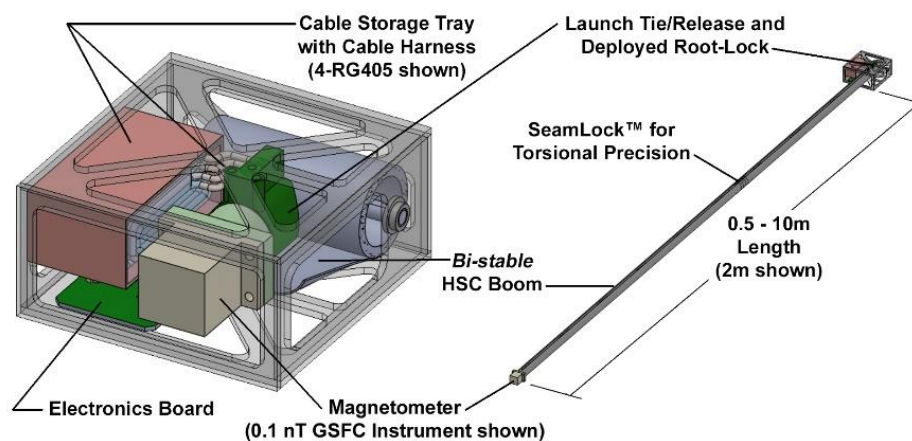


Figure 86: Magnetometer deployment using roll out tube for a NASA cube satellite [115].

Slit tubes are made of curved bi-stable composite tubular structures [116]. These tubes are structurally stable in a rolled configuration around a reel (1<sup>st</sup> state), then when deployed their weave curves their cross section to form a C shape, to create a rigid beam that can support weight along its length (2<sup>nd</sup> state) [116]. The transition from the first state to the second state can be done by mechanically unrolling the slit tube under control, or by using the tension in the rolled states to self-deploy the tube in a spring like action [117].

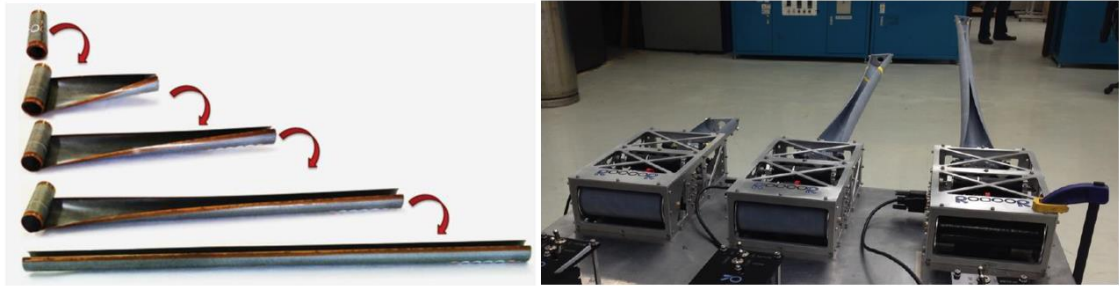


Figure 87: (Left) Slit tube boom deployment stages. (Right) slit tube deployment mechanism designed by Rocco [117].

A slit tube boom is preferred on a simpler rope/cord mechanism because it provides a rigid axis whose end position should not swing due to the motion of the X-Y axis arm, or the expected cooling vent air with speeds up to 10 Km/h [25]. It is necessary to keep the entire scanner deployment mechanism rigid, minimize the hardware and sampling strategy metrological errors, because the position of the end effector will be calculated using the position feedback of the sensor arm and slit tube extension length. [Refer to Section 3.2 for details].

The slit tubes' rigidity when deployed allows the extension length ( $\Delta z$ ) of the tube to be calculated by counting the number of turns ( $n_{turns}$ ) the tube reel performs and the reel diameter ( $\phi_{reel}$ ),

$$\Delta z = \pi \times \phi_{reel} \times n_{turns} \quad \text{Equation 9}$$

For a more accurate  $\Delta z$  value, the changes in reel diameter as the slit tube is rolled on to the reel, and the expansion factor in the boom and folded tube due to the temperature and sensor module weight must be included Equation 9.

Wires and sensor circuitry can even be imbedded into the boom composite weave, to create a neater and more compact sensor deployment arrangement, with no hanging wire from the robot to the sensors. This is currently under development for space industries, where solar panels and sensors are being embedded into self-deployed slit tube on cube satellites [117].

At the end of the slit tube's operational life, the compactness of its folded state will ease its decommissioning process by allowing it to fit into decommissioning containers without the need for disassembling or cutting into short length pieces.

More tailored slit tube booms can also be created to bend or curve around obstacles and into gaps of interest as they deploy, these bends are induced by modifying the composite layout angles and thicknesses along the slit tube length [118][119]. This should be considered in future research and proposals for task specific extendable booms.

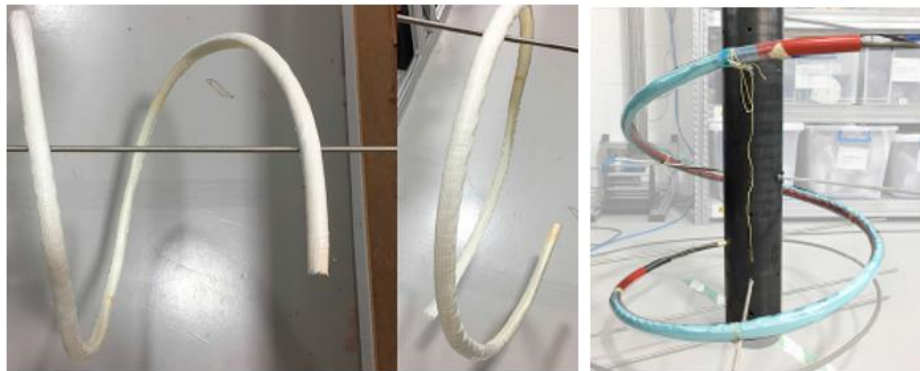


Figure 88: Helical bi-stable slit tube unwrapping around a beam [119].

#### 4.6.4 Stillage hopping

In storage facilities where there are no overhead cranes to place the robot on top of the stillages at the far end of the vaults and stacking trucks access is inhibited, the robot would be able to move itself across the top of the stillage stacks on its own. The robot only needs to be placed on top of an accessible stillage stack, where it will make its way onto the inaccessible stacks (inaccessible by stacking trucks) by performing the following steps:

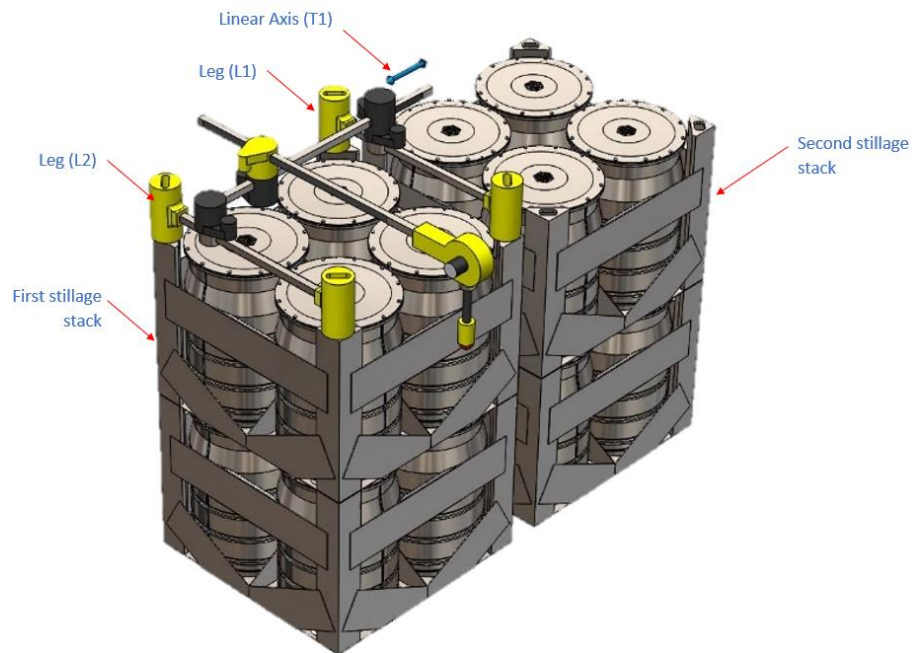


Figure 89: Step 1 in the stillage hop process.

- 1) The two twistlocks on leg (L1) release from the first stillage and Leg (L1) moves forward along the (T1) axis to align with the nearest twistlock holes on the second stillage using a rack and pinion mechanism like that of axis (B) described in Figure 84. Axis (L1) and (L2) may occasionally need to rotate to pan and rotate leg (L1) to compensate for misalignments in the stillage stacks.

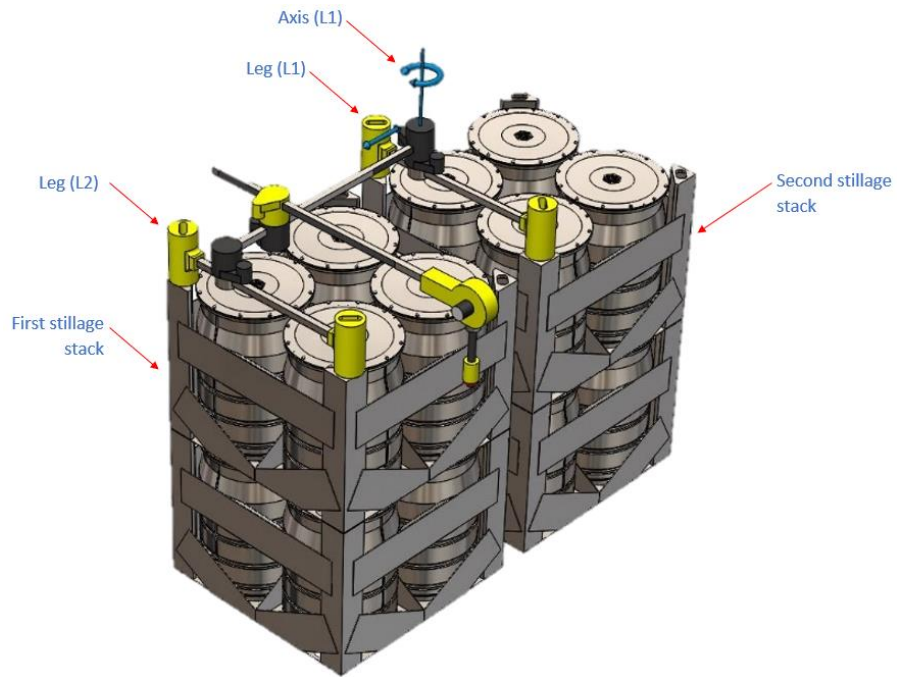


Figure 90: Step 2 in the stillage hop process.

- 2) Leg (L1) twist lock anchors the robot to the second stillage, then release the twist lock on Leg (L2) off the first stillage.

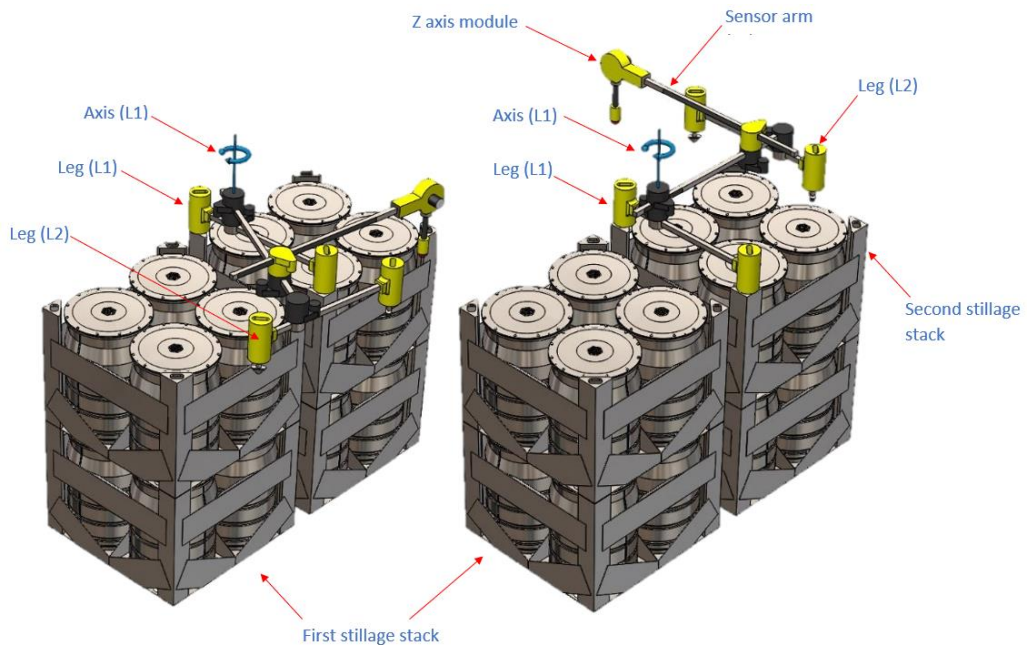


Figure 91: Step 3 in the stillage hop process.

- 3) Axis (L1) is activated to rotate the entire robot around, and onto the top of the second stillage. Axis (A) and (B) of the sensor arm should

also move during this manoeuvre to minimise the forces on the stillages and anchors, by controlling the robot's centre of gravity using the Z axis and sensor modules weights as a counterbalance.

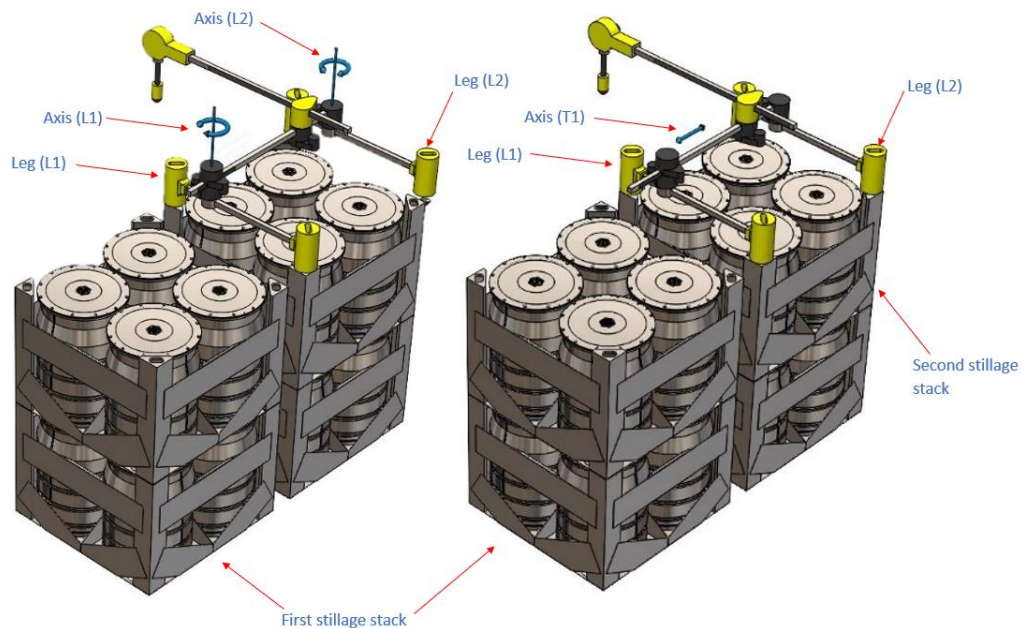


Figure 92: Step 4 in the stillage hop process.

- 4) Axis (L2) is then activated to rotate Leg (L2) to align it with the second stillage stack far end twistlock apertures, and linear axis (T1) is used to move the leg (L2) back towards the twistlock apertures to finish the alignment process.
- 5) The twist lock on leg (L2) then anchors onto the second stillage and the origin of the robot is recalibrated to the new  $K_{XYZ}$  offset values, based on the robot's final configuration on the second stillage.

This allows the robot to manoeuvre and access all the drums in the vault, except for the unlikely scenario where a stillage column have a different number of tiers. This is an unlikely scenario to occur at the far end of the vaults because the stillages are expected to always be stacked from the back to front to maximize the efficiency of space usage.

On the other hand, the front newest stillage stack will have a high likelihood of having different column tier numbers because the column tiers won't be added/exist yet. This will make it unsuitable for the robot to move from them on to the further back stillages. Therefore, it will be



crucial to emplace the robot on the first complete stack while accessible before a new incomplete stack is added to the vault.

The front most incomplete stillage stacks could be temporarily disregarded during this robot's inspection process because this stack will contain the newest drums, which won't be expected to have aged yet. It will be easier to perform the first inspection on the newest drums using other means before they enter the vault.

#### 4.6.5 Power source and drives

One of the main criteria of the robotic inspection required by the proposed robot is to CM&I the drums over long time periods, to assess the changes caused by the ageing of their contents and structures. This process can take many years or even decades, therefore the robot too must be able to operate for many years constantly. Which eliminates the suitability of using batteries to power the robot for many reasons. Batteries require recharging and so will require the robot to move back and forth in the vault to access recharging stations or power sources. This is not ideal due to the complex process required to move the robot across many stillages and being off loaded from the top of the stillages to a charging station. Moreover the deterioration of batteries capacity and power over time [120], will cause multiple battery changes during the robot's life span, which will increase the amount of contaminated corrosive decommissioning product (the deteriorated batteries). Therefore, a constant power source in the form of a tether/umbilical will be more suitable to power the robot and all its auxiliaries.

The use of tethered power source will benefit the robot in multiple ways,

- 1- It will provide a continuous and reliable electrical and/or hydraulic power source that do not degrade overtime like batteries [120].
- 2- Keep the electrical and/or hydraulic power sources away from the robot, in accessible areas that are easy to access for maintenance.
- 3- Some electronics and equipment can be moved away from the robot into radiation shielded enclosures to increase their operational life expectancy, as well as reduce the robot's overall weight.

- 4- Placing hydraulic oil reservoirs and pumps away from the robot allows oil changes and pumps maintenance while the robot is in operation.

The tethered power source will also have some disadvantage, some of which may be possible to overcome, and others will be a compromise.

1. The tether will have a likelihood of entanglement and/or damage during the robot's locomotion and will make retrieving the robot in a catastrophic failure scenario more complicated.
2. The robot's motors must be strong enough to move the robot's body as well as drag the weight of a tether that is long enough to reach the far end of the vault when hopping across stillage stacks.
3. Extra equipment and reels will be required to pull back and house the tether while the robot is closer to the front of the vault [121].
4. If hydraulic power is used, complicated multi core tethers will be required to carry different individual hydraulic lines along with multicore cables while being radiation shielded [87].

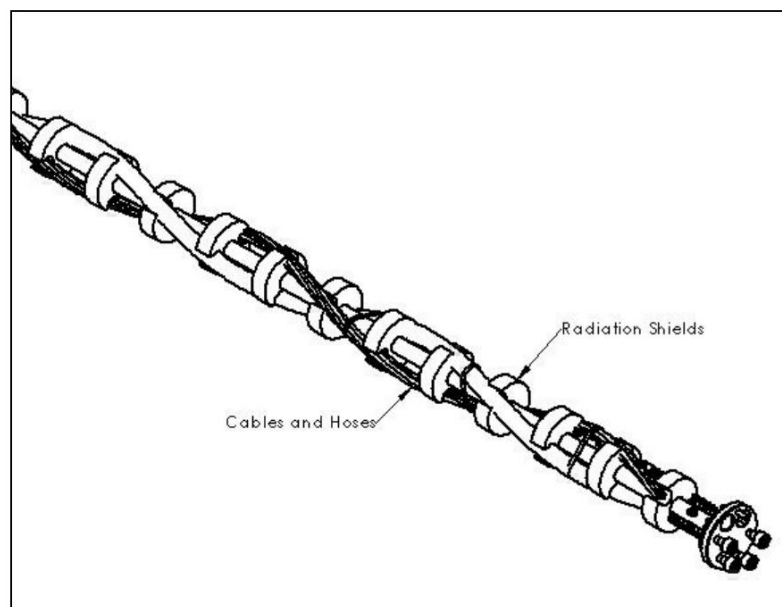


Figure 93: Radiation shielding tether power sources in radioactive environment [87].

5. Slip rings will be essential to avoid twisting the tether during the rotation of the robot while hopping across stillages, and in between power source and tether reel to allow tether reeling [121]. This will be complicated if multiple hydraulic lines are used.

These disadvantages and compromises in the use of tethered power source will be the determining factor in the choice between electromagnetic or hydraulic axis motors. The choice will be based on designers and manufacturers,

- 1- Available motors' size, weight, speed, and torque.
- 2- Tether complexity and weight per meter, compared to the motor's torque and the vault size.
- 3- Complexity and compatibility of the slip ring connections mechanism between the robot and tether.
- 4- Size and clamping force required by the anchoring mechanism in relation to the overall robot and tether moment arm during the stillage hopping process.
- 5- International and national standards and legislations that the motors need to meet before being used inside a nuclear ILW vault.
- 6- The overall budget of the project and the cost estimations from the motor and tether manufacturers to provide a motor that can meet all the operational and legislative requirements.

The results of these points will vary between designers, manufactures, budgets, and operational legislations and standards, making the choice between electromagnetic and hydraulic motors dependant on where and by whom they will be made and used.

#### 4.6.6 Navigation and sensor localisation

Once the drive mechanism is decided and the robot is able to move and manoeuvre within the vault, it needs to know its state and location within the vaults, to navigate to points of interest. This may not be possible to achieve using the common most localisation technologies like GPS or SLAM as described in Section 4.3 [107][108][109][110]. However, the answer to the navigation challenge in this specific scenario can be in the form of a very simple dead reckoning count.

This passive robot proposed can only move across stillages one at a time (discretised count and distance), and the stillages are stacked in constant/known patterns with known sizes. Thus, the robot simply needs to keep count of how many stillage it hopped across in each direction, to find its current location in the  $XY_{plane}$ , relative to its starting point. This

will be complemented by the presence of the robot itself over the stillages, which will give it direct line of sight of the walls for location reference. An altimeter can then be used to obtain the absolute Z axis position relative to sea level and comparing that to the vault's floor altitude compared to sea level, will give the robot's Z position relative to the vault's floor to complete the  $K_{XYZ}$ . The sensor module location can be identified using the  $K_{XYZ}$  in Equation 8 and Equation 9.

#### 4.6.7 Sensor module

Creating a modular sensor housing and gimbal, will ease the process of sensor maintenance and changes, to account for different and future scanning/probing technologies. (The ideal sensors of choice are described in Section 3.4)

The Sensor module will contain a 2-axis gimbal, a 360° axis in the  $XY_{plane}$ , and a 90° axis perpendicular to the  $XY_{plane}$ , as shown in Figure 81 and Figure 85. This will provide the sensors with a panoramic view of its surroundings and maximise the direct line of sight access to all the stillage and drum faces.

The use of camera electromechanical gimbals instead of multiple sensors pointing in different directions to gain the panoramic view, will increase the number of moving parts, but increase the system reliability by reducing the number electronics that have a probability of failure due to ionising radiation in the ILW vault.

#### 4.6.8 Automation and swarming

The monitoring of the nuclear decommissioning product containers, is expected to continue for hundreds of years, prior to the backfill process of the storage vaults [10]. Given that the ILW containers geometrical changes described in Section 2.7 can take decades to show significance [13], it is important that any CMS used to dimensionally scan/inspect the container, be both accurate and precise enough to detect the subtle changes over long time periods (possibly decades). This will require accurate and repetitive processing that should avoid human errors and judgment, for the inspection data to remain consistent for comparability.

Direct tele-operation of any robots by humans in the process of nuclear decommissioning and CM&I can be slow, while the legacy waste inventory that needs processing is astronomical [88]. This combined with situational awareness difficulties during manual controls of robots, caused by operators lack of depth perception from controls via shielding windows or cameras [88] ,emphasise the need for some level of automation in the inspection process. Nevertheless, due to the variety of stillage designs and ILW drums that have been packed and stored over the years, it is suggested that the proposed robot operates as a semi-autonomous system to appeal to the safety conservative nuclear industry [88]. The proposed system should rely on human operators to control and monitor the process of transporting and anchoring the robot onto the top of containers' stacks, and the repetitive process of deploying the sensor module to all points and angles of interest should be automated. Automation of the sensor module deployment is encouraged because it will only be performing the motions required to cover the external surfaces of the cuboid volume enclosing the containers stack, in a controlled repetitive environment with no unexpected obstacle or humans present.

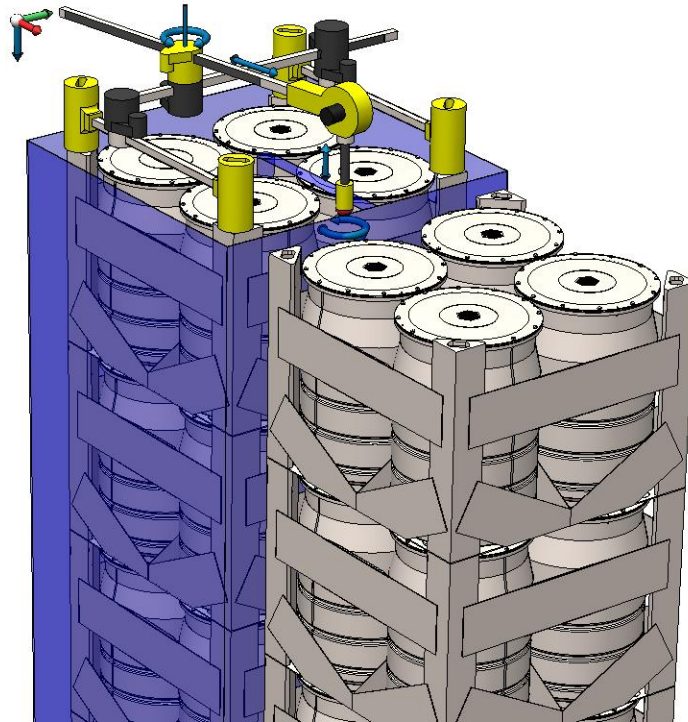


Figure 94: Highlighted in blue is the area surrounding the stillage stacks that will always be clear of obstacles, where a path for the sensor module to travel through can be created.

The automation of the scanning process will also allow the operators to deploy multiple robots (swarm) into the vault, focusing on the safety critical parts of the inspection process, and saving time by automating the repetitive inspection motion. The use of a swarm of robots to inspect all the containers in the vault regularly will be necessary due to the large quantity of the containers requiring monitoring.

At the UK Sellafield site, 69,600 m<sup>3</sup> of legacy ILW waste must be placed into 179,000 storage containers [88]. If the proposed robot can hypothetically inspect 1 of these containers per hour and operate all year round without breaks, it will need 20.4 years to inspect all the containers at Sellafield. This ambitious estimate does not include time lost in hopping across container stacks, maintenance, down time, and the inspection. This highlights the need for both the automation and use of a robotic swarms, to significantly reduce the inspection process time to a reasonable value, and to provide repetitive inspection results from individual containers to use in data comparison and extrapolations.

The true inspection time of an individual ILW 500 L drum in-situ using the proposed systems will depend on the robots' actuators speed, probing technology used, and data acquisition and processing time. These factors will vary between the sensor and robot designers, manufacturers, end users' budgets, and international and national operation speeds permitted by the safety legislations covering the ILW vaults. Thus, no true estimate of the inspection time per container can be given at this stage of the project.

#### 4.6.9 Digital simulation

Access to the inspection subject (used ILW drums and stillages) and the vaults for testing the robot concept is not feasible at this stage of the project, due to the radioactive nature and safety standards in the nuclear industry. Digital simulations and prototypes will be needed first to raise the concept TRL and ensure its trustworthiness before committing to real life testing.

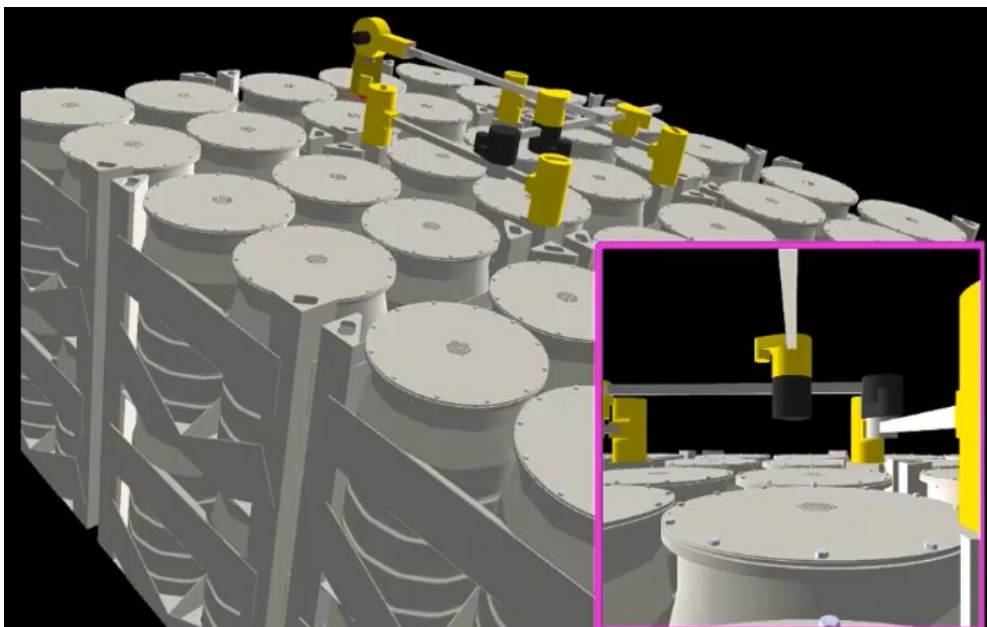


Figure 95: Virtual Simulation illustrating the proposed robot mounted on a stillage and performing a visual scan. The view on the bottom right is the sensor module POV at this robot state.

To virtually test the concept and functionality of the proposed robot, the robot and its environment were modelled on CAD, to visually illustrate the layout and recommended components sizes. From there, the models

of the robot's individual components were uploaded into a software developed in "Processing" IDE to visually simulate the robot's manoeuvrability and range of motion, to verify its ability to access the spaces required by the sensors to perform the inspection tasks. It will also aid in debugging the robot top level controls and provide a platform for users to visually observe different manoeuvres and motion patterns during development.

Each model/component of the virtual robot was given a high-level java class, which contained the components' position, vector, and orientation to allow the software keep track of the individual components' location and motion profile. This was used to assign each limb of the robot its own control rules and restrictions, to test the overall manoeuvrability of the robot and its ability to reach the points of interest using the range of motion available to it. This gave a visual representation of the robots reach and the collision points.

This visual representation will aid the process of creating and optimising the motion patterns needed to collect the largest amount of data in the most efficient way and provide a digital twin of the robot's expected layout state. If a digital twin of the robot is synchronised with the real robot's limbs position feedback, it will provide the operators with a 3-dimensional representation of the robot's layout/state to reduce the need of external camera or shielded window access to view of the robot's state during tele-operation.

Unlike Equation 8 and Equation 9 used to determine the sensor module location in Section 4.6.1 and 4.6.2. The origins points of all the limbs and components in the virtual robot move in relation to the 0 point (origin) in the 3D volume assigned in the software, because they do not have a real life physical constrain or anchor points. Therefore, the motion equations of the sensor module and virtual limbs are replaced with 3D matrix transformations to represent the desired motions in relation to an external datum/origin.



Rotation matrix around X-axis of an object (pivot point)

$$\begin{bmatrix} 1 & 0 & 0 \\ 0 & \cos\theta & -\sin\theta \\ 0 & \sin\theta & \cos\theta \end{bmatrix} \times \begin{bmatrix} X \\ Y \\ Z \end{bmatrix} = \begin{bmatrix} X' \\ Y' \\ Z' \end{bmatrix} \quad \text{Equation 10}$$

Rotation matrix around Y-axis of an object (pivot point)

$$\begin{bmatrix} \cos\theta & 0 & \sin\theta \\ 0 & 1 & 0 \\ -\sin\theta & 0 & \cos\theta \end{bmatrix} \times \begin{bmatrix} X \\ Y \\ Z \end{bmatrix} = \begin{bmatrix} X' \\ Y' \\ Z' \end{bmatrix} \quad \text{Equation 11}$$

Rotation matrix around Z-axis of an object (pivot point)

$$\begin{bmatrix} \cos\theta & -\sin\theta & 0 \\ \sin\theta & \cos\theta & 0 \\ 0 & 0 & 1 \end{bmatrix} \times \begin{bmatrix} X \\ Y \\ Z \end{bmatrix} = \begin{bmatrix} X' \\ Y' \\ Z' \end{bmatrix} \quad \text{Equation 12}$$

Appendix 8.1 contains the key java functions and classes created to move the robot models bodies in relation to each other and a fixed volume origin.

This digital simulation allowed the software to track the sensor module location and orientation to use them to create a **point of view (POV)** of the sensor module's field of vision. This represents the expected sensors and operators POV during operation, and visually clarifies how limited the field of view is from the accessible gaps.

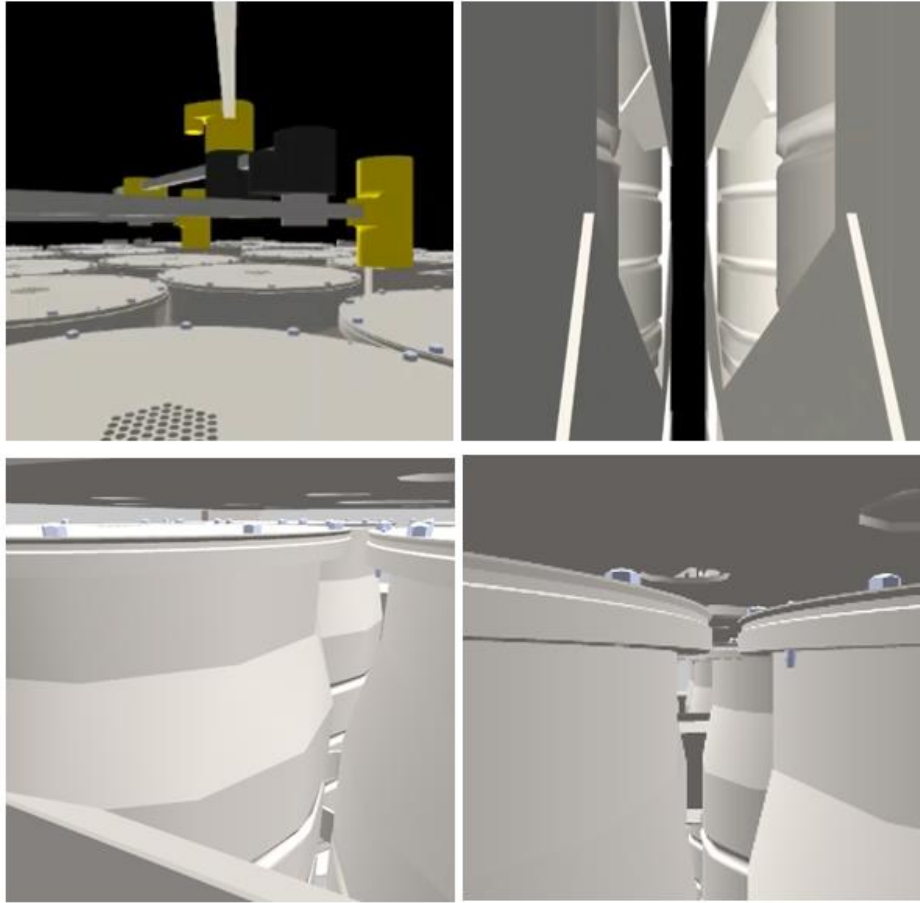


Figure 96: Simulation of POV of optical sensor/camera observing the container from the Sensor module.

This representation of the limited field of vision emphasizes the challenges that would face a photogrammetry or laser scanner and the need for a different mean to inspect beyond direct line of sight.

The route of writing a software script was preferred over standard CAD software, because

- It can be used by any windows user without software subscriptions.
- Allow future integration with other scripts/software to process the data collected from the sensor module POV.
- Allow future integration with other scripts/software to optimise the data collection process/manoeuvres of the robot.
- It can be used as a platform for experiencing/practicing manual controls of the robot.

- Directly controlling a scale model of the robot while displaying a digital twin to compare the virtual manoeuvres to scaled real-life ones.

#### 4.6.10 Mechanical Prototype

After modeling and simulating the robot's motion virtually, a 15 % scale robot was designed and built to test the motion algorithm and the robot's maneuverability in real life. 15 % scale was chosen to ensure the components sizes were small enough to be built using the available 3D printers and suit standard off the shelf motors. Many lessons were learnt from the scale model that were not considered in the concept CAD and virtual models.

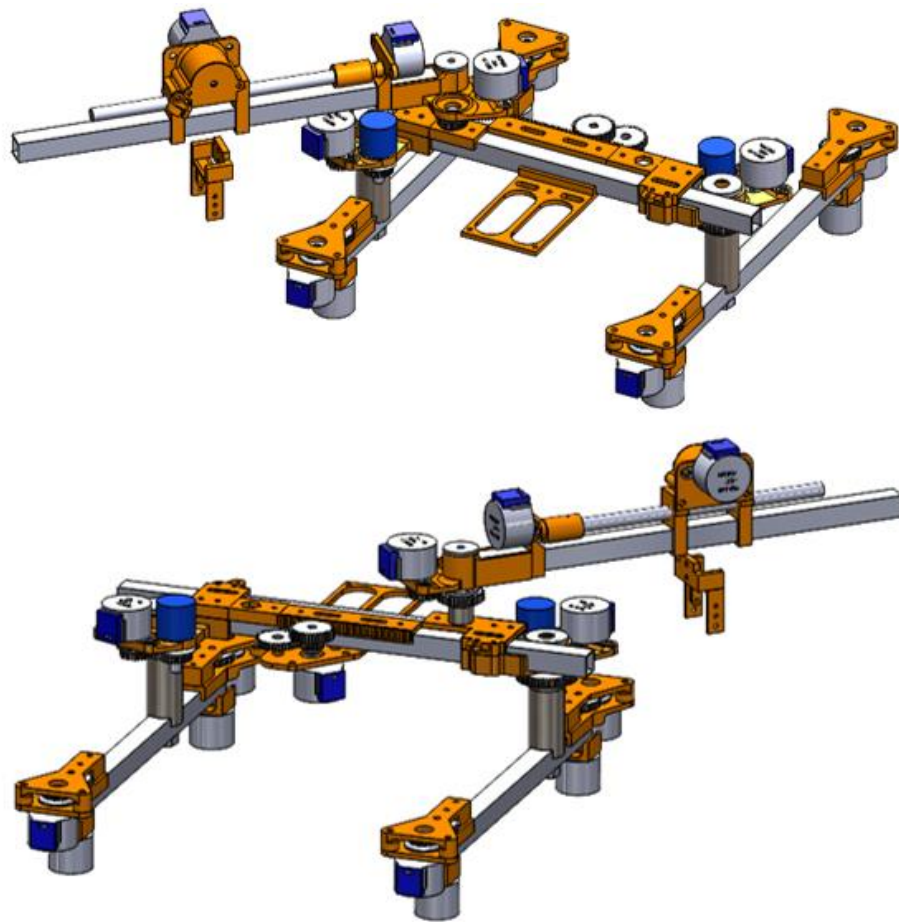


Figure 97: Isometric views of the latest CAD model of the 15 % scale robot prototype.

The 15 % scale robot arms' rotation mechanism was not identical to the real one, due to mechanical scalability factors and differences in forces experienced by the arms. The scale robot's frame is constructed from 3D-printed parts and aluminium channels and used off the shelf motors, drivers, and electronic components.

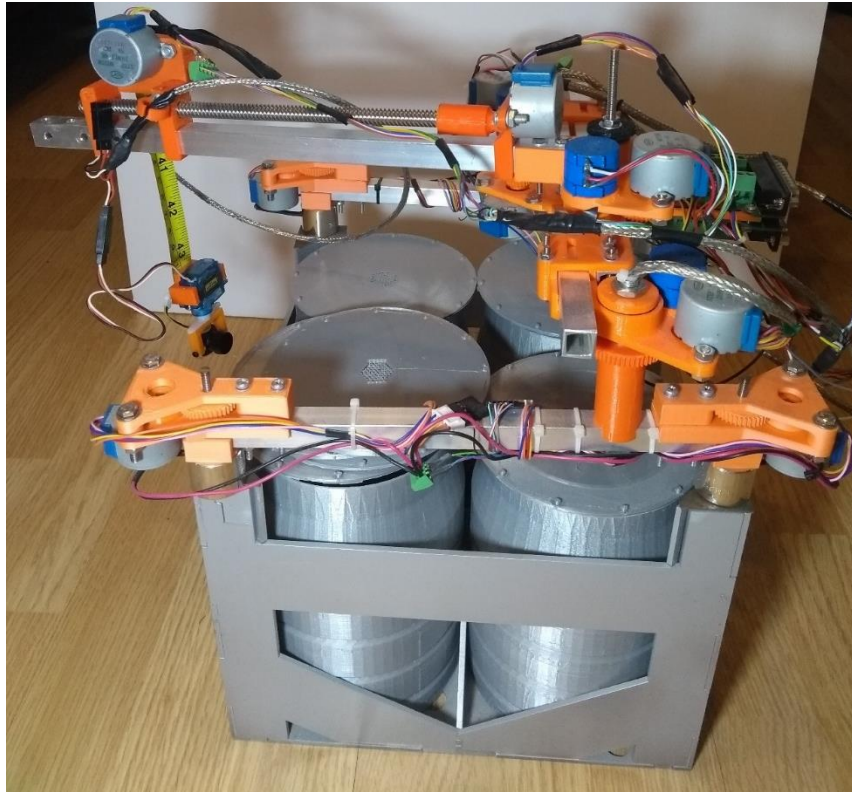


Figure 98: 15 % scale model of the proposed robot anchored onto a 15 % scale mock 500 L ILW stillage and drums.

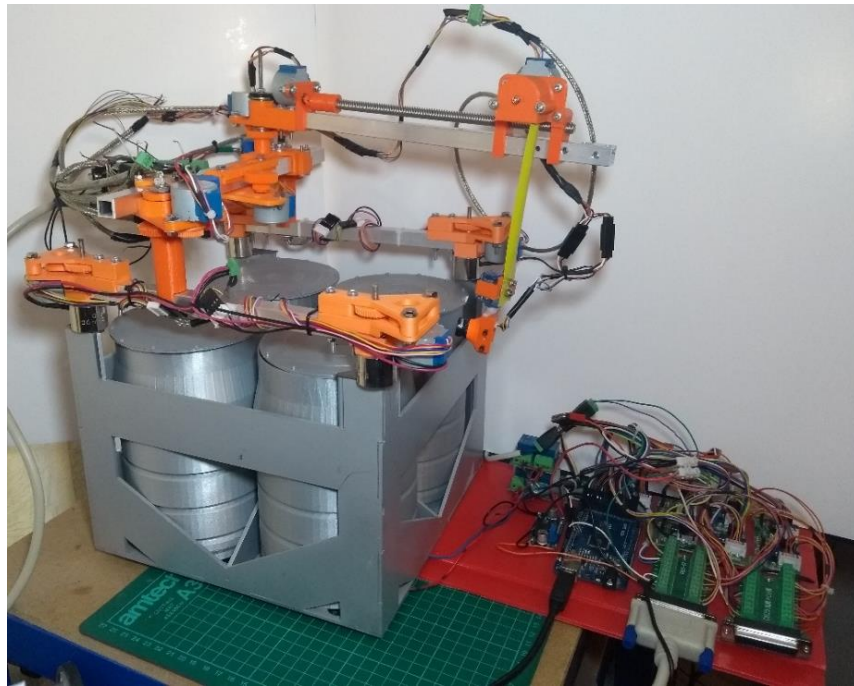


Figure 99: 15 % scale model of the proposed robot connected to its controller and motor drivers.

The scale model had its own challenges during the design and build process due to the scalability of certain components. Creating a functioning twist lock mechanism out of 3D printed parts was too weak to use and therefore it was replaced with an electromagnet to anchor the robot into the mock stillage. This is not representative of the anchoring mechanism but represent the result of the anchoring process. Despite the anchoring mechanism being fundamentally different, the scale electromagnetic anchor highlighted the need for a clearance space for the twist lock to move up above the stillage during the alignment process before it drops and anchors to the stillage. This was performed using geared threaded shafts to move the robot up and down to create the clearance for the swinging arms and anchoring modules.

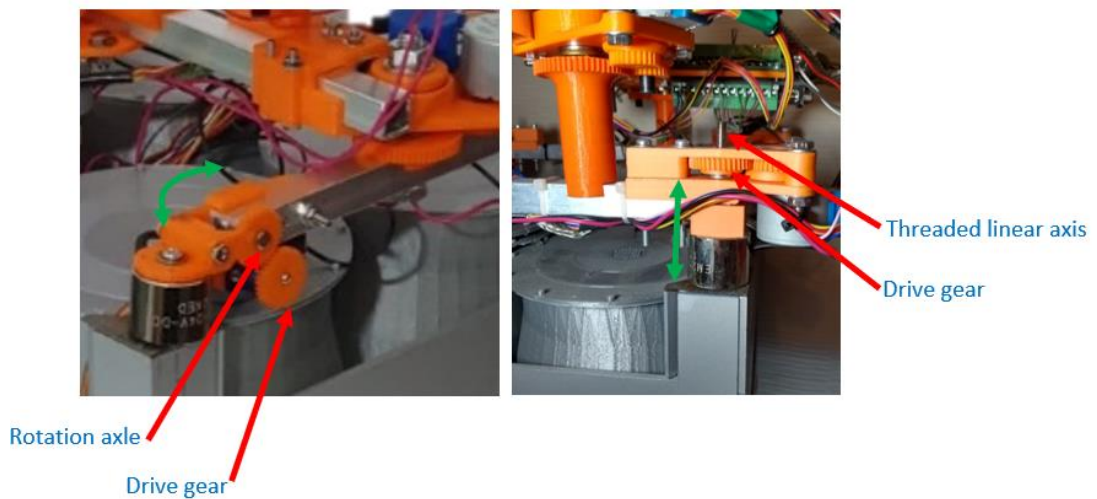


Figure 100: (Left) First iteration of clearance mechanism used to create a gap between the mock stillage and the scale robot. (Right) final linear mechanism used to create a gap between the mock stillage and the scale robot.

A similar mechanism will be required in the final robot to provide the clearance needed for the twistlock mechanism to access the containers lifting apertures as per Figure 82.

Other mechanisms such as cable management and connection links between the robot and the control modules were completely different in the scale model to what would be required in the final operational robot. The shielded tether described in Section 4.6.5 was replaced with a standard multicore D-sub cable and connectors to power the motors and receive position feedback. The D-sub connectors were relatively large compared to the scale robots' body and required large mountings compared to the robot's frame. Moreover, standard off the shelf slip rings were too large to fit through the legs' shafts, which caused constant cable twisting, entanglement, and damage during testing. This will not be the case in the full-scale robot, but it provides a reminder to how important the cable management in the final robot will be to avoid entanglement or catastrophic failure.

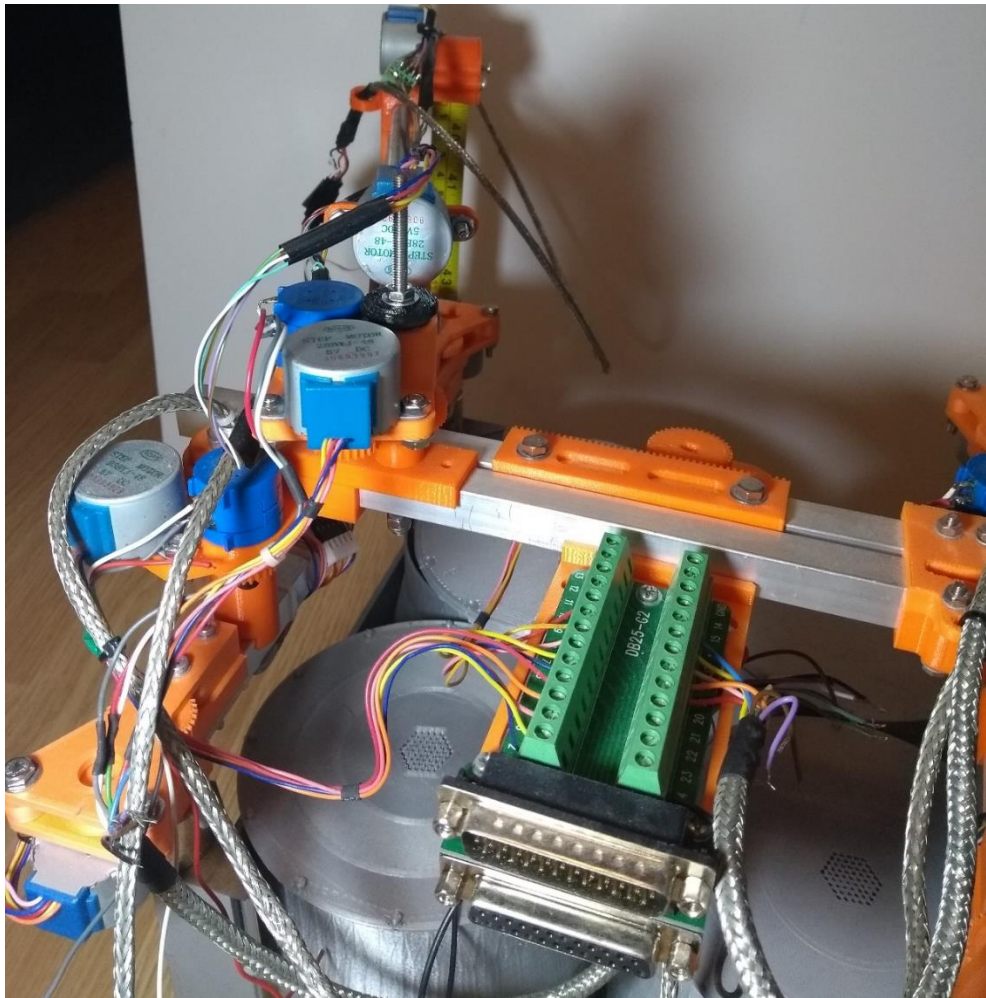


Figure 101: Cable management and D-Sub connectors used to power and interact with the scale robot.

The scale robot was equipped with a video camera with 120° view angle to validate the simulated views described in Section 4.6.9. The camera view from the scale model were challenged by the lighting and the image focus was challenged by the camera's close proximity to the mock. This was not a problem in the virtual simulation because the simulations models did not have a reflective surface, and the views were created digitally independent of the physical properties of camera lenses and optical sensor.

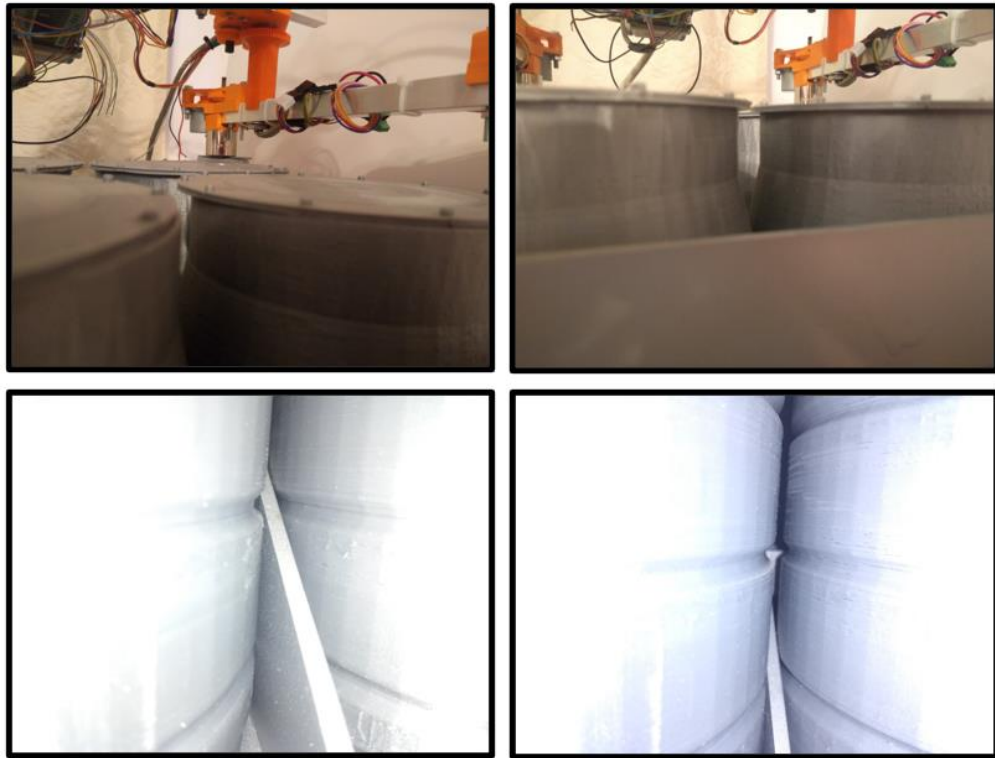


Figure 102: Views of the 3D printed 15 % ILW drum models from a video camera deployed by the 15 % scale robot.

#### 4.6.11 Compromises and future work

In summary this proposed passive robot provides a stable platform to deploy inspection sensors into the constrained inspection volume between ILW containers, to access the maximum surface area of the containers in direct line of sight while in-situ.

The robot is designed to maximise the inspection probes stability using existing ILW containers features and rigid structures (both robotic and environmental) to minimise coordinate measurements hardware errors. Its sensor module will carry the 3 sensors proposed in Section 3.3.5 to provide the ideal sampling strategy for sensor fusion and fitting algorithms required to minimise the coordinate measurements errors in the specific task of inspecting ILW 500 L drums in-situ.

The use of tether (umbilical) to power and control will provide the endurance and reliability required to operate and scan for prolonged time at the cost of increasing the design and deployment process complexity. The use of tether will improve the robot's reliability and



reduce its weight by moving some of the electronics and heavy components out of the robot away from the radiation zones inside the vaults.

The prototype of the robot proved the feasibility of the idea in small scale and highlighted some of the challenges that were not present in virtual simulations.

As swarm of robots is recommended to perform an adequate number of scans due to the large quantity of containers that require scanning relative to the expected scanning processes speeds. The final robot detailed designs will differ between users depending on their operation budgets and the national and international regulations required for it to operate in a specific vault.

#### 4.7 Summary

Existing research and literature proved the feasibility and reliability of different types of sensor delivery and automation mechanisms in the nuclear asset industries, this included manipulators, rovers and aerial deployment methods [122]. This was used as a platform in this Chapter to optimise the proofed techniques, to create hybrid CMS robotic platforms for the task of CM&I ILW 500 L drums in-situ.

Two robotic systems were proposed to provide the required access for the inspection tasks. A UAV is proposed to deploy cameras/optical scanners for quick inspection of points of interest, and a passive crane like robot to deploy different types of inspection tools for detailed inspection of ILW 500 L drums in-situ.

The passive crane like robotic system will be more suited to long term inspection process due to its endurance, and its passive stability will give it an advantage in the deployment of sensors that require high alignment accuracy such as the air couple ultrasonic transducers.

The UAV system proposed will provide the advantage of quick inspections, by flying direct to points of interest for quick inspections at the cost of precision and endurance.

## Chapter 5: Ultrasonic inspection of ILW 500 L drums

### 5.1 Introduction

Ultrasonic transducers could offer a tool for non-destructive non-contact inspection of the ILW 500 L drums. This Chapter will explore the literature review of the ultrasonic inspection methods described in Section 3.3.4 further and evaluate the theory behind the ultrasonic inspection proposed in Section 3.3.4. It will include a brief overview of the non-contact ultrasonic tools, concepts investigated, and fundamentals, and focus on the physical and practical limitations of non-contact ultrasonic transducers in the circumferential measurement of ILW 500 L drums in-situ.

### 5.2 Transducer selection

Ultrasonic waves of a known velocity ( $V_{wave}$ ) can be generated on the surface of an object, and the time it takes the wave to travel from the transmission/generation point to the receiving/detection point commonly known as **Time Of Flight (T.O.F)**, can be used to calculate the distance the wave travelled, on that object's surface.

$$\text{distance traveled by wave} = V_{wave} \times T.O.F \quad \text{Equation 13}$$

Therefore, if an ultrasonic wave of a known  $V_{wave}$  is generated and directed to travel along the ILW 500 L drum's periphery (circumference), the T.O.F of that wave can be used to measure the drum's circumference.

Non-contact air(gas)-coupled piezoelectric Transducers and **Electro-Magnetic Acoustic Transducers (EMATs)** were nominated in Section 3.4.3 based on the restrictions described 3.3.4.1, as the ideal methods of transduction to generate and detect ultrasonic waves onto and off ILW 500 L drums. This section will evaluate and test these nominated transducers to validate their use in the inspection tasks required.

#### 5.2.1 EMATs

Commercially available non-contact EMATs were available to test the technology suitability in the NDT of the ILW 500 L drums. An experiment was performed to test if a sample drum is ferro-magnetic or electrically

conductive enough for an EMATs to be able to generate an acoustic wave onto its shell [Section 3.3.4.2.2], using a commercially available EMAT.

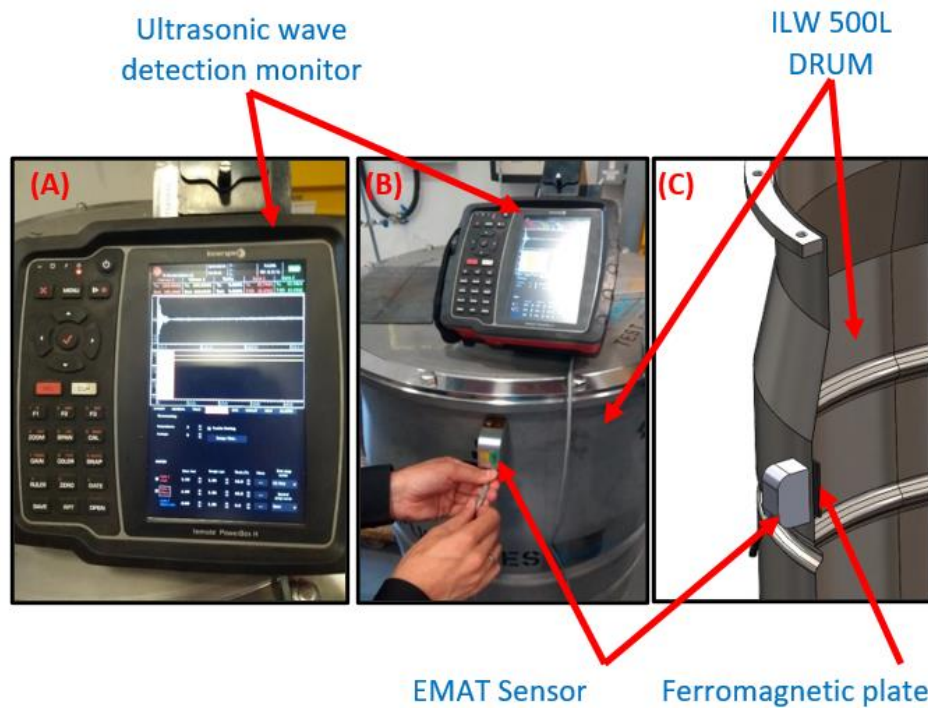


Figure 103: (A) EMAT transducer monitor showing no readings of waves or reflections detected from the setup in picture (B). (B) INNERSPEC Technologies testing a commercially available EMAT transducer to generate acoustic waves across the ILW drum circumference. (C) setup of an EMAT transducer with a ferromagnetic plate on the inner side of the drum.

The EMAT transducer used in the experiment on its own was not capable of generating/detecting any signals from the drum directly as seen in Figure 103 (A) and Figure 103 (B). However, when the test was repeated with a ferromagnetic steel plate placed on the inner side of the drum as per Figure 103 (C), an ultrasonic signal was detected by the equipment. This indicated that the drum's material was not electrically conductive or magnetic enough to generate a wave directly into the drum's shell, but an acoustic wave can be conducted from a ferromagnetic material subjected to the EMAT electromagnetic field, on to the drum's shell. Although this technique will not be suitable for the inspection of the ILW 500 L in the field because the drums will be packed with encapsulating cement matrix (waste-form) [17] (See Figure 5), it validates the possibility

using a layer of ferromagnetic tape on the drum's external surface, to create the same effects as that of the steel plate. Unfortunately, this idea was dismissed too as it requires moving the drums out of their resting place to apply/stick the ferromagnetic material on to them. This defies the in-situ and retro non-modifiable environment inspection methods targeted by this project, eliminating the use of EMATs in the ILW containers inspection. However if the EMAT used had high enough energy EMATs to predominantly rely on the Lorenz forces to generate an acoustic wave into the paramagnetic stainless-steel using alternating high voltage coils as explained in Section 3.3.4.2.2, it will be able to generate the required ultrasonic waves [76].

Robotic deployment of high electromagnetic forces reliant EMATs is challenged by the electromagnetic interference of robotic servos and motor which masks their Pulse echo signals (needed for distance measurement) with electromagnetic noise [123]. This can be reduced using ferrite shielding or eliminated by switching off all the deployment electromagnetic devices during the EMAT scans [123], however it highlights the importance of understanding the electromagnetic compatibility (EMC) of the EMATs in the ILW vault environment. If the EMAT's electromagnetic pulses are strong enough to generate an electromagnetic field in the paramagnetic ILW container's shell using the Lorenz effect, it will likely have a similar effect on the ferromagnetic and paramagnetic contents inside the ILW containers in its range. Therefore, more research is required to understand the effects of the strong pulsing electro-magnetic fields on the ILW waste stability, before exposing it to strong EMAT electromagnetic fields.

### 5.2.2 Air(gas)-coupled piezoelectric ultrasonic transducers

Section 3.3.4.1 explained the importance of coupling mediums in the transfer of acoustic energy from a piezoelectric transducer element onto a workpiece, and Section 3.3.4.2.3 described the energy losses that the air(gas) coupled piezoelectric transducers has to overcome for their acoustic wave output to reach the workpiece.

After the acoustic waves from the air(gas) coupled piezoelectric ultrasonic transducers lose most of its energy due to the acoustic

impedance mismatch caused by the gas coupling [71], the remaining longitudinal acoustic wave energy that reach the solid workpiece will be refracted due to the change in medium which the wave is travelling in (change from gas(air) to solid(workpiece)) [82] [81]. The refraction of the waves will follow Snell's law as described in Figure 104. [82] [81].

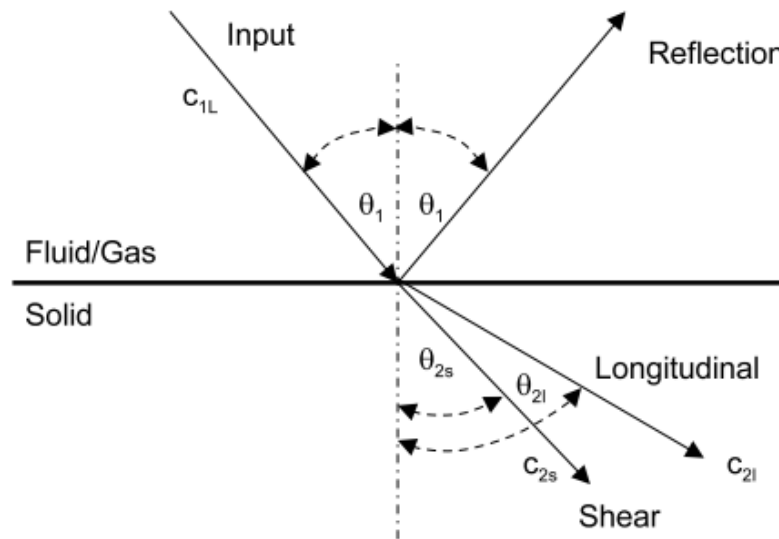


Figure 104: Mode conversion at fluid/solid boundary [81].

$$\frac{c_{1L}}{\sin(\theta_{1L})} = \frac{c_{2L}}{\sin(\theta_{2L})} = \frac{c_{2S}}{\sin(\theta_{2S})} \quad \text{Equation 14}$$

This wave refraction can then travel into or along the workpiece surface depending on the type and/or mode of the wave generated into the material [81][124]. If the refraction angle is high enough to reach the workpiece surface ( $\theta_2 = 90^\circ$ ), the wave will travel along the boundary of the solid workpiece creating a Rayleigh waves [81], where the particles on the surface of the workpiece exhibits localised elliptical motion [82]. This elliptical motion of the material particles decays exponentially as depth increases, causing the wave's vibration amplitude to be over 90 % lower at a depth of one wavelength [82].

## Rayleigh Wave

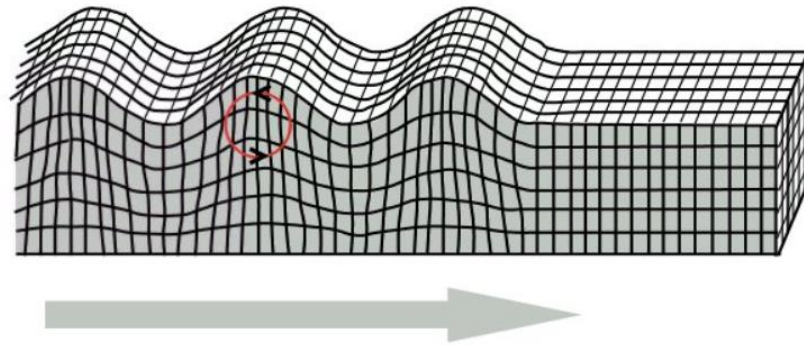


Figure 105: Rayleigh wave propagation along matter surface.

If the workpiece is thin enough for the Rayleigh waves troughs to reach the opposite surface of the material, the wave will components propagate through both surfaces forming Lamb waves [82]. Lamb waves are a combination of shear and longitudinal components that phase match at the material boundaries [81]. This combination can be realised in an infinite number of symmetrical and anti-symmetrical modes, generally referred to as  $A_0$ ,  $A_1$ ,  $A_2$  ... and  $S_0$ ,  $S_1$ ,  $S_2$  ... respectively, where the fundamental modes,  $A_0$  and  $S_0$ , are the only modes to exist at all frequencies-thickness products [81].

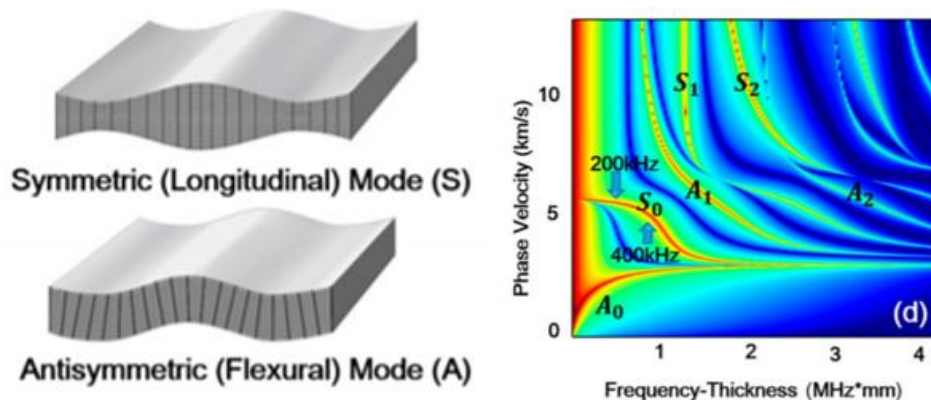


Figure 106: (Left) Compressional waves in a plate symmetric Longitudinal mode “S” and antisymmetric Flexural mode “A”. (Right) Dispersion curves of Lamb waves in an aluminium plate: phase velocity Vs frequency [124].

Figure 106 show the Lamb wave propagation velocity dependency on the wave’s frequency and sample thickness, this is referred to as the

frequency-thickness product [81]. This relationship between the excitation frequency of a Lamb wave travelling in a plate with constant thickness and the velocity of the different wave modes is referred to as dispersion curve[81].

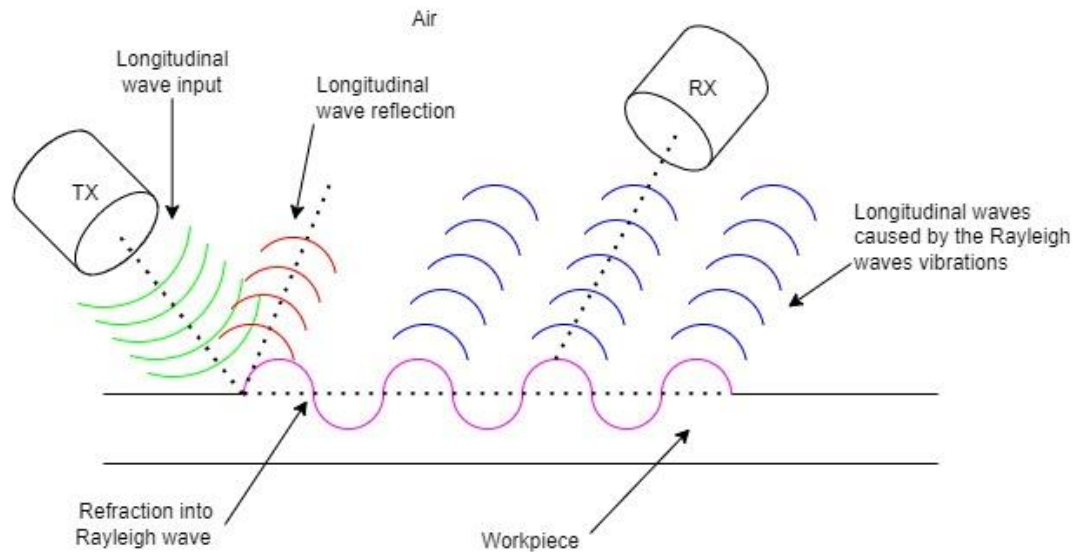


Figure 107: Illustration of how Rayleigh waves caused by induced waves refraction create multiple longitudinal waves sources along its route along a workpiece surface.

As the Rayleigh or Lamb waves travel along the workpiece, they vibrate the layer of air in contact with the workpiece surface, that in return generate another longitudinal acoustic wave in the air at the points where the wave is propagating. This longitudinal wave is generated in the exact opposite way in which the longitudinal wave was refracted into the Lamb or Rayleigh waves. From there the longitudinal waves traveling in the air can then be detected using high sensitivity piezoelectric ultrasonic receivers, that convert these longitudinal wave vibrations in the air into voltage oscillations [81]. These voltage oscillations are then traced using an oscilloscope to identify the longitudinal waves peaks and troughs.

An initial test was performed to identify if the air coupled piezoelectric ultrasonic transducers can indeed generate an acoustic wave on the surface or through the body of an ILW 500 L drum sample, and to confirm that the wave can be detected at any point along the surface on which the wave is travelling as per Figure 107.

To identify the expected angles to refract a Rayleigh or Lamb wave along a 500 L ILW drum surface, “Disperse” software was used to generate the dispersion curves that represent the wave velocities and critical angles required to create a surface refraction of the wave, in relation to the waves’ frequency and medium properties (material in which the waves travel).

“Disperse” parameters were set to calculate the wave velocities in a flat stainless-steel surface 2.33 mm thick to match the wall thickness of an ILW 500 L drum [15], with 20 ° Celsius air medium above and below the stainless-steel surfaces, to simulate the air temperature in the lab where the physical validation of this simulation will be conducted. The cylindrical body of the drum is approximated as a flat surface, because the ratio of drum’s wall thickness to the drum’s external wall radius is 0.0058 % only, and material thickness to radius ratios below 10 % can be safely treated as flat plates in Lamb wave dispersion curve simulations [125].

No damping effects is assumed in the software calculation/simulation at this stage.



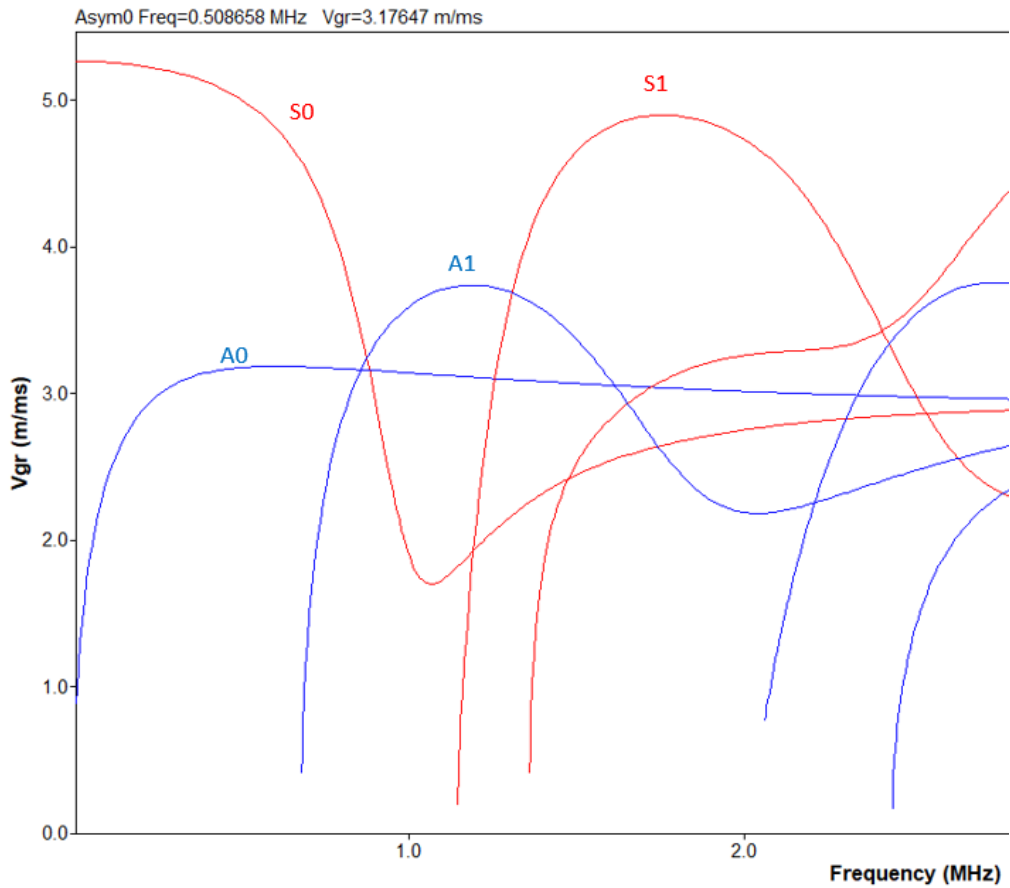


Figure 108: Dispersion curve created using 'Disperse' software showing different wave modes and their group velocity ( $V_{gr}$ ) in relation to the wave mode frequencies ( $f$ ) while travelling through a 2.33 mm thick stainless-steel plate.

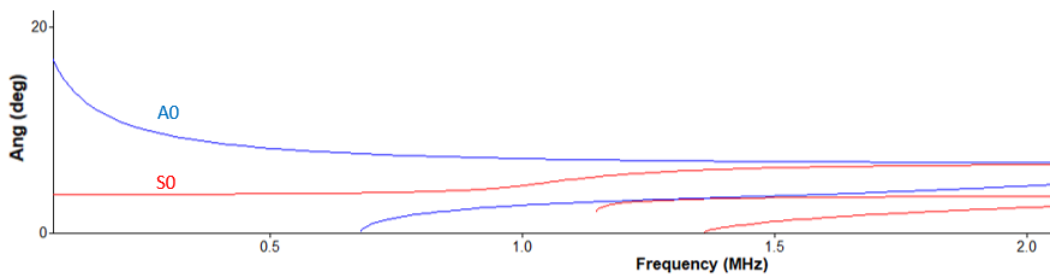


Figure 109: Dispersion curve created using 'Disperse' software showing different wave modes and their angle of incident in relation to the excitation frequencies ( $f$ ) while travelling through a 2.33 mm thick plate.

Figure 108 shows the dispersion curve of the wave's group velocity  $V_{gr}$  in relation to the induced wave frequencies ( $f$ ). While Figure 109 shows the critical angles that will create a wave refraction along the surface of a 2.33 mm thick stainless-steel plate. The group velocity of a wave is the velocity with which the overall envelope shape of a wave's amplitudes propagates through space, therefore  $V_{gr}$  will be the parameter used to describe the wave velocity in the context of this project.

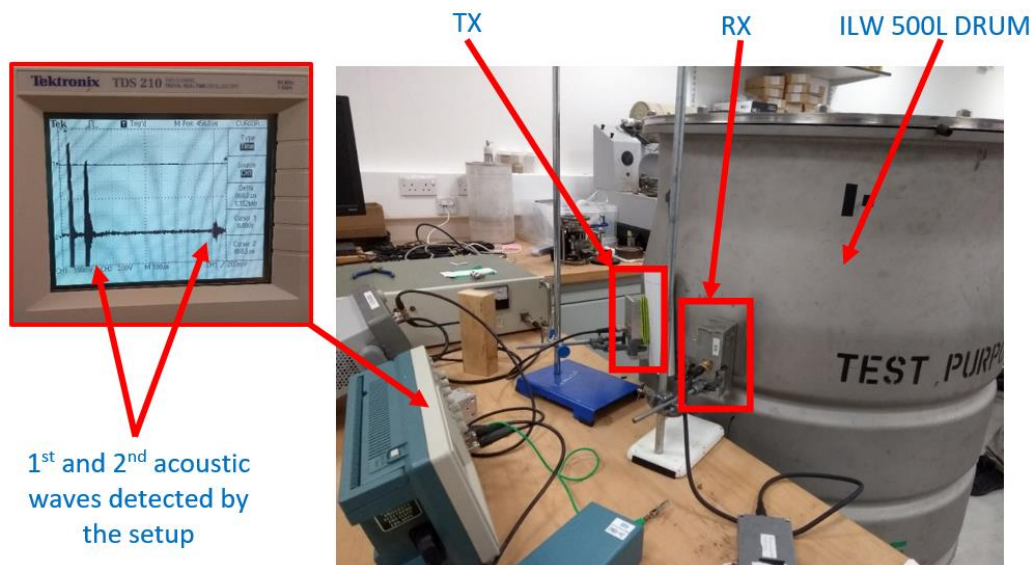


Figure 110: Air couple transmitter (TX) and receiver (RX) setup generating and receiving a wave on/through the surface of an empty ILW 500 L drum sample and an oscilloscope view of the acoustic waves detected by the receiver during the successful wave generation/detection.

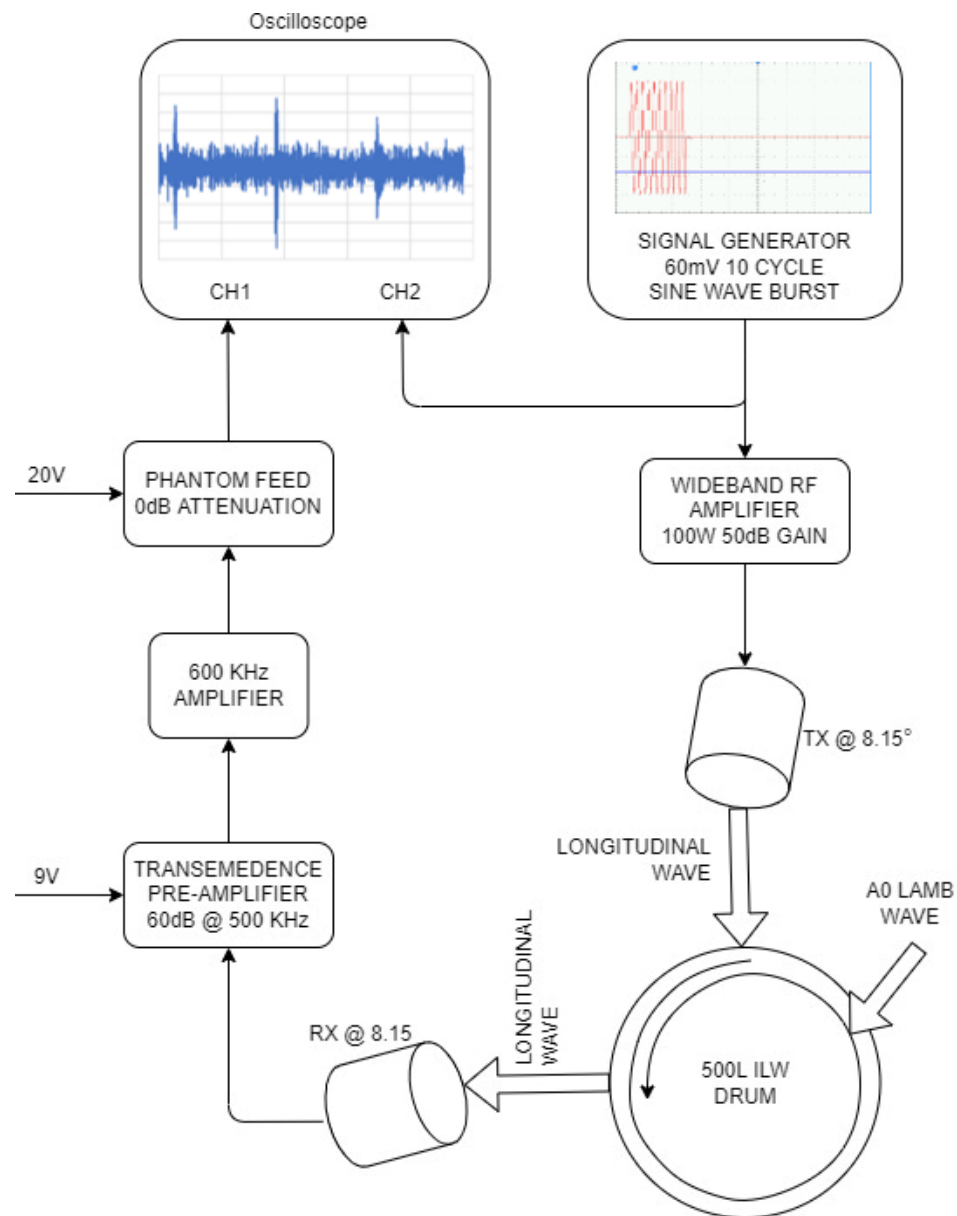


Figure 111: Schematic of the equipment used to generate and detect an A0 wave along the circumference of an ILW 500 L drum.

A set of air-coupled transducers were available to test if it was practically possible to generate the acoustic waves along the circumference of a 500 L ILW drum to measure its circumference and validate the ‘Disperse’ software dispersion curve results. The transducers were used to generate a 0.5 MHz burst of 10 waves onto a sample drum surface from a transmitter (TX) set at an 8.15 ° angle tangential to the drum surface, and an amplified receiver (RX) set at the same angle to detect any incoming longitudinal waves off the drum surface as per Figure 107.

The 0.5 MHz wave burst frequency was chosen to be as close as possible to the TX electrical resonance to output the most energy from the TX, while being close to the RX mechanical resonance to optimise the signal generated by the RX element vibrations. The  $8.15^\circ$  is the matching angle of incidence at 0.5 MHz as per Figure 109 required to refract an antisymmetric A0 Lamb wave into the drum's surface. The A0 was chosen because the rate of change in its group velocity  $V_{gr}$  is shallower than that of the S0 wave mode at the frequencies in which the transducers operate. This should theoretically reduce the  $V_{gr}$  uncertainty caused by any uncertainties in the generated frequencies or the drum's material properties. An A0 wave generated at an angle of  $8.15^\circ$  at 0.5 MHz should have an expected  $V_{gr}$  of 3.17647 m/ms as per Figure 108.

The 0.5 MHz burst excitations of the transducer were powered using a 60mV 0.5MHz sinusoidal signal from a signal generator that was amplified using a 1000W 50dB wideband amplifier. The signal generator's signal amplitude and burst length of 10 sinusoidal cycles were chosen to maximise the transducer's energy output without overheating and burning the TX piezoelectric element. The signal from the RX was amplified using a transimpedance amplifier first to change it from a current signal to a usable voltage signal, which was then amplified using a signal amplifier as per Figure 111. The transimpedance amplifier was powered using a 9V battery while the phantom feed powered the inline 600KHz amplifier as per Figure 111. Ideally a 500KHz amplifier should have been used in the experiment to match the operational frequency of the system (0.5MHz) to maximise the amplification efficiency, but this was not available at the time of the experiment.

The TX and RX angles were set to  $8.15^\circ$  and slowly moved in both directions until Lamb waves were detected in the form of peaks appearing on the oscilloscope display as seen on Figure 110.

To validate the type of wave detected by the oscilloscope (Rayleigh or Lamb), a soft acoustic dampening material was pushed against the internal and external surfaces of the sample drum alternately, while an acoustic wave was travelling along its external circumference and being detected using the setup described. The test showed that when an acoustic dampener is applied on either the internal or external surface of

the drum, it dampened the waves' amplitude until it was no longer detected by the receiver. This meant that the wave was travelling at both the internal and external surfaces of the drum simultaneously and so they are Lamb waves that travel throughout the drum's shell. Otherwise, If the waves were travelling along the external surface only as Rayleigh waves, the waves amplitude/characteristics would have not been affected by the dampener on the internal surface of the drum.

The oscilloscope in Figure 110 was set to a digital averaging of 64 and the readings were saved and processed using MATLAB software.

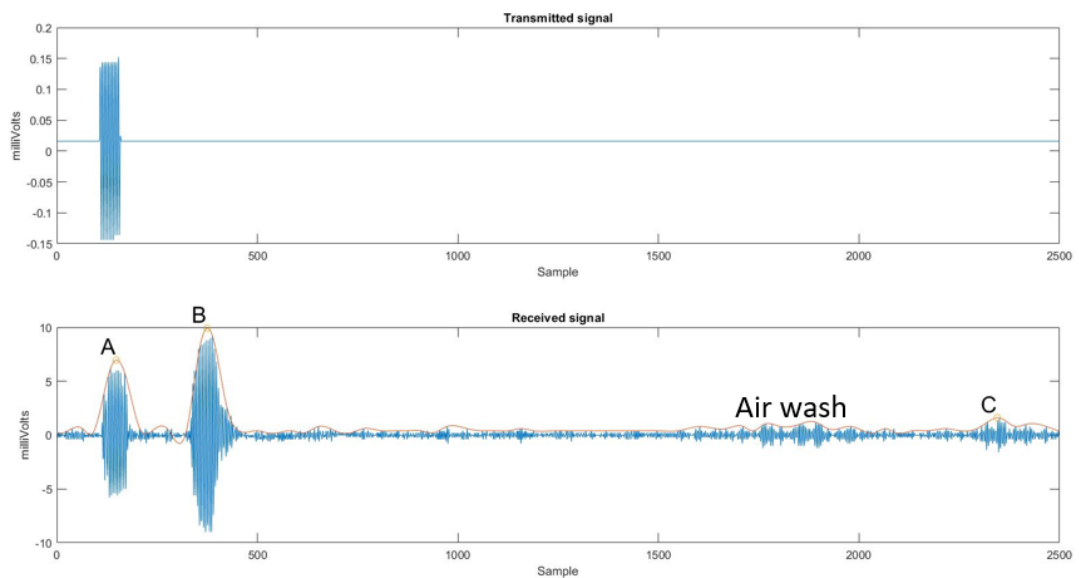


Figure 112: (Top) Oscilloscope readings from the signal generator before amplification. (Bottom) Oscilloscope readings of signal detected by the receiver (Blue), and wave envelope (red)

Peak 'A' in Figure 112 is the electromagnetic interference (EMI) noise induced in the received signal, from the high energy signal transmitter amplifier pulse. This peak appears when the high energy output signal amplifier is turned on and remains present in the oscilloscope readings, even if the transmitter and receiver are pointing into the air away from the sample and not detecting or generating any useful information. This is further confirmed by its synchronicity with the sine waves from the signal generator pulses. A full investigation on the source of the EMI and system susceptibility to it will be investigated in Section 6.3.3.

The spacing between peak 'A' and peak 'B' in Figure 112 changes with the movement of the receiver along the circumference of the drum. This means that peak 'B' is the 1st peak indicating a Lamb wave detection off the surface of the ILW 500 L drum, because it shifts to the right as the receiver location is moved further away from the transmitter wave induction location.

Once the Lamb wave is detected off the surface of the drum at peak 'B', the wave continues to travel along the drum circumference and gets detected again by the receiver at the same point location of detection at peak 'C'. This is confirmed when moving the receiver to change the location of peak 'B', and the time between peak 'B' and 'C' remains constant, indicating that the time between peak 'B' and 'C', is the time ( $T.O.F_{Circumference}$ ) for a Lamb wave to travel along the full circumference of a drum, and peak 'C' is the 2nd Lamb wave detected by the receiver.

The small peaks (**air wash**) appearing on Figure 112 prior to peak 'C', are not Lamb or Rayleigh waves. These peaks disappear when an obstacle is placed between the transmitter and receiver to stop the direct air motion from the transmitter to the receiver. This proves that these peaks are a result of the burst of air caused by the initial longitudinal wave transmission from the TX, leaking out into its surroundings forming air currents that travel to the RX and get detected as noise. The TX and RX do not need to be in direct line of sight for these air currents to be detected because they can follow the drum's surface contours/bends using the Coanda effect to reach the RX [126]. Permanently placing a solid obstacle between the transmitter and receiver may completely stop this air wash from reaching the RX, to eliminate some false readings and improve the SNR.

In summary the acoustic wave travels from the TX to the RX via the drum surface as following,

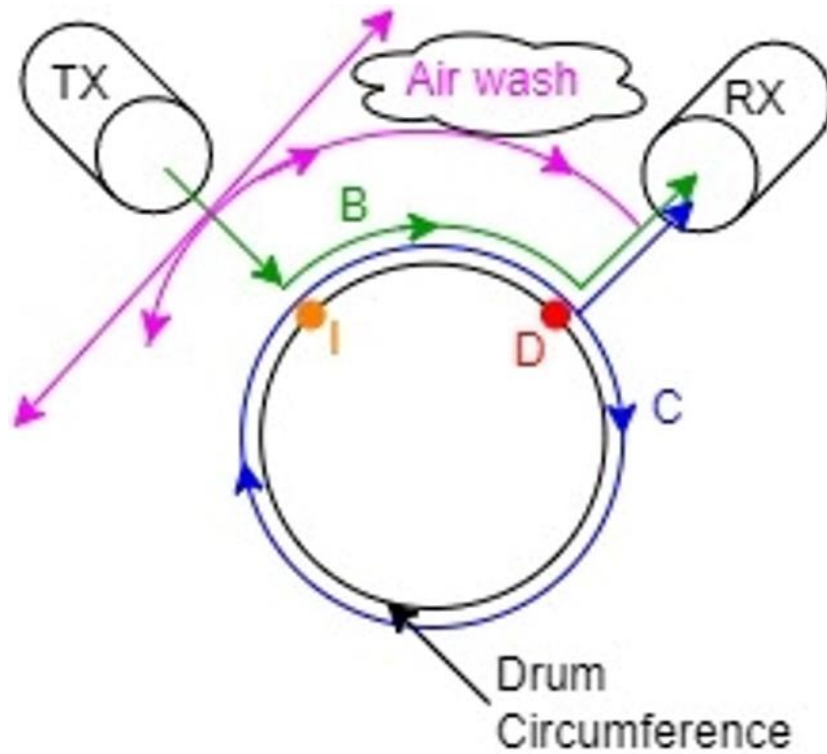


Figure 113: Predicted ultrasonic wave path to, along and from drum surface.

TX	Ultrasonic transmitter.
RX	Ultrasonic receiver.
I	Incident point where longitudinal waves induce a Lamb wave into the drum's shell.
D	Point where the longitudinal wave detected by the RX were generated from the travelling Lamb wave as per Figure 107.
$B_{path}$	Path of the acoustic waves that caused the signal detection at peak 'B' in Figure 112.
$C_{path}$	Path of the ultrasonic wave that caused the acoustic wave detection at peak 'C' in Figure 112.
Air wash	Air wash travelling from TX to RX close to drum circumference.

### Important notes:

1. Path **B** and **C** overlap in real life with drum circumference but kept separate in Figure 113 for visual clarity.
2. The mechanism in which the incident point '**I**' and detection point '**D**' are created was explained earlier in Figure 104 and Figure 107.

The acoustic wave traveling along path  $B_{path}$ , travels as:

- $B_1$ : Longitudinal wave from travelling from TX to the drum's point of **incidence 'I'** where it induces a Lamb wave.
- $B_2$ : Lamb wave from point '**I**', along the drum circumference to the point of **detection 'D'** which the RX is aimed at.
- $B_3$ : Longitudinal wave from point '**D**' to RX causing the detection of peak '**B**' on Figure 112.

While the longitudinal wave in  $B_3$  travels to RX, the Lamb wave created in  $B_2$  continues to travel along the drum circumference through path  $C_{path}$  as:

- $C_1$ : A Lamb wave along the entire drum circumference, from point '**D**' all around the drums' circumference until it reaches the point '**D**' again which the RX is aimed at.
- $C_2$ : It then repeats what happened at  $B_2$  and travel as longitudinal wave from point '**D**' to RX causing the detection of peak '**C**' on Figure 112

Given that the time for the longitudinal wave to travel from point '**D**' to the **RX** is the same in both path  $B_{path}$  and  $C_{path}$ , the difference between the detection times of peaks '**B**' and '**C**' ( $t_{B \rightarrow C}$ ) will be the time of flight for a Lamb wave to travel along the circumference of the drum once " $T.O.F_{Circumference}$ ". (This will be visually explained further in Section 5.3). This means that the drum's circumference ( $Circumference_{ultrasonic}$ ) can be calculated by multiplying the Lamb wave's group velocity  $V_{gr}$  identified from the "Disperse" dispersion curve in Figure 108 ( $V_{gr} = 3.17647 \text{ m/ms} @ 0.5\text{MHz}$ ) by the  $T.O.F_{Circumference}$ , which is the time between the peaks '**B**' and '**C**' in



Figure 112. To locate the peak times of the signal demonstrated in Figure 112, the signal was enveloped using the MATLAB built in envelope detector,

```
envelope_line = envelope(Signal,25,'peak');
```

Ideally the front edge of the peak should be used as the identifier of the lamb wave presence because it is the leading edge of the lamb wave however this is challenged by the presence of noise in the signals and inconsistency in the peak shapes. Consequently, the highest point in the peak provides a more robust point of measurement between two signals assuming that the true (unmeasured) width of the signal remains constant.

The envelope detector, envelopes the input signal using a spline interpolation over local maxima separated by at least 25 samples (half the transmitted signal sample width to satisfy Nyquist's theorem). The peak of these splines is then considered as the wave location on the X axis (time) of the readings. Larger envelop sample numbers enveloped more of the noise alongside the visually identified wave and skewed the envelope peak location away from the peaks. Smaller envelop sample numbers created multiple peaks within the identified peak 'B' band and enveloped more of the noise surrounding the visually detected waves which reduced the Signal to Noise Ratio (SNR).

A peak location detector was then used to locate the enveloped signal peaks on the X-axis (time axis) that exceed the threshold of 1.5 on the Y-axis, which is just under the visually detected Y-axis value of 1.61 at peak C.

```
[peaks_y,peaks_x] = findpeaks(envelope_line,1,'MinPeakHeight',1.5);
```

This method can accidentally identify air wash or background noise peaks as Lamb wave peaks and skew the measurement results if not tuned properly. Therefore, a more advanced signal time detection and identification algorithms capable of filtering out anomalies may be needed for the readings postprocessing to be fully automated.

The oscilloscope operated at a horizontal scale of  $1 \times 10^{-4}$ s per division and the scale horizontal scale has 10 divisions and generated a reading of 2500 samples.

$$\begin{aligned}
 \therefore T.O.F_{Circumference} &= t_{B \rightarrow C} \\
 &= \frac{(C_X \text{ coordinate} - B_X \text{ coordinate})}{\text{sampling frequency}} \\
 &= (C_X \text{ coordinate} - B_X \text{ coordinate}) \\
 &\quad \times \left( \frac{\text{oscilloscope horizontal scale} \times 10}{\text{samples}} \right)
 \end{aligned} \tag{Equation 15}$$

X coordinate value of peak 'C' ( $C_X \text{ coordinate}$ ) from Figure 112 is **2345**, and X coordinate value of peak 'B' ( $B_X \text{ coordinate}$ ) from Figure 112 is **375**. Substituting these values into Equation 15,

$$\begin{aligned}
 T.O.F_{Circumference} &= (2345 - 375) \\
 &\quad \times \left( \frac{(1 \times 10^{-4} \text{s}) \times 10}{2500} \right) = 788 \times 10^{-6} \text{s} \\
 &= 0.788 \text{ ms}
 \end{aligned} \tag{Equation 16}$$

$$\begin{aligned}
 \therefore Cicumference_{ultrasonic} &= V_{gr} \times T.O.F_{Circumference} \\
 &= 3.17647 \text{ m/ms} \times 0.788 \text{ ms} \\
 &= 2.503 \text{m} = 2503 \text{mm}
 \end{aligned} \tag{Equation 17}$$

The circumference ( $Cicumference_{tape}$ ) of the drum was measured using a soft measuring tape (tailor tape measure) to validate the ultrasonic readings and quantify the drum's diameter measurement ( $D$ ) error. The measuring tape measurements had a repeatability of 1 mm.

$$\begin{aligned}
 D_{ultrasonic} &= \frac{Cicumference_{ultrasonic}}{\pi} = \frac{2503}{\pi} \\
 &= 796.7 \text{ mm}
 \end{aligned} \tag{Equation 18}$$

$$\begin{aligned}
 D_{tape} &= \frac{Cicumference_{tape}}{\pi} = \frac{2501 \pm 1}{\pi} \\
 &= 796.1 \pm \frac{1}{\pi} \text{ mm}
 \end{aligned} \tag{Equation 19}$$

Thus, the overall percentage difference between  $D_{tape}$  and  $D_{ultrasonic}$  can be calculated as

$$100 \times \left[ \frac{(796.7 \pm \frac{1}{\pi}) - 796.1}{796.7 \pm \frac{1}{\pi}} \right]_{max} = 0.12 \% \quad \text{Equation 20}$$

A difference in measurements of 0.12 % can confirm that the wave being generated on and detected off the sample drum surface is definitely the expected A0 Lamb wave, and with an estimated velocity  $V_{gr}$  of 3.17647 m/ms as per the dispersion curve in Figure 108.

This nominates the air coupled piezo electric transducer as the method of choice to measure the circumference of the ILW 500 L drums while in-situ without the need of accessing the entire drum circumference. The remainder of this Chapter will validate the accuracy of the system and improve the measurement techniques to account for introduced real life sample variables such as the drum content and cracks.

### 5.3 Wave detection optimisation

After establishing the possibility of using air coupled transducers to generate and detect ultrasonic Lamb waves to measure the sample drum circumference in Section 5.2.2, the test was repeated with increased oscilloscope sensitivity and time range to improve the signal detection observed in Figure 112. Another observation from the test in Section 5.2.2 was the signal amplitude sensitivity to the transmitter and receiver angle of incidence, needed to create the desired wave refraction successfully. To optimise the transmitter and receiver angles and positions, 3D-printed wedges (see Figure 114) were used to set the exact angle between the transmitter and receiver on the round body of the sample. The wedge has a curved side that sits on the sample face and an 8.15° angled side to align the transmitter and receiver angles to the sample's tangential line.

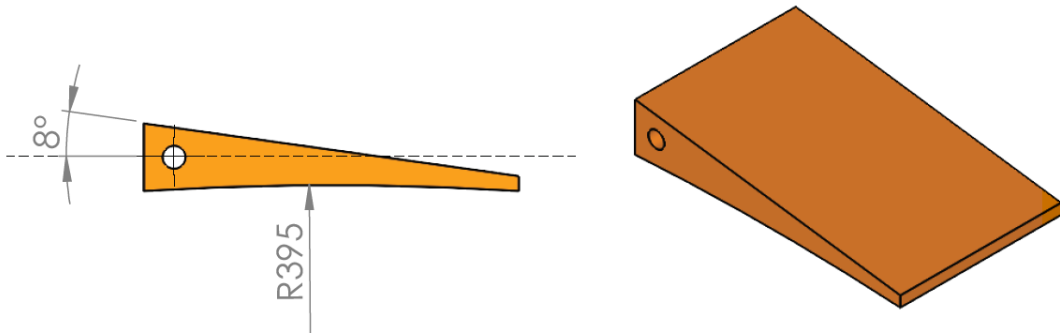


Figure 114: CAD of wedge used to align the transducers 8.15 ° tangent to the drum/sample circumference.

The optimisation of the angle of incident on the transmitter and receiver setup using the new wedge, along with the 128 signal averaging of the readings on the oscilloscope, improved the detection of the 2<sup>nd</sup> peak significantly, but increased the noise in the signal due higher sensitivity setting on the oscilloscope compared to the initial tests.

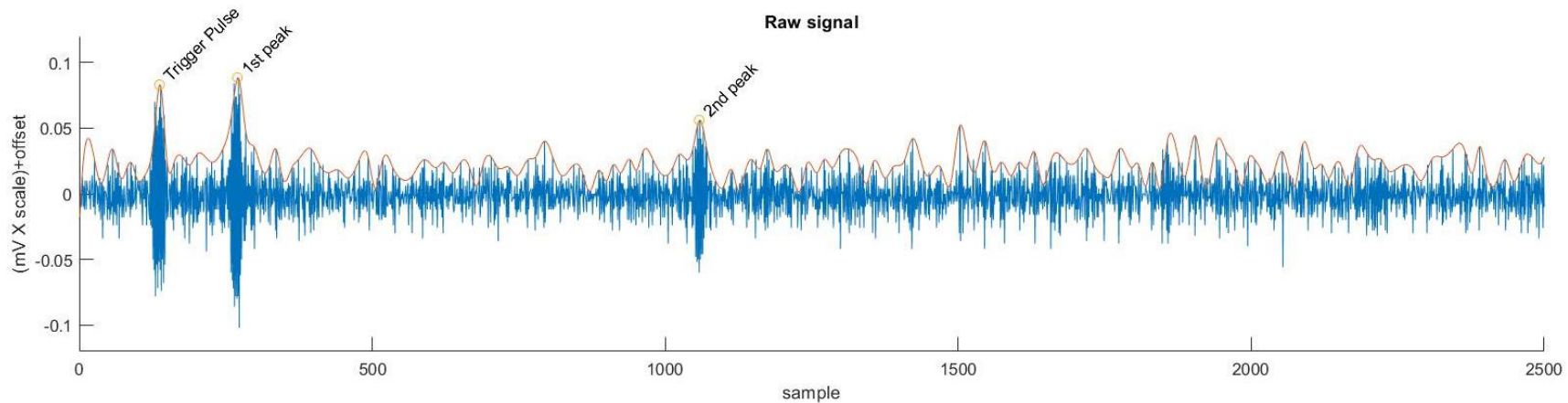


Figure 115: Raw signal in Blue and wave envelope in red, and wave envelope and peak points detected by the MATLAB code in red.

To remove this noise and improve the peaks' location accuracy and SNR, the readings were analysed using MATLAB signal analyser, to identify the properties of the peaks of interest, and filter out the introduced noise.

The signal analyser normalised the signal frequencies components and identified the power factor "dB" of each frequency components at each section of the signal as seen Figure 116. The wave analyser indicated the highest energy levels at the 1<sup>st</sup> and 2<sup>nd</sup> peaks to be around the -36 dB to -45 dB range at the normalised frequency of  $0.95\pi$  rads/sample and above, this can be seen in the normalised frequency spectrum analysis at the bottom of Figure 116. Moreover, the data also showed signs of a possible 3<sup>rd</sup> peak at a time gap after the 2<sup>nd</sup> peak, close to the time gap between the 1<sup>st</sup> and 2<sup>nd</sup> peaks in the form of high dB regions at the bottom window of Figure 116. This indicated that the wave may have enough energy to travel around the drum more than once and create a detectable 3<sup>rd</sup> peak.

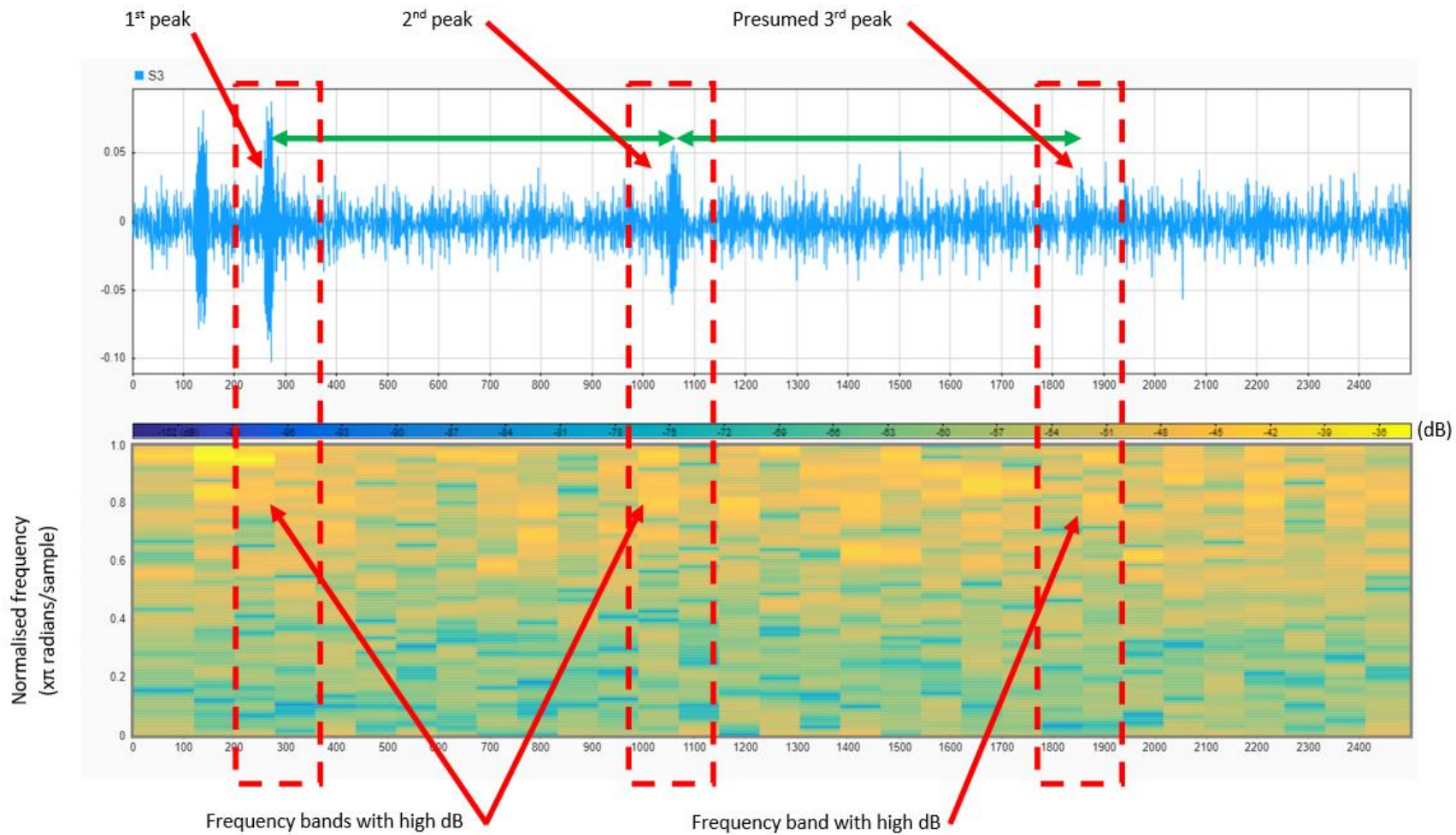


Figure 116: MATLAB signal analyser, showing the amplitudes of the normalised frequencies spectrums along the sample.

To confirm if the signal contained a 3rd peak, the signal was filtered using a highpass signal filter of  $0.95\pi$  rads/sample in MATLAB to only show the signal peaks detected by the frequency analyser and filter out everything else. The filtered signals were then enveloped using the same envelope detector as previously, and envelope of 10 samples, provided the closest envelop to the filtered signal.

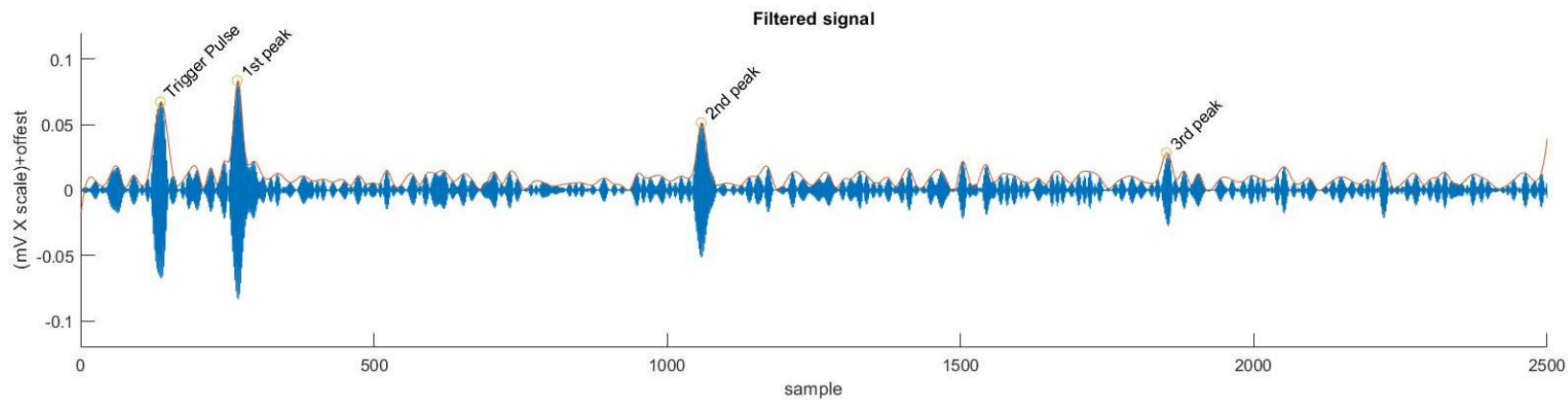


Figure 117: Filtered signal with a  $0.95\pi$  rads/sample highpass signal filter in blue, and wave envelope and peak points detected by the MATLAB code in red.

```
filtered_signal = highpass(raw_signal,0.95);  
peakBand = 10;  
filtered_envelope_line = envelope(filtered_signal,peakBand,'peak');
```

```
[filtered_peaks_y,filtered_peaks_x] =  
findpeaks(filtered_envelope_line,1,'MinPeakHeight',0.025);
```

The highpass filter, improved the SNR enough to show a 3<sup>rd</sup> extra peak with the same time gap between it and the 2<sup>nd</sup> peak, as that between the 1<sup>st</sup> and 2<sup>nd</sup> Lamb wave peaks. Confirming that that the Lamb waves have enough energy to travel along the circumference of the drum more than once, and that the time gap between the Lamb wave peaks ( $T.O.F_{Circumference}$ ) is independent of the transmitter (TX) and receiver (RX) locations around the drum's circumference.

## 5.4 Numerical validation

After establishing and proving the possibility of detecting a 3<sup>rd</sup> signal peak from the Lamb waves travelling along the circumference of an ILW 500 L drum, the following theory can be assumed.



If a Lamb wave is travelling clockwise through a single cross-sectional layer along the drum circumference, and the initial wave transmitted from TX to RX is always in the direction where the distance from TX and RX is expected to be the shortest as per Figure 118, the following should apply,

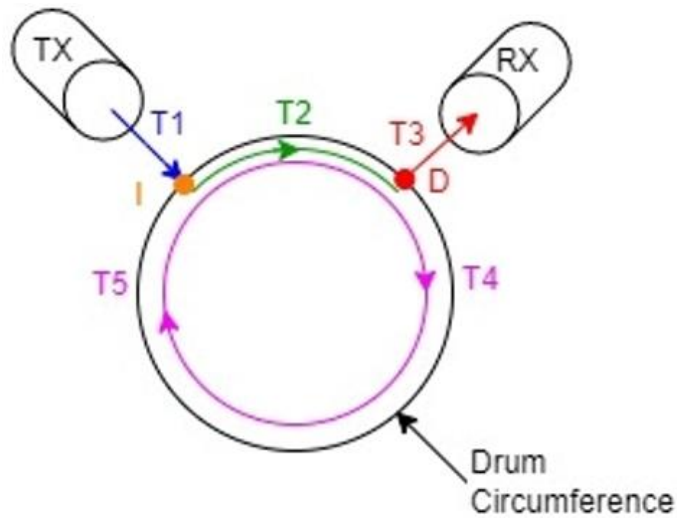


Figure 118: Illustration of waves paths to, from and around the drum circumference.

TX	Ultrasonic transmitter.
RX	Ultrasonic receiver.
I	Incident point where longitudinal waves induce a Lamb wave into the drum's shell.
D	Point where the longitudinal wave detected by the RX is generated from the travelling Lamb wave.
T1	T.O.F of a longitudinal wave from TX to 'I' through air.
$T_{TX \rightarrow I}$	
T2	T.O.F of a Lamb wave from 'I' to 'D' along drum circumference.
$T_{I \rightarrow D}$	
T3	T.O.F of longitudinal wave from 'D' RX through air.
$T_{D \rightarrow RX}$	
T4	T.O.F of the Lamb wave travelling along the entire drum circumference for the 1 <sup>st</sup> time.
$T.O.F_{1st\ Circumference}$	
T5	T.O.F of the Lamb wave travelling along the entire drum circumference for the 2 <sup>nd</sup> time.
$T.O.F_{2nd\ Circumference}$	

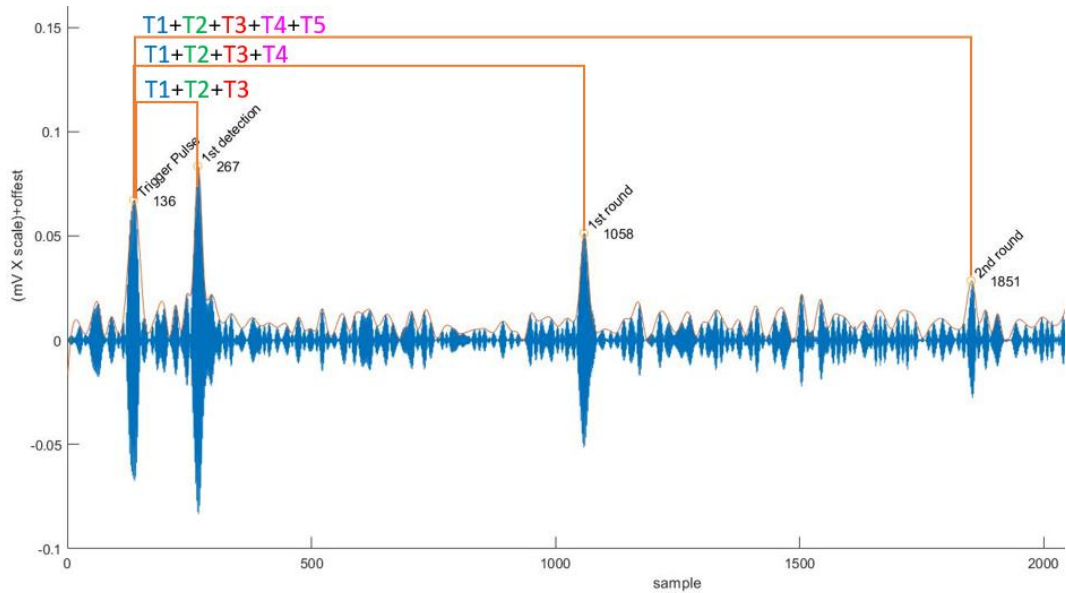


Figure 119: Sample reading from Figure 117 with T.O.F from Figure 118 highlighted.

1st peak detection will occur at

$$time_{1st\ detection} = T1 + T2 + T3$$

or

$$time_{1st\ detection} = T_{TX \rightarrow I} + T_{I \cup D} + T_{D \rightarrow RX}$$

Equation 21

2nd detection will occur at

$$time_{2nd\ detection} = T1 + T2 + T4 + T3$$

or

$$\begin{aligned} time_{2nd\ detection} &= T_{TX \rightarrow I} + T_{I \cup D} + T.O.F_{1st\ Circumference} \\ &+ T_{D \rightarrow RX} \end{aligned}$$

Equation 22

3rd detection will occur at

$$time_{3rd\ detection} = T1 + T2 + T4 + T5 + T3$$

or

$$\begin{aligned} time_{3rd\ detection} &= T_{TX \rightarrow I} + T_{I \cup D} + T.O.F_{1st\ Circumference} \\ &+ T.O.F_{2nd\ Circumference} + T_{D \rightarrow RX} \end{aligned}$$

Equation 23

From this information, we can isolate the  $T.O.F_{1st\ Circumference}$  and  $T.O.F_{2nd\ Circumference}$  to allow us to calculate the drum circumference using the Lamb wave velocity in the sample drum shell ( $V_{gr} = 3.17647\ m/ms @0.5\ Mhz$ ) acquired in Section 5.2.2 using the 'Disperse' software.

$$\begin{aligned} time_{2^{nd}\ detection} - time_{1^{st}\ detection} &= (T1 + T2 + T4 + T3) - (T1 + T2 + T3) = T4 \\ &= T.O.F_{1st\ Circumference} \end{aligned}$$

Equation 24

$$\begin{aligned} time_{2^{nd}\ detection} - time_{1^{st}\ detection} &= (2^{nd}\ peak_X\ coordinate - 1^{st}\ peak_X\ coordinate) \\ &\times \left( \frac{oscilloscope\ horizontal\ scale \times 10}{samples} \right) = (1058 - 267) \times \left( \frac{(2.5 \times 10^{-4} s) \times 10}{2500} \right) \\ &= 791 \times 10^{-6} s = 0.791\ ms \end{aligned}$$

Equation 25

$$\begin{aligned} circumference_{1^{st}\ round} &= V_{gr} \times T.O.F_{1st\ Circumference} \\ &= V_{gr} \times (time_{2^{nd}\ detection} - time_{1^{st}\ detection}) = 3.17647\ m/ms \times 0.791\ ms \\ &= 2.513m = 2513mm \end{aligned}$$

Equation 26

Similarly

$$\begin{aligned} time_{3^{rd}\ detection} - time_{2^{nd}\ detection} &= (T1 + T2 + T4 + T5 + T3) - (T1 + T2 + T4 + T3) = T5 \\ &= T.O.F_{2nd\ Circumference} \end{aligned}$$

Equation 27

$$\begin{aligned}
& time_{3^{rd}detection} - time_{2^{nd}detection} \\
&= (3^{rd} peak_X coordinate - 2^{nd} peak_X coordinate) \\
&\times \left( \frac{oscilloscope horizontal scale \times 10}{samples} \right) = (1851 - 1058) \times \left( \frac{(2.5 \times 10^{-4} s) \times 10}{2500} \right) \\
&= 793 \times 10^{-6} s = 0.793 \text{ ms}
\end{aligned}$$

Equation 28

$$\begin{aligned}
circumference_{2^{nd} round} &= V_{gr} \times T.O.F_{2^{nd} Circumference} \\
&= V_{gr} \times (time_{3^{rd}detection} - time_{2^{nd}detection}) = 3.17647 \text{ m/ms} \times 0.793 \text{ ms} \\
&= 2.519 \text{ m} = 2519 \text{ mm}
\end{aligned}$$

Equation 29

The 0.02 ms difference between  $T.O.F_{1^{st} Circumference}$  and  $T.O.F_{2^{nd} Circumference}$  have resulted in a circumferential difference of 4.0 mm between the two measurements. An overall average  $T.O.F_{avg Circumference}$  of the two circumferences can be calculated using  $time_{3^{rd}peak}$  and  $time_{1^{st}peak}$  readings only.

$$\begin{aligned}
T.O.F_{avg Circumference} &= \frac{T.O.F_{1^{st}Circumference} + T.O.F_{2^{nd}Circumference}}{2} \\
&= \frac{[time_{2^{nd}detection} - time_{1^{st}detection}] + [time_{3^{rd}detection} - time_{2^{nd}detection}]}{2} \\
&= \left( \frac{time_{3^{rd}detection} - time_{1^{st}detection}}{2} \right)
\end{aligned}$$

Equation 30

---


$$\begin{aligned}
& \text{time}_{3^{\text{rd}} \text{ detection}} - \text{time}_{1^{\text{st}} \text{ detection}} = \\
& = (3^{\text{rd}} \text{ peak}_{X\text{-coordinate}} - 1^{\text{st}} \text{ peak}_{X\text{-coordinate}}) \\
& \times \left( \frac{\text{oscilloscope horizontal scale} \times 10}{\text{samples}} \right) = (1851 - 267) \times \left( \frac{(2.5 \times 10^{-4} \text{ s}) \times 10}{2500} \right) \\
& = 1584 \times 10^{-6} \text{ s} = 1.584 \text{ ms}
\end{aligned}$$

Equation 31

---

$$\begin{aligned}
\text{circumference}_{\text{avg}} &= V_{gr} \times \left( \frac{\text{time}_{3^{\text{rd}} \text{ detection}} - \text{time}_{1^{\text{st}} \text{ detection}}}{2} \right) \\
&= 3.17647 \text{ m/ms} \times \left( \frac{1.584}{2} \right) \text{ ms} = 2.516 \text{ m} = 2516 \pm 4.33 \text{ mm}
\end{aligned}$$

Equation 32

The *circumference<sub>avg</sub>* from the Lamb wave measurement is  $2516 \pm 4.33$  mm, compared to the  $2501 \pm 1$  mm from the tape measurement. The  $V_{gr}$  value in the *circumference<sub>avg</sub>* calculation assumes an uncertainty of  $\pm 0.00547$  m/ms, because the drum's nominal thickness of 2.33 mm can fall to 2.00 mm during the manufacturing process [130]. Thus, assuming that the nominal thickness of 2.33 mm is true 95% of the Lamb's wave journey around the drum with a  $V_{gr}$  of 3.17647 m/ms and 2.00 mm with a  $V_{gr}$  of 3.067 m/ms during the remaining 5% as a worst case scenario (see 5.6.2 Figure 129 for  $V_{gr}$  vs thickness dispersion curves), the uncertainty in the  $V_{gr}$  equates to 0.00547 m/ms which yields an uncertainty in the *circumference<sub>avg</sub>* of 4.33 mm.

Although the true thickness of the drum's shell can be considered as the largest source of uncertainty in the  $V_{gr}$  of the measurements, the differences between the tape and ultrasonic measurement could also be caused by differences

between the theoretical and real-life material properties used to estimate the wave velocity as will be detailed in Section 5.6.

From an analytical perspective, the wave exact position identification from the signal readings is main contributor to the  $T.O.F_{Circumference}$  uncertainty. This is further exacerbated by in the presence of noise peaks close to the peaks of interest caused by increasing the oscilloscope sensitivity. As the oscilloscope sensitivity is increased to detect the third peak, more background noise is detected by the oscilloscope which can change the signal peak shape causing a shift in the highest point location. This phenomenon is observed more notably in the data acquired in Section 5.5 Figure 123. Therefore, a practical method is required to confirm the true velocity of the Lamb waves generated and the data processing methods.

$T.O.F_{1st\ Circumference}$  and  $T.O.F_{2nd\ Circumference}$ , come from the same wave mode travelling in the medium, therefore,

$$\therefore T.O.F_{1st\ Circumference} \approx T.O.F_{2nd\ Circumference} \approx T.O.F_{Circumference} \quad \text{Equation 33}$$

Therefore, if the wave has enough energy to go around the drum more than twice, the detections should occur at synchronous interval,

$$time_{1st\ detection} = T_{TX \rightarrow I} + T_{I \cup D} + T_{D \rightarrow RX}$$

$$time_{2nd\ detection} = T_{TX \rightarrow I} + T_{I \cup D} + T_{D \rightarrow RX} + T.O.F_{Circumference}$$

$$time_{3rd\ detection} = T_{TX \rightarrow I} + T_{I \cup D} + T_{D \rightarrow RX} + 2T.O.F_{Circumference}$$

$$\therefore \mathit{time}_{n^{th} \text{ detection}} = T_{TX \rightarrow I} + T_{I \cup D} + T_{D \rightarrow RX} + (n - 1)T.O.F_{Circumference}$$

Equation 34

Where n is the number of waves detected per TX pulse excitation.

This synchronicity in the Lamb wave detections times can be used to validate the oscilloscope readings to filter out anomalies and air-wash peaks similar to those experienced and described in Section 5.2.2 Figure 112.

The  $Cicumference_{ultrasonic}$  can be generalised as

$$Cicumference_{ultrasonic} = V_{gr} \times (\mathit{time}_{n^{th} \text{ detection}} - \mathit{time}_{(n-1)^{th} \text{ detection}})$$

Equation 35

and the  $circumference_{avg}$  generalised as

$$Cicumference_{avg} = V_{gr} \times \left( \frac{\mathit{time}_{n^{th} \text{ detection}} - \mathit{time}_{(n-count)^{th} \text{ detection}}}{count} \right)$$

Equation 36

Where “count” is the number of  $T.O.F_{Circumference}$  used to measure the average drum circumference.

## 5.5 Measuring $V_{gr}$

An experiment was conducted to validate the  $V_{gr}$  of the Lamb wave acquired from ‘Disperse’ software dispersion curve in Section 5.2.2. The air coupled ultrasonic inspection equipment was setup identical to the setup described in Section 5.2.2 Figure 110 and Figure 111, with the only difference being the location of the RX compared to the TX. The RX was

set at 300 mm arc length away from the TX and moved in increments of  $\Delta D = 100$  mm arc length for every reading up to mm arc length of 800 mm.



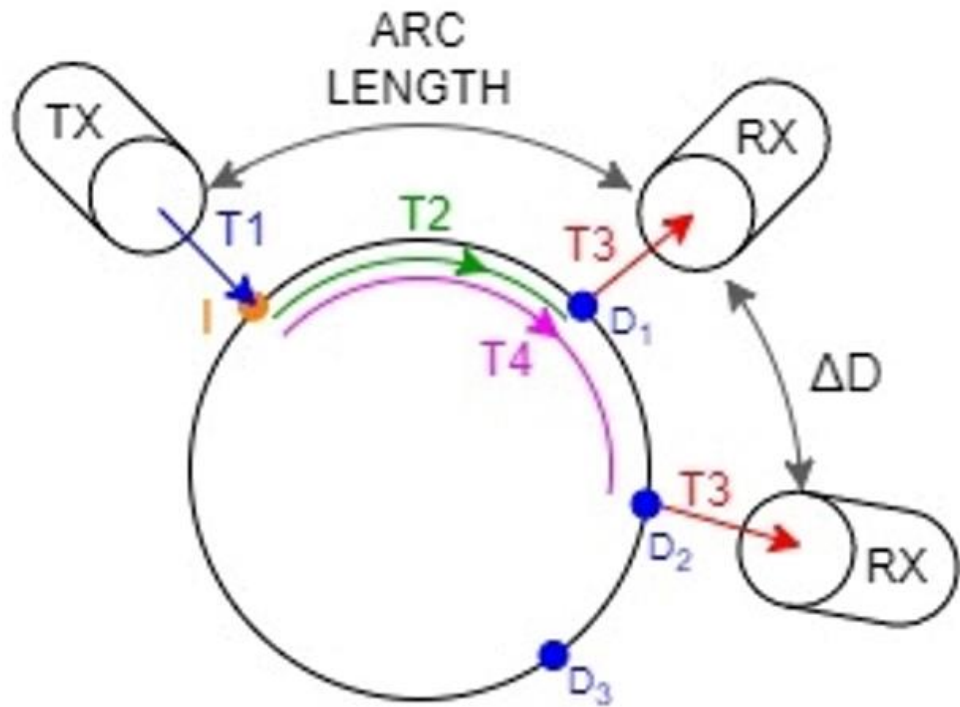


Figure 120: Illustration of wave path while being detected by RX at different detection points off the drum circumference.

<b>TX</b>	Ultrasonic transmitter.
<b>RX</b>	Ultrasonic receiver.
<b>I</b>	Incident point where longitudinal waves induce a Lamb wave into the drum's shell.
<b>D<sub>1</sub></b> <b>D<sub>2</sub></b> <b>D<sub>3</sub></b>	Points where the longitudinal wave detected by the RX were generated from the travelling Lamb waves.
<b>T1</b>	T.O.F of a longitudinal wave from TX to 'I' through air
<b>T2</b>	T.O.F of a Lamb wave from 'I' to 'D <sub>1</sub> ' along the drum circumference
<b>T3</b>	T.O.F of longitudinal wave from 'D <sub>n</sub> ' to RX through air
<b>T4</b>	T.O.F of a Lamb wave from 'I' to 'D <sub>2</sub> ' along the drum circumference
<b>Arc length</b>	The distance measured between the wedges used to align and position the transducers.
<b>ΔD</b>	Difference in the Arc length measurements

The time difference between the trigger pulse and the 1<sup>st</sup> wave detection was used to measure the Lamb wave speed ( $V_{gr}$ ), using the difference in time ( $\Delta T$ ) the Lamb wave take to travel a change in distance ( $\Delta D$ ). This was accomplished by eliminating the longitudinal waves T.O.F to and from the drum (T1 and T3 in Figure 120) from the overall 1<sup>st</sup> detection T.O.F by assuming the following:

The 1<sup>st</sup> wave detection in the 1<sup>st</sup> RX position as per Figure 120 occurs at,

$$T_{P1} = T1 + T2 + T3 \quad \text{Equation 37}$$

The 1<sup>st</sup> wave detection in the 2<sup>nd</sup> RX position as per Figure 120 occurs at

$$T_{P2} = T1 + T4 + T3 \quad \text{Equation 38}$$

Therefore, the difference in time ( $\Delta T$ ) between the detection of the waves from the two RX positions is,

$$\begin{aligned} \Delta T = T_{P2} - T_{P1} &= [T1 + T4 + T3] - [T1 + T2 + T3] \\ &= T4 - T2 \end{aligned} \quad \text{Equation 39}$$

In practice this will only remain true as long as a wedge is used to keep the distance between transducers and the drum constant, and the environmental parameters of the air gap between the transducer and the drum do not change. Otherwise, the components of  $T1$  and  $T3$  in  $T_{P1}$  and  $T_{P2}$  will be different and will not completely cancel each other in the equation.

Moreover,  $T2$  will be the T.O.F of a wave travelling from the wave induction point (I) to the detection point ( $D_1$ ) in Figure 120. The arc length is the distance measured between the wedges used to align the align and position the transducers. Therefore, in order to compensate for the difference between the true distance travelled and the measured distance, the constant ( $c$ ) is introduced. The constant ( $c$ ) can be a positive or negative value depending on the transducers and wedges geometry, and where the wave incidence and detection points are relative to the transducers body. The constant ( $c$ ) will only be valid for the equipment used and will change if the equipment geometries change.

Thus,

$$T2 = \left( \frac{ARC\ length + c}{V_{gr}} \right) \quad \text{Equation 40}$$

and

$$T4 = \left( \frac{ARC\ length + c + \Delta D}{V_{gr}} \right) \quad \text{Equation 41}$$

Where  $\Delta D$  is the difference in the arc length measurements.

Based on Equation 39,

$$\begin{aligned} \Delta T &= T4 - T2 \\ &= \left( \frac{ARC\ length + c + \Delta D}{V_{gr}} \right) \\ &\quad - \left( \frac{ARC\ length + c}{V_{gr}} \right) = \frac{\Delta D}{V_{gr}} \end{aligned} \quad \text{Equation 42}$$

Rearranging Equation 42

$$V_{gr} = \frac{\Delta D}{\Delta T} \quad \text{Equation 43}$$

The experiment was performed with an initial 'ARC length' of 300 mm to minimise air wash noise, and  $\Delta D$  increments of 100 mm to create significant change in the time stamps to minimise measurement aliasing caused by the peak location error compared to the actual peak location changes. The wave detection signals from the experiment at each  $\Delta D$  increment was recorded and analysed using the MATLAB signal analyser as previously done in Section 5.3. The RX signal peaked at -20 dB occurred at normalised signal frequencies in the range of  $0.2 \pi$  rads/sample.

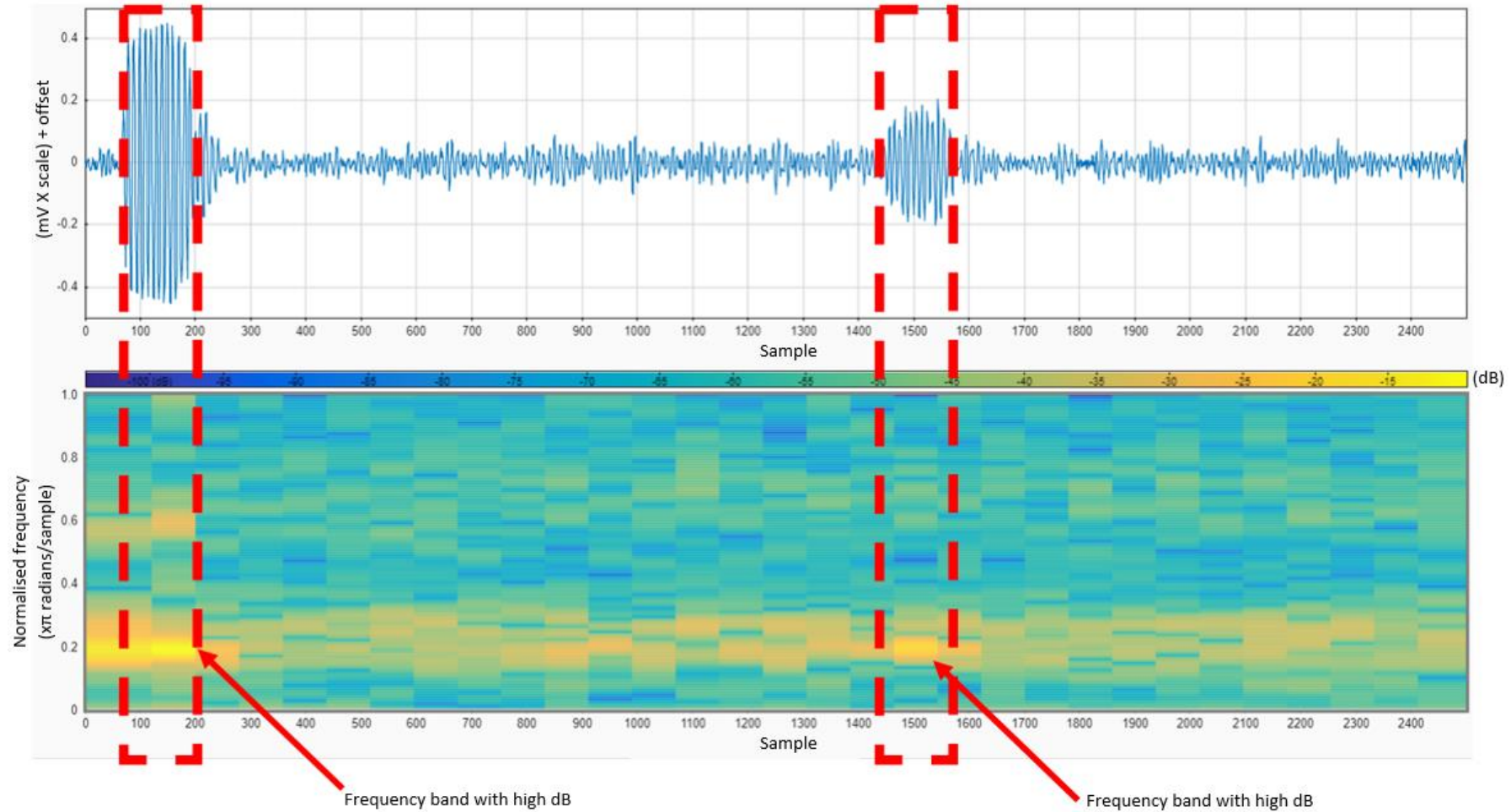


Figure 121: MATLAB signal analyser, showing the frequencies at  $0.2 \pi$  rads/sample having the highest energy levels of -20 dB in line with the raw signal above.

A MATLAB bandpass signal filter was used to filter the signals between  $0.18$  and  $0.22 \pi$  rads/sample to improve the SNR, and a peak envelop of 30 samples was used to envelope/detect the peaks of the Lamb wave signals, using,

```
filtered_signal = bandpass(raw_signal,[0.18 0.22]);  
envelope_line = envelope(filtered_signal,30,'peak');
```

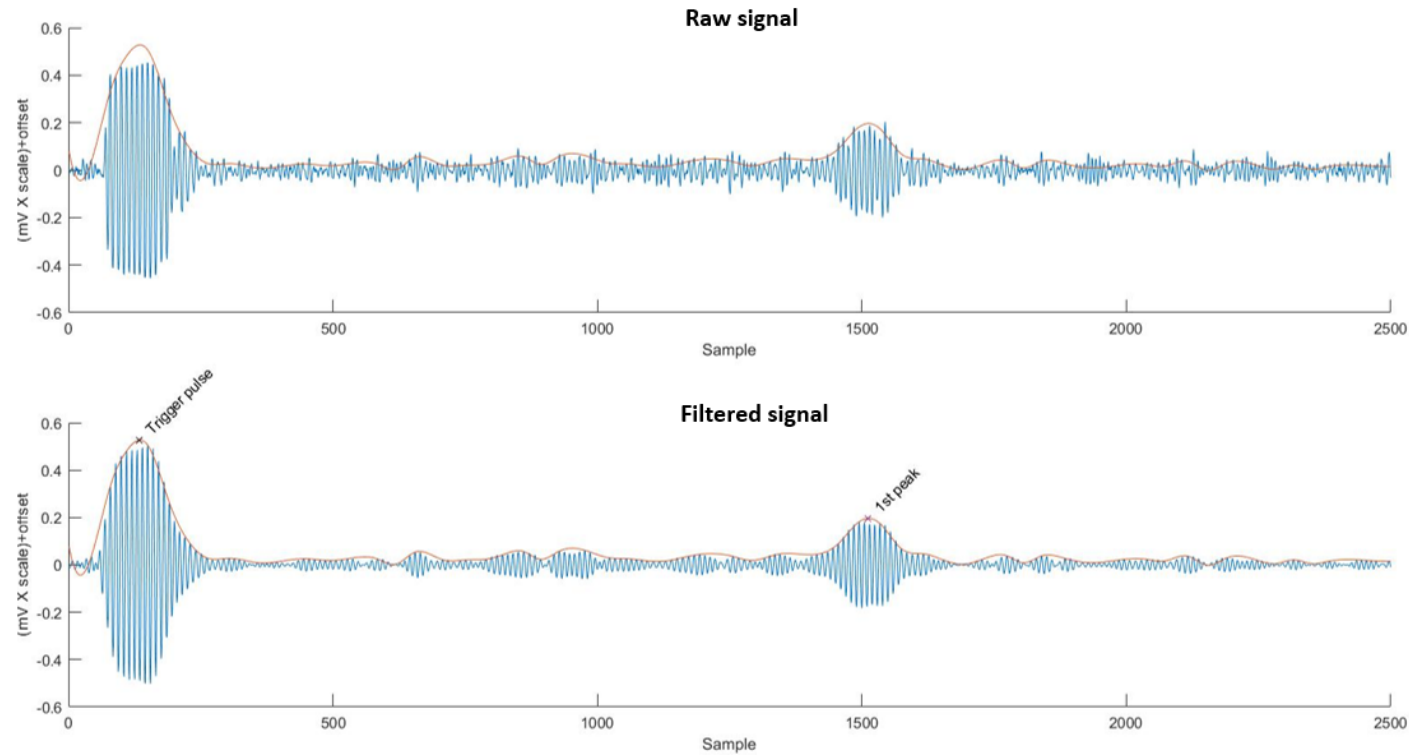


Figure 122: (Top) Raw data with a 30 samples peak envelope detection. (Bottom) Filtered reading with a  $0.18$  to  $0.22 \pi$  rads/sample bandpass signal filter and a 30 samples peak envelope.

Figure 123 demonstrates the peak locations identified from the filtered ultrasonic measurements using,  
`[peaks_y,peaks_x] = findpeaks(envelope_line,1,'MinPeakHeight',0.1)`.

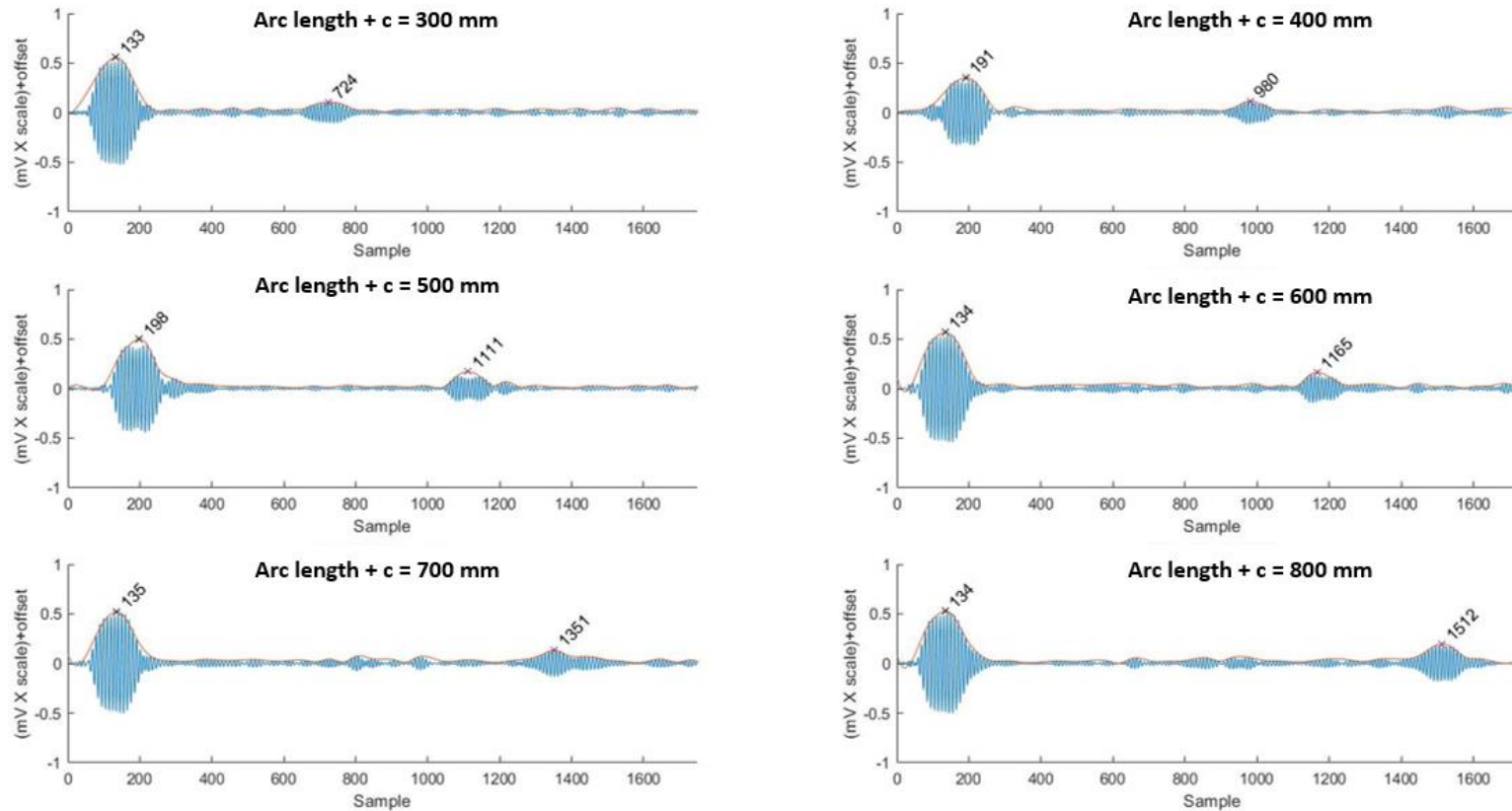


Figure 123: Peak detection samples of a Lamb wave being detected from the setup described in Figure 120 at different locations on the drum circumference.

<i>arc length + c</i> (mm)	Trigger pulse sample number	1st peak sample number	T.O.F in sample = trigger pulse – 1st peak (samples)	$\Delta sample$	$\Delta T = \frac{\Delta sample \times}{\text{horizontal scale} \times 10}$ (ms)	$V_{gr} = \frac{\Delta D}{\Delta T}$ (m/ms)
300	133	724	591	-	-	-
400	191	980	789	198	0.0396	2.5253
500	198	1111	913	124	0.0248	4.0323
600	134	1165	1031	118	0.0236	4.2373
700	135	1351	1216	185	0.0370	2.7027
800	134	1512	1378	162	0.0324	3.0864
				Average	0.0315	3.3168
				Std dev	0.0071	0.7772
				Percentage deviation	22.6%	23.4%

$$\frac{\text{Simulated } V_{gr}}{\text{Average } V_{gr}} \times 100 = \frac{3.17647 \text{ m/ms}}{3.31678 \text{ m/ms}} \times 100 = 95.77 \%$$

Equation 44

Although the average and simulated  $V_{gr}$  values are within 5 % of each other, the percentage of deviation in the  $V_{gr}$  per run during the test exceeded 20 %. This is a considerable deviation that can invalidate the results. This deviation can potentially be a result of human error during measuring the distances between the TX and RX, or due to changes in the lab environmental or differences in the localised material properties of the sample.

An inconsistency in the amplitude of the lamb waves detected was also noticed. This is believed to be a result of electromagnetic noise components close to the lamb wave detection. The noise components were high close to samples 800 and 1000 as observed from the “Arc length + c = 600mm” and “Arc length + c = 700mm” plots. This noise component lies directly in the location of the peaks on “Arc length + c = 30mm” and “Arc length + c = 40mm” which could be the reason for the inconsistencies in their amplitude. An investigation on the effects of electromagnetic noise and filtering parameters on the signal amplitude and quality will be detailed in Section 6.3.

To overcome the human factor uncertainties and the uncertainty associated with measuring the T.O.F components of the longitudinal waves traveling from the TX to the sample and off the sample onto RX, a different experiment was needed to remove the human factor from the measurements, to confirm the true source of the error.

A set of five samples of different diameters 120 mm high X 2.5 mm thick were rolled from 316 stainless steel sheets and welded shut to represent a horizontal cross section of a 500 L ILW drum. 2.5 mm thick sheets were used instead of the 2.33 mm of the real drums due to raw material availability limitations, and to identify the significance of the material thicknesses on the wave velocities. Figure 124 illustrates the manufacturing drawing used to fabricate the samples.



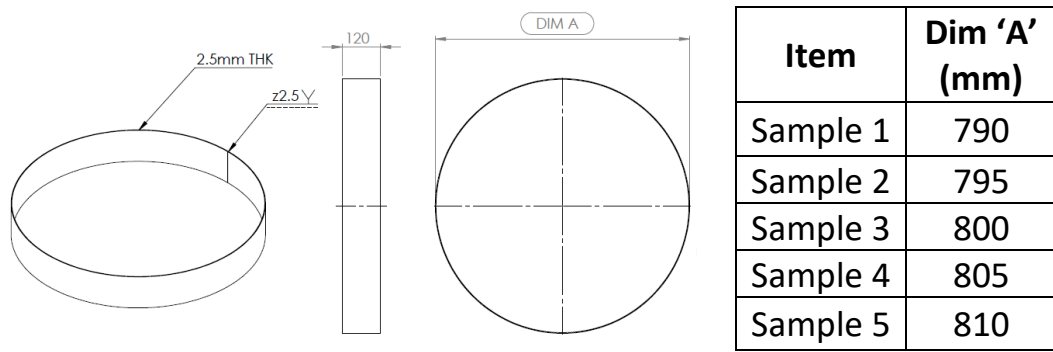


Figure 124: Manufacturing drawing of 5 different diameter test sample

A simulation was run on 'Disperse' software with the identical parameters as Section 5.2.2 Figure 108 except for the material thickness being set to 2.5 mm instead of 2.33 mm to match the material used in the sample. The simulations resulted in a  $V_{gr}$  of 3.18013 m/ms at 0.5 MHz compared to the 3.17647 m/ms of the 2.33 mm thick plate, and an angle of incidence of 8.05° at the 0.5 MHz frequency compared to the 8.15° of the 2.33 mm thick plate.

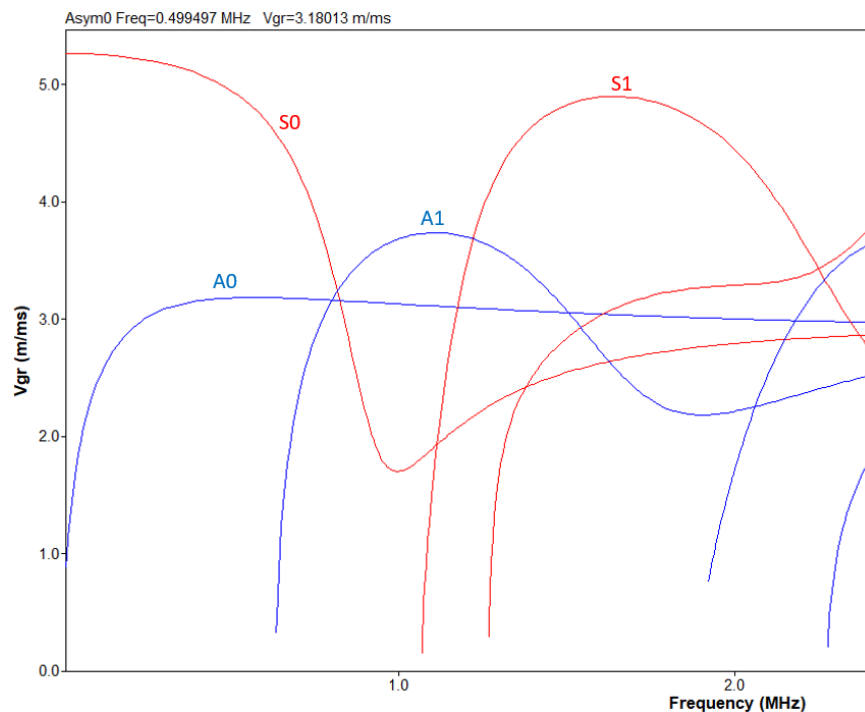


Figure 125: Lamb wave dispersion curve created using 'Disperse' software showing different wave modes and their wave group velocity

( $V_{gr}$ ) change in relation to induced wave frequencies ( $f$ ) while travelling through a 2.5 mm thick plate.

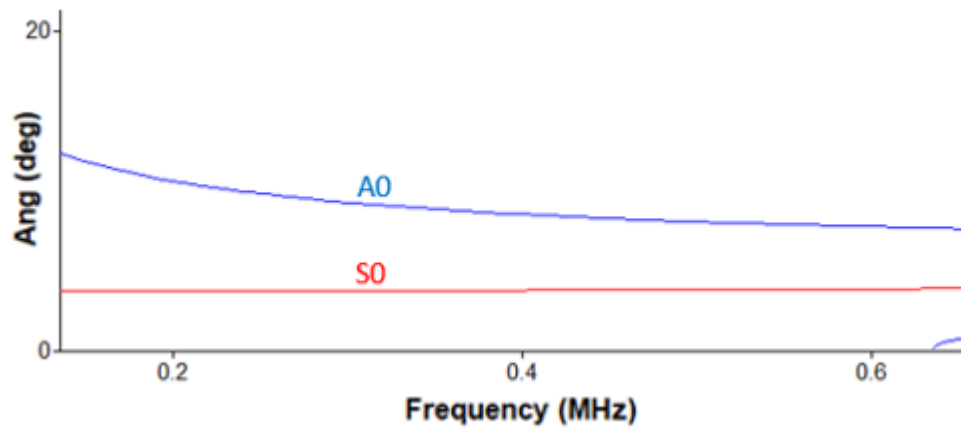


Figure 126: Lamb wave dispersion curve created using ‘Disperse’ software showing different wave modes and their angle of incident in relation to induced wave frequencies ( $f$ ) while travelling through a 2.5 mm thick plate.

The air coupled ultrasonic inspection equipment was set identical to the setup described in Section 5.2.2 Figure 111. The circumference of every sample was measured using a soft measuring tape and recorded after manufacture, this is necessary to ensure that the sample measurement used in any calculations is as built and considers the errors and dimensional uncertainties from the manufacturing process.

Item	<i>Cicumference</i> <sub>tape</sub> (mm)
Sample 1	2483
Sample 2	2498
Sample 3	2516
Sample 4	2532
Sample 5	2544

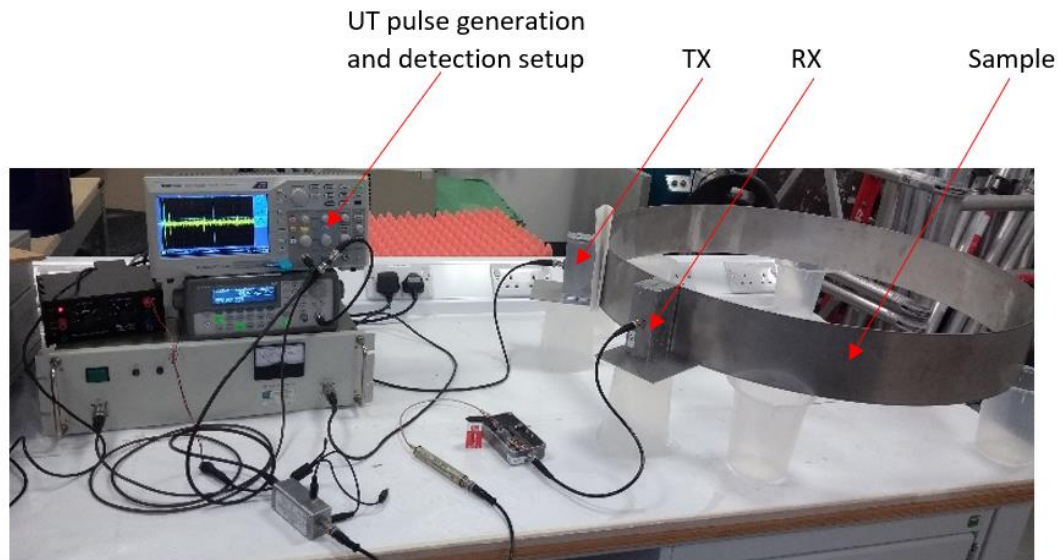


Figure 127: Setup used to validate the accuracy of the circumferential measurement using Lamb waves

Four readings were taken from each sample and the time between the 1<sup>st</sup> and 2<sup>nd</sup> peak detection ( $T.O.F_{1st\ Circumference}$ ) was logged to measure the T.O.F of the wave's 1<sup>st</sup> round around the drum circumference, and the time between the 2<sup>nd</sup> and 3<sup>rd</sup> ( $T.O.F_{2nd\ Circumference}$ ) as the T.O.F of the wave's 2<sup>nd</sup> round around the drum. The two T.O.Fs were averaged and multiplied by the expected wave velocity ( $V_{gr(simulation)} = 3.1194\ m/ms @ 0.5\ MHz$ ) from Figure 125 to calculate the drum circumference from the ultrasonic signal readings.

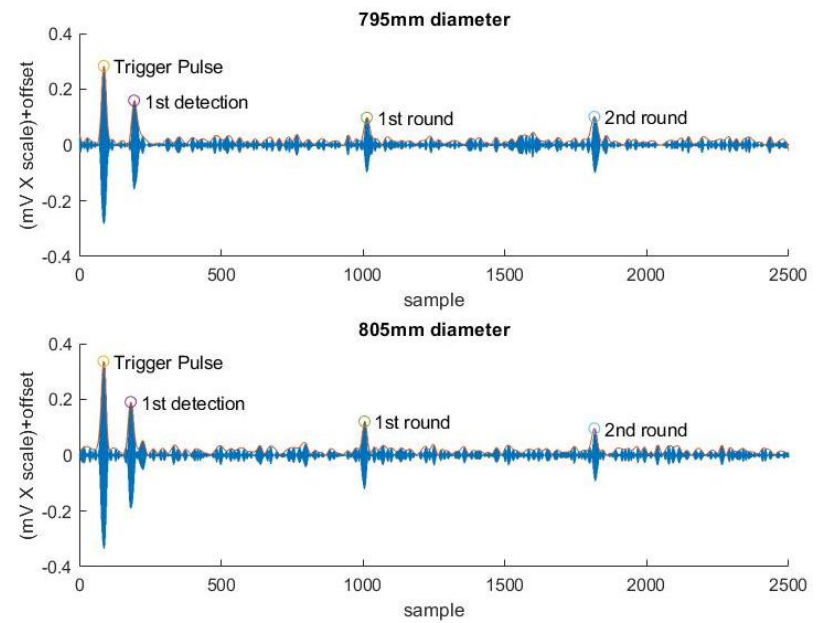
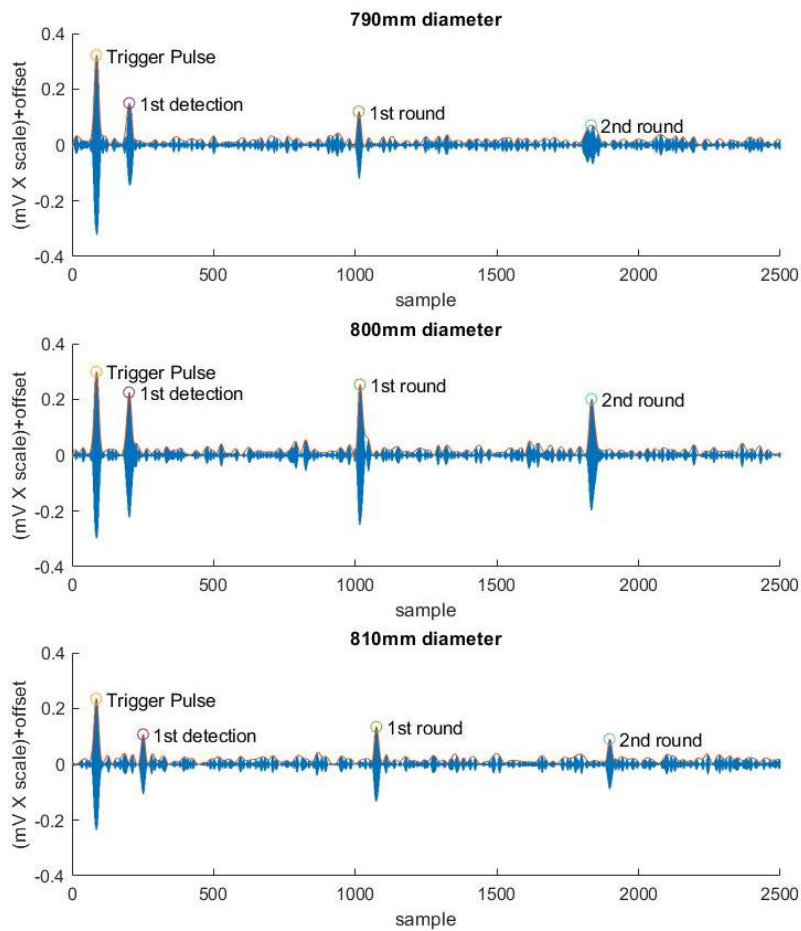


Figure 128: Filtered oscilloscope readings of signals detected by the receiver from 5 different drum cross section samples identical in every way except for the overall 5mm difference in diameters as shown in Figure 124.

$$T.O.F_{1st\ Circumference} = (2^{nd}\text{Peak} - 1^{st}\text{Peak}) \times \left( \frac{\text{horizontal scale} \times 10}{\text{samples}} \right)$$

$$T.O.F_{2nd\ Circumference} = (3^{rd}\text{Peak} - 2^{nd}\text{Peak}) \times \left( \frac{\text{horizontal scale} \times 10}{\text{samples}} \right)$$

$$T.O.F_{avg\ Circumference} = (3^{rd}\text{Peak} - 1^{st}\text{Peak}) \times \left( \frac{\text{horizontal scale} \times 10}{\text{samples}} \right)$$

$$T.O.F_{avg} = \frac{\sum_{v_{T.O.F_{avg\ Circumference} \in \text{sample no.}} T.O.F_{avg\ Circumference}}}{4}$$

$$v_{gr_{2 \rightarrow 1}} = \frac{Cicumference_{tape}}{T.O.F_{1st\ Circumference}}$$

$$v_{gr_{3 \rightarrow 2}} = \frac{Cicumference_{tape}}{T.O.F_{2nd\ Circumference}}$$

$$v_{gr_{3 \rightarrow 1}} = \frac{Cicumference_{tape}}{T.O.F_{avg\ Circumference}}$$

$$v_{gr_{2 \rightarrow 1}\ avg} = \frac{\sum_{v_{gr_{2 \rightarrow 1} \in \text{sample no.}} v_{gr_{2 \rightarrow 1}}}{4}$$

$$v_{gr_{3 \rightarrow 2}\ avg} = \frac{\sum_{v_{gr_{3 \rightarrow 2} \in \text{sample no.}} v_{gr_{3 \rightarrow 2}}}{4}$$

$$v_{gr_{3 \rightarrow 1}\ avg} = \frac{\sum_{v_{gr_{3 \rightarrow 1} \in \text{sample no.}} v_{gr_{3 \rightarrow 1}}}{4}$$

$$v_{gr(\text{measured})} = \frac{\sum_{v_{gr_{3 \rightarrow 1}\ avg \in \text{sample no.}} v_{gr_{3 \rightarrow 1}\ avg}}{4}$$

Item	1 <sup>st</sup> peak	2 <sup>nd</sup> peak	3 <sup>rd</sup> peak	T. O. F <sub>1st Circumference</sub> (ms)	Average T. O. F <sub>1st Circumference</sub>	Standard deviation T. O. F <sub>1st Circumference</sub>	T. O. F <sub>2nd Circumference</sub> (ms)	Average T. O. F <sub>2nd Circumference</sub>	Standard deviation	T. O. F <sub>avg Circumference</sub> (ms)	T. O. F <sub>avg</sub> (ms)	T. O. F <sub>avg</sub> Standard deviation
Sample 1	206	1014	1817	0.808	0.807	0.002	0.803	0.803	0.002	0.8055	0.805	0.001
	202	1006	1812	0.804			0.806			0.805		
	201	1007	1809	0.806			0.802			0.804		
	199	1007	1808	0.808			0.801			0.8045		
Sample 2	193	1013	1815	0.82	0.809	0.007	0.802	0.813	0.006	0.811	0.811	0.001
	211	1021	1838	0.81			0.817			0.8135		
	217	1020	1837	0.803			0.817			0.81		
	218	1022	1839	0.804			0.817			0.8105		
Sample 3	201	1018	1834	0.817	0.817	0.001	0.816	0.817	0.001	0.8165	0.817	0.000
	201	1016	1833	0.815			0.817			0.816		
	200	1018	1834	0.818			0.816			0.817		
	200	1016	1833	0.816			0.817			0.8165		
Sample 4	184	1004	1815	0.82	0.821	0.002	0.811	0.812	0.001	0.8155	0.817	0.001
	184	1003	1817	0.819			0.814			0.8165		
	182	1004	1816	0.822			0.812			0.817		
	181	1005	1815	0.824			0.81			0.817		
Sample 5	173	998	1873	0.825	0.824	0.002	0.875	0.834	0.024	0.85	0.829	0.012
	174	1001	1820	0.827			0.819			0.823		
	254	1075	1893	0.821			0.818			0.8195		
	251	1074	1897	0.823			0.823			0.823		
Average deviation (T. O. F <sub>avg</sub> deviation)											0.003	

Item	$V_{gr_{2 \rightarrow 1} avg}$ (m/ms)	$V_{gr_{3 \rightarrow 2} avg}$ (m/ms)	$V_{gr_{3 \rightarrow 1}}$ (m/ms)
Sample 1	3.0787	3.0922	3.0854
Sample 2	3.0868	3.0716	3.0792
Sample 3	3.0814	3.0814	3.0814
Sample 4	3.0831	3.1192	3.1010
Sample 5	3.0874	3.0513	3.0692
Average	3.0835	3.0831	3.0833
Standard deviation	0.0033	0.0225	0.0104

The overall average  $V_{gr(measured)}$  from the experiment is  $3.0844 \pm 0.0104$  m/ms using 2 peak detections, compared to the  $V_{gr(simulation)}$  of 3.1194 m/ms. This is a percentage difference of 1.16 %.

Using the  $V_{gr(measured)}$  and the uncertainty and the deviation in  $T.O.F_{avg}$  of  $T.O.F_{avg deviation} = 0.003$  ms, the measurement uncertainty can be estimated as

$$\begin{aligned}
 & \text{measurement uncertainty} \\
 &= \text{Cicumference}_{deviation} \\
 &= V_{gr(measured)} \times T.O.F_{avg deviation} \\
 &= 3.0833 \text{ m/ms} \times 0.003 \text{ ms} = 9.34 \text{ mm} \quad \text{Equation 45}
 \end{aligned}$$

This uncertainty equates to a measurement error in a healthy 800 mm diameter ILW drum of

$$\begin{aligned}
 & \text{Percentage error} \\
 &= 100 \times \frac{\text{measurement uncertainty}}{\text{Cicumference}_{healthy drum}} \\
 &= 100 \times \frac{9.34}{800\pi} = 0.37\% \quad \text{Equation 46}
 \end{aligned}$$

Given that the T.O.Fs in the individual measurements were acquired using the same method, any offsets in the T.O.F will likely be similar and therefore cancel out when measuring synchronous results as described in Equation 33 and Equation 34. This leaves the  $V_{gr}$  as a more probable source of error, where the  $V_{gr}$  changes due to the sample material

properties. Although all the samples were machined out of the same stainless-steel sheet, they were manually rolled into different diameters and welded shut into cylinders. This will vary the residual stresses and material embrittlement of the samples due to the different bending radiuses and manual heating for fabrication and welding. This can be reduced in future experimental samples by heat treating the samples after rolling as done on the real ILW drums, to relieve the internal stresses build up caused by the machining processes.

Variations in material properties between different ILW drums inside the vaults are very likely too, due to the difference in environments and radiation level that they have been exposed to for different amount of time based on their age, which will result in variations in  $V_{gr}$  [127] [128] [129]. Consequently, real life inconsistencies must be identified and considered in the measurements to achieve accurate results.

## 5.6 Real-life inconsistencies

Although both the drum and samples are made of 316 stainless-steel, the sheet material used to manufacture the real drums are expected to have higher quality assurance standards compared to the commercially available materials. This combined with different machining processes and material working and welding temperatures, will affect the material work hardening and so alter the acoustic properties of the materials post machining [127] [128].

### 5.6.1 Manufacturing work hardening

The differences in work hardening rates may introduce inconsistencies in inspection results between the round test samples, the new empty unused drums, and the old drums currently operating in the ILW vaults. This is important to note because it is likely that the modern fabrication techniques used in the manufacturing of the recently manufactured drums, differs from the manufacturing techniques and technologies that were available in the 60s/70s, when the first sets of drums are presumed to have been manufactured. This makes the manufacturing date of a given drum a variable that needs to be considered, when estimating the acoustic properties of that drum's material for calculating the  $V_{gr}$  of the



Lamb waves used to inspect it. Even if we assume that the manufacturing processes was indeed perfected many decades ago and all the drums have been manufactured consistently. The limitations in the accuracy of the modern manufacturing techniques, is still enough to cause a significant variation in the material thickness and weld properties, causing significant measurement errors when using the proposed Lamb wave inspection technique. Therefore, it is very important to understand the variabilities in the test subjects and be able to accommodate or eliminate their effects on the inspection methods, to make the use of Lamb wave in circumferential measurements a viable inspection technique.

### 5.6.2 Manufacturing tolerances

The sensitivity in the wave's  $V_{gr}$  to subtle changes in material thicknesses may also be problematic because the drums' wall thickness is allowed to drop from 2.33mm down to 2.00 during the manufacturing process [130] This subtle variations in thickness due to the initial manufacture will vary the wave velocity between 3.067 m/ms and 3.17647 m/ms based on dispersion curves from 'Disperse' software in Figure 129. This is 3.5 % difference in  $V_{gr}$  compared to the 1.16 % error observed in Section 5.5 which caused a 9.3m mm circumferential measurement errors.

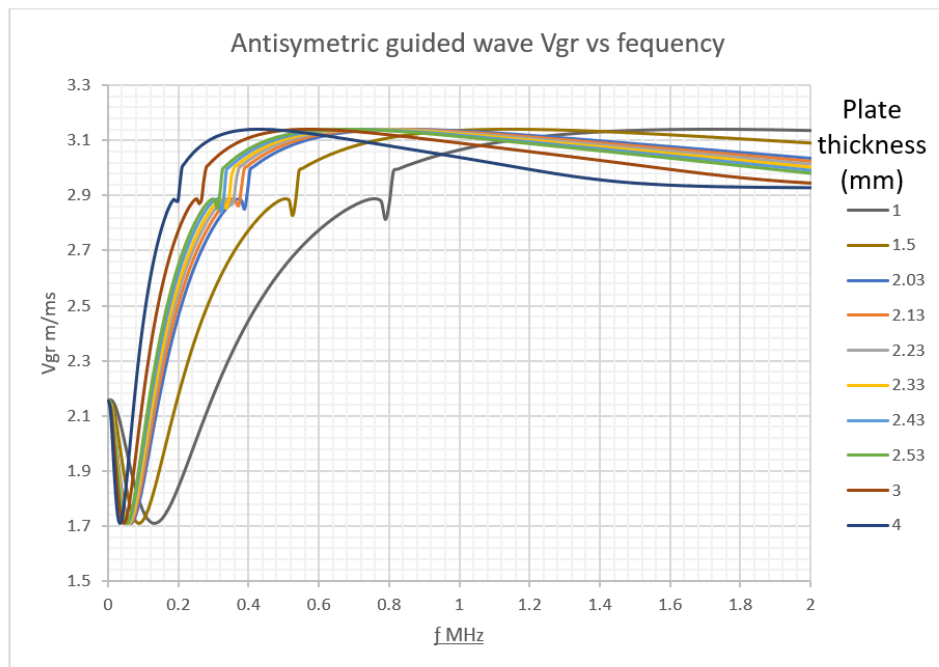


Figure 129: Antisymmetric A0 Lamb wave group velocity  $V_{gr}$  vs  $f$  of different stainless-steel plate thicknesses. This data is generated using ‘Disperse’ with the same settings described in Section 5.2.2 with the plate thickness as the variable.

Although it can be tempting to simplify this by using an average nominal thickness value for the wall thickness in the  $V_{gr}$  dispersion simulation to minimise the errors caused by the thickness variations, the distribution of the thickness along the circumferences is also unknown, and the nominal thickness may be skewed toward either ends of the spectrum. However, by observing the  $V_{gr}$  vs  $f$  changes in relation to different material thicknesses as per Figure 129, we can observe distinctive relations and patterns that can help overcome the thickness variation.

Avoiding frequencies above the 1 MHz margin will reduce the number of different wave modes that may be generated at a given  $f$  and angle as per the dispersion curves in Figure 108 and Figure 109. This is important because generating multiple wave modes with different  $V_{gr}$  values simultaneously will result in multiple wave patterns being detected by the RX, which will complicate the identification of the individual pattern’s T.O.F gaps described in Section 5.6.

Avoiding the use of frequencies below 0.4 MHz will reduce the step changes in the  $V_{gr}$  in relation to frequency and thickness variations as per Figure 129 to reduce the  $V_{gr}$  error range. Figure 129 indicates a cross over at the 0.07 MHz frequency margin where the  $V_{gr}$  values would be almost identical for all the thickness in the range between 2mm and 3mm, which the drums' thickness variations fall in. This can potentially eliminate the thickness variation effects on the  $V_{gr}$  and circumferential measurement.

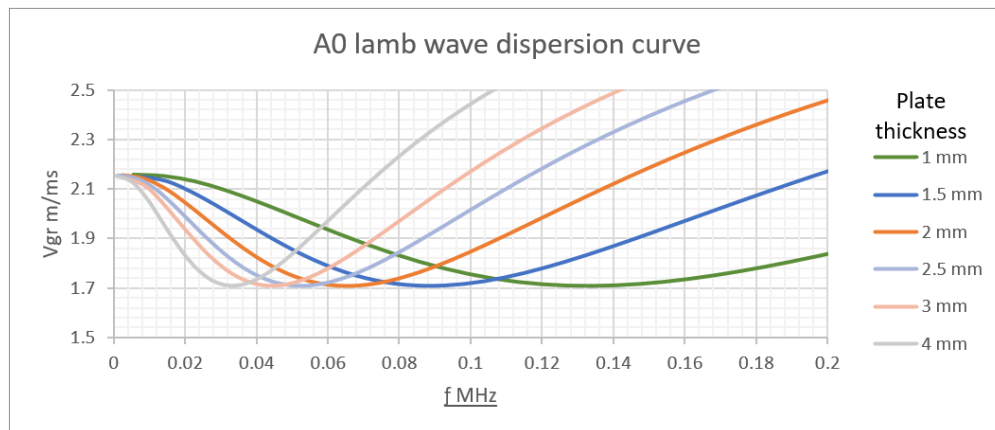


Figure 130: Antisymmetric A0 Lamb wave  $V_{gr}$  vs  $f$  of different plate thicknesses at  $f$  range between 0 and 0.2MHz.

Alternatively, the lowest  $V_{gr}$  at any material thickness is around  $1.71 \text{ m/ms}$ . Meaning that if a transmitter and receiver can be made to generate and detect waves using a frequency sweep between 0.02 MHz and 0.2 MHz, the longest circumference detected during the frequency sweep will correlate with the lowest  $V_{gr}$  value of  $1.71 \text{ m/ms}$  at the trough of the  $V_{gr}$  vs  $f$  curve. This would both eliminate the variations in  $V_{gr}$  and make it a constant, as well as identify the possible nominal average thickness of the drum wall at the circumferential cross-section being inspected. For example, if the longest circumference measured during the frequency sweep is detect at 0.05 MHz, then the nominal wall thickness would be 2.5mm, and if the same frequency sweep is done many years after and the lowest  $V_{gr}$  is detect at 0.09 MHz, then the new nominal thickness would be 1.0 mm as per Figure 130. This change in nominal thickness would then be contributed to a possibility of internal material corrosion/erosion inside the drum, if not overshadowed by the

effects of other parameters such as stresses and embrittlement which can also change the entire dispersion curve of the ultrasonic waves.

### 5.6.3 Radiation embrittlement

Assuming a perfected drum manufacturing process, and the manufacturing of a transmitter and receivers that can operate effectively at all the frequency ranges required to perform the frequency sweep described in Section 5.6.2 is possible, a number of non-controllable variables that will have a significant effect on the  $V_{gr}$  of the Lamb wave will still persist.

Although it may be possible to predict the long-term changes to an individual drum's structure based on the controlled storage environment described in Section 2.5. The changes to the drums' caused by their own content or its neighbours' content may not be possible without full knowledge of each drums' content layout, location, and storage history. The variable and inconsistent radioactive content stored in the drums will expose the individual drums' walls to irregular and localised ionizing radiation from its content, or random ionising nuclides coming from its neighbouring or other nearby ILW containers in the store. This ionising radiation will cause embrittlement in the 316 stainless steel [129] from which the drums are made, and affect the material behaviour and wave propagation, because brittle stainless steel will not have the same flexibility to stretch and compress to propagate the Lamb wave as described in Section 5.2.2. The changes in elasticity of the material as its brittleness increase, causes an increase in the wave attenuation and reduces the guided waves velocity, the reduction in wave velocity is amplified by the increase in wave frequency [131].

## 5.6.4 Cementitious immobilisation



Figure 131: Left-Cut views of nuclear waste drums containing different types and layouts and of nuclear decommissioning products [132].  
Right- Metallic scrap material embedded in immobilising cementitious matrix inside an ILW 500 L drum [132]

The majority of the ILW decommissioning plants in the UK encapsulate the radioactive waste material in the ILW containers using a cementitious grout composites, made of Ordinary Portland Cement (OPC) and blastfurnace slag at a ratio of 1:3 with occasional increase up to 1:9 [133]. Less frequently this grouts may be prepared with Pulverised Fuel Ash PFA rather than slag [133]. The grout particle sizes and overall porosity varies with different mixing procedures, treatment temperatures, age, and additives [133], adding to the number of different grout properties that can be in contact with the drums' internal surfaces at any point inside a given sample. This combined with the possibility of trapped air gaps in the grout mixture due to the variable waste composition, along with the different contact forces caused by the grout expansion due to the hydration effects described in Section 2.7, will create an almost unpredictable medium in which the Lamb waves will contact while travelling along the internal side of the drums' wall.

A simulation was run using 'Disperse' software with the same setting as per Section 5.2.2 with one of the materials in contact with the metal surface being basic construction concrete instead of air. Construction concrete is used as a simplification of the immobilising cementitious matrix in the simulation, because of its composition similarity to the ILW containers immobilisation grout [133]. When the metal plate in the

simulation is in direct contact with cement as expected at the internal surface of the drum wall, the Lamb waves dispersion curves significantly change compared to being in contact with air as seen in Figure 132.

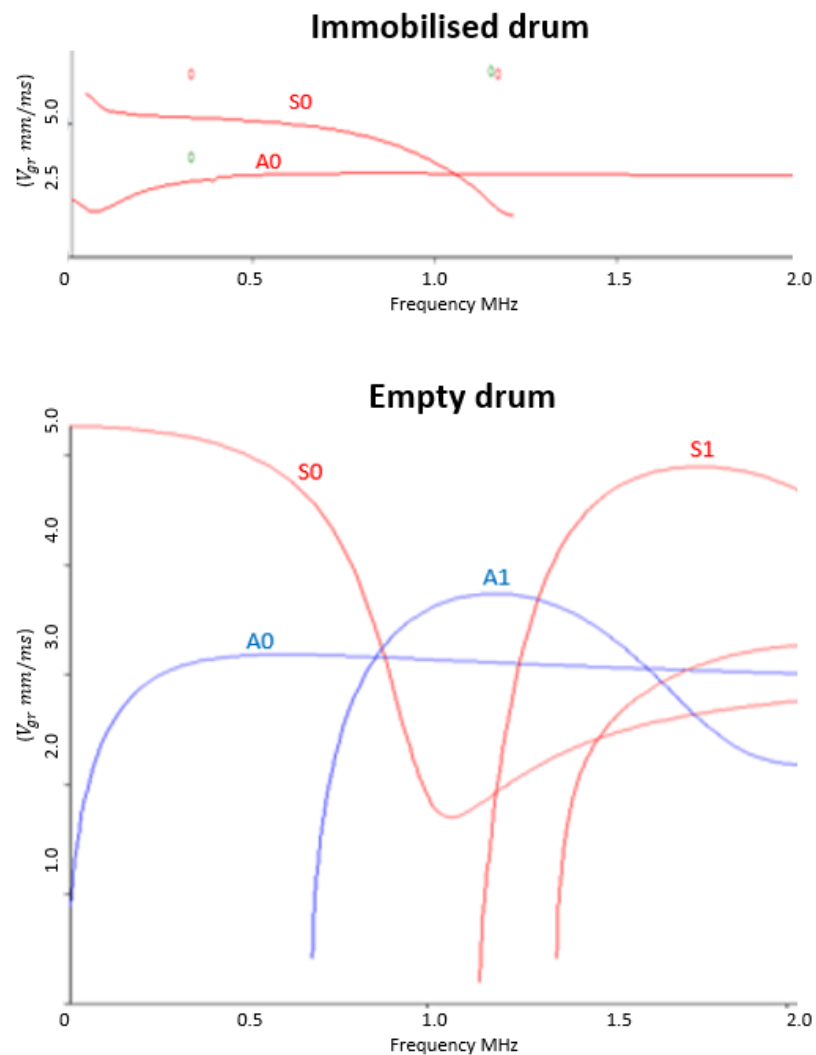


Figure 132: (Top) Lamb wave dispersion curve created using 'Disperse' software showing different wave modes and their wave group velocity ( $V_{gr}$ ) change in relation to induced wave frequencies ( $f$ ) while travelling through a 316 stainless-steel sheet with air on one layer and concrete/cement on the other layer to represent an immobilised drum. (Bottom) Lamb wave dispersion curve created using 'Disperse' software showing different wave modes and their wave group velocity ( $V_{gr}$ ) change in relation to induced wave frequencies ( $f$ ) while travelling through a 316 stainless-steel sheet with air on both layers of the sheet to represent an airgap between the concrete/ cement and the drum's wall.

According to the dispersion curve acquired from 'Disperse' software in Figure 132, the  $V_{gr}$  of the A0 lamb wave in stainless-steel with one of its layers in air and the other in contact with concrete is  $3.060 \text{ m/ms}$ , compared to  $3.176 \text{ m/ms}$  when both layers were in contact with air. This difference in  $V_{gr}$  creates a difference in circumferential measurement from 2.502 m and 2.841 m when multiplied by the  $0.788 \text{ ms}$   $T.O.F_{Circumference}$ . The simulation also provided an angle of incidence of  $90^\circ$ , which is unfeasible to produce using an air coupled transducer, thus further validation of these results is required. This will be attempted in Section 6.4,

Moreover, any air gaps between the cement and the drums' inner layer caused by the air bubbles trapped during cement pouring, or long-term changes in cement volumes due to shrinkages as it cures followed by inconsistent expansions caused by moisture changes over time, will cause inconsistencies in the dampening effects on the waves, as their medium alters between air and cement during their journey along the drums' circumference. The presence of water and fluids in the drum from decommissioning product or moisture can reduce the wave peak amplitude up to 21 % compared to dry wave amplitudes [134].



Figure 133: Showing potential gap between cement and the wall due to air bubbles [64].

This means that a single dispersion curve, to predict the Lamb waves behaviour as they contact different material at different stages in their journey along the drum's circumference is not possible, due the unpredictable changes in mediums in which the waves travel in. In other words, each circumferential layer of the drum will have a different overall average wave velocity depending on the presence and frequency of air bubbles and moisture along their periphery.

## 5.7 The average drum

As the number of possible variables that can significantly affect the Lamb waves propagating around an ILW 500 L drum increase, the number of possible combinations in which multiple variables exist and effect the waves differently will increase. For example, if we consider the following 12 variables to have an equal probability being average. i.e., each variable has a 50 % chance of being average/mean value, and 50 % chance of not being average/abnormal and causing a significant change in the Lamb waves  $V_{gr}$ .

Such variable include:



- Immobilising material in contact with the drum shell
- Immobilising material air gaps (bubbles) frequency and size
- Immobilising material moisture level
- Drums' shell mechanical stresses due to Immobilising material expansion
- Drums' shell localised embrittlement due to ionizing radiation
- Drums' localised temperature changes due to content activity
- Localised drum's shell internal corrosion
- Localised drum's shell external corrosion
- External air humidity due to store location/season
- Varying drum's shell thicknesses along the periphery
- Drums' stainless-steel work hardening, and embrittlement caused by the manufacturing process
- Variations in drums' weld seams

The probability of all the 12 variables being “average” in any given drum at random will be,

$$\begin{aligned}
 &P(\text{All 12 variable are average}) \\
 &= P(\text{1 variable being average})^{\text{number of variable}} \quad \text{Equation 47} \\
 &= 0.5^{12} = \frac{1}{4096}
 \end{aligned}$$

This means that the chance of any given drum picked at random to have all its variable being “average” is 1: 4096. This ratio will increase as the number of variables and likelihood of a variable being irregular or “not-average” increase. In reality, more variables are expected, and the variables will have interdependent weights (not always 50 %), but only 12 with equal weights are chosen here for concept simplification.

Thus, creating Lamb wave dispersion curves from variables “average” values that have a probability of 1 in 4096 to be correct, is likely to yield measurement results that are more wrong than correct. This fits the jaggedness principal where one cannot apply one-dimensional thinking to characteristics that have many weakly-related dimensions [135], for example a cockpit designed to fit an average pilot using average values of 140 different physical characteristics, from 4063 different pilots, fits nobody [136].

Therefore, it is necessary to find a new method of determining the properties of the Lamb waves propagating around every specific drum, without needing to simplify all the possible variables into their average values.

The possibility and practicality of methods that can be used to measure the drums' circumferences using Lamb waves and  $V_{gr}$  without prior knowledge of the individual drum's specific parameters or content will be evaluated in Chapter 6.

## 5.8 Summary

It is potentially possible to measure the circumference of an ILW drum using non-contact air coupled ultrasonic transducers with limited access to the drum's circumference. The transducers can induce Lamb waves that travel along the drums' circumference, whose T.O.F measurements can be used to calculate the drums' circumference.

Dispersion curves from computer simulations can be a great tool to identify the modes, properties, and velocities ( $V_{gr}$ ) of the Lamb waves used in the circumferential measurements of the drums. However, due to the high number of variables between ILW drums' structures, content, and age, it is unlikely to find an ideal average dispersion curve using computer simulation that would be suitable for providing the data necessary to inspect all the drums stored in the vaults. Consequently, it is necessary to find a new method other than simple dispersion curves from computer simulation, to identify and analyse the Lamb wave behaviour and  $V_{gr}$ , as it propagates around a random imperfect aged drum in the ILW vault, without prior knowledge of the drums content or structural details.

## Chapter 6: Ultrasonic Lamb wave inspection of varying samples

### 6.1 Introduction

The detection of the Lamb waves for the 3<sup>rd</sup> time as it travels around the ILW 500 L drum circumference in Section 5.3, allowed for the validation of the T.O.F of the Lamb waves used in the circumferential direction. Meanwhile, the work hardening, stresses and embrittlement caused by the aging of ILW 500 L drum, and possible expansion of their contents, changes the drum shells' properties as described in Section 5.6. This in return changes the dispersion curves of the Lamb waves used in the circumferential measurements of the drums. Thus, a practical and reliable method is required to identify the Lamb waves' velocities ( $V_{gr}$ ) and angles of incidence, without prior knowledge of the drums' properties or contents.

This chapter will pursue the methods needed to improve the ultrasonic inspection process by optimising the transduction of the Lamb waves into and off the ILW 500 L drums, in an attempt to demonstrate real life simulation of ILW waste-form expansion and quantise the effect of the drum's contents on the Lamb wave propagation along the drum's circumference. It will also propose methodology to detect cracks and/or corrosion defects using the propagating Lamb waves properties, and propose a tool to identify the defect location based on detection patterns.

### 6.2 Remote transducers angle control and sweeping

To deploy an air coupled ultrasonic transducers using the "Passive ILW inspection robot" described in section 4.6, the sensor module will need to align the ultrasonic transducers, to the angle of incidence required to refract a Lamb wave into the ILW 500 L drum shells as described in Section 5.2.2.

In Section 5.2.2 Figure 109, an incidence angle of 8.15 ° was required to refract the longitudinal waves from the air-coupled piezoelectric transducer into the Lamb waves that will travel along the drum's periphery. This was initially achieved manually using manual

measurement tools, then optimised using the fixed angle 3D printed wedge described in Figure 114. However, this Lamb wave angle of incidence will be subject to change depending on the longitudinal waves properties as well as the workpiece properties and content as described in Section 5.6. Consequently, for the air coupled piezoelectric transducers to transduce the acoustic waves successfully onto and off varying samples, the angle of incidence alignment tool needs to be adjustable to sweep a range of angles until the correct angle of incidence is matched. This tool must be remotely controllable, integrate with robotic deployment methods, and maintain the non-invasive, no-contact operation target of the project. These requirements were achieved in a gimbal that was designed and built to automatically align the transducers tangentially to any metallic/conductive surface.

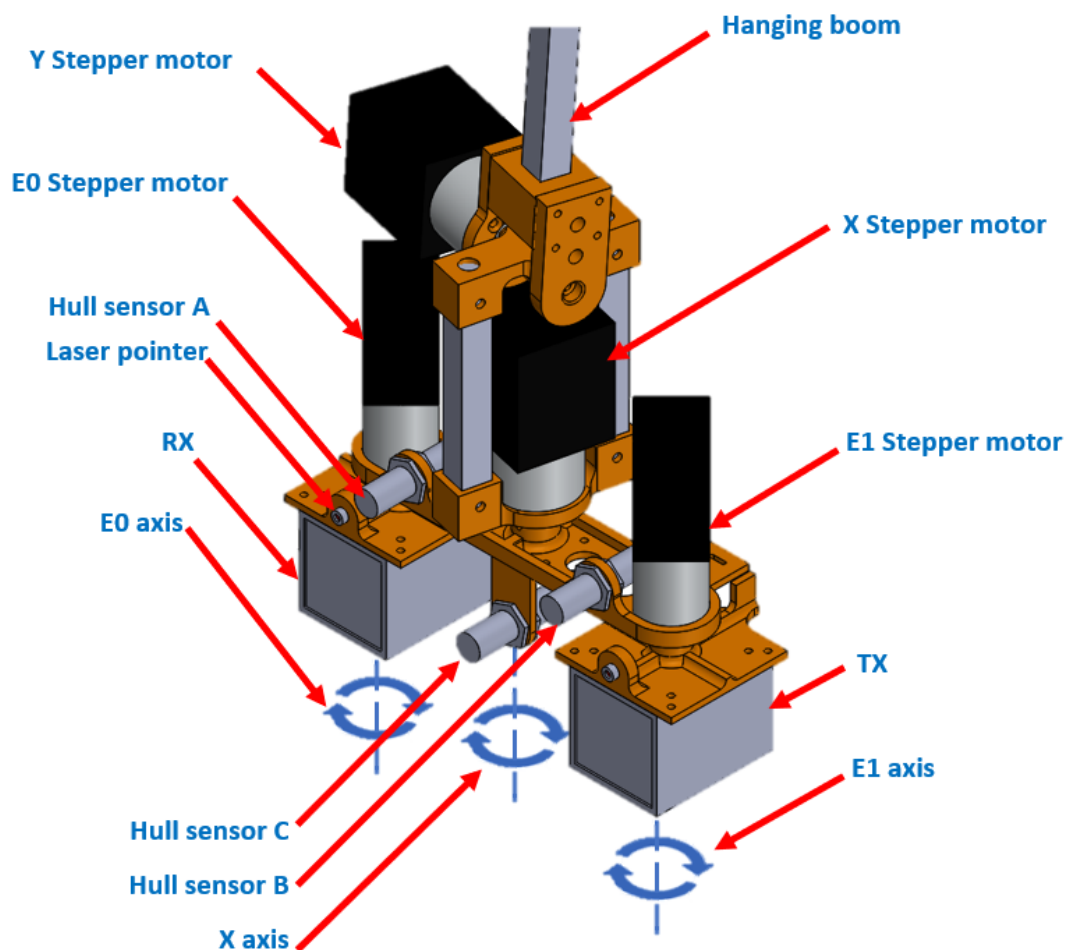


Figure 134: CAD of the proposed gimbal mechanism required to align and control the air-coupled transducers TX and RX angles to achieve the desired Lamb wave refraction and detection.

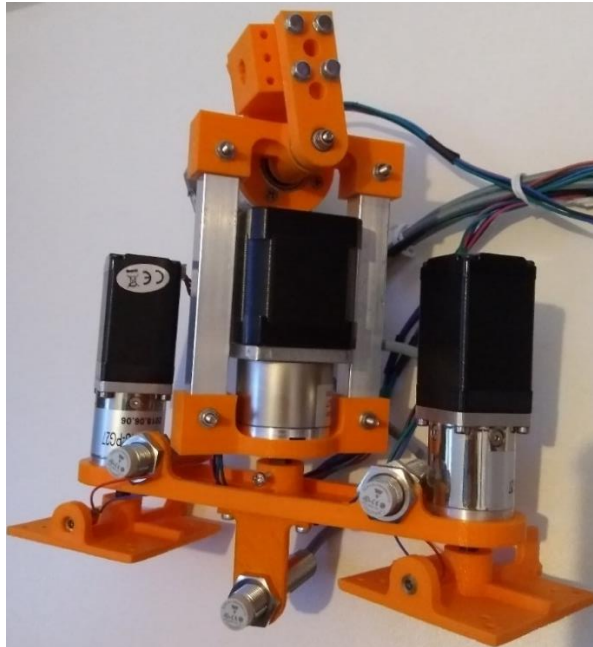


Figure 135: Prototype of the proposed gimbal mechanism required to align and control the air-coupled transducers TX and RX angles to achieve the desired Lamb wave refraction and detection.

The angle control gimbal mechanism uses a set of stepper motors to move the ultrasonic transducer in and along different axis, and 3 non-contact hall effect sensors ('A', 'B' and 'C') to triangulate and align the gimbal X and Y axis tangential to the workpiece with accuracies up to 0.06 °. The hall effect sensors trigger electric signals when their fields are at a minimum pre-set distance from a conductive surface (the workpiece surface), these signals are then used by the control computer to locate the gimbal axis in relation to the samples and adjust its motion accordingly. Once the gimbal is aligned tangentially to the drum circumference, axis E0 and E1 will control the transducers' angle of incidence in relation to the workpiece surface. The use of 2 independent controllable axis to align a TX and RX angles independently is necessary to decide the direction in which the transducer is pointing for defect detection. The defect detection using the RX direction process will be explained in detail in Section 6.5.

The prototype gimbal was designed to be hanging from a boom as annotated in Figure 134. In the ILW vault scenario, this boom will be the slit tube boom deployed by the passive robot described in Section 4.6.3.

Initially, a KUKA robot manipulator arm was planned to simulate the movement of the passive ILW inspection robot described in Section 4.6, but that was not possible at the time of experimentation due to access limitations to the KUKA robots. Consequently, an alternative standalone gimbal (Figure 136) was created to accommodate the extra axis required from the robot to align the angle control gimbal mechanism to the sample. This also required rotating the entire setup to allow it to sit on a bench, instead of hang from a moving mount (robot arm), while maintaining the software alignment algorithm.

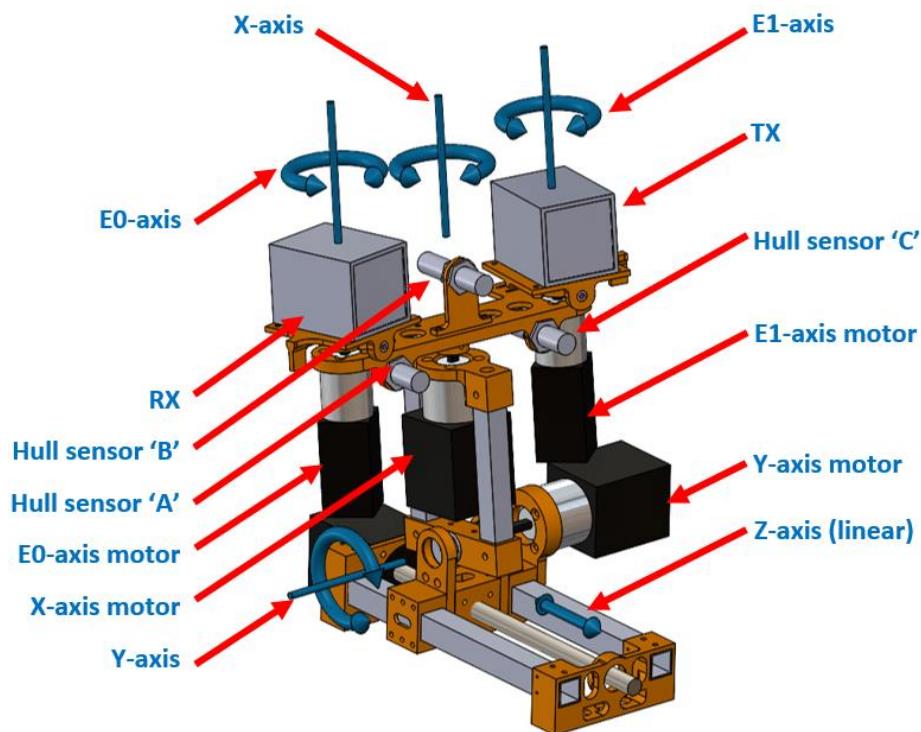


Figure 136: CAD of the gimbal mechanism created to compensate for the missing axis required to align and control the ultrasonic transducers TX and RX angles to achieve the desired Lamb wave refraction and detection.

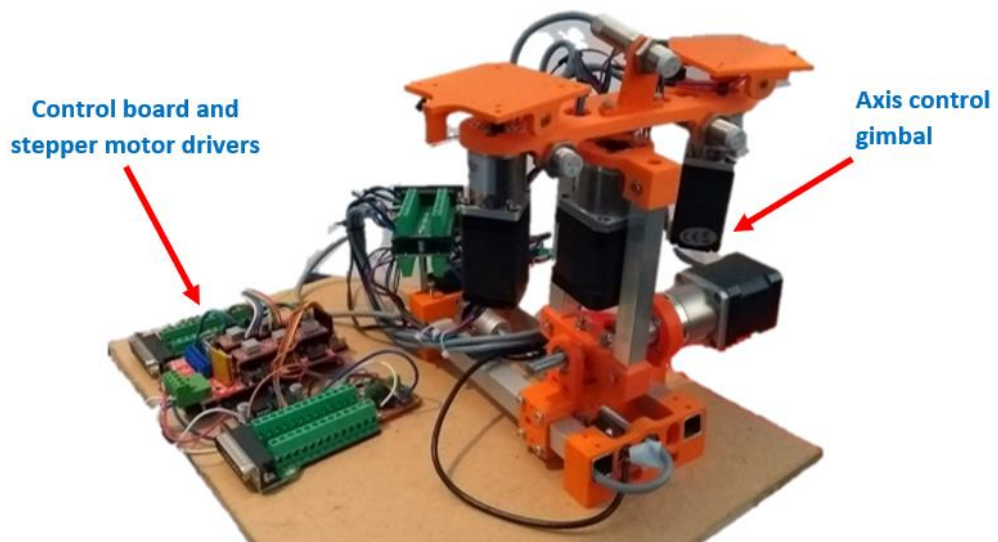


Figure 137: Gimbal mechanism created to compensate for the missing axis required to align and control the air-coupled transducers TX and RX angles to achieve the desired Lamb wave refraction and detection.

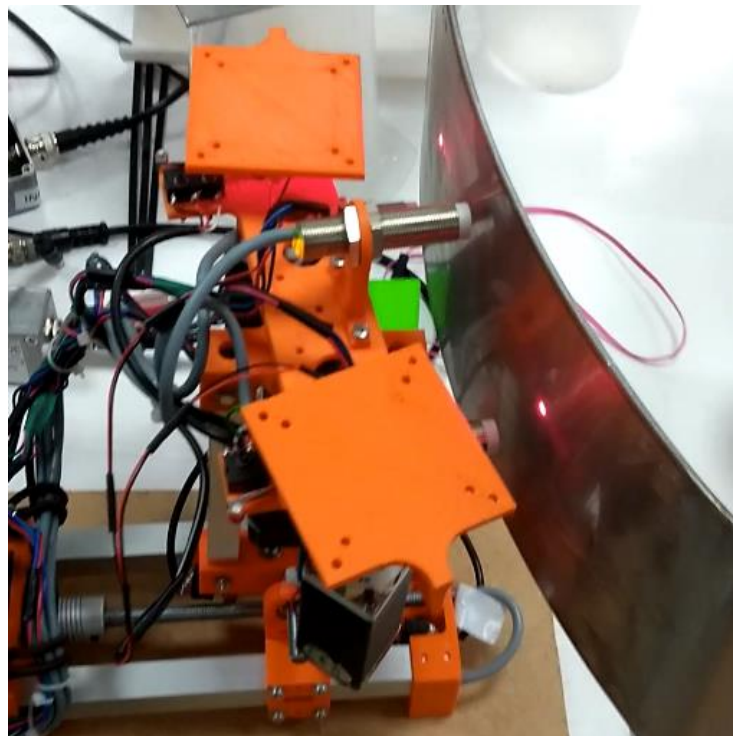


Figure 138: Gimbal mechanism aligning the transducer mounts with a cylindrical stainless-steel sample.

The gimbal angle control computer used the stepper motors to align the transduce mount with the sample using the following algorithm,

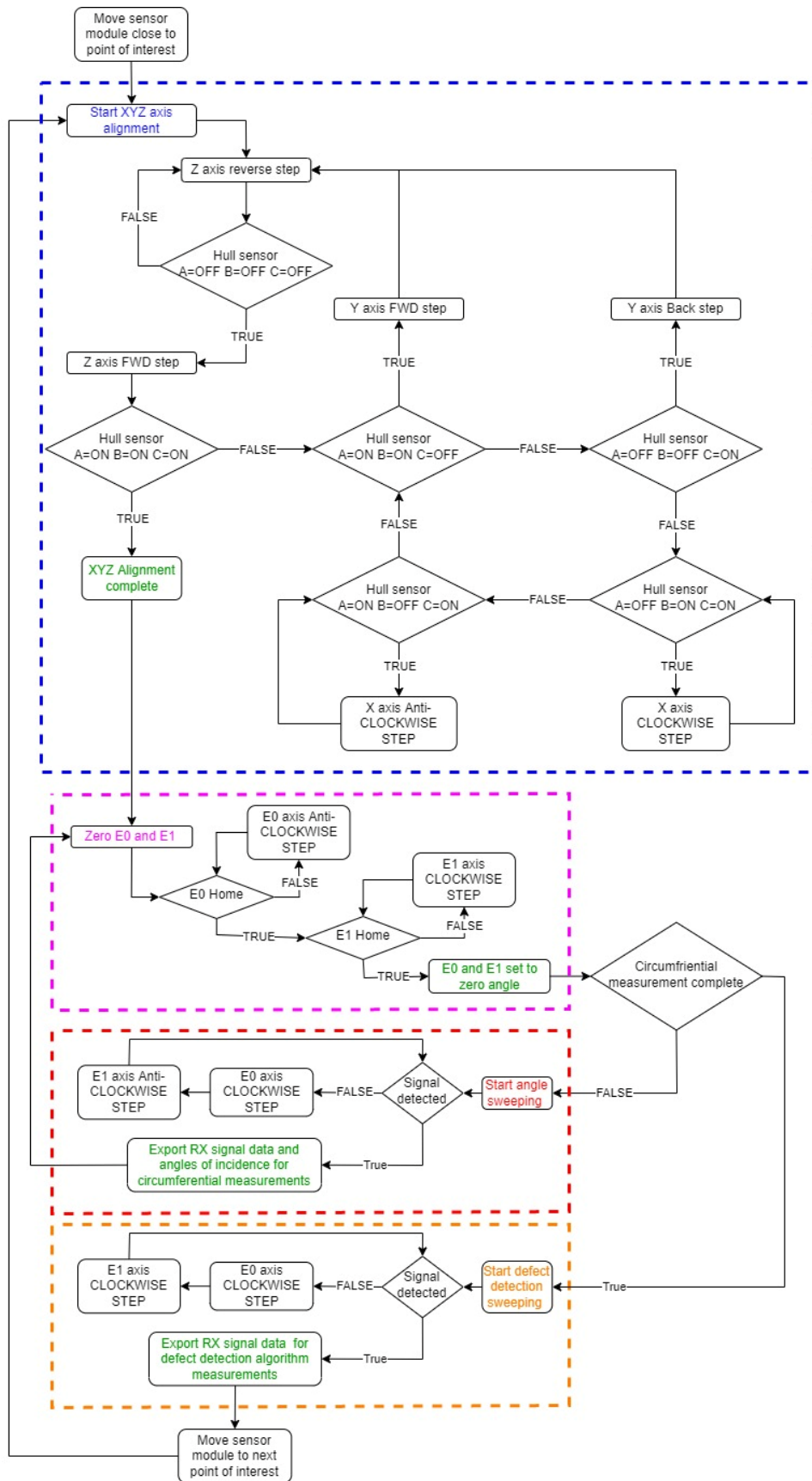


Figure 139: Software algorithm for gimbal alignment.



The algorithm in Figure 139 can be transferred onto the passive robot control by replacing the Z axis from this setup with the linear axis 'B' of the passive robot described in Figure 81. The only difference between the "start angle sweep" and "start defect detection sweep" is that direction of the E0 and E1 motors sweep angle. In "start angle sweep" section the E0 and E1 will move the transducers to aim towards each other, and in "start defect detection sweep" the transducers move in the same direction (parallel to each other). This difference is necessary for the defect scenario identification process which will be described in detail in Section 6.5.

Currently the signal validity assessment (Signal detected) used in both "start angle sweep" and "start defect detection sweep" is judged manually by the operator. To automate this stage of the process, an integrable signal detection oscilloscope will be required to pass on the detected signal to a programable computer to validate and assess the validity and quality of the detected signal in real-time and be able to communicate with robot and gimbal to adjust the E0 and E1 automatically to attain the clearest results. Section 6.5 will also describe the theoretical methods in which the signal validation can be assessed, however automating such processes will require a great deal of programming and automation integration beyond the scope of the project. Nevertheless, automating the process must be considered in future work to completely automate the scanning process and minimise human interaction and judgment.

**Note:** The gimbal setup described is for concept illustration and control method validation only and cannot be used in industrial nuclear operation scenarios without major modifications to meet the nuclear industry operational, electrical, and structural standards and requirements of the facility it needs to operate in. Thus, accuracy and reliability of the system will change with the design changes required to meet industrial standards and the control. The control algorithm presented in Figure 139 is a top-level representation only and require additional steps to operate in practice.

## 6.3 Signal acquisition optimisation

After establishing the means to deploy the transducers into the positions of interest using the passive robot in Section 4.6 and developing a system to align its angles to the drums' circumferences in Section 6.2, this Section will focus on optimising the acquisition process of the data from the Ultrasonic receiver.

The oscilloscopes used in Section 5.3 and Section 5.5 to validate and optimise the Lamb wave detections, had a sampling record length of 2500 samples. Setting the oscilloscopes to a horizontal time range of 2.5mS and data acquisition averaging of 256 provided a signal which revealed a 3<sup>rd</sup> Lamb wave detection peak, after the post processing using the MATLAB filtering algorithms described in Section 5.3. This meant that the after a certain point, the Lamb waves can be masked by the signal noise and signal filtering is required to detect any more detection peaks after that point.

To achieve better signal filtering and acquisition, an **Agilent Infiniium MS08104A** oscilloscope capable generating a sampling record length of 50000 was acquired. The MS08104A oscilloscope has a sampling rate **4 Mega samples per second** and a reading averaging of up to **6400000**.

### 6.3.1 Signal averaging and data acquisition time

To test the new oscilloscope ability in acquiring and filtering the signals from the RX amplifier, an experiment was performed using the setup configuration used in Figure 111, and Sample 3 from Section 5.5 Figure 124 was used as the work piece. The TX and RX were placed 500 mm arc length apart to avoid air wash and aliasing between the trigger pulse and the 1<sup>st</sup> detection peaks observed in Section 5.2.2. The oscilloscope time scale was set to **1 mS** (10 mS detection span), and scans of the sample were performed while incrementally increasing acquisition digital averaging for noise filtration. The MS08104A digital default averaging increases exponentially in multiples of 4 from 16 to 6400000. The oscilloscope allowed the averaging process to be paused, and the readings saved at any point of the averaging cycle.

Readings were acquired using the digital default averaging of 16, 64, 256, 1024, 4086, and incomplete averaging cycles paused at 2000, 3000, and 5000.

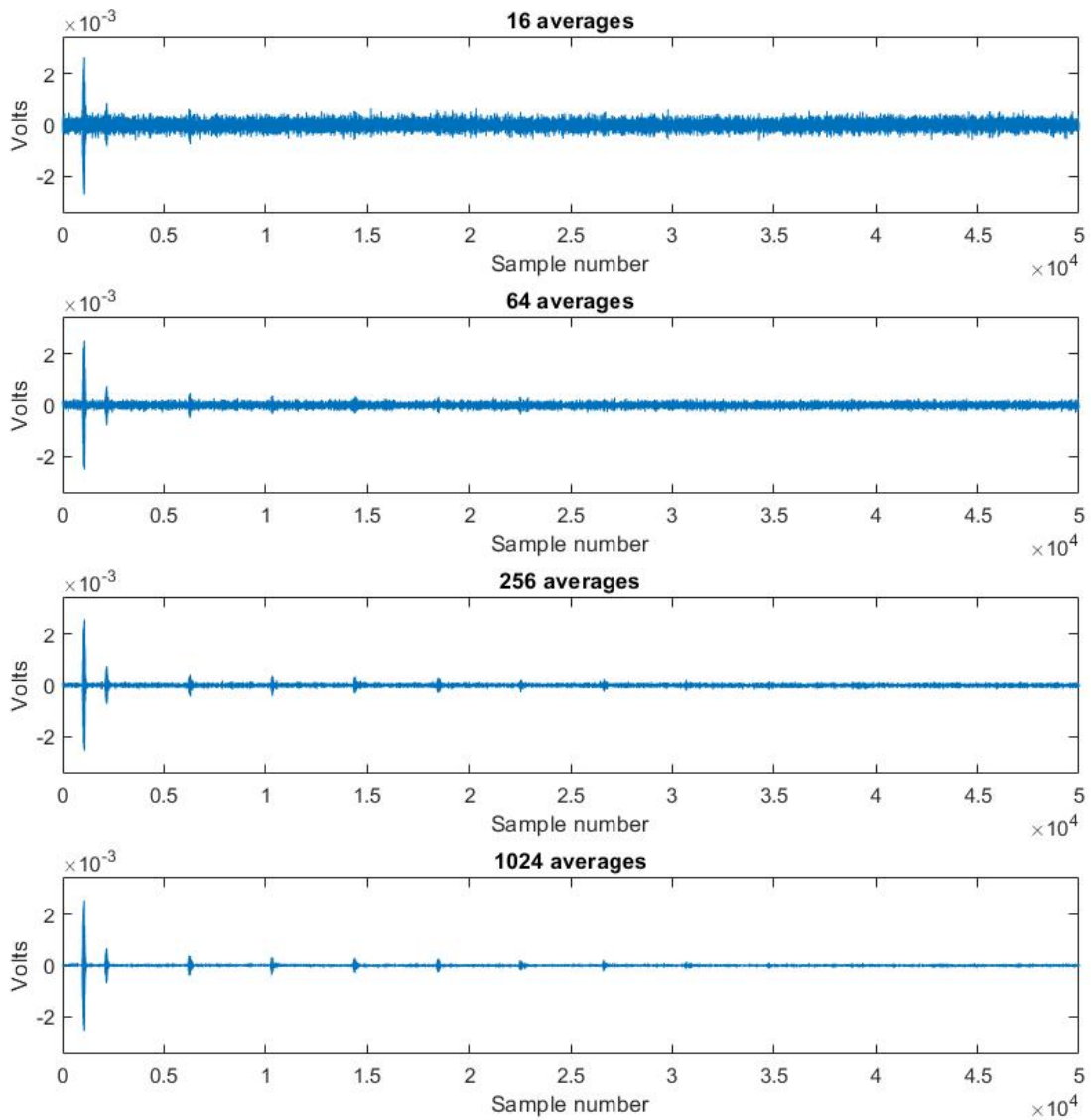


Figure 140: Effects of oscilloscope averaging of 16, 64, 256 and 1024 on the SNR of amplified Lamb waves detected by the RX off an 800 mm diameter 2.5 mm thick 316 stainless steel circular sample.

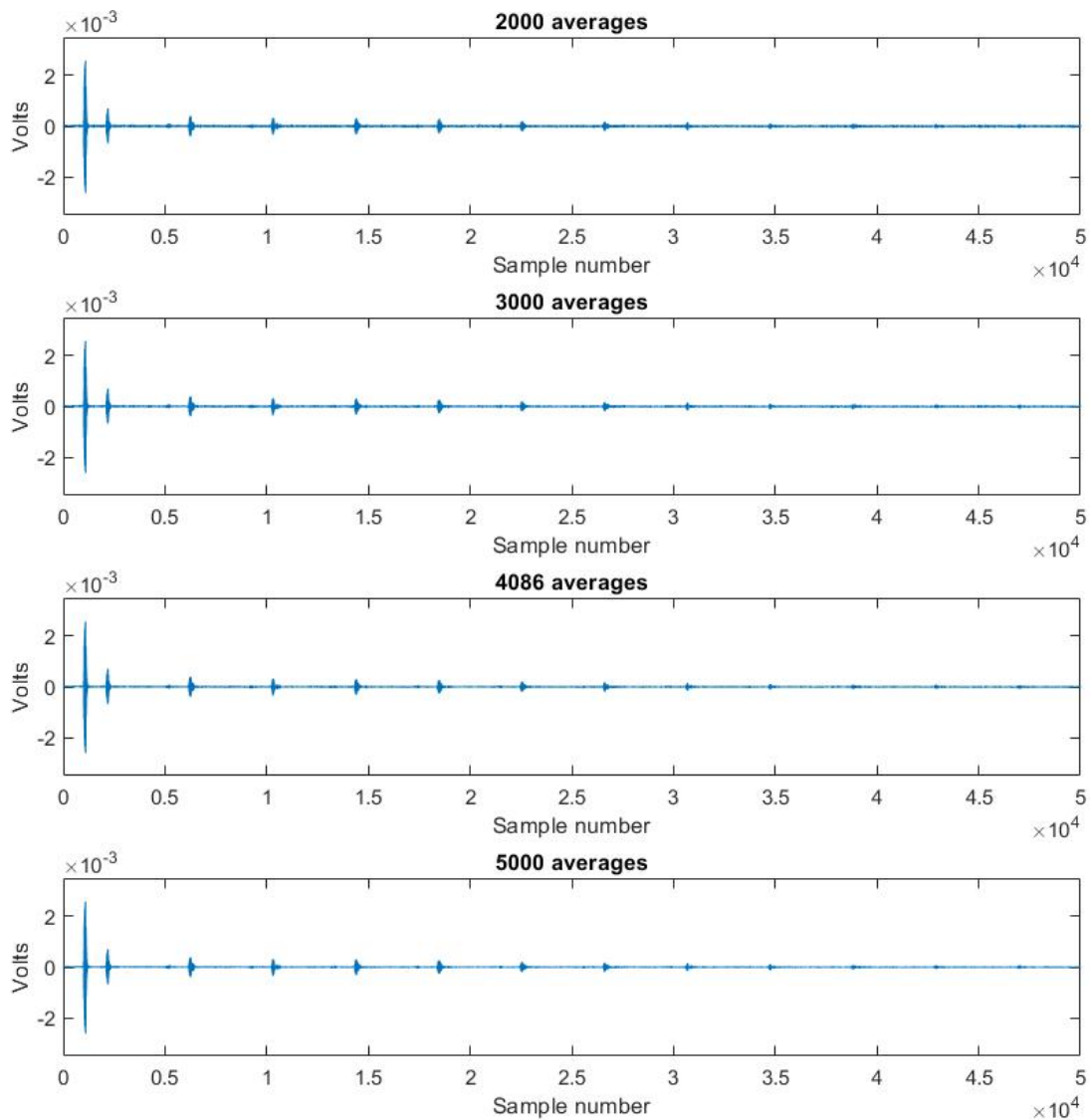


Figure 141: Effects of oscilloscope averaging of 2000, 3000, 4086 and 5000 on the SNR of amplified Lamb waves detected by the RX off an 800 mm diameter 2.5 mm thick 316 stainless steel circular sample.

Figure 140 and Figure 141 show how the signal clarity increases, and noise is reduced as the number of digital averaging is increased. The higher sample length of 50000 alone was enough to detect 7 different peaks at 256 averaging without post processing, compared to the 2 peaks detected at 2500 sample length from the previous oscilloscope.

The SNR of each reading compared to the 5000 averages were compared for a quantitative comparison using the MATLAB SNR function,

```
SNR_vs_5000avgb = snr(raw_signal(:),raw_signal_500avg(:));
```

Oscilloscope sample averages	Acquisition time (s)	SNR of reading vs 5000 averages reading (dB)
16	0.16	6.828
64	0.64	2.756
256	2.56	1.047
1024	10.24	0.242
2000	20.00	0.138
3000	30.00	0.076
4086	40.86	0.035
5000	50.00	-

The drop in SNR was under 0.1 dB after 3000 averages, therefore 3000 averages was recommended for all readings collected using this current setup, because it provides an optimum SNR in relation to the acquisition time. The raw data collected from the 3000 average was enveloped and its peaks' locations identified using MATLAB as previously done in Section 5.2.2 and Section 5.3 (The low pass filters used in Section 5.3 were not used in the following instances).

```
envelope_line = envelope(abs(raw_signal(:)),150,'peak');
```

```
[peaks_y_coordinate,peaks_x_coordinate] =  
findpeaks(envelope_line,1,'MinPeakHeight',0.00015);
```

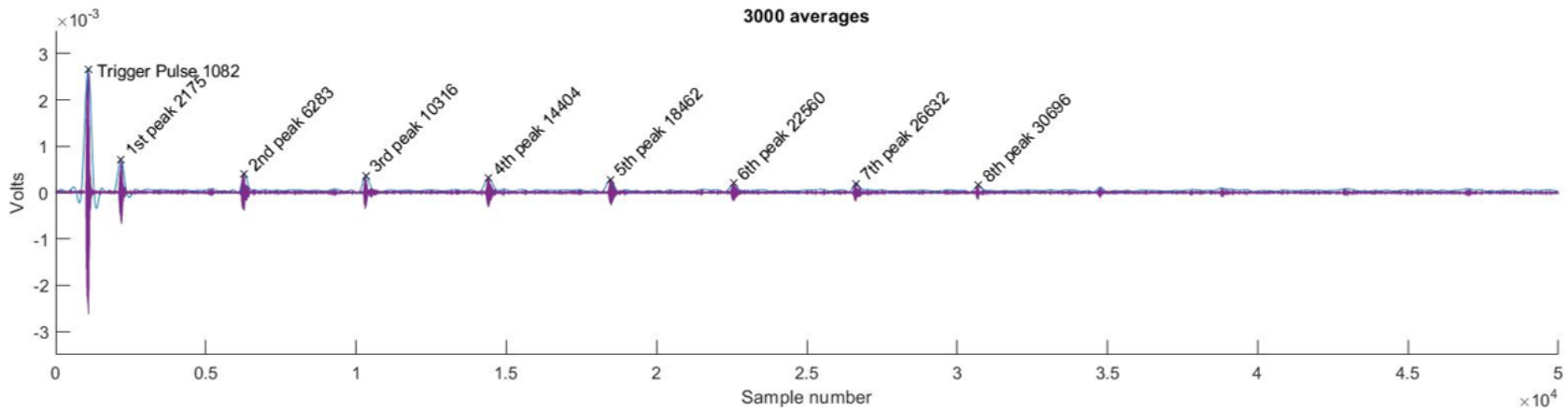


Figure 142: Detection of the Lamb wave for the 8<sup>th</sup> time from the a 3000 averages signal reading.

The MATLAB peak detection algorithm was able to detect the 8 synchronous peaks after the trigger pulse using a peak threshold of 0.00015 and envelope of 150 samples. Figure 143 illustrates the sample numbers of each peak from Figure 142, and the trend line joining the.

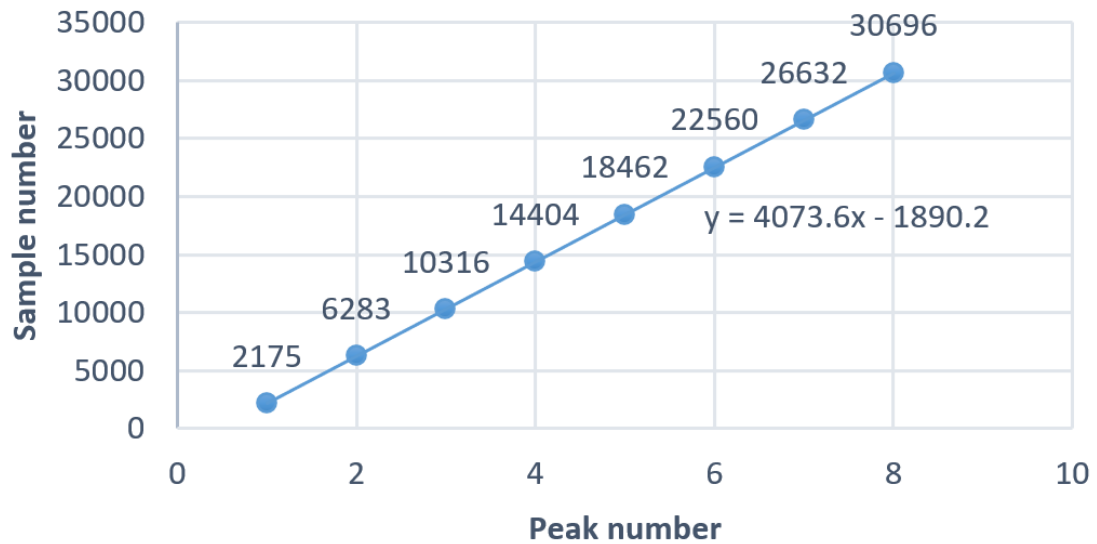


Figure 143: Plot of the peak number against the location peak sample number from Figure 142, and line of best fit that joins all sample numbers.

<b>n</b>	<b><math>(n + 1)_{peak} X coordinate - n_{peak} X coordinate</math></b>	<b><math>T.O.F_{n^{th} Circumference}</math> (mS)</b>	<b>Average from the n=1 and n=2</b>
1	6283 - 2175 = 4108	0.8216	0.8141
2	10316 - 6283 = 4033	0.8066	

The trend line in Figure 143 validates the synchronicity of the peaks and provides an average gradient of 4073.6 samples between the peaks based on the trend line equation from Figure 143. This equates to a difference in  $T.O.F$  between each sample of,

$$\begin{aligned}
 T.O.F_{n^{th} Circumference} &= (\Delta x - \text{coordinates}) \\
 &\times \left( \frac{\text{oscilloscope horizontal scale} \times 10}{\text{samples}} \right) \\
 &= (4073.6) \times \left( \frac{1mS \times 10}{50000} \right) = 0.8145 \text{ ms} \quad \text{Equation 48}
 \end{aligned}$$

The average  $T.O.F_{Circumference}$  from n=1 and n=2 only is 814 ms compared to the 817 ms result acquired from the same number of  $T.O.F_{Circumference}$  in Section 5.5, and the overall average from all 7  $T.O.F_{Circumference}$  was 0.8145 ms based on Figure 143 and Equation 51.

### 6.3.2 Aliasing

When the peak detection threshold used in Figure 142 was reduced to 0.000075, further synchronous peaks (approximately 4074 samples apart) beyond the 8 detected in Figure 142 were observed.



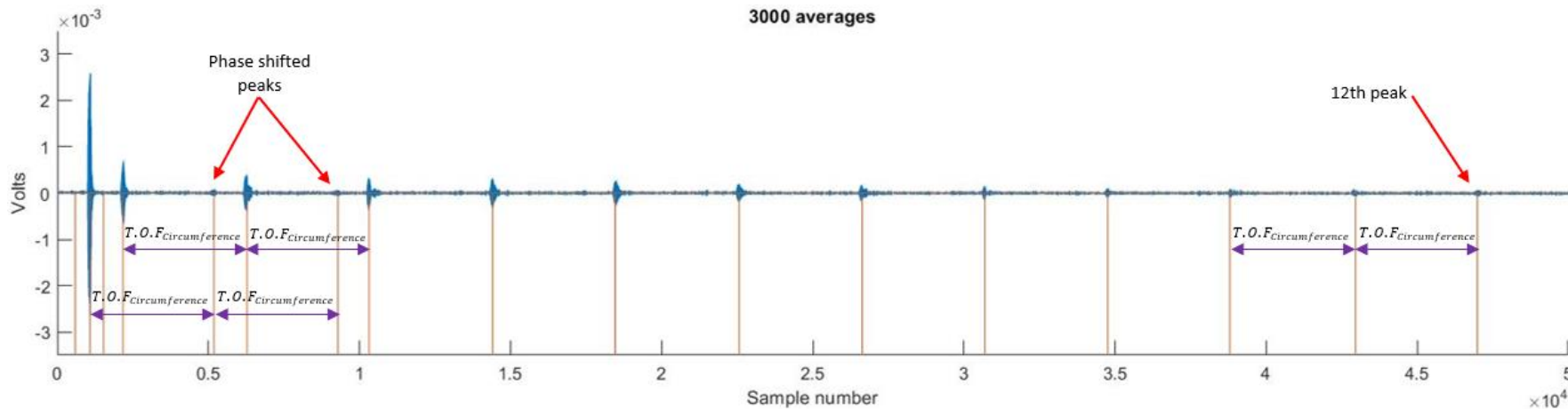


Figure 144: Detection of the Lamb wave for the 12<sup>th</sup> time from the a 3000 averages signal reading, and the observation of phases shifted synchronous peaks near the start of the signal.

Figure 144 shows the 12<sup>th</sup> peak in the pattern being detected indicating that the guided waves have enough energy to travel around the drum at least 11 times. Moreover, the low threshold was also able to detect a phase shifted pattern with the same  $T.O.F_{circumference}$  appearing before the 2<sup>nd</sup> and 3<sup>rd</sup> main peaks as seen on the left of Figure 144. This phase shifted pattern was more prominent at 4086 averages reading and appeared enough times to show synchronicity with a time period that matches the initial guided A0 wave.

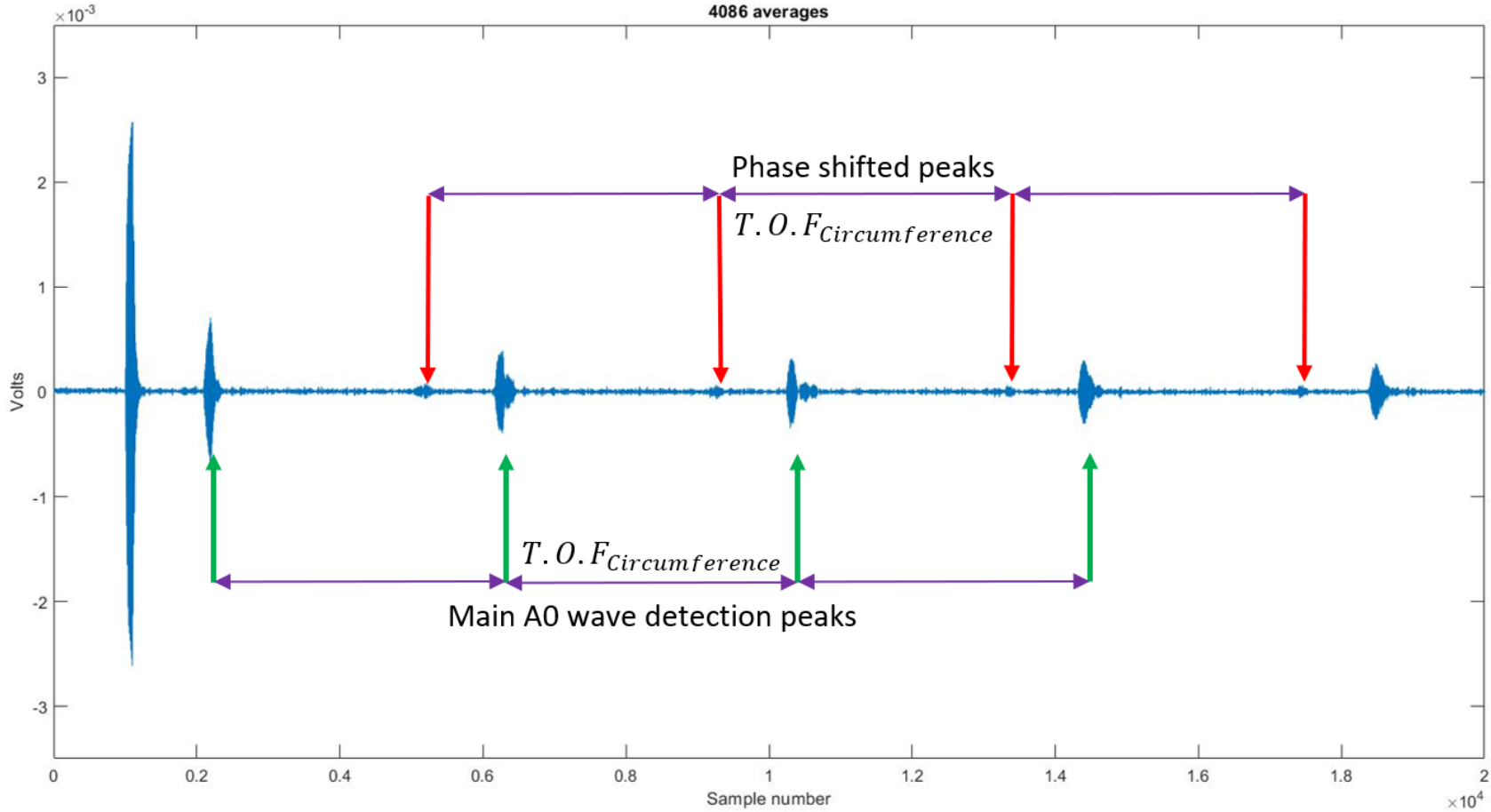


Figure 145: Small phase shifted peaks with  $T.O.F_{Circumference}$  synchronicity near the initial Lamb wave detection peaks in the 4068 averages reading.

Based on the dispersion curves in Figure 109, all the wave modes possible at the 0.5 MHz which the ultrasonic transmitter was operating at during experiment, occurred at angles of incidence below 3 °. This eliminates the possibility of a different wave mode being generated and detected at the 8.15 ° angle of incidence used during the experiment.

If the phased shifted peaks were a result of a defect in the workpiece, a reflected Lamb wave would be detectable when the RX is set at 171.15 °. However, no Lamb waves were detectable when the test was repeated with the RX set to 171.15. The theory behind this argument will be explained in detail and validated in Section 6.5.

The last possibility is that these small peaks are aliases caused by remaining energy from the previous wave still travelling around the drum circumference beyond the 11<sup>th</sup> time, being detected during the current wave detection window. Signal aliases can be misidentified peaks or wave forms caused by the sampling rate of the oscilloscope.

In this instance, the oscilloscope sampling period is triggered by excitation burst from the ultrasonic transmitter. Once the oscilloscope sampling is triggered by the excitation burst, it will record data for the length of the sampling period. Once a second excitation burst is detected by the oscilloscope, a new sampling period will be started, and a new set of wave peaks will be detected by the oscilloscope.

If the sampling period is shorter than the time it takes a wave travelling around the drum to decay to an undetectable amplitude, the peaks that occurred after the sampling period end will not be detected by the oscilloscope.

If a second excitation burst happens before the wave travelling around the drum from the first excitation burst decays to an undetectable amplitude, a second set of wave peaks will be generated by the second excitation which will travel around the drum along with the waves from the first burst. The second burst would also trigger the oscilloscope sampling period which will detect both sets of waves indiscriminately. Thus, the remnants of wave peaks from the first excitation burst would be considered as aliases (false reading) in the second sampling

period because they can be misidentified as wave peaks from the second excitation burst in the second sample period.

This effect can skew the oscilloscope average readings because it would be using hundreds of sample periods that have aliased peaks from different wave excitation bursts. To test this theory, the oscilloscope sampling period was extended to 20 ms to view two consecutive excitation bursts that are 10 ms apart and compare the synchronicity of the questionable peaks after the second excitation burst with the peaks from the first excitation burst.

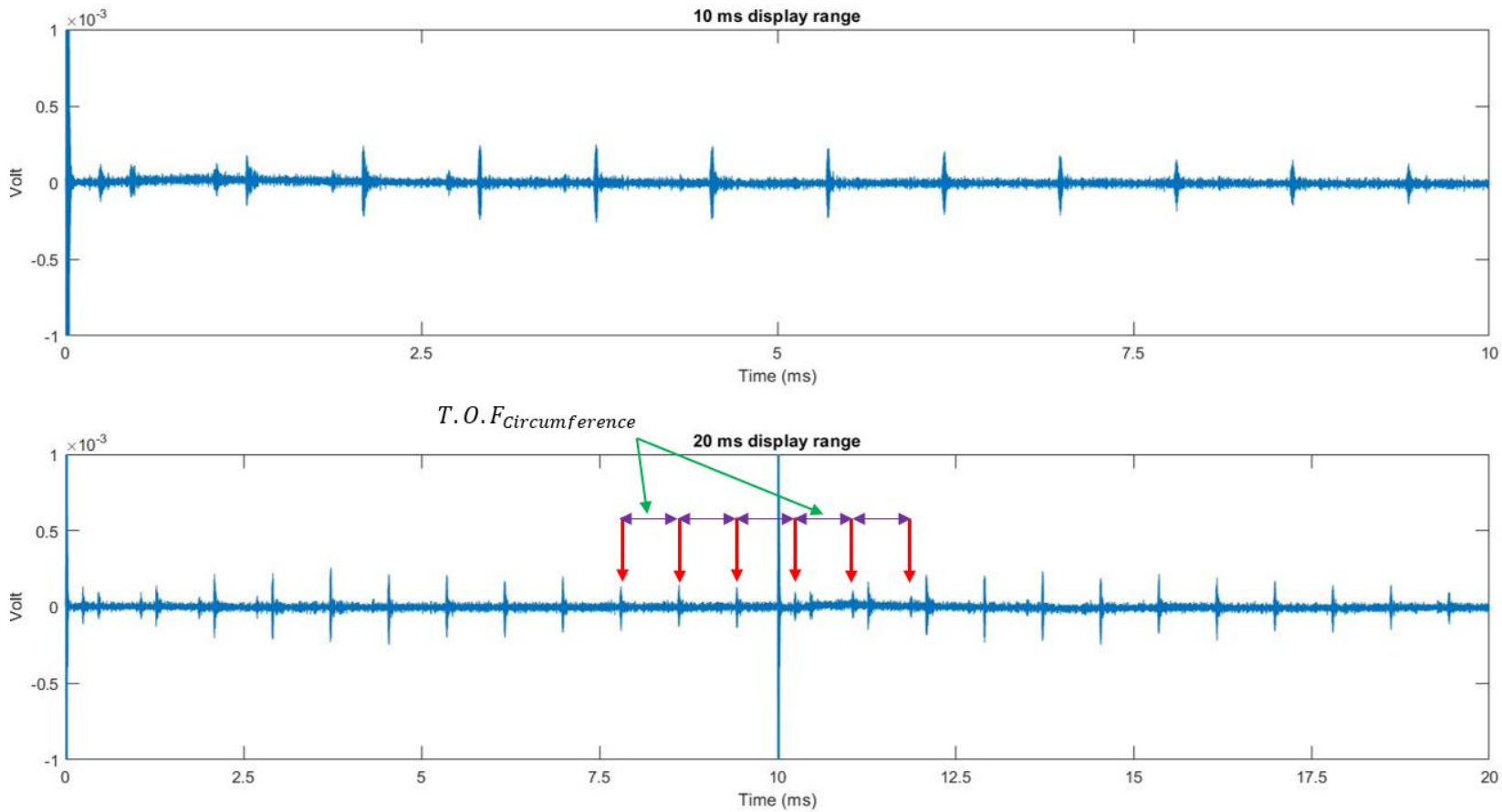


Figure 146: (Top) Lamb wave detection pattern using a 10 ms oscilloscope sampling period and 10 ms excitation burst period. (Bottom) The same Lamb wave detection pattern using a 20 ms oscilloscope sampling period and 10 ms excitation burst period.

Figure 146 (Bottom) demonstrates an oscilloscope sampling period that include two consecutive burst excitations and how the phase shifted waves pattern highlighted in Figure 145 that occurs in the second burst excitation are synchronous with the peaks of the first burst excitation. This indicates that the waves are aliases caused by overlapping of sampling period data.

To validate this finding, an experiment was performed using the same ultrasonic setup and stainless-steel sample as the previous experiment, with different oscilloscope sampling periods and different wave generator excitation burst periods. The burst period is the time between every pulse of waves generated by the frequency generator to transmit a longitudinal wave out of the TX, in this case this refers to the burst of 10 sinusoidal waves generated by the frequency generator as described in Figure 111 which are amplified and turned into a longitudinal waves using the TX piezoelectric element. These 10 sinusoidal wave bursts are also used to trigger the acquisition cycle of the oscilloscope to allow it to start recording the signal from the RX. Therefore, increasing the burst period will increase the time between every Lamb wave generated into the Stainless-steel sample using the TX, as well as increase the waiting time between every signal recording used in the signal averaging process described in Section 6.3.1.

The excitation burst periods were increased incrementally by 10 ms and two sampling periods for each excitation burst was recorded. The first sampling period was equal to the excitation burst and the second sampling period was twice the excitation burst to sample two consecutive excitation bursts as seen in Figure 147.

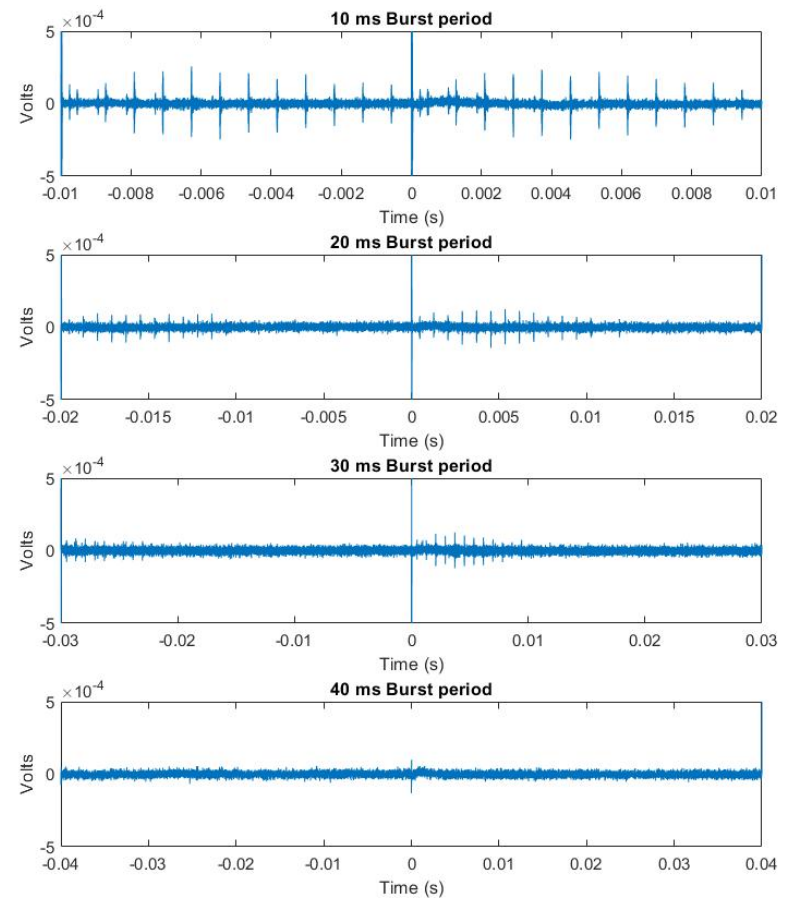
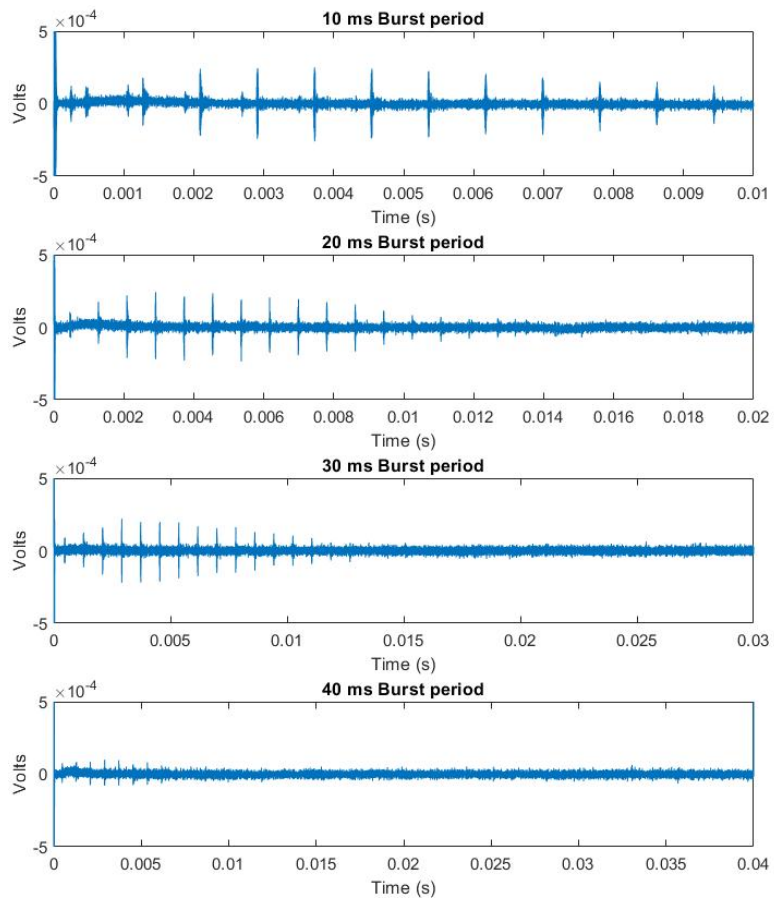


Figure 147: (Left) Lamb wave detection patterns detected while using different excitation burst periods. (Right) Lamb wave detection patterns of two successive excitations using different burst periods.

It was observed in Figure 147 that as the burst period was increased, the wave patterns were pushed apart eliminating the aliasing/overlapping of the detection patterns at the cost of reduced SNR. The experiment was repeated using different wave burst periods and constant sampling period to evaluate the source of the drop in SNR (See Figure 148).

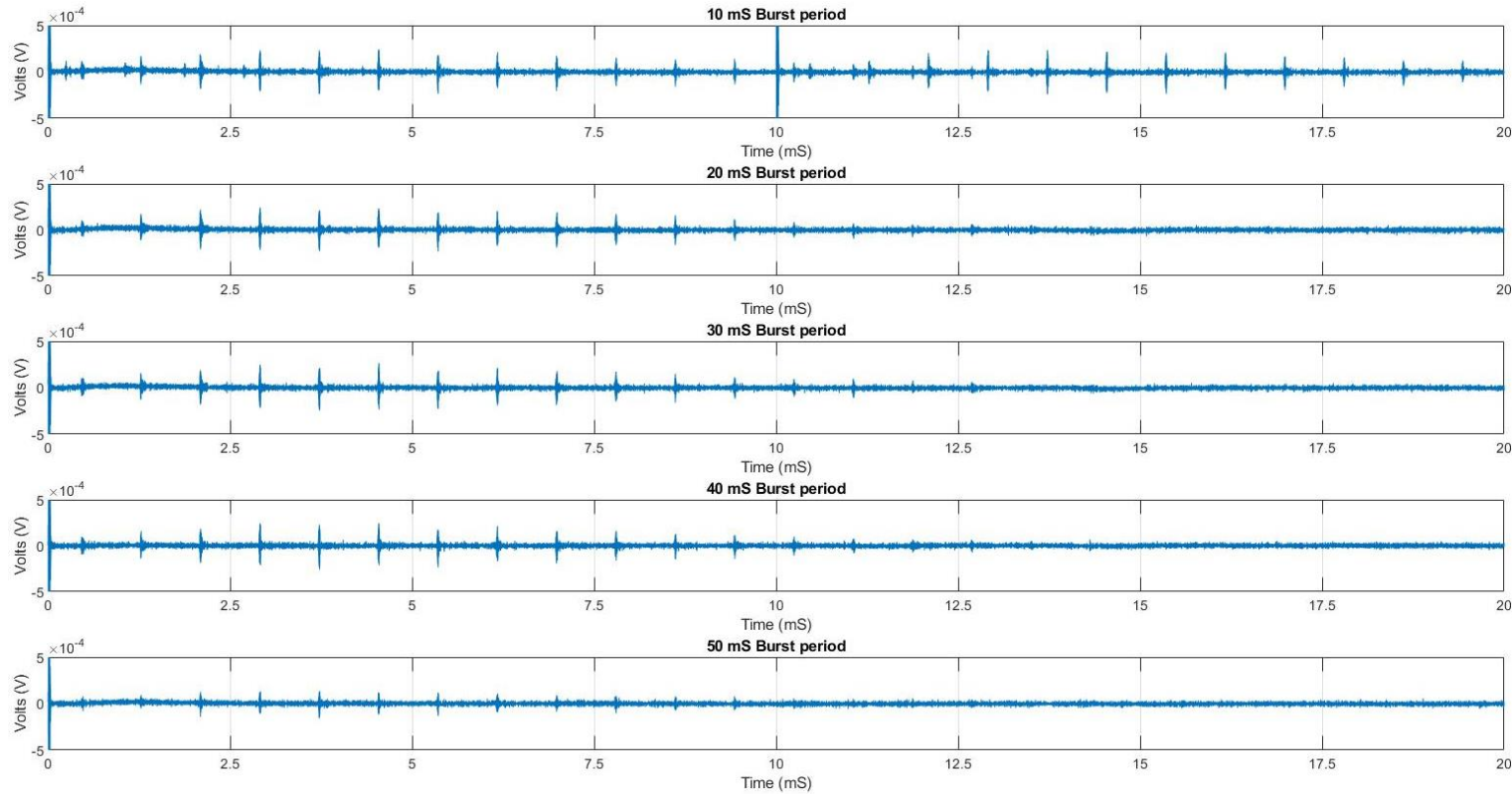


Figure 148: Lamb wave detection patterns acquired using different excitation burst periods and a constant oscilloscope sampling period of 20 ms.



Figure 148 indicates that the SNR falls as the excitation burst period increase.

<b>Excitation burst period (mS)</b>	<b>SNR compared to rigger pulse at 10 mS trigger pulse rate</b>	<b>Acquisition time (s)</b>
10	-	30
20	-2.920	60
30	-2.909	90
40	-3.080	120
50	-7.945	150

Table 4: SNR of the data acquired using an oscilloscope with 20 ms sample and different excitation burst periods relative to the sample acquired using 10 ms excitation burst period.

The SNR in Table 4 is acquired using the following Matlab function,

```
SNR_vs_SNR_10ms = snr(raw_signal),raw_signal_10ms);
```

The fall in SNR in relation to the increase in excitation burst period could be caused by the background noise having more component in the longer time frame needed to create the 3000 averages with the increased time between the acquisition triggers.

Although increasing excitation burst rate from 10 mS to 20 ms removed the aliasing and only reduced the SNR by -2.920 dB, it increased the acquisition time of the 3000 averages from 30 second to 1 minute, because the individual acquisitions of sampling periods are triggered by the excitation burst pulses. Consequently, it can be argued that being aware of the aliasing peaks and developing a system to identify them in the detection patterns, is more beneficial from an efficiency perspective than physically removing them using longer excitation burst periods.

To observe the aliasing peaks magnitude in comparison to the Lamb wave detection peaks , the TX and RX were setup with different distances apart as previously done in Section 5.5 Figure 120.

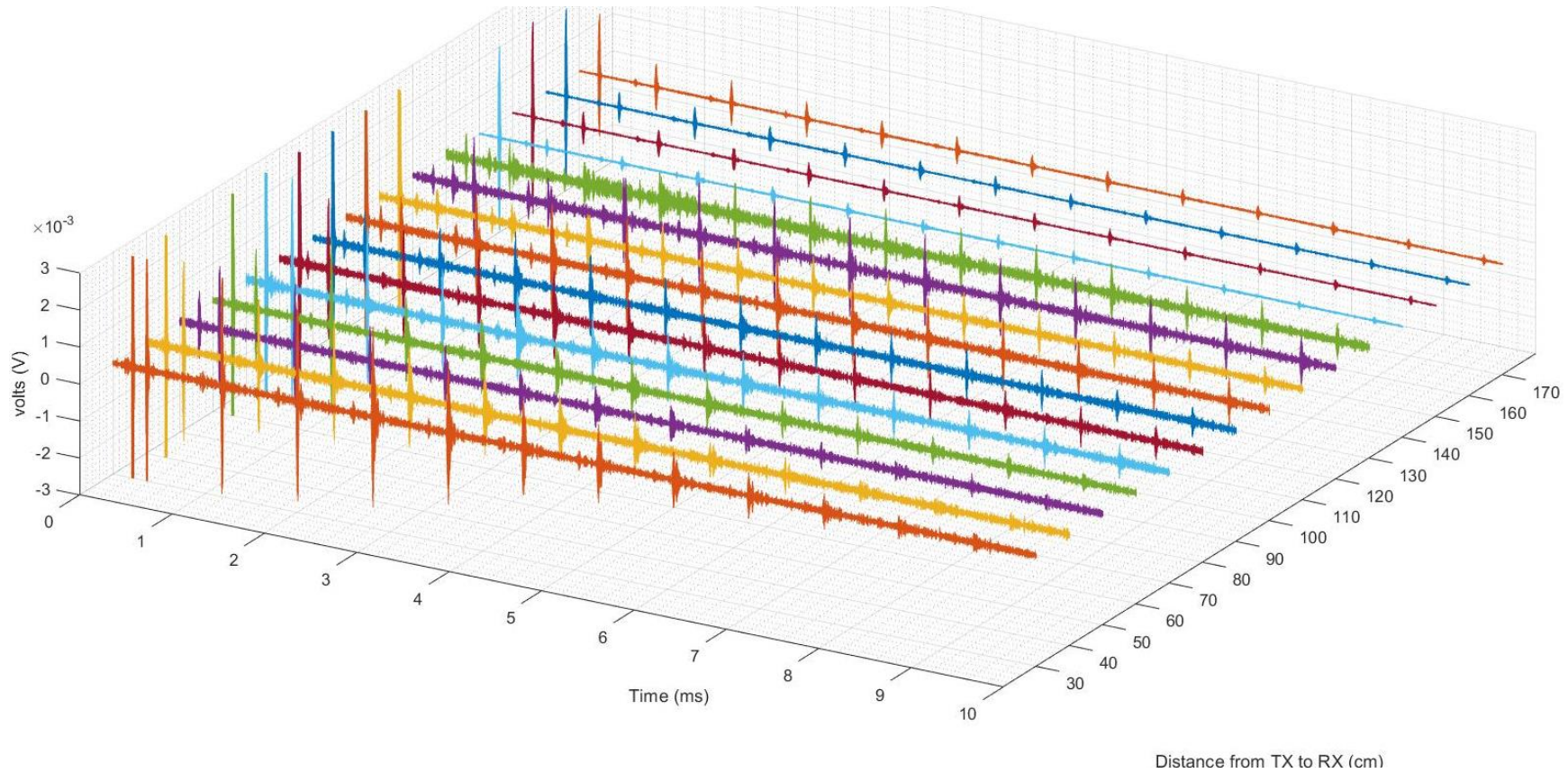


Figure 149: 3D plot of the signals detected (Volts vs Time) at different distances between TX and RX.

To make the relationship between the signals in the 3D plot visually easier to observe, the signals are placed above each other, and their magnitude scaled uniformly in Figure 150.

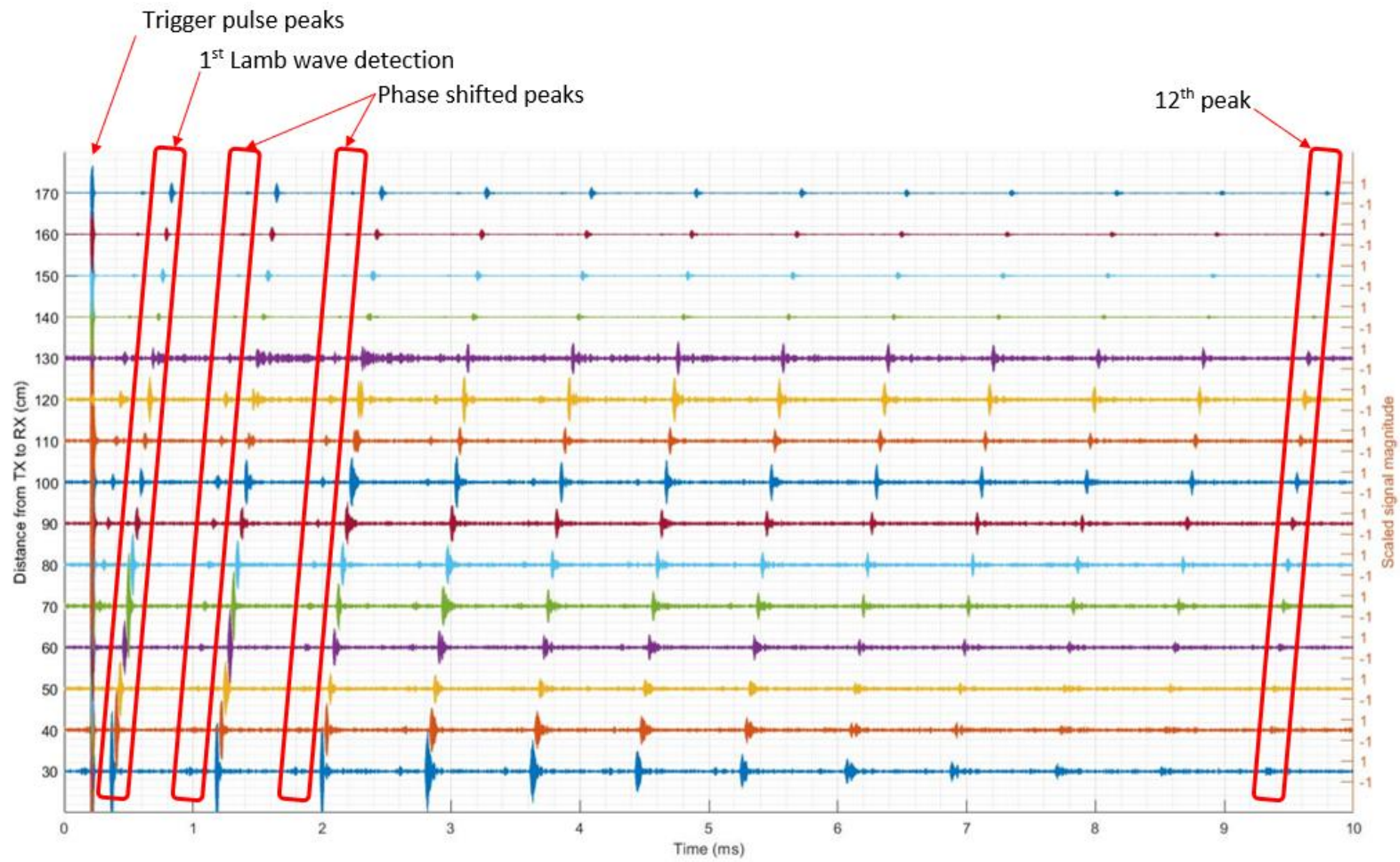


Figure 150: 2D representation of the 3D plot of the signal detected (Volts vs Time) at different distance between the TX incidence point and RX detection point.

Figure 150 highlighted significant inconsistencies in the data acquired, which can complicate the development of an automated system for the aliasing detection. However, it highlighted a number of noise sources that needed to be considered. The inconsistency in the wave amplitudes with TX and RX 1.4 m apart or more compared to the rest of the readings was attributed to the change in cable used to connect the RX to the transimpedance preamplifier from a 0.40 m BNC to a 1.2 m, to allow the RX to reach the far end of the bench. When repeating the measurement under 1.4 m spacing using the longer cable the amplitude dropped as expected, but no aliasing was observed in the readings. Therefore, the data from the shorter cable was used in Figure 150, because it is intended to observe the aliasing and identify it, not remove it.

To quantify the drop in signal amplitude caused by the cables swap, a different control test was performed, where the distance between the TX and RX was kept constant and the cable length change was the only variable. Three standard **50  $\Omega$**  impedance BNC cables with length 40 cm, 120 cm and 300 cm were available to test.

<b>Cable length (cm)</b>	<b>BNC cable sheath resistance (<math>\Omega</math>)</b>	<b>BNC cable inner core resistance (<math>\Omega</math>)</b>
<b>40</b>	0.5	0.5
<b>120</b>	0.7	0.7
<b>300</b>	1.7	0.8

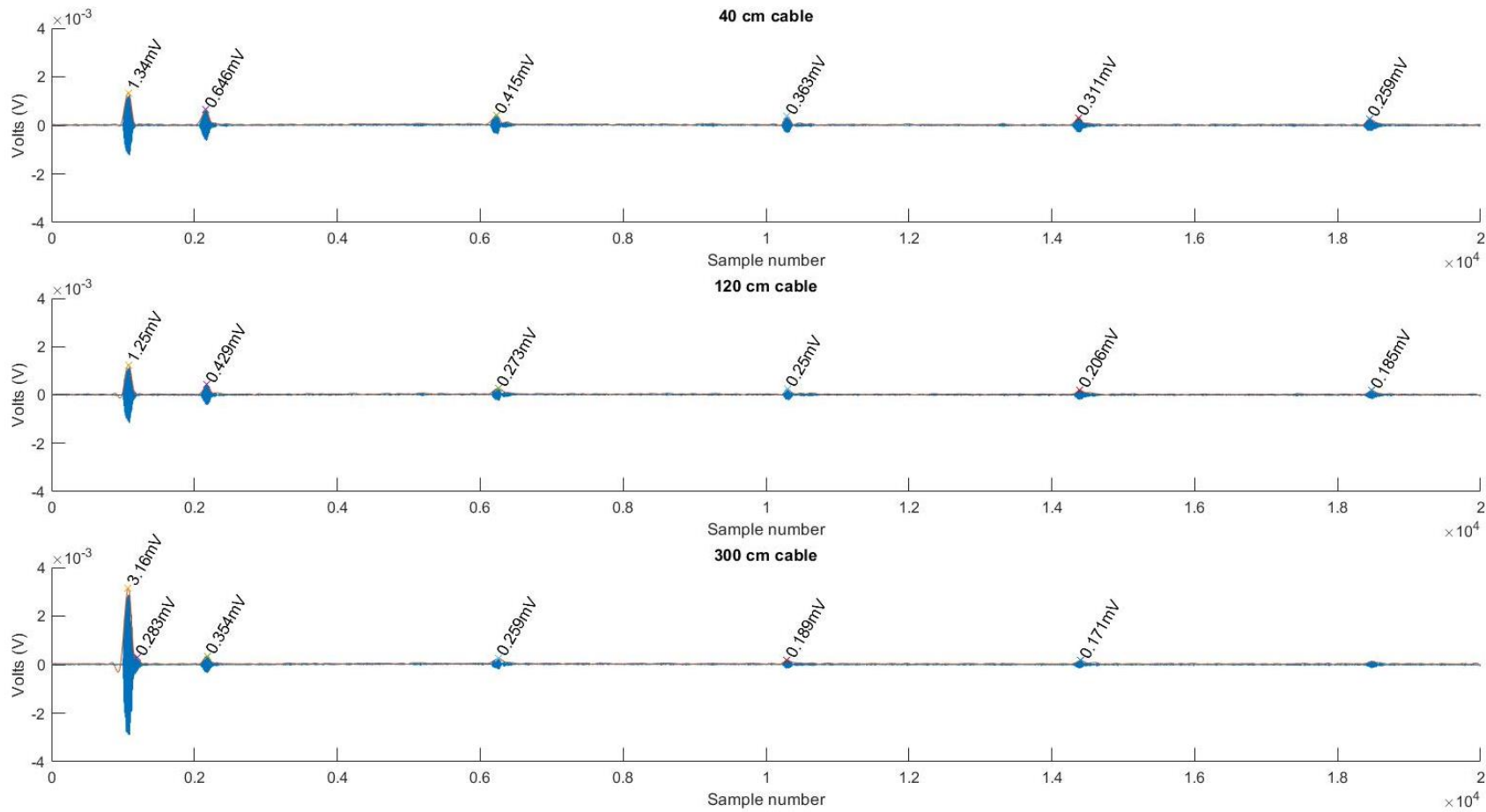


Figure 151: Lamb wave peak detections using different BNC cable length between the RX and the transimpedance amplifier.

Cable length (cm)	Trigger pulse peak (mv)	Lamb wave detection peak amplitude (mV)			
		1 <sup>st</sup> detection	2 <sup>nd</sup> detection	4 <sup>th</sup> detection	3 <sup>rd</sup> detection
40	1.340	0.646	0.415	0.363	0.311
120	1.250	0.429	0.273	0.250	0.206
300	3.160	0.354	0.259	0.189	0.171

During the test the neither the sample nor the RX and TX were allowed to move during the cable swap. Therefore, the amplitude drops in the Lamb wave signals detected is a direct result of the change in cable length only. This proved that even though all three cables were rated at 50  $\Omega$  impedance, their resistance and length had an effect on the signal amplitude and SNR.

The test also showed a significant increase in the amplitude of the trigger pulse in the 300 cm cable, indicating that it was more susceptible to radiated electromagnetic interference (EMI) from the TX trigger pulse described in Section 5.2.2.

### 6.3.3 Noise and Electromagnetic interference

To test the cables and RX amplifiers susceptibility to the TX trigger pulse EMI, the RX and its signal amplification components were laid out in different direction relative to the TX signal amplification components as shown in Figure 152.

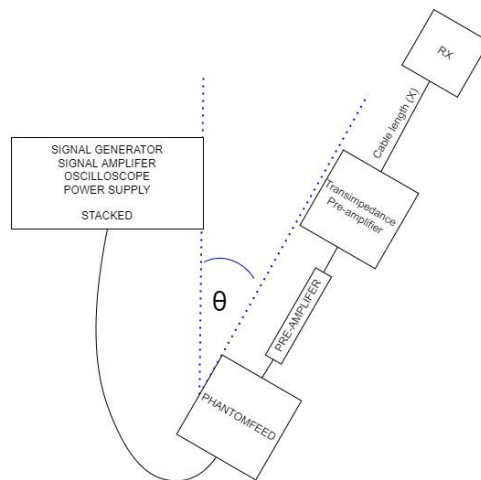


Figure 152: Top view of equipment layout on the experiment bench (components sizes and spacing not to scale)

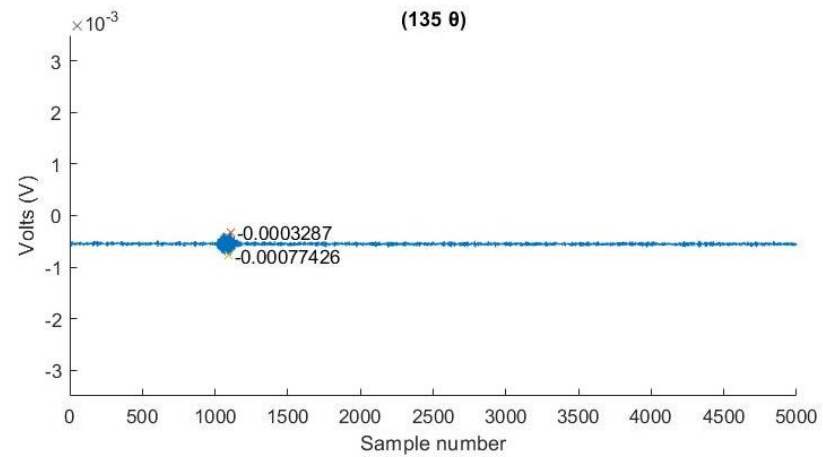
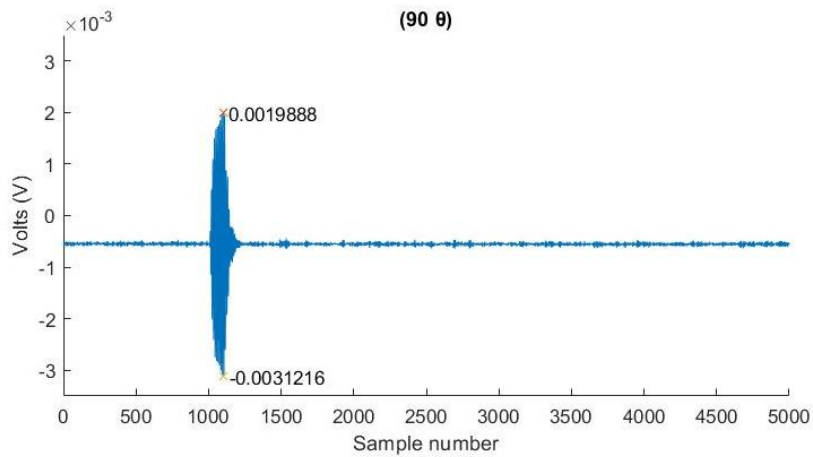
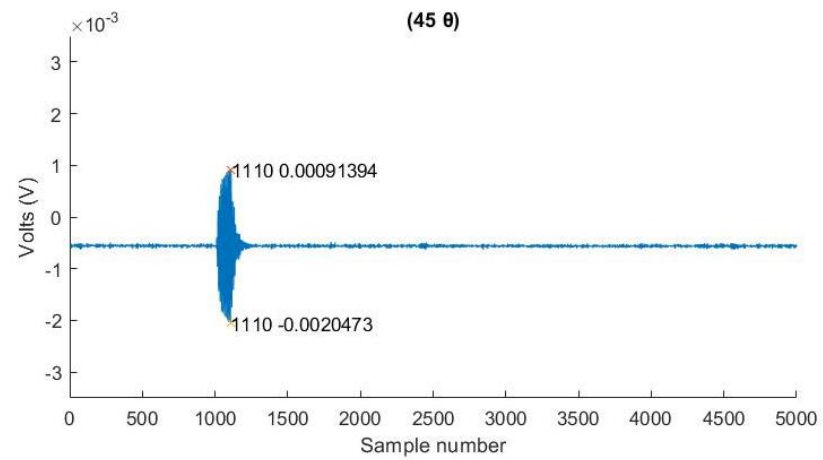
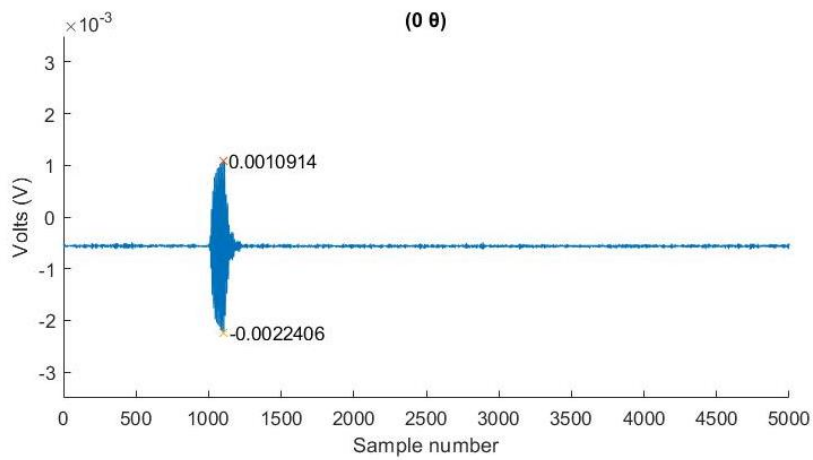


Figure 153: Trigger pulse EMI with the RX and RX signal amplification components placed in different angle to the TX signal amplification components.

<b>Angle (<math>\theta</math>)</b>	<b>Mean Peak to peak (mV)</b>	<b>Standard deviation of average volt (<math>\mu</math>V)</b>	<b>Mean average volt (<math>\mu</math>V)</b>
<b>0 (Parallel)</b>	3.352	3.68	569.5
<b>45 (CW)</b>	3.011	5.49	559.7
<b>90 (Perpendicular)</b>	5.150	2.43	559.6
<b>135 (CW)</b>	0.542	1.71	552.9

The variations in the trigger pulse interference detection amplitude “Mean Peak to peak (mV)” and the deviation in the background noise average voltage “Standard deviation of average volt ( $\mu$ V)” in relation to the angle in which the equipment is laid out at, proves that aside from power losses in the cables, radiated EMI had a significant role in the signal quality and amplitude. The susceptibility of the equipment to radiated EMI is likely a factor of the sensitivity of the equipment themselves, combined with the number of EMI sources in the environment in which the experiments were conducted [137]. It is very difficult to identify all the sources of EMI in a given location [138] outside an EMI isolated chamber, but the number and effect of EMI sources can be estimated using statistical methods such as Higher Order Statistics [138].

Therefore, any equipment used in future work and the final inspection system, must be electromagnetically shielded, and calibrated to the background EMI of the location it is operating in before every scan, to minimise the EMI in the readings. This will be particularly critical if the wave generation and receiver signal amplification equipment are too large to fit close to the transducers in the gaps between the stillages and have to be place on board the robot chassis or outside the vaults. If the signal generation and amplification equipment are placed far from the ultrasonic transducers and connected to the transducers using long cables, the increase in the cable length will increase the likelihood of parts of it to be exposed to EMI.



### 6.3.4 Optimisation summary

In summary, digital filtering and processing of the transducers signal can provide a tool to increase the SNR significantly, to observe the Lamb wave detection patterns created when the Lamb waves travel around the drum multiple times. The importance of detecting these patterns will be explained in Section 6.5, where the patterns will be used to validate and identify defect scenarios.

The use of signal acquisition averaging can greatly enhance the SNR from the transducers at the cost of time. In this project, 3000 averages have been chosen as the optimal sample acquisition averaging value for the equipment and setup used. This however will differ when using other equipment or operational environments because of the differences in equipment sensitivity, SNR, and background noises in different environments.

The excitation burst period used to create the Lamb waves can cause signal aliasing effect if the detected wave patterns from different excitation bursts interfere. This aliasing can be eliminated by increasing the burst periods to allow the Lamb waves to attenuate to an undetectable amplitude between the excitation periods, at the cost of acquisition time and SNR. It is also noted that the long acquisition time caused by increasing the excitation burst periods have reduced the SNR, therefore it is recommended to find means of identifying and digitally filtering out the aliasing signals instead of increasing the burst period and acquisition time.

Due to the sensitivity of the equipment and the magnitude of the detected signal compared to the background noise amplitude, adequate screening and earthing of the equipment is necessary to enhance the SNR. Increasing the RX sensitivity further is not recommended because it will make the RX susceptible to picking up more background noise, however increasing the TX transmission power may allow it to create Lamb waves with higher amplitudes that are easier to detect by the RX.

## 6.4 Cementitious encapsulation effects on Lamb waves propagation.

After establishing a reliable mean of inducing and detecting Lamb waves into and off the 500 L ILW drum and recognising some of the possible anomalies and aliases that would affect the Lamb waves detections readings. This section will focus on practically validating the theoretical effects caused by the encapsulation cement contact with the ILW drums' shell described in Section 5.6.4.

If the expansions and bulges in the drum shells describe in Section 2.7 are indeed happening due to dimensional changes in the drums' contents, these contents would have to apply physical loading onto the internal wall of the drum's shell to push it out in the form of hoop stresses [139]. Therefore, a test was devised to create hoop stresses onto a round stainless-steel using a round cement moulding with composition identical to that used in the immobilisation of ILW, to practically observe the effect of the cement pressure on the Lamb waves propagation.

### 6.4.1 Cementitious contents expansion simulation

Given that the expansion in cement due to moisture or chemical reactions can take tens of years to happen [13], it will not be practical to replicate and control reliably in the lab to physically simulate expansions. Alternatively mechanical expansion can be generated and controlled to replicate the desired effects.

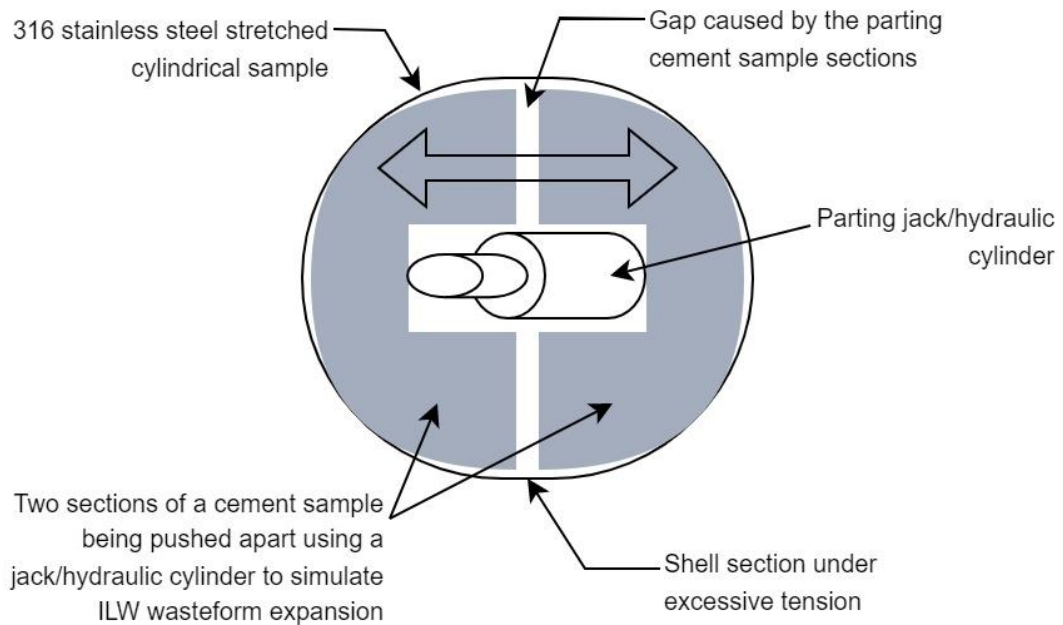


Figure 154: Simulated expansion of immobilisation cement using parting sections.

Creating radial forces mechanically in a circular stainless-steel sample using two or more parting solid sections as per Figure 154 will create gaps where the solids separate. These gaps will not be exposed to the radial force perpendicular to the central axis intended, and instead cause localised tensile forces where sections of the stainless-steel will be pulled apart by the parting sections of the cement moulding. This will create uneven hoop stresses in the shell, because the remaining surfaces in contact with the cement moulding will be held in place by the friction between them and the cement moulding. To overcome this problem and created a uniform hoop stress into the sample shells, the cylindrical stainless-steel test samples used previously used in Section 5.5 were replaced with a tapered sample as per Figure 155.

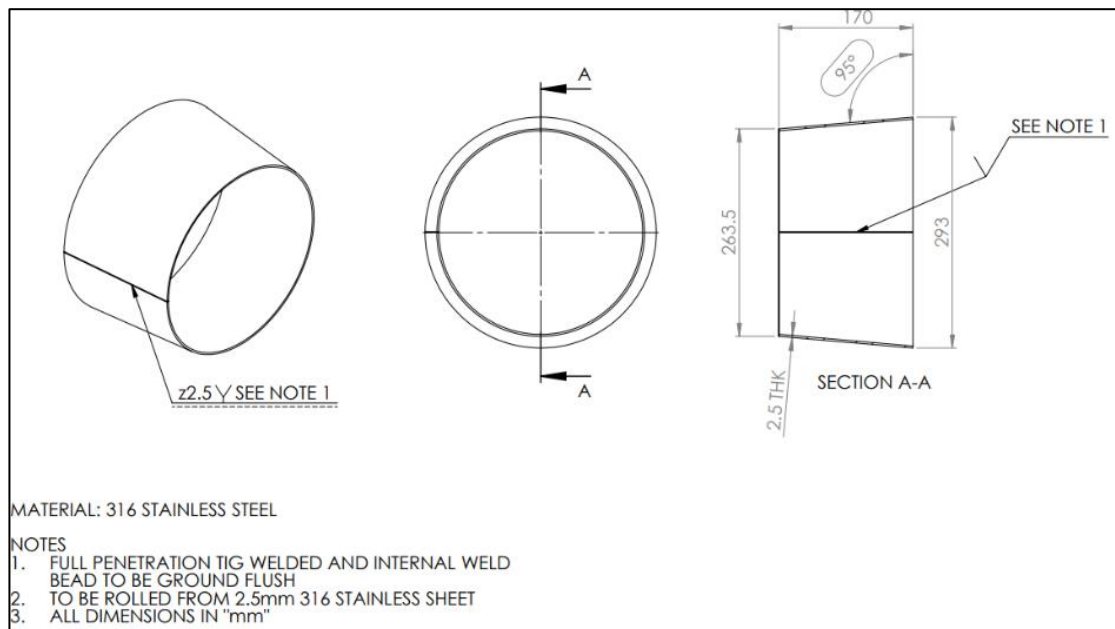


Figure 155: Manufacturing drawing of tapered 316 Stainless-steel sample used to simulate ILW 500 L drum in pressured state.

The tapered stainless-steel sample is designed to enclose a matching tapered cement moulding which will be pressed into it, to convert controllable clamping force into a radial force, by using the cement moulding taper as a wedge. This radial force from the wedge will simulate a uniform pressure build-up inside the stainless-steel sample. A 5 ° taper was chosen to keep the angle as shallow as possible to minimise the transduction losses caused by the workpiece curvature [81] while being steep enough for ease and accuracy of manufacturable.

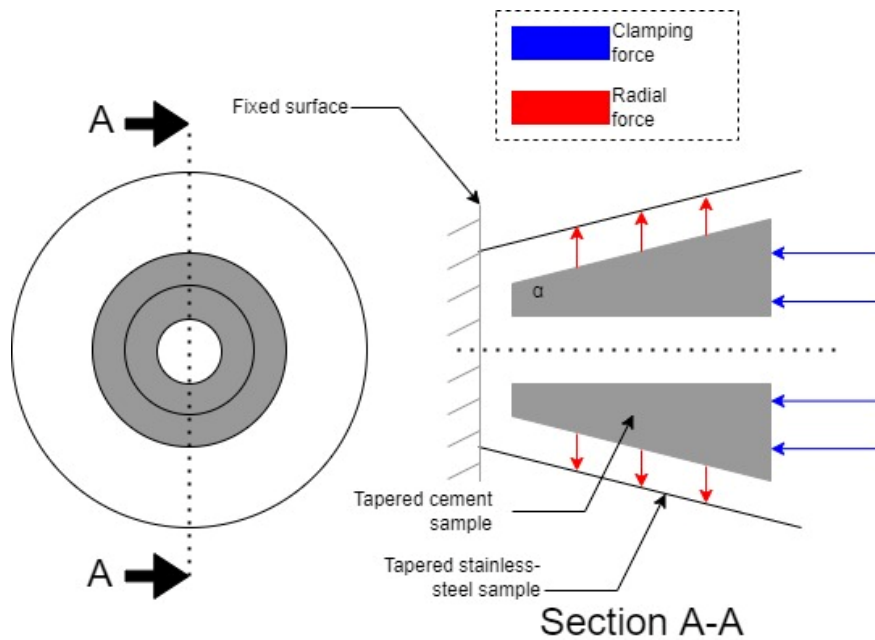


Figure 156: Mechanical clamping force to hoop stress conversion (Taper angle and space between the stainless steel and cement exaggerated for clarity)

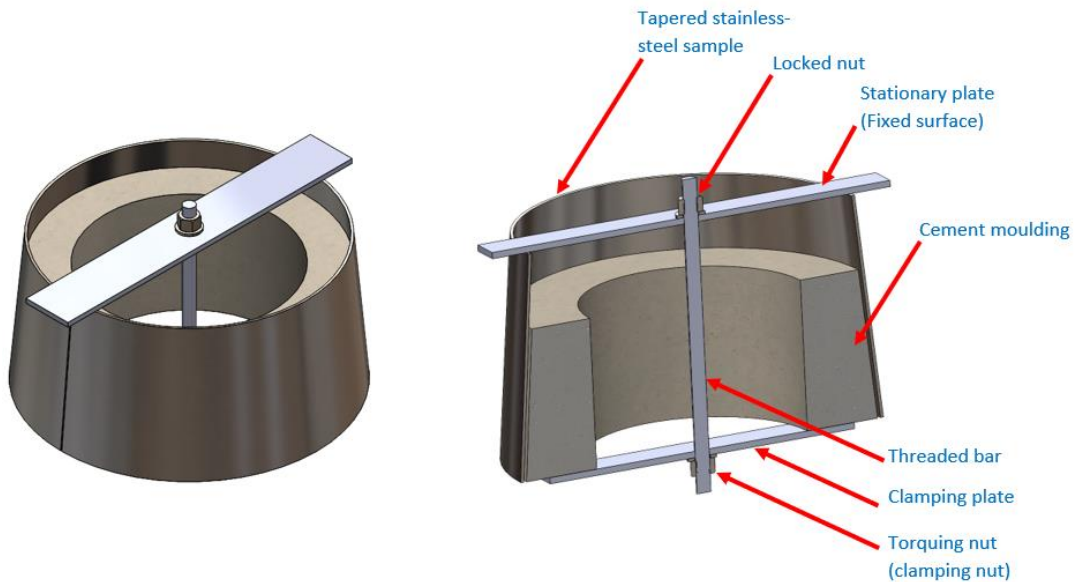


Figure 157: (Left) 3D CAD model of cement moulding being pressed into a Stainless-steel tapered sample using an M12 threaded bar cross section view of the setup. (Right) Cross-sectional view of the clamping arrangement. (The circular disc used for clamping are replaced with a rectangular plate in image for visual clarity)

A pair of steel discs and an M12 threaded bar fastener arrangement were used to press the cement mould into the tapered sample as per Figure 156 to create the clamping force. Torquing the M12 fasteners nut on the threaded bar in a dumbbell arrangement, pushes the clamping plates closer together which in return presses the cement moulding into the stainless-steel sample. The clamping force of the fastener dumbbell arrangement was controlled using a torque meter between the nut and the torquing wrench.

#### 6.4.2 Practical limitations

The tapered stainless-steel sample diameter was limited to a maximum diameter of 300mm due to the limitation in the cement moulding size. To create the tapered cement shape, a 7-piece mould was fabricated and turned in a lathe to achieve the best circularity and taper possible, this limited the mould size to 440 mm to fit in the machine and creating a moulding cavity of 300 mm maximum diameter. This sample diameter compromise caused by using lathe was necessary to minimise potential gaps between the stainless-steel sample and the cement for uniform loading.

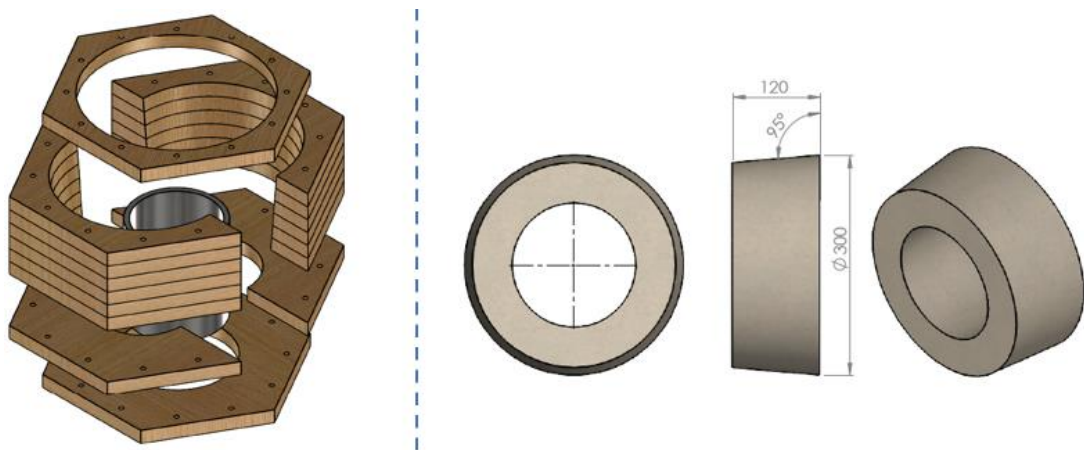


Figure 158: (Left) CAD of 7 piece cement mould designed to be made from wood and machined on a lathe. (Right) Maximum cement moulding size expected from the mould.



Figure 159: 7 piece wooden mould and cement moulding release.

After pouring and releasing the cement moulding, the test equipment was setup as previously done in Section 5.2.2 Figure 111, with the tapered stainless-steel sample as the workpiece and the new Agilent Infinium MS08104A oscilloscope for data acquisition. The tapered stainless-steel sample was manufactured from the same 316 2.5 mm sheets that was used to fabricate the five samples used in Section 5.5 thus the Lamb wave dispersion curve used in 5.2.2 and Section 5.5. will still apply when the sample is empty.

Despite the drop in overall sample diameter from 800 mm to approximately 275 mm (The cross section diameter at the centre of the tapered sample where the waves are expected to be travelling), the behaviour of the wave can still be approximated as if it is travelling in a flat plate, because thickness to outer-radius ratios is still well below 10 % [125] as previously explained in Section 5.2.2.

Consequently, the expected angle of incidence required to refract the A0 Lamb waves into the sample will remain as  $8.15^\circ$  and  $V_{gr} = 3.0834 \text{ m/ms}$  as previously measured in Section 5.5.

The  $8.15^\circ$  wedge described in Section 5.3 Figure 114 was not suitable for aligning the ultrasonic transducers to the tapered sample, because of the tapered sample's varying diameter. Similarly, the angle alignment tool developed in Section 6.2 did not provide the variation in the distances between the TX and RX that would be required to measure the Lamb waves'  $V_{gr}$ . Therefore, a new pair of wedges were 3D printed to align the transducers  $8.15^\circ$  tangential to the sample circumference and parallel to the  $5^\circ$  slanting surface.

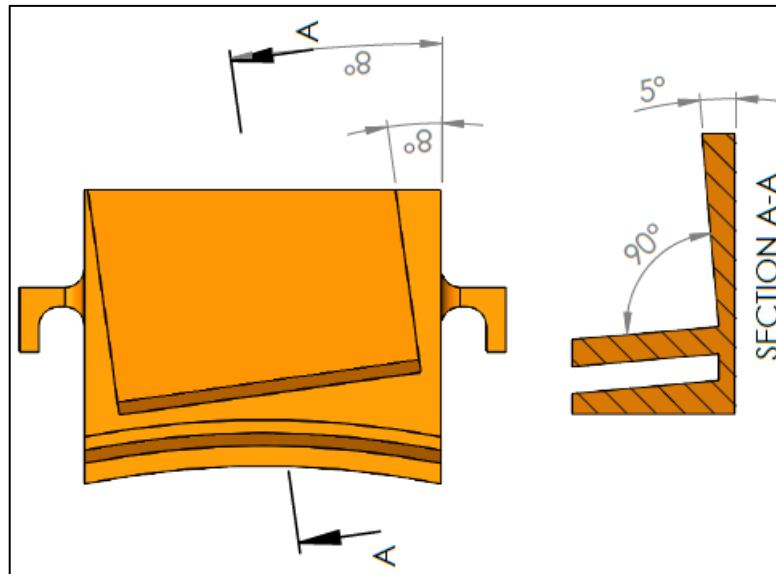


Figure 160: 8.15 ° degree hanging wedge for a 5 ° tapered sample.

Unlike the wedge from Figure 114, a pair of wedges were required in this scenario because the wedge shape is chiral, and require a mirror version to allow the transducers to be aimed towards each other.

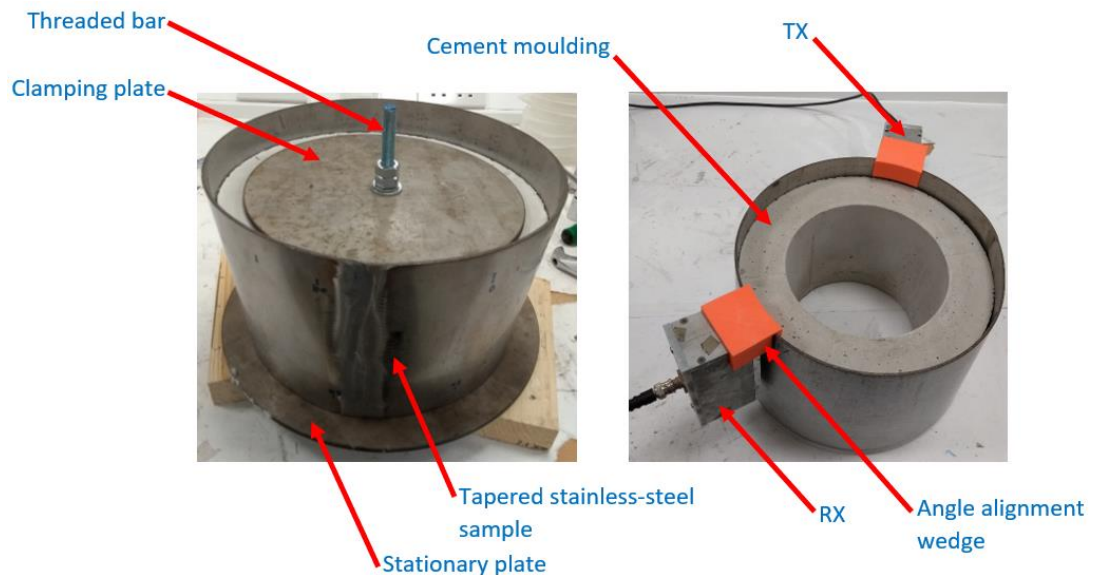


Figure 161: (Left) Cement moulding being pressed into the Stainless-steel tapered sample using an M12 threaded bar. (Right) TX and RX mounted onto the tapered sample using the 3D printed mounting wedge.

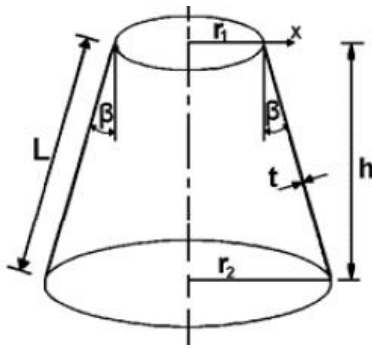


The test was initially run using the tapered sample empty, then repeated with the cement moulding resting inside it, then the cement moulding was pressed in as described in Figure 157 and the clamping nuts torque was increased by 10 Nm starting from 20 Nm. 20 Nm was used as the starting point to be within the registrable range of the digital torqued wrench available for the experiment.

On each run, the spacing between the TX and RX was increased incrementally by 100 m, starting from 200 mm to minimise the airwash noise effect, up to 700 mm to cover as much as possible of the sample circumference. The measurements were taken from the sides of the transducers while hanging on the side of the taper as seen in Figure 161. This means that that true distance the waves travelled is shorter than the measured dimensions due to the transducer geometry, and the diameter change in the taper shape, but the incremental changes will remain constant due to the symmetry of the setup.

The experiment was stopped at 40 Nm clamping fastener torque, because the threaded bar and nuts started to show signs of yielding, and the clamping plates started to deform. This meant that the torque force was no longer being converted into hoop force only and a portion of it is being lost in the deformation of the plates and fasteners.

The cured cement moulding measured height  $h = 105$  mm, largest circumference of 826 mm and taper angle  $\beta = 5^\circ$ . Thus, the surface area of the moulding in contact with the stainless steel during the test was,



$$\begin{aligned}
 A &= \pi(r_1 + r_2) \\
 &\times \sqrt{(r_2 - r_1)^2 + h^2}
 \end{aligned}
 \quad \text{Equation 49}$$

Figure 162: Truncated cone dimension [140].

---


$$r_2 = \frac{0.826}{2\pi} = 0.13 \text{ m} \quad \text{Equation 50}$$

---


$$\begin{aligned}
 r_1 &= r_2 - h \cos(90 - \beta) \\
 &= 0.13 - 0.105 \cos(90 - 5) = 0.12 \text{ m}
 \end{aligned}
 \quad \text{Equation 51}$$

---


$$\begin{aligned}
 A &= \pi(r_1 + r_2) \sqrt{(r_2 - r_1)^2 + h^2} \\
 &= \pi(0.13 + 0.12) \\
 &\times \sqrt{(0.13 - 0.12)^2 + 0.105^2} = 0.08 \text{ m}^2
 \end{aligned}
 \quad \text{Equation 52}$$

The force conversion from clamping force into radial force can be represented as a wedge free body. Assuming,

- The clamping force is directly converted in to hoop force with no loses in the deformation of the clamping plate, fasteners, stainless-steel sample, or cement moulding.
- No slipping between the cement moulding and the stainless-steel at steady state.
- The radial force is uniform and perpendicular to the taper central axis.
- Zinc plated fasteners coefficient of friction  $c = 0.2$  [141].
- M12 threaded bar major diameter of 12 mm (0.012m).
- Friction coefficient between dry cement moulding and the stainless approximated as  $\mu = 0.57$  [142].

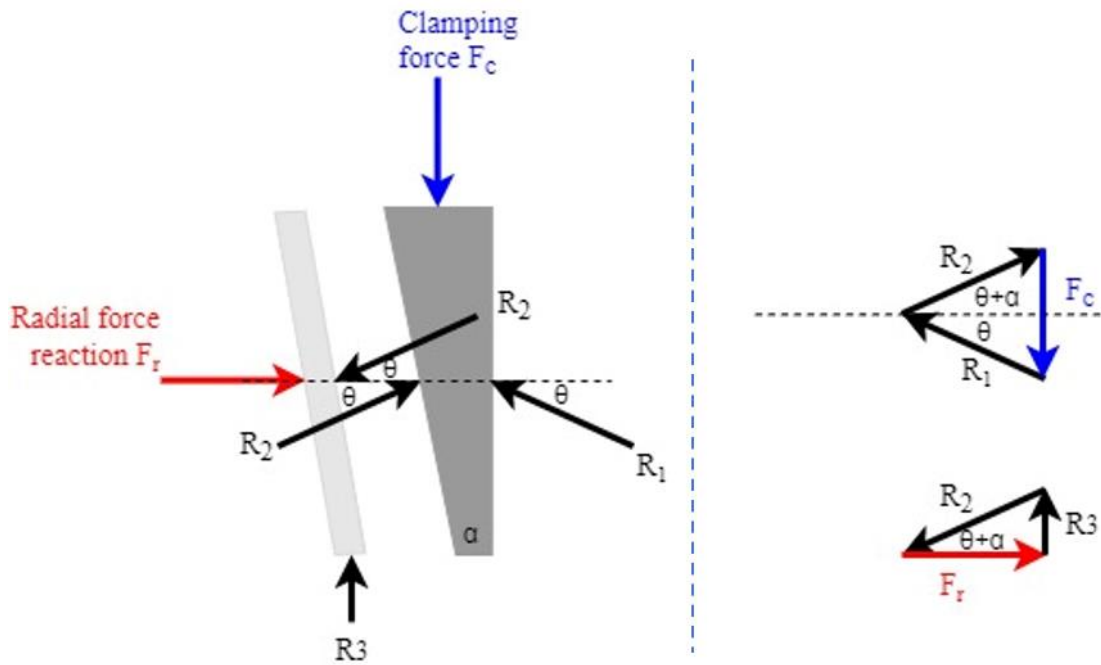


Figure 163: Free body diagram representing the transformation of the clamping force into hoop force.  $R_1$  and  $R_2$  are the angled component of  $F_c$ , while  $R_2$  and  $R_3$  are the component of  $F_{radial}$  as demonstrated on the force component diagrams on right.

Clamping force  $F_c$  at 40Nm Torque,

$$F_c = \frac{T}{cd} = \frac{40Nm}{0.2 \times 0.012m} = 16.66 \text{ KN} \quad \text{Equation 53}$$

Reactions  $R_1$  and  $R_2$  are inclined at an angle  $\theta$  from their respective normals and are in the direction opposite to the motion [143].

$$\mu = \tan(\theta) \quad \text{Equation 54}$$

$$\therefore \theta = \tan^{-1}(\mu) = \tan^{-1}(0.57) = 29.68^\circ \quad \text{Equation 55}$$

Based on the free body diagram,

$$R_2 \cos(\theta + \alpha) = R_1 \cos(\theta) \quad \text{Equation 56}$$

$$\begin{aligned} \therefore R_1 &= \frac{\cos(\theta + \alpha)}{\cos(\theta)} R_2 = \frac{\cos(29.68^\circ + 5)}{\cos(29.68^\circ)} R_2 \\ &= \frac{0.82}{0.87} R_2 = 0.94 R_2 \end{aligned} \quad \text{Equation 57}$$

---


$$F_c = R_2 \sin(\theta + \alpha) + R_1 \sin(\theta) \quad \text{Equation 58}$$

---


$$\begin{aligned} \therefore 16.66 \text{KN} &= R_2 \sin(29.68^\circ + 5) \\ &+ 0.94R_2 \sin(29.68^\circ) = 1.03R_2 \quad \text{Equation 59} \\ \Rightarrow R_2 &= 12.82 \text{KN} \end{aligned}$$

---


$$\begin{aligned} F_{\text{radial}} &= R_2 \cos(\theta + \alpha) \\ &= 12.82 \text{KN} \cos(29.68^\circ + 5) \quad \text{Equation 60} \\ &= 10.54 \text{KN} \end{aligned}$$

---

This means that the pressure force experienced by the stainless sample shell is

$$P = \frac{R_2}{A} = \frac{12.82}{0.08 \text{m}^2} = 160.25 \text{KN/m}^2 \quad \text{Equation 61}$$

The highest torque used during the experiment did not cause any measurable expansion in the diameter of the stainless-steel samples. To identify the actual internal pressure required to increase a 500 L ILW drum diameter from 800 mm to 804 mm as observed by Nirex solution [6] in Section 2.6, a static stress analysis simulation was performed on the drum CAD model created in Section 2.8 using SOLIDWORKS static finite element analysis. The analysis assumed a uniform pressure loading on the internal surfaces of the drum and used the lid mating flange as the anchor surface for the simulation process. The flange contact surface was chosen as an anchor point, because it is the thickest component of the drum structure based on the manufacturing drawings acquired from B.N.F.L (See Figure 8), and thus the least likely part of the structure to be deformed by the pressure. The applied pressure in the analysis was increased until the deformation results of 2 mm was estimated by the analyser as seen in Figure 164.

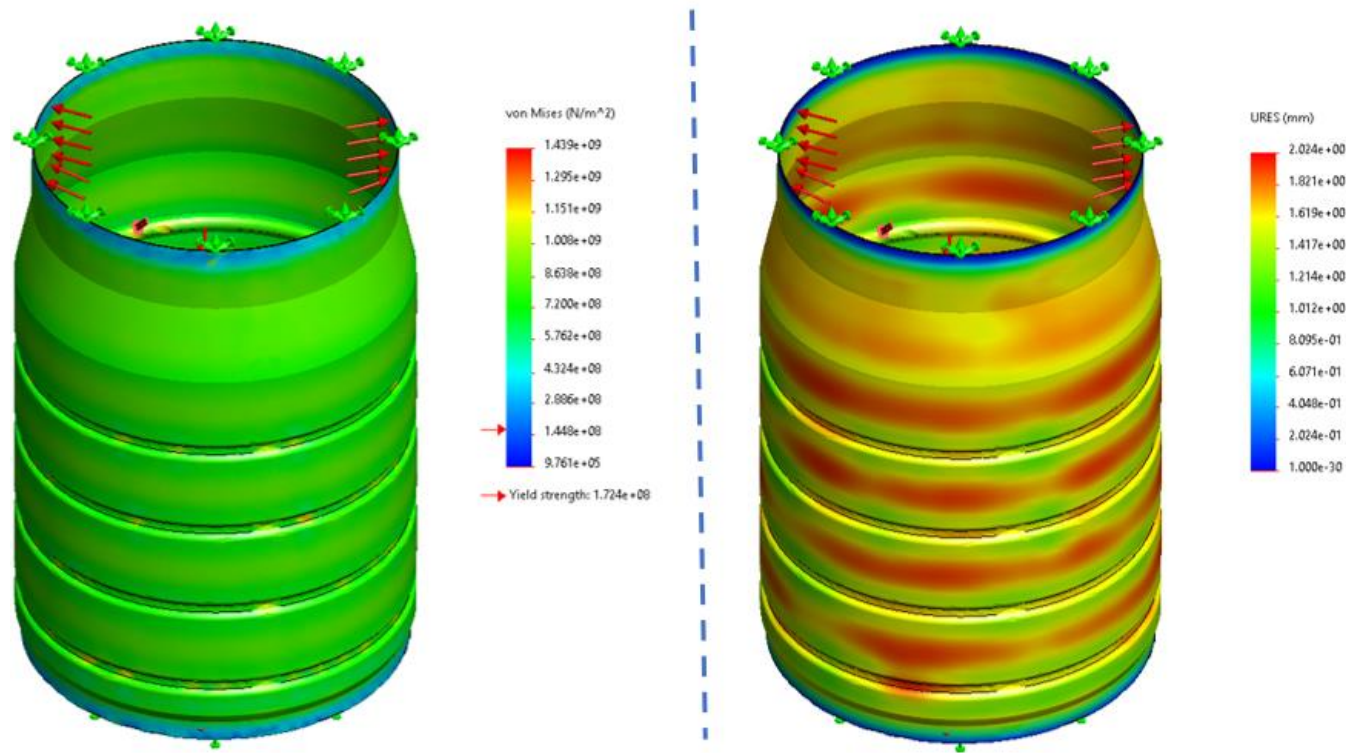


Figure 164: (Left) SOLIDWORKS FEA simulation results presenting the mechanical stresses experienced by an 800 mm diameter ILW 500 L drum with a 2.33 mm wall expanded to 804 mm (URES=2mm) due to uniform pressure of  $5.3 \times 10^6 \text{ N/m}^2$  on its internal shell wall. (Right) Resultant displacement (URES) of the drum shell due to the pressure loading from the simulation.

The analysis showed that a minimum pressure of  $5.3 \times 10^6 \text{ N/m}^2$  is required to create a deformation of 2.0 mm in the drum shell, to produce the 4.0 mm overall change in diameter.

To validate the simulation, the drum shell is simplified as a simple thin wall cylinder with 800 mm outer diameter and wall thickness of  $t = 2.33$  mm, and the hoop stress ( $\sigma_\theta$ ) [144] in a cylinder equation used to confirm the stresses observed by the computer simulation.

The mean diameter of the cylinder ( $D_m$ ) will be,

$$\begin{aligned} D_m &= d - t = 800 - 2.33 = 797.67 \text{ mm} \\ &= 797.67 \times 10^{-3} \text{ m} \end{aligned} \quad \text{Equation 62}$$

---


$$\begin{aligned} \therefore \sigma_\theta &= \frac{PD_m}{2t} = \frac{(5.3 \times 10^6) \times 797.67 \times 10^{-3}}{2(2.33 \times 10^{-3})} \\ &= 9.07 \times 10^8 \text{ N/m}^2 \end{aligned} \quad \text{Equation 63}$$

The simplified hoop stress matches the stresses observed by the simulation in the majority of the drum surface seen in Figure 164, thus validating the simulation.

### 6.4.3 Observations

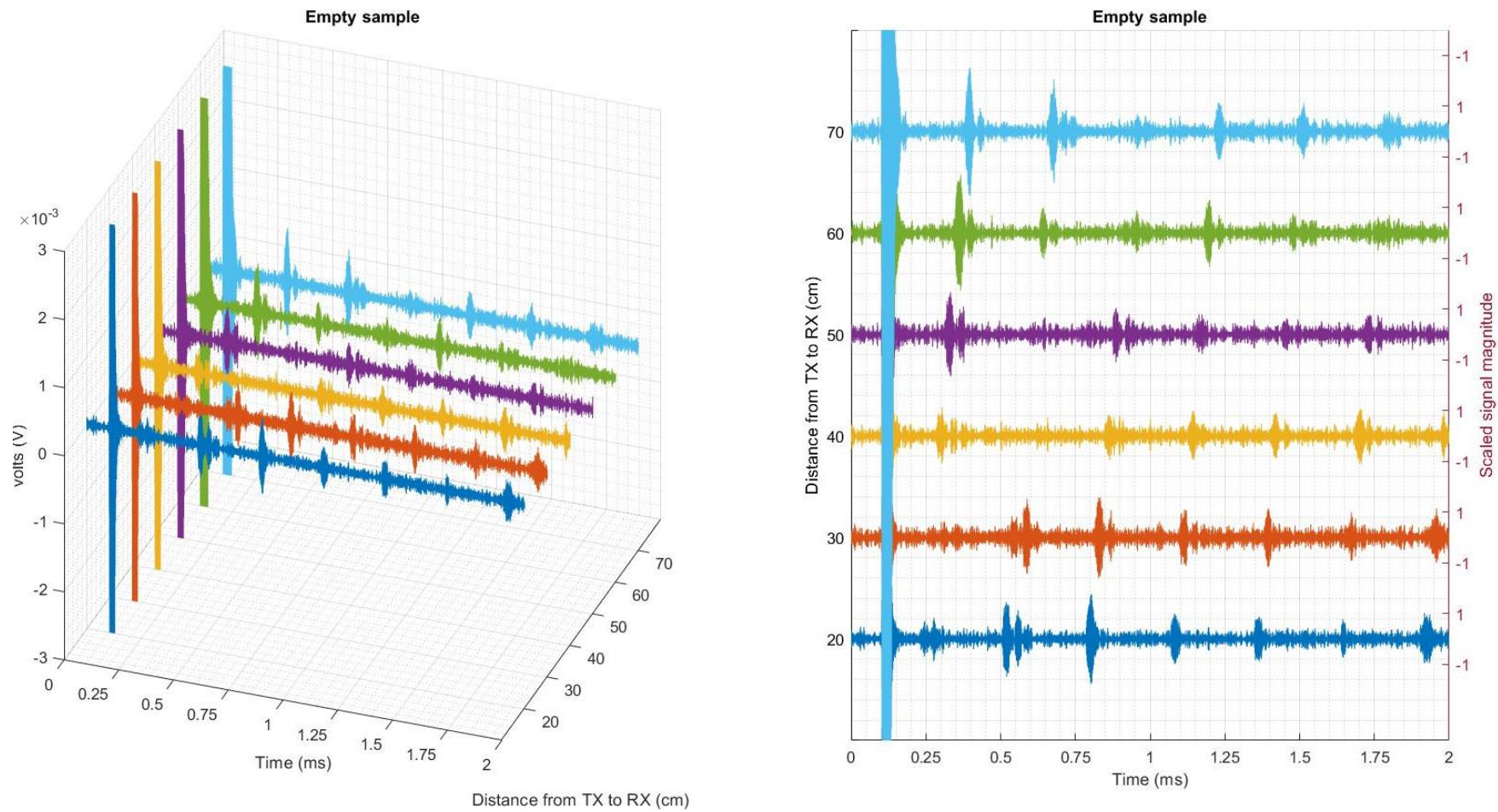


Figure 165: Lamb waves detection patterns from the tapered stainless-steel sample.

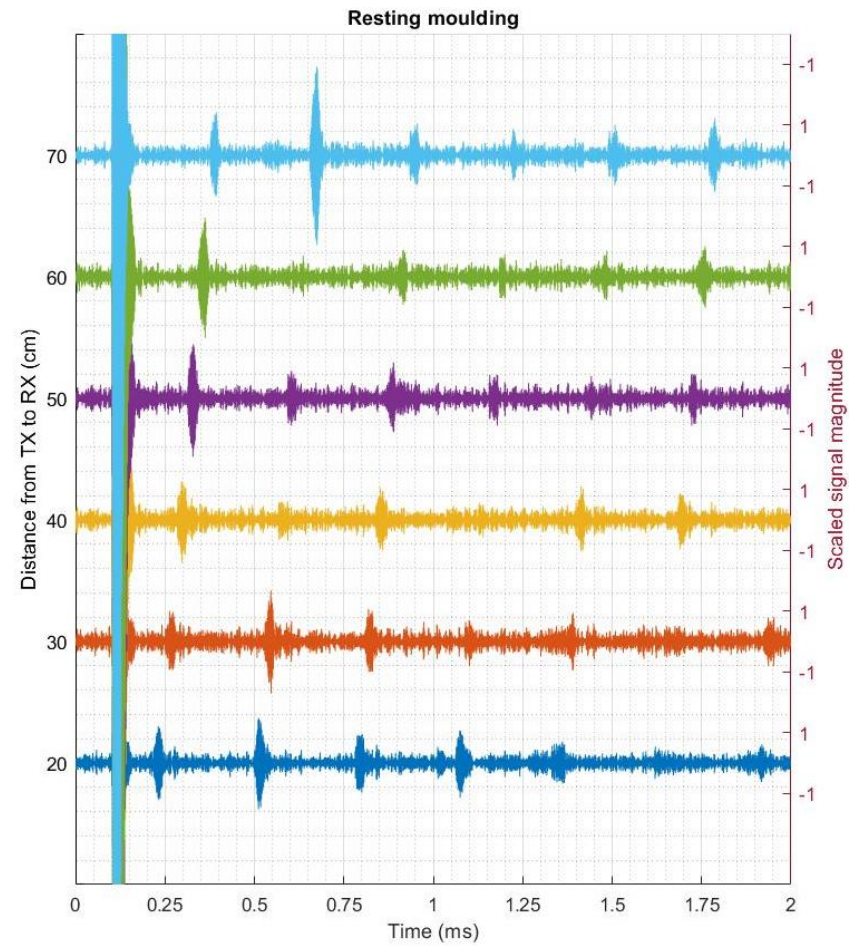
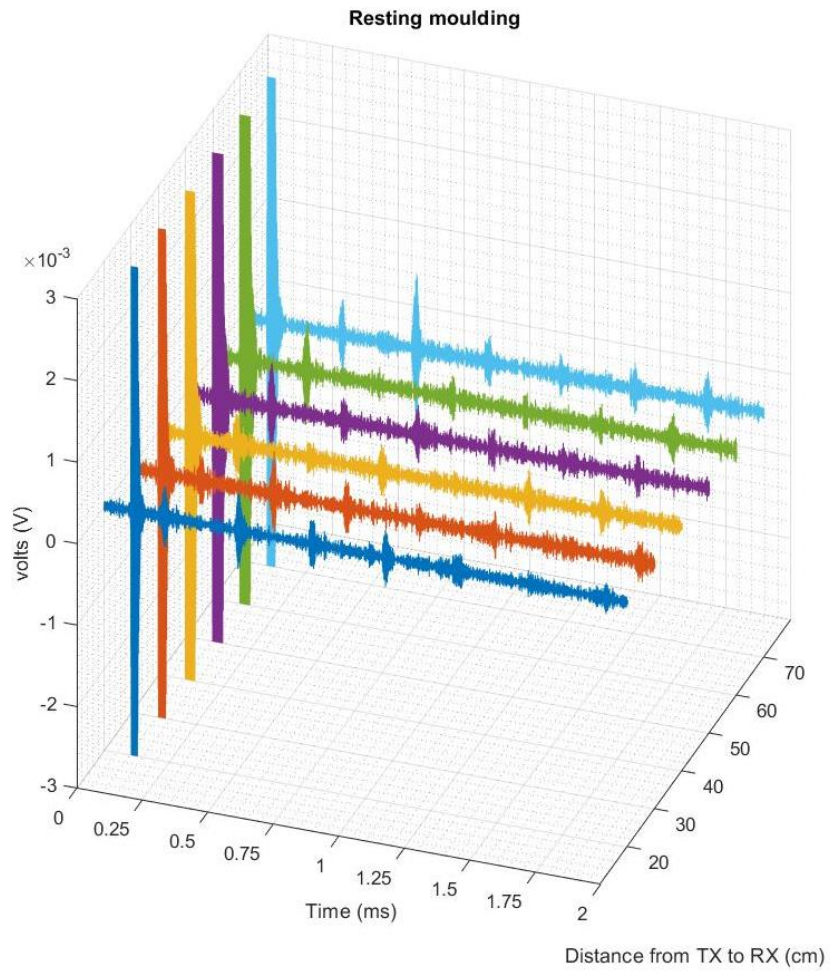


Figure 166: Lamb waves detection patterns from the tapered stainless-steel sample with the cement moulding resting inside it.



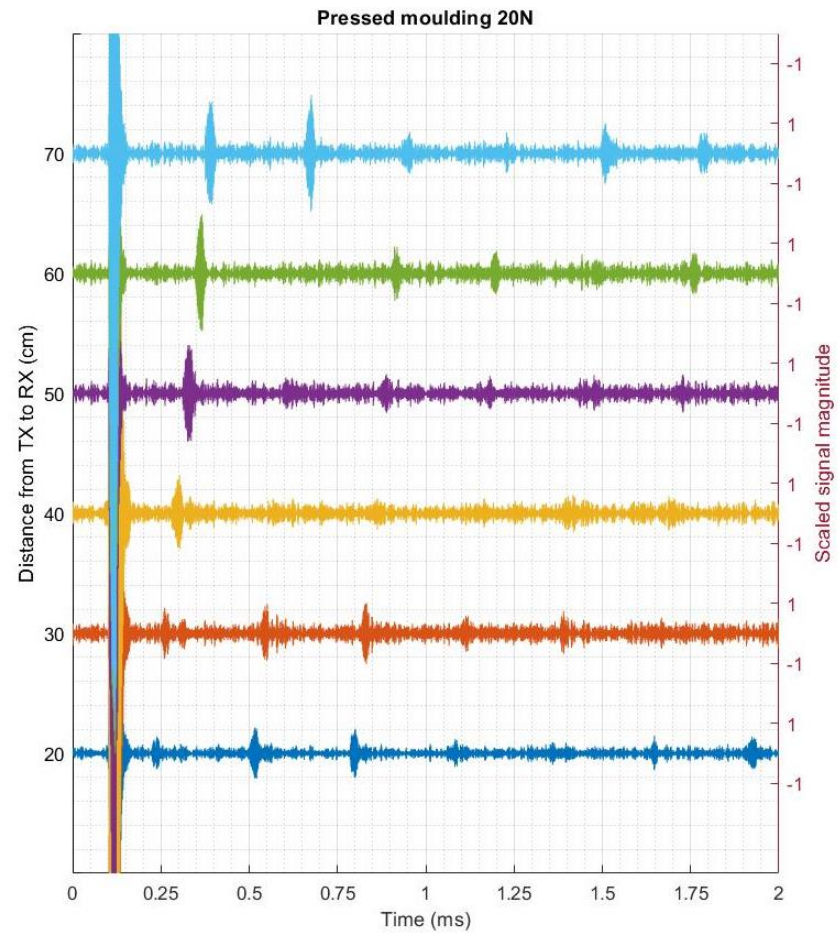
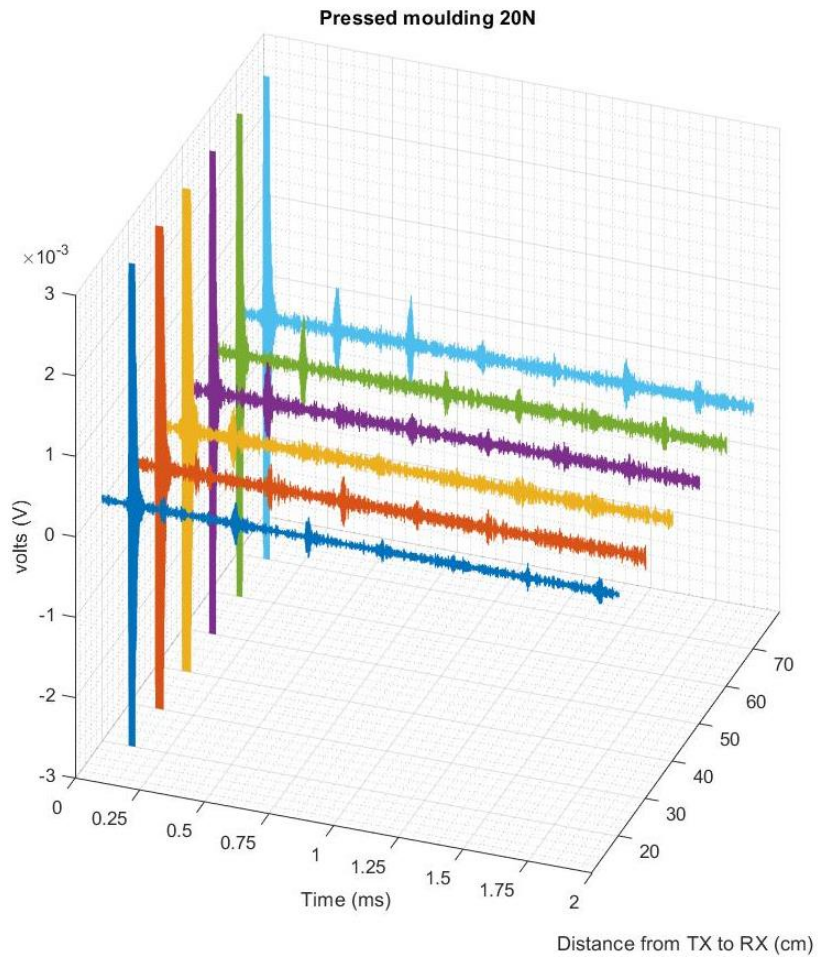


Figure 167: Lamb waves detection patterns from the tapered stainless-steel sample with the cement moulding pressed into it using an M12 threaded bar torqued to 20N.

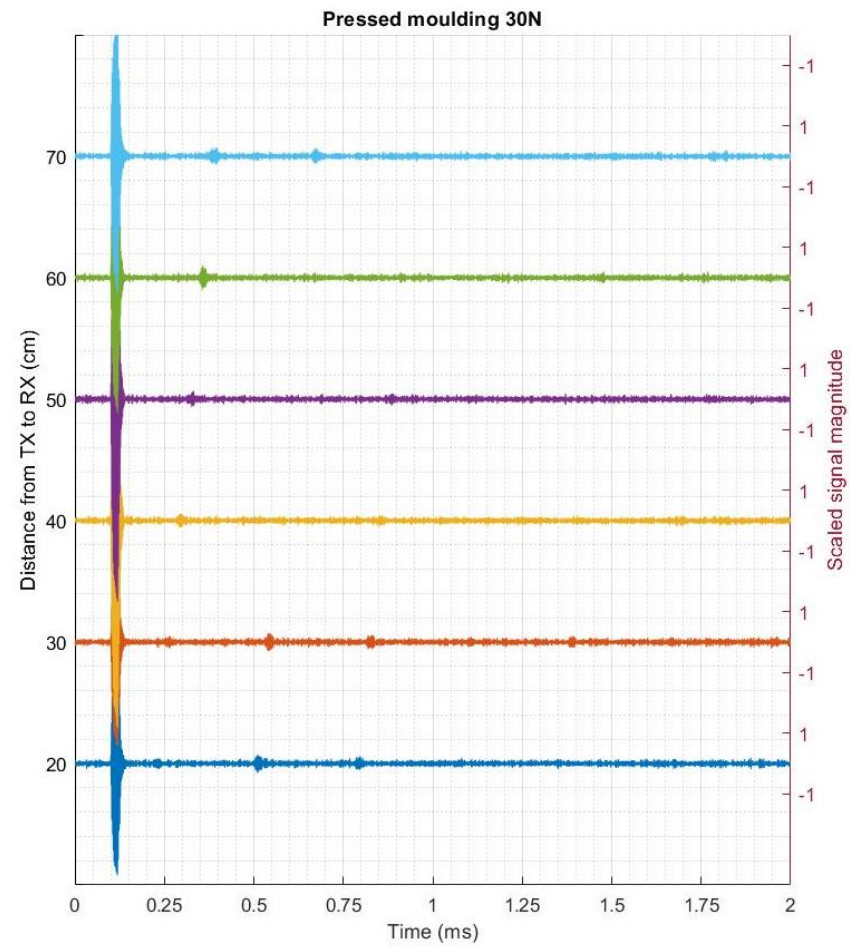
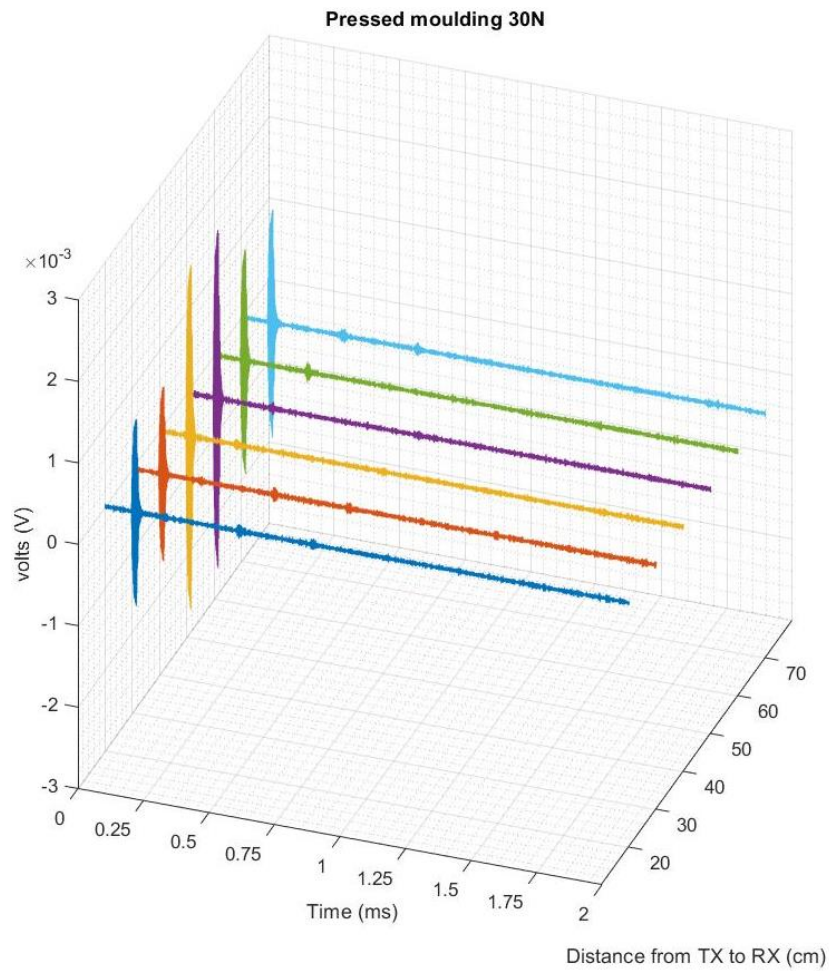


Figure 168: Lamb waves detection patterns from the tapered stainless-steel sample with the cement moulding pressed into it using an M12 threaded bar torqued to 30N.

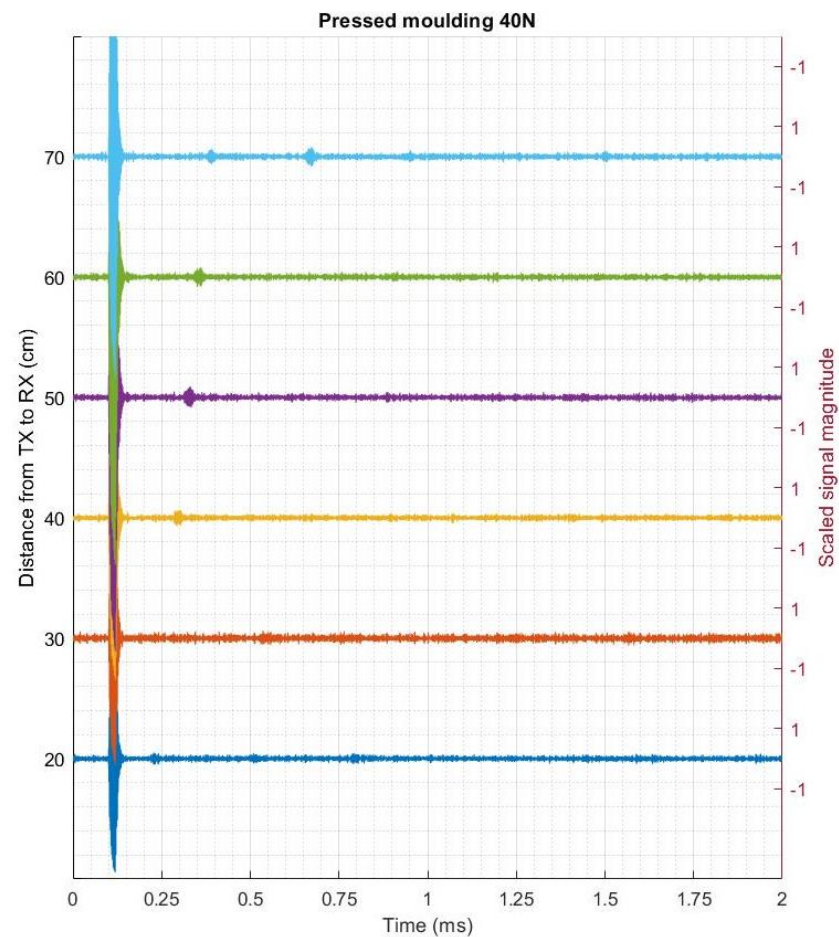
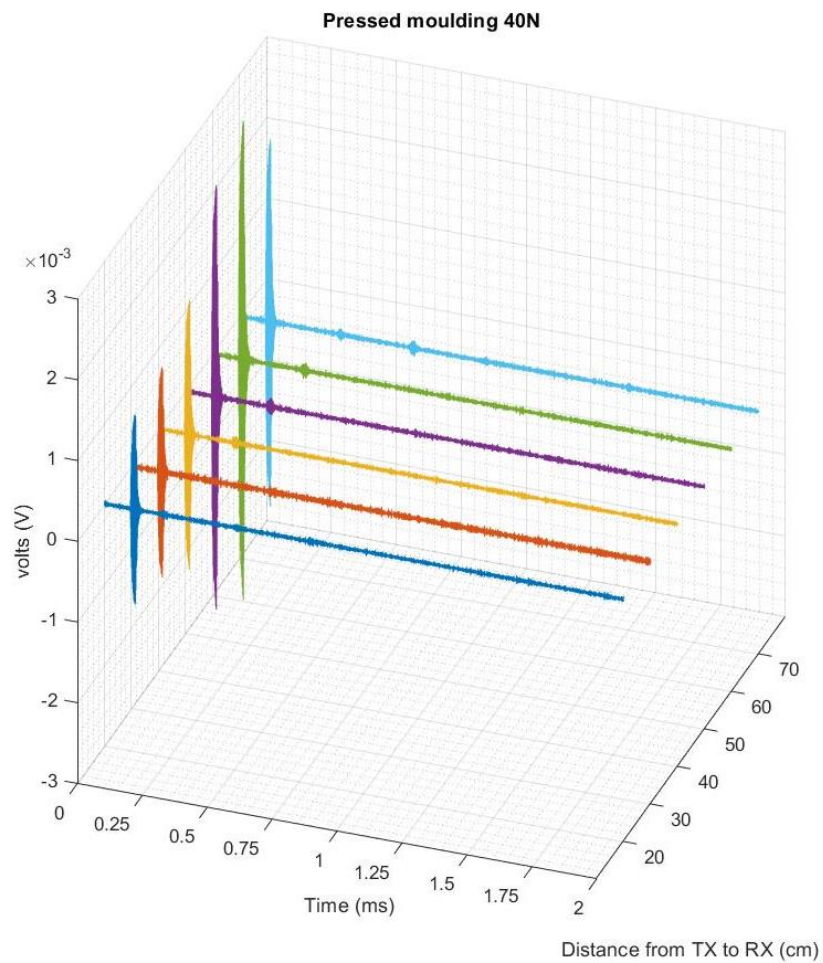


Figure 169: Lamb waves detection patterns from the tapered stainless-steel sample with the cement moulding pressed into it using an M12 threaded bar torqued to 40N.

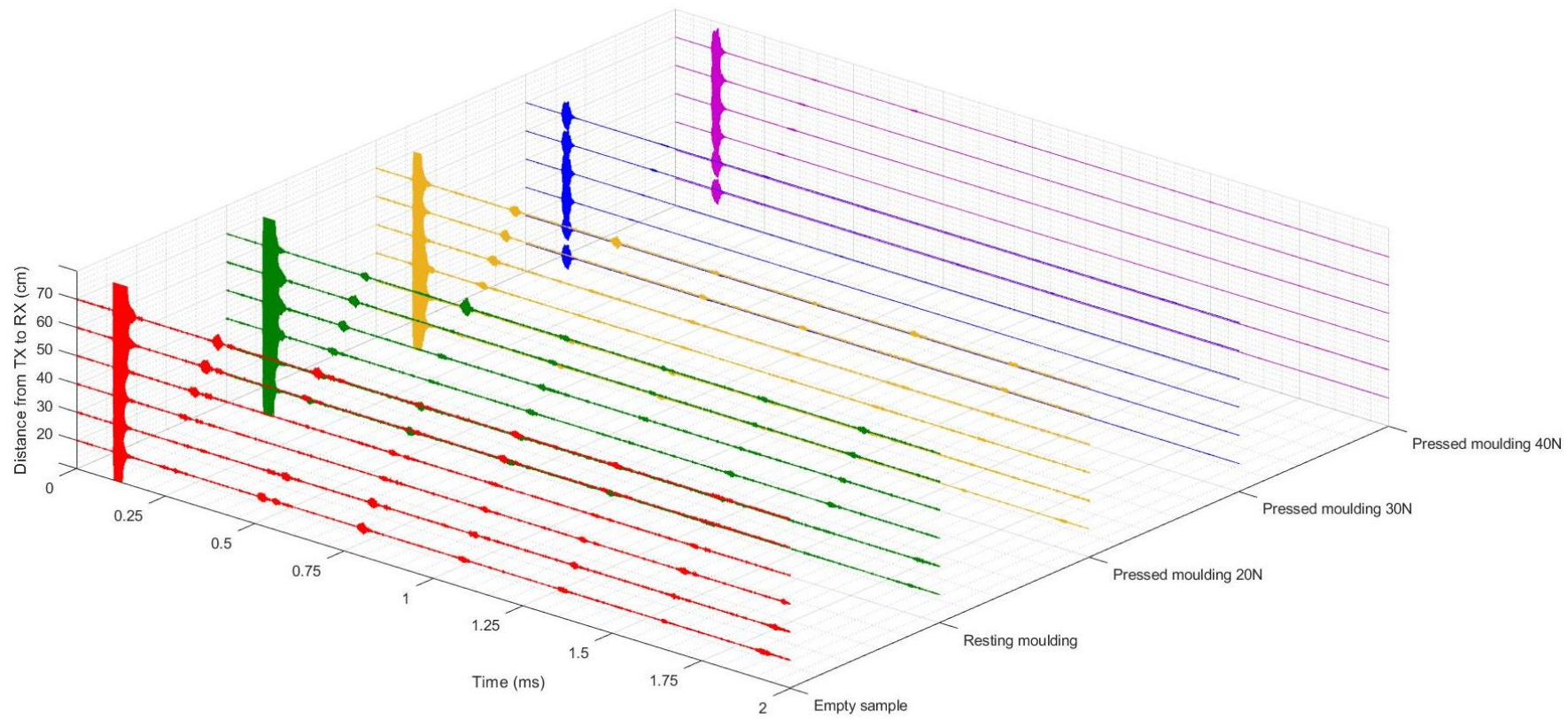


Figure 170: 3D representation of the Lamb waves detection patterns from the tapered stainless-steel sample with different setting for comparison.

Sample	Observation
<p><b>Empty sample</b> Figure 165</p>	<p>-Aliasing in the peaks, indicating that the Lamb wave are detectable after travelling around the circumference for more the 2.0 ms, similar to the observation observed in Section 6.3.2. -The amplitude of the 1<sup>st</sup> Lamb wave detection is larger with TX and RX spacing of 400 mm or more.</p>
<p><b>Resting moulding</b> Figure 166</p>	<p>-Clear Lamb wave detection pattern with no aliasing, indicating that the waves travelling around the circumference are no longer detectable after 2.0 ms, to cause the aliasing observed previously in Figure 165. -The shape of the 1<sup>st</sup> Lamb wave detection peak at all TX and RX spacings is more defined and clearer compared to the empty sample peaks in Figure 165.</p>
<p><b>Pressed moulding 20N</b> Figure 167</p>	<p>- Drop in the amplitude of the peaks detected when distances between TX and RX is 400 mm and below. - The 2<sup>nd</sup> peak at 600 mm between TX and RX is missing.</p>
<p><b>Pressed moulding 30N</b> Figure 168</p>	<p>- Significant drop in the amplitude of all the detected peaks, indicating either a significant drop in the amplitude of the Lamb waves, or a change in the angles of incidence causing losses in the detection due to the wedge fixed angle.</p>
<p><b>Pressed moulding 40N</b> Figure 169</p>	<p>- Further drop in the peak's amplitude. - Only the 1<sup>st</sup> or 2<sup>nd</sup> Lamb wave detections peaks are observable.</p>

The data from plots Figure 165, Figure 166, Figure 167, Figure 168, Figure 169 were compiled together to observe the effect of the cement moulding presence and pressure on detected Lamb waves.

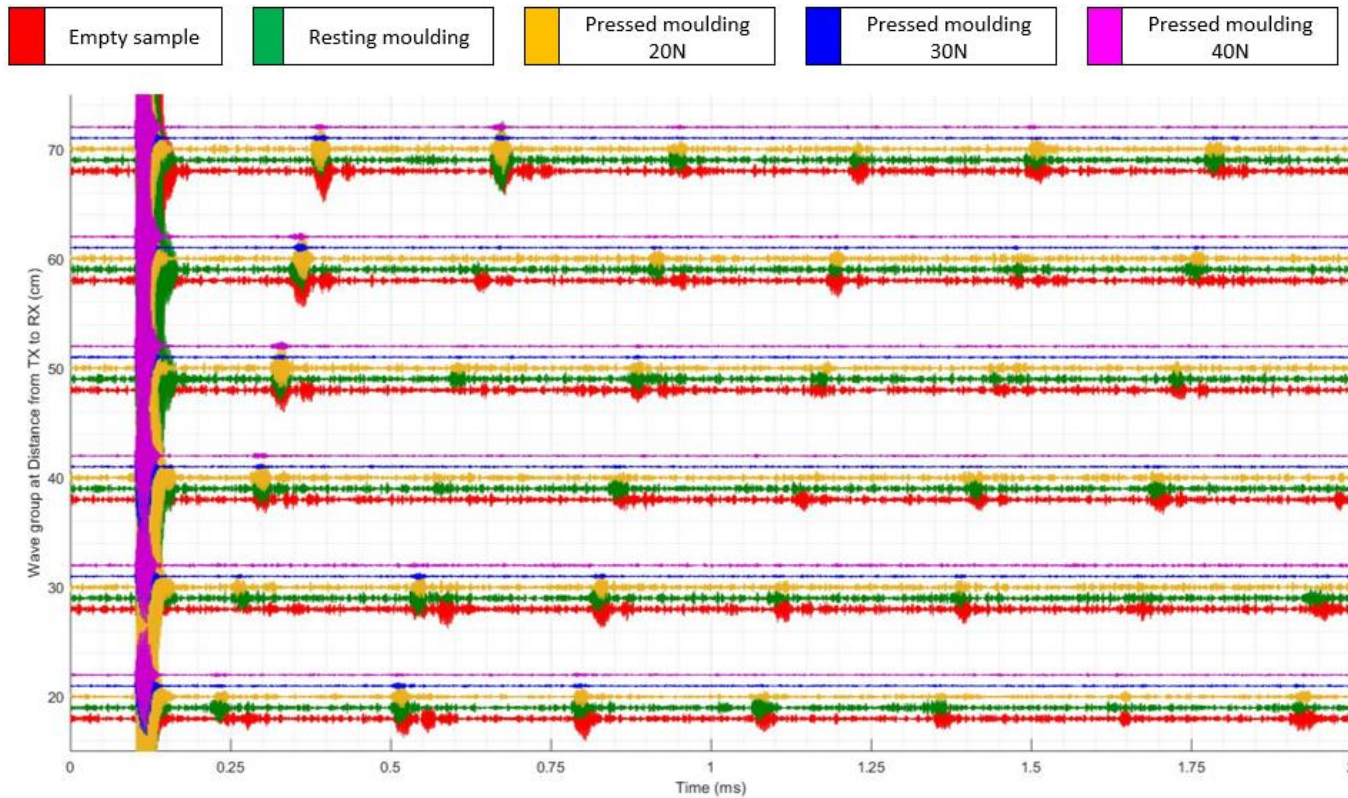


Figure 171: 2D visual representation of the data from Figure 170 with readings from each scenario grouped together based on the distance from TX and RX in which the data is acquired. (Vertical axis in this plot refers to groups of signals and not exact values. Refer to previous plots for true data values.)

Contrasting to the results from the dispersion curves in Section 5.6.4 Figure 132, the presence of the cement moulding had no noticeable change on the  $V_{gr}$  of the Lamb waves as seen in Figure 171. Upon closer inspection in Figure 172, Figure 173, Figure 174 and Figure 175, the signal peak locations only fluctuate but remain within the same minor grid lines. A more sensitive detection of the peaks observed in the samples with the pressed moulding will be required to confirm this claim. This was not possible during the experiment due to the power limitations of TX which limited the peak amplitude, combined with the restricted sensitivity of the RX and its amplifier.

It is also noticed that the amplitude of the waves detected differed depending on the RX location, this can be seen when comparing the signals with TX and RX spaced 20 cm and 70 cm as seen in the figures Figure 172, Figure 173, Figure 174 and Figure 175. During both scans the TX was not moved indicating that the effect is caused by the RX location. This is likely caused by the true angle observed by the wedge at that location compared to the imperfect circularity of the sample.

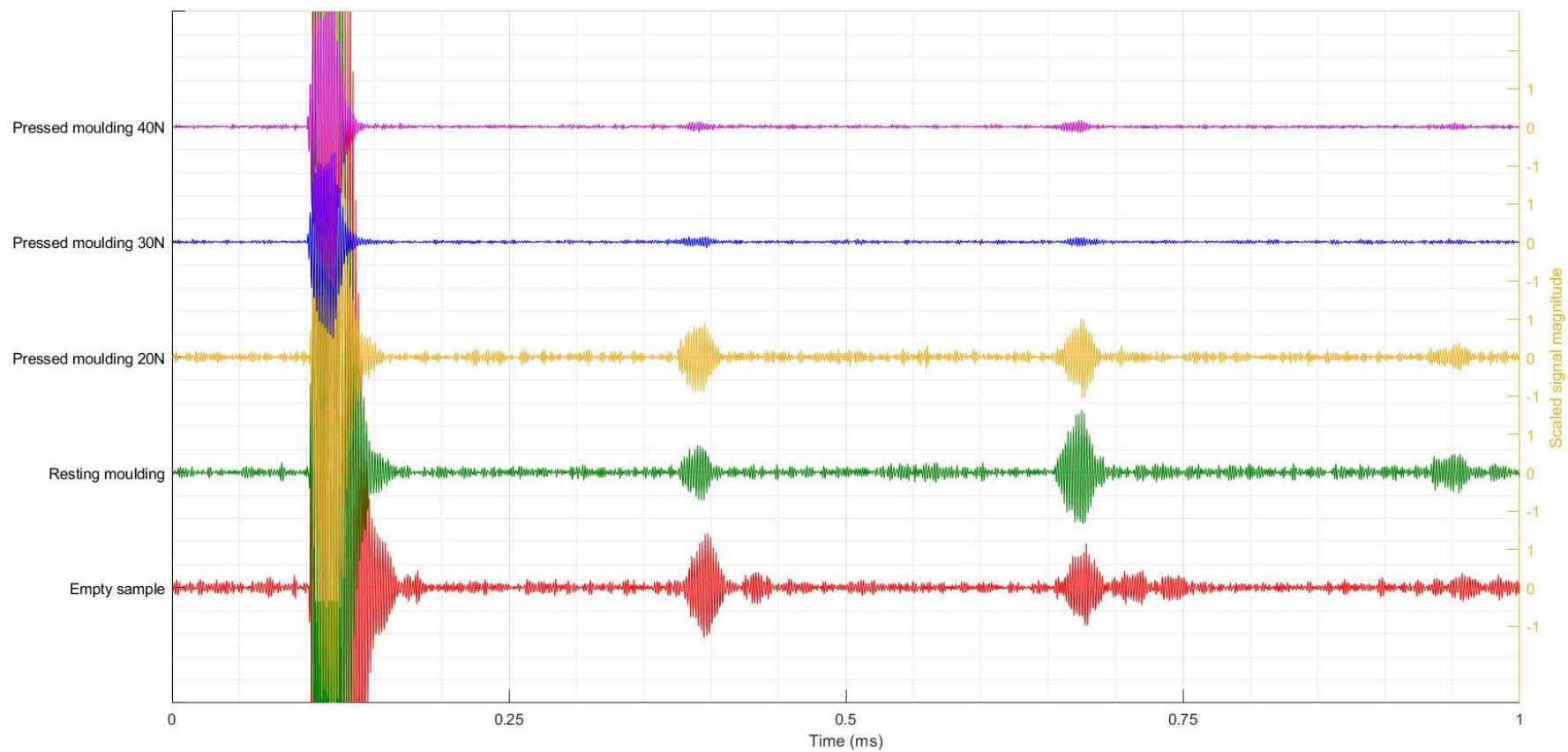


Figure 172: Lamb wave detections with TX and RX spaced at 70 cm.



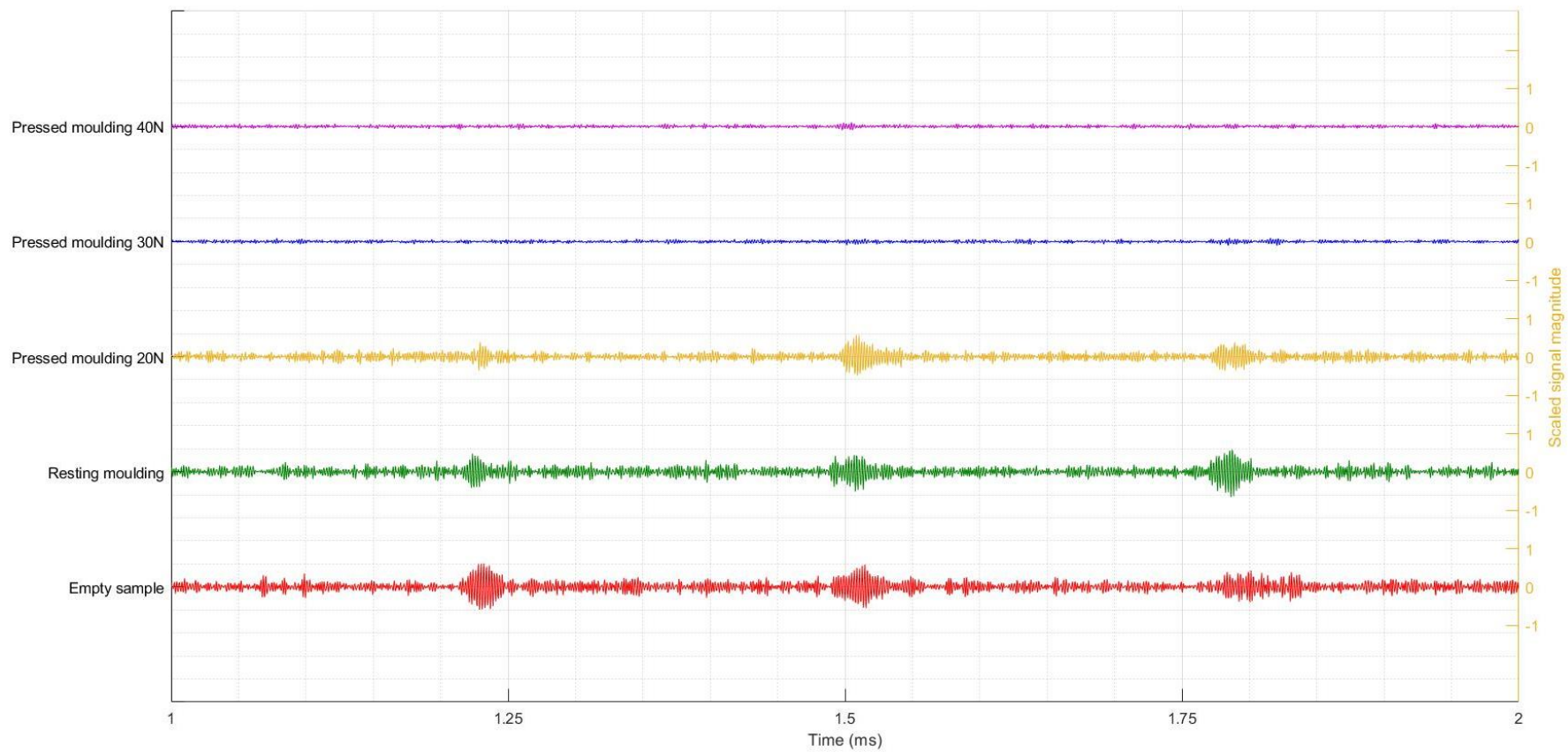


Figure 173: Lamb wave detections with TX and RX spaced at 70 cm.

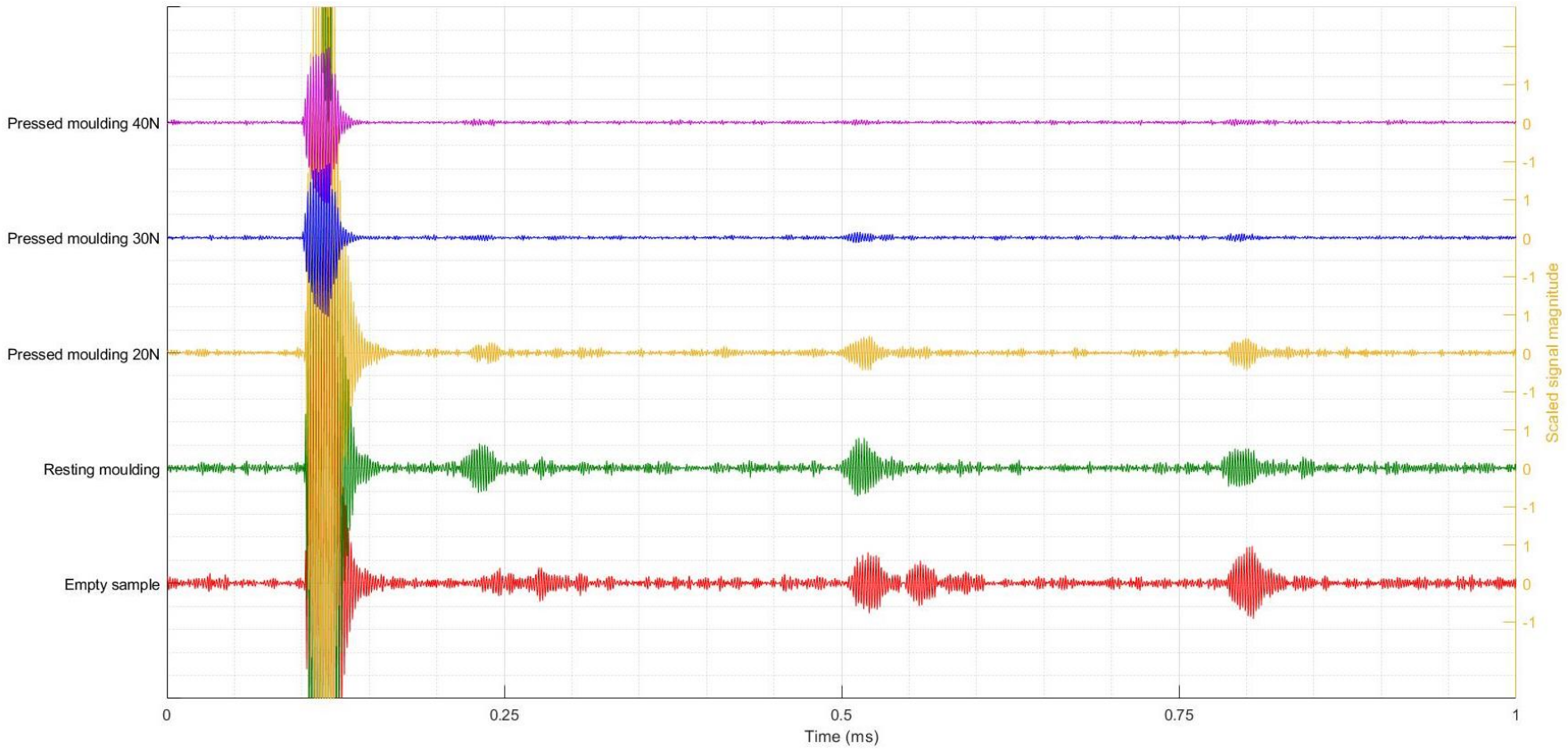


Figure 174: Lamb wave detections with TX and RX spaced at 20 cm.

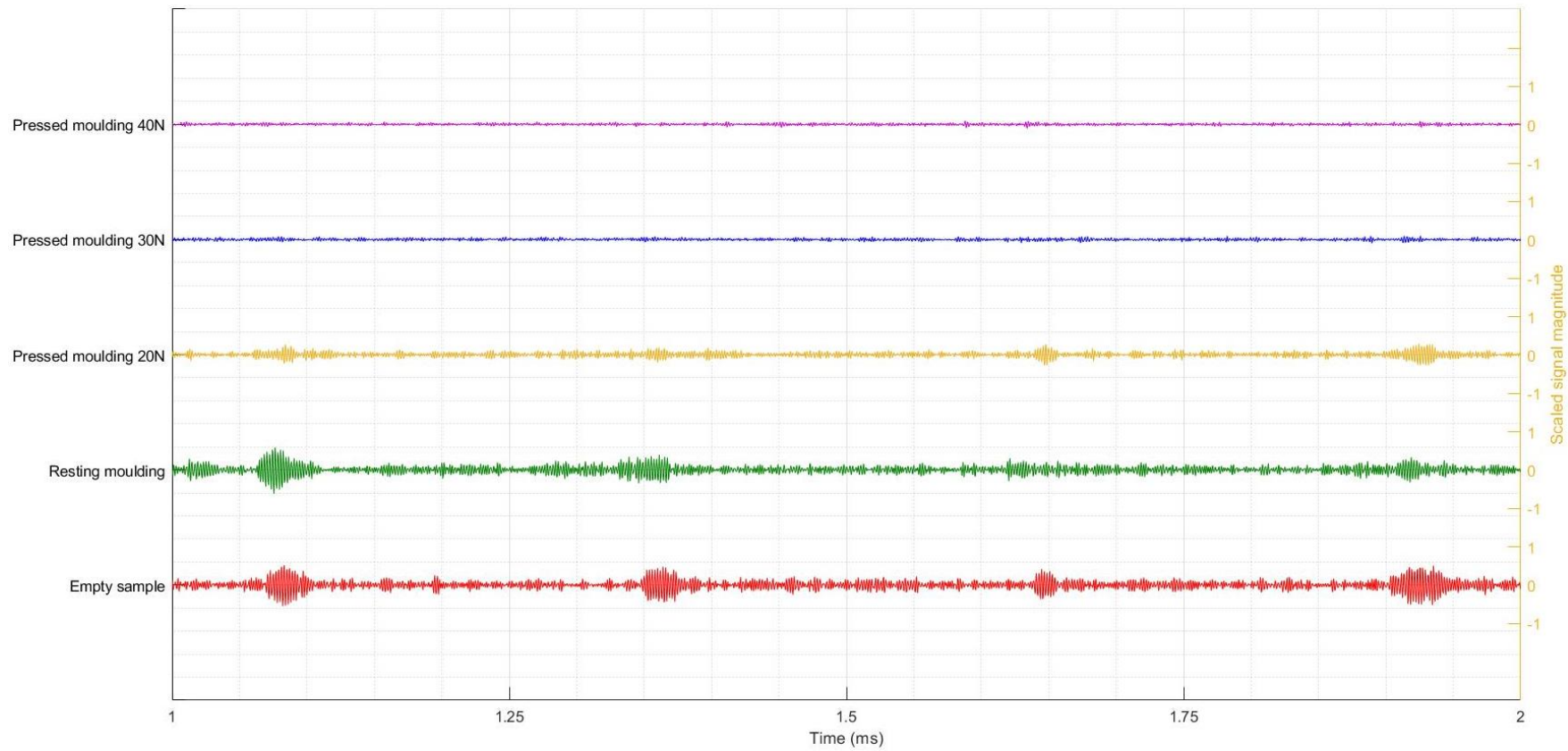


Figure 175: Lamb wave detections with TX and RX spaced at 20 cm.

#### 6.4.4 Predictions and future improvements

The experiment results observed in Section 6.4.3 proved that the Lamb waves amplitudes are significantly damped by the cement exerting pressure on the workpiece wall. This pressure would increase the true contact surface between the cement mould and the sample wall causing an increase in the dampening effect, and the transition from the dispersion curve estimated for a stainless-steel sample in air to the dispersion curve of a stainless-steel plate with cement on one of its surfaces as described in Section 5.6.4 Figure 132.

Given that the setup was able to detect the Lamb wave 6 times in the “Resting moulding” scenario, compared to 1 low amplitude detection in the “Pressed moulding 40N” scenario, it can be assumed that the  $160.25 \times 10^3 \text{ N/m}^2$  pressure applied lead to a cement surface contact that dampened the Lamb wave propagation by a factor of 6.

Given that that pressure required to expand the ILW 500 L drum model in simulation by 4.0 mm as described in Figure 164 was of  $5.3 \times 10^6 \text{ N/m}^2$ , it is very likely that such pressure will cause enough contact between the rough cementitious surface and the drum walls to dampen the Lamb waves to the point of being undetectable, considering the results from the  $160.25 \times 10^3 \text{ N/m}^2$  pressure scenario. Thus, an ultrasonic transmitter with a significantly higher energy output will be required to generate a detectable Lamb wave at the higher pressures.

Moreover, unlike the experiment where the stainless-steel sample did not expand, if the pressures forces exerted were high enough to cause the actual expansion in the metal, these forces will lead to stresses in the surfaces of the sample which would change the Lamb waves velocities [145].

Although increasing the ultrasonic receiver sensitivity may be helpful in detecting lower amplitude waves, it will also be more susceptible to background noise due to the ambient air movement, thus will require more filtering and/or averaging as previously done in Section 5.3 and Section 6.3. This may increase the acquisition time to an unpractical point, considering both the averaging acquisition times described in

Section 6.3.1 and the concept of performing this process at multiple angles during the transducers sweeping process described in Section 6.2.

The use of the threaded bar and fasteners to create the clamping force, which was then converted into internal pressure by utilising the tapered shape wedge effect was successful. However, the accuracy of the clamping force is suboptimal due to the frictions and deformation in the fasteners' threads. This can be improved by using a hydraulic press to accurately apply and measure the clamping forces. This was not possible during this test due to the safety requirements and risks associated with using high pressure in the lab.

The simulation and calculation used to predict the internal pressure required to deform the ILW 500 L drum shell by 4.0 mm in diameter, indicated that the drum's material would pass its yield point at the experienced stress. This means that the drum shell would plastically deform at that stage and not return to its original shape after the pressure is removed. Given that the pressure in real life is caused by an expanding solid (the drums' contents), the pressure will no longer be applied if the solid contents displacement is not exceeding the container new volume after its shell yields. In other words, once the drum reaches the yield point due to internal pressures, it will permanently expand/deform, this will increase its volume and reduce the pressure inside it because the pressure was exerted by a solid content with a finite volume that will only exert pressures upon a shell if the shell is smaller than the content volume, which is not the cases in a plasticly deformed drum.

Once the drum's shell is plastically deformed to the shape of the expanded contents. If the pressure experienced by the drum shells do indeed drop after it plastically deforms, the Lamb waves will have a better chance of travelling around the drum without significant dampening, and the lamb wave properties will only change in accordance with the new material properties of the yielded drum shell. Validating this theory will require a new multi-physic simulation that can take into account the time factor and changes in pressure caused by an expanding solid instead of a constant force.

## 6.5 Defect and discontinuity detection

In the unlikely event where there is a crack/discontinuity or a cavity/defect in the ILW 500 L drums' shell with a sharp enough edge capable of reflecting a Lamb wave, the flow pattern of the Lamb waves around the drum circumference should theoretically differ from that in Figure 118.

### 6.5.1 Scenario 1: Defect after the first RX detection point

Assuming a defect is present at the largest distance between a TX and RX in a cross section of finite thickness of the ILW drum sample being scanned for circumferential measurement. The defect would be expected to reflect the wave back along the circumference of the drum, and result in the following flow/path of acoustic waves,

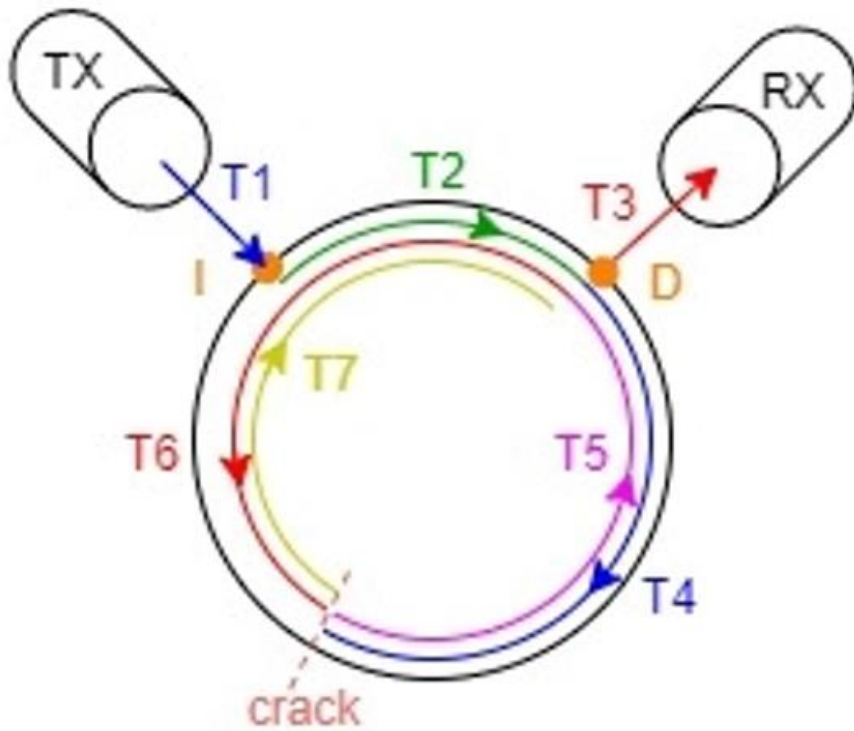


Figure 176: Illustration of wave paths to, from and around the circumference of a cylindrical sample with a discontinuity/defect at the largest distance between TX and RX

<b>TX</b>	Ultrasonic transmitter.
<b>RX</b>	Ultrasonic receiver.
<b>I</b>	Incident point where longitudinal waves induce a Lamb wave into the drum's shell
<b>D</b>	Point where the longitudinal wave detected by the RX were generated from the travelling Lamb wave.
<b>T1→</b> <b><math>T_{TX \rightarrow I}</math></b>	T.O.F of an ultrasonic wave from TX to drum through air.
<b>T2↻</b> <b><math>T_{I \rightarrow D}</math></b>	T.O.F of a Lamb wave from 'I' to 'D' along drum circumference.
<b>T3→</b> <b><math>T_{D \rightarrow RX}</math></b>	T.O.F of longitudinal wave from 'D' to RX through air.
<b>T4↻</b>	T.O.F of Lamb wave from point 'D' to the crack/discontinuity.
<b>T5↻</b>	T.O.F of the Lamb wave reflected by the crack/discontinuity back to point 'D'.
<b>T6↻</b>	T.O.F of reflected Lamb wave from point 'D' to opposite side of the crack/discontinuity.
<b>T7↻</b>	T.O.F of the Lamb wave reflected from the opposite side of the crack/discontinuity back to point 'D'.

In this scenario, the Lamb waves should travel along the circumference in both the clockwise and anticlockwise directions, as they are being reflected by the defect. As these waves pass the detection point 'D' which the RX is aimed at, they will generate a longitudinal acoustic wave that will be detected by the RX in the same process describe in Section 5.2.2. However, the longitudinal wave coming out of the detection point will be generated in two different angles this time. The first angle will be at the  $8.15^\circ$  for the reasons described in Section 5.2.2, whereas the second set will also be at  $8.15^\circ$  but in the opposite direction, because the Lamb wave reflected from the defect will be travelling anticlockwise as per Figure 176. This makes the longitudinal waves generated by the anticlockwise waves appear at  $171.85^\circ$  compared to the longitudinal waves generated by the clockwise waves.

The -6 dB acceptance angles of air-coupled piezoelectric transducers is less than  $0.66^\circ$  [81], this means that the relative amplitude of the longitudinal waves observed by the receiver drops by half if the receiver is  $0.66^\circ$  away from the original  $8.15^\circ$ . This drop in the observed longitudinal waves amplitude is exponential [146], thus if the reflected waves intercept the receiver at  $171.85^\circ$  while the receiver is aimed at  $8.15^\circ$  as illustrated in Figure 177, the observed longitudinal wave amplitude will be negligible and will not be detected by the receiver.

Similarly, if the RX is turned around to  $171.85^\circ$  and was able to detect any peaks, these peaks will be a result of lamb wave reflections that are caused by defect in the drum's circumference. This is visually demonstrated in Figure 177 for clarity.



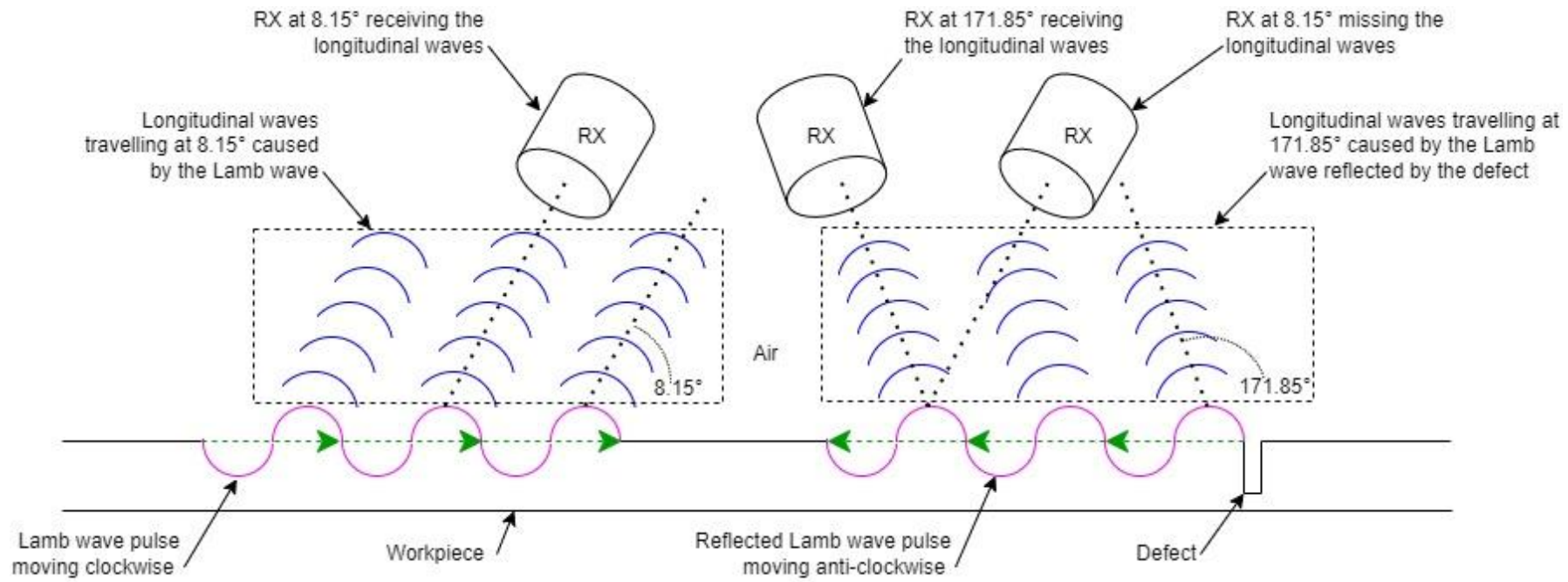


Figure 177: Longitudinal waves travelling at 171.85 ° caused by Lamb waves travelling in the anticlockwise direction.

**Note:** Figure 177 is not to scale, the angles and wave sizes drawn are exaggerated for visual clarity.

If we assume that the RX is set at the initial 8.15 ° angle of incident setup and is detecting the clockwise waves only, the wave peak detection times should be as following based on Figure 176,

$$\text{Assuming a negligible defect thickness} \left\{ \begin{array}{l} T5_{\cup} + T6_{\cup} = T \cdot O \cdot F_{Circumference} \\ T4_{\cup} + T7_{\cup} = T \cdot O \cdot F_{Circumference} \\ T4 = T5 = T_{D \cup crack} \\ T6 = T7 = T_{D \cup crack} \end{array} \right. \quad \text{Equation 64}$$

The 1<sup>st</sup> wave detection should theoretically occur at

$$\begin{aligned} time_{1^{st} \text{ detection}} &= T1_{\rightarrow} + T2_{\cup} + T3_{\rightarrow} \\ &\text{or} \\ &= T_{TX \rightarrow I} + T_{I \cup D} + T_{D \rightarrow RX} \end{aligned} \quad \text{Equation 65}$$

and the 2<sup>nd</sup> wave detection should occur at

$$\begin{aligned} time_{2^{nd} \text{ detection}} &= T1_{\rightarrow} + T2_{\cup} + T4_{\cup} + T5_{\cup} + T6_{\cup} + T7_{\cup} + T3_{\rightarrow} \\ &= T1_{\rightarrow} + T2_{\cup} + (T4_{\cup} + T7_{\cup})T \cdot O \cdot F_{Circumference} \\ &\quad + (T5_{\cup} + T6_{\cup})T \cdot O \cdot F_{Circumference} + T3_{\rightarrow} \\ &= T1_{\rightarrow} + T2_{\cup} + T3_{\rightarrow} + 2T \cdot O \cdot F_{Circumference} \\ &\text{Or} \\ &= T_{TX \rightarrow I} + T_{I \cup D} + T_{D \rightarrow RX} + 2T \cdot O \cdot F_{Circumference} \end{aligned} \quad \text{Equation 66}$$

---

From there, the waves will repeat the same pattern from T4 to T7 as they bounce back and forth by the defect before creating another longitudinal wave towards the RX. Therefore the 3<sup>rd</sup> wave detection should occur at

$$\begin{aligned}
 time_{3^{rd} \text{ detection}} &= time_{2^{nd} \text{ detection}} + T4_{\cup} + T5_{\cup} + T6_{\cup} + T7_{\cup} \\
 &= (T1_{\rightarrow} + T2_{\cup} + T3_{\rightarrow} + 2T \cdot O \cdot F_{Circumference}) \\
 &\quad + (T4_{\leftarrow} + T5_{\leftarrow} + T6_{\leftarrow} + T7_{\leftarrow}) 2T \cdot O \cdot F_{Circumference} \\
 &= T1_{\rightarrow} + T2_{\cup} + T3_{\rightarrow} + 4T \cdot O \cdot F_{Circumference}
 \end{aligned}$$

Or

$$= T_{TX \rightarrow I} + T_{I \cup D} + T_{D \rightarrow RX} + 4T \cdot O \cdot F_{Circumference}$$

Equation 67

---

Therefore if the Lamb wave have enough energy to keep bouncing back and forth, the  $time_{n^{th} detection}$  should follow the pattern

$$time_{1^{st} detection} = T_{TX \rightarrow I} + T_{I \cup D} + T_{D \rightarrow RX}$$

$$time_{2^{nd} detection} = T_{TX \rightarrow I} + T_{I \cup D} + T_{D \rightarrow RX} + 2T.O.F_{Circumference}$$

$$time_{3^{rd} detection} = T_{TX \rightarrow I} + T_{I \cup D} + T_{D \rightarrow RX} + 4T.O.F_{Circumference}$$

$$time_{n^{th} detection} = T_{TX \rightarrow I} + T_{I \cup D} + T_{D \rightarrow RX} + 2(n - 1)T.O.F_{Circumference} \quad \text{Equation 68}$$

Where n is the number of waves detected per TX pulse excitation

The equations above shows that measuring the drum's circumference should still be possible by isolating the  $T.O.F_{Circumference}$  using the peak detection as done previously Section 5.2.2 and 5.4, and the wave peaks synchronicity can be used to validate the reading.

$$\begin{aligned} time_{2^{nd} detection} - time_{1^{st} detection} &= (T_{TX \rightarrow I} + T_{I \cup D} + T_{D \rightarrow RX} + 2T.O.F_{Circumference}) - (T_{TX \rightarrow I} + T_{I \cup D} + T_{D \rightarrow RX} +) \\ &= 2T.O.F_{Circumference} \end{aligned} \quad \text{Equation 69}$$

And similarly

$$\begin{aligned}
 & \mathit{time}_{3^{rd} \text{ detection}} - \mathit{time}_{2^{nd} \text{ detection}} \\
 &= (T_{TX \rightarrow I} + T_{I \cup D} + T_{D \rightarrow RX} + 4T \cdot O \cdot F_{Circumference}) \\
 &- (T_{TX \rightarrow I} + T_{I \cup D} + T_{D \rightarrow RX} + 2T \cdot O \cdot F_{Circumference}) = \mathbf{2T \cdot O \cdot F_{Circumference}}
 \end{aligned}
 \tag{Equation 70}$$

This can be generalised as,

$$\begin{aligned}
 & \mathit{time}_{n^{th} \text{ detection}} - \mathit{time}_{(n-1)^{th} \text{ detection}} \\
 &= (T_{TX \rightarrow I} + T_{I \cup D} + T_{D \rightarrow RX} + 2(n-1)T \cdot O \cdot F_{Circumference}) \\
 &- (T_{TX \rightarrow I} + T_{I \cup D} + T_{D \rightarrow RX} + 2((n-1) - 1)T \cdot O \cdot F_{Circumference}) \\
 &= \mathbf{2T \cdot O \cdot F_{Circumference}}
 \end{aligned}
 \tag{Equation 71}$$

$$\begin{aligned}
 \therefore \mathbf{Cicumference}_{ultrasonic} &= V_{gr} \times T \cdot O \cdot F_{Circumference} \\
 &= V_{gr} \times \frac{\mathit{time}_{n^{th} \text{ detection}} - \mathit{time}_{(n-1)^{th} \text{ detection}}}{2}
 \end{aligned}
 \tag{Equation 72}$$

Now if the Rx is rotated to face the 171.85 ° to detect the longitudinal wave from the Lamb wave traveling anticlockwise, the 1<sup>st</sup> peak detection will occur at

$$\mathit{time}_{1^{st} \text{ anticlock detection}} = T1_{\rightarrow} + T2_{\cup} + T4_{\cup} + T5_{\cup} + T3_{\rightarrow}
 \tag{Equation 73}$$

The anticlockwise waves detected in this scenario should also follow a synchronous pattern which should help to validate them

$$\begin{aligned}
 time_{2^{st} anticlock detection} &= time_{1^{st} anticlock detection} + T6_{\cup} + T7_{\cup} + T4_{\cup} + T5_{\cup} \\
 &= time_{1^{st} anticlock detection} + (T4_{\ominus} + T5_{\ominus} + T6_{\ominus} + T7_{\ominus})2T.O.F_{Circumference} \\
 &= time_{1^{st} anticlock detection} + 2T.O.F_{Circumference}
 \end{aligned}$$

Equation 74

Following this pattern, the  $n^{th}$  detection should be at

$$time_{n^{th} anticlock detection} = T1_{\rightarrow} + T2_{\cup} + T4_{\cup} + T5_{\cup} + T3_{\rightarrow} + (2n)T.O.F_{Circumference}$$

Equation 75

Since  $T4_{\cup} = T5_{\cup} = T_{D\cup crack}$ , where ( $T_{D\cup crack}$ ) is the time for a Lamb wave to travel from point 'D' to the defect in the clockwise direction,

$$\begin{aligned}
 time_{n^{th} anticlock detection} &= T1_{\rightarrow} + T2_{\cup} + T4_{\ominus} + T5_{\ominus} T_{D\cup crack} + T3_{\rightarrow} + (2n)T.O.F_{Circumference} \\
 &= T_{TX \rightarrow I} + T_{I \cup D} + T_{D \rightarrow RX} + 2T_{D\cup crack} + (2n)T.O.F_{Circumference}
 \end{aligned}$$

Equation 76

To isolate  $T_{D\cup crack}$

$$\begin{aligned}
 time_{1^{st} anticlock detection} - time_{1^{st} detection} \\
 &= (T1_{\rightarrow} + T2_{\cup} + T4_{\cup} + T5_{\cup} + T3_{\rightarrow}) - (T1_{\rightarrow} + T2_{\cup} + T3_{\rightarrow}) = T4_{\cup} + T5_{\cup} \\
 &= 2T_{D\cup crack}
 \end{aligned}$$

Equation 77

---

This means that the distance between 'D' in Figure 176 and the crack/defect in the clockwise direction can be calculated using,

$$\mathit{distance}_{D\cup\text{crack}} = V_{gr} \times T_{D\cup\text{crack}} = V_{gr} \times \left( \frac{\mathit{time}_{1^{st}\text{ anticlock detection}} - \mathit{time}_{1^{st}\text{ detection}}}{2} \right)$$

Equation 78

---

### 6.5.2 Scenario 2: Defect in the path from TX to RX

If the defect occurred between the TX and RX as per Figure 178 and the RX is set to 8.15° angle of incident, then the following should apply,

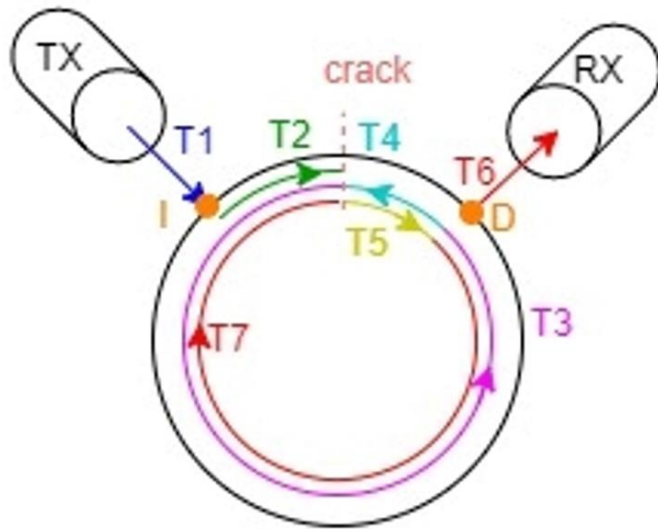


Figure 178: Illustration of wave paths to, from and around the circumference with a defect present in the shortest distance between TX and RX.

<b>TX</b>	Ultrasonic transmitter.
<b>RX</b>	Ultrasonic receiver.
<b>I</b>	Incident point where longitudinal waves induce a Lamb wave into the drum's shell.
<b>D</b>	Point where the longitudinal wave detected by the RX were generated from the travelling Lamb waves.
<b>T1→</b> <b><math>T_{TX \rightarrow I}</math></b>	T.O.F of an ultrasonic wave from TX to drum through air.
<b>T2↻</b>	T.O.F of a Lamb wave from 'I' to the crack/defect.
<b>T3↻</b>	T.O.F of the Lamb wave reflected by the crack/defect back to point 'D'.
<b>T4↻</b>	T.O.F of Lamb wave from point 'D' to opposite side of the crack/defect.
<b>T5↻</b>	T.O.F of the Lamb wave reflected by the crack back to point 'D'.
<b>T6→</b> <b><math>T_{D \rightarrow RX}</math></b>	T.O.F of longitudinal wave from point 'D' to RX through air.
<b>T7↻</b>	T.O.F of Lamb wave from point 'D' back to the crack/defect.



$$\text{Assuming a negligible defect thickness} \left\{ \begin{array}{l} T3_{\cup} + T4_{\cup} = T.O.F_{Circumference} \\ T5_{\cup} + T7_{\cup} = T.O.F_{Circumference} \\ T3 = T7 = T_{D \cup crack} \\ T2_{\cup} + T4_{\cup} = T_{I \cup D} \\ T4 = T5 \\ T2_{\cup} + T5_{\cup} = T_{I \cup D} \end{array} \right. \quad \text{Equation 79}$$

1<sup>st</sup> wave detection should occur at

$$\begin{aligned} time_{1^{st} \text{ detection}} &= T1_{\rightarrow} + T2_{\cup} + T3_{\cup} + T4_{\cup} + T5_{\cup} + T6_{\rightarrow} \\ &= T1_{\rightarrow} + (T2_{\cup} + T5_{\cup})T_{I \cup D} + (T3_{\cup} + T4_{\cup})T.O.F_{Circumference} + T6_{\rightarrow} \\ &= \mathbf{T_{TX \rightarrow I} + T_{I \cup D} + T_{D \rightarrow RX} + T.O.F_{Circumference}} \end{aligned} \quad \text{Equation 80}$$

After the 2<sup>nd</sup> detection is detected, the wave flow pattern will repeat in the same behaviour as it did from T7 to T9. This makes the 2<sup>nd</sup> peak appear

$$\begin{aligned} time_{2^{nd} \text{ detection}} &= time_{1^{st} \text{ detection}} + (T7_{\cup} + T3_{\cup} + T4_{\cup} + T5_{\cup}) \\ &= time_{1^{st} \text{ detection}} + (T7_{\cup} + T3_{\cup} + T4_{\cup} + T5_{\cup})2T.O.F_{Circumference} \\ &= \mathbf{T_{TX \rightarrow I} + T_{I \cup D} + T_{D \rightarrow RX} + 3T.O.F_{Circumference}} \end{aligned} \quad \text{Equation 81}$$

And the 3<sup>rd</sup> wave detection should occur at

$$\begin{aligned}
 time_{3^{rd} \text{ detection}} &= time_{2^{nd} \text{ detection}} + (T_{7\cup} + T_{3\cup} + T_{4\cup} + T_{5\cup}) \\
 &= time_{2^{nd} \text{ detection}} + (T_{7\cup} + T_{3\cup} + T_{4\cup} + T_{5\cup})2T.O.F_{Circumference} = \\
 &= T_{TX \rightarrow I} + T_{I\cup D} + T_{D \rightarrow RX} + 5T.O.F_{Circumference}
 \end{aligned}$$

Equation 82

Therefore if the Lamb wave has enough energy to keep bouncing back and forth, the  $time_{n^{th} \text{ detection}}$  should follow the pattern

$$\begin{aligned}
 time_{1^{st} \text{ detection}} &= T_{TX \rightarrow I} + T_{I\cup D} + T_{D \rightarrow RX} + T.O.F_{Circumference} \\
 time_{2^{nd} \text{ detection}} &= T_{TX \rightarrow I} + T_{I\cup D} + T_{D \rightarrow RX} + 3T.O.F_{Circumference} \\
 time_{3^{rd} \text{ detection}} &= T_{TX \rightarrow I} + T_{I\cup D} + T_{D \rightarrow RX} + 5T.O.F_{Circumference}
 \end{aligned}$$

$$\therefore time_{n^{th} \text{ detection}} = T_{TX \rightarrow I} + T_{I\cup D} + T_{D \rightarrow RX} + (2n - 1)T.O.F_{Circumference}$$

Equation 83

Again, in this scenario the equations above show that circumference measurements should still be possible by isolating the  $T.O.F_{Circumference}$  using,

$$\begin{aligned}
 time_{n^{th} \text{ detection}} - time_{(n-1)^{th} \text{ detection}} &= (T_{TX \rightarrow I} + T_{I\cup D} + T_{D \rightarrow RX} + (2n - 1)T.O.F_{Circumference}) \\
 &- (T_{TX \rightarrow I} + T_{I\cup D} + T_{D \rightarrow RX} + (2(n - 1) - 1)T.O.F_{Circumference}) \\
 &= 2T.O.F_{Circumference}
 \end{aligned}$$

Equation 84

---


$$\begin{aligned}
Circumference_{ultrasonic} &= V_{gr} \times T.O.F_{Circumference} \\
&= V_{gr} \times \left( \frac{\mathbf{time}_{n^{th} \text{ detection}} - \mathbf{time}_{(n-1)^{th} \text{ detection}}}{2} \right)
\end{aligned}$$

Equation 85

---

If the Rx is rotated to face the  $171.85^\circ$  to detect the longitudinal wave from the Lamb wave traveling anticlockwise only, the 1<sup>st</sup> peak detection will occur at

$$\mathbf{time}_{1^{st} \text{ anticlock detection}} = T1_{\rightarrow} + T2_{\cup} + T3_{\cup} + T6_{\rightarrow}$$

Equation 86

---


$$\begin{aligned}
\mathbf{time}_{2^{st} \text{ anticlock detection}} &= \mathbf{time}_{1^{st} \text{ anticlock detection}} + T4_{\cup} + T5_{\cup} + T7_{\cup} + T3_{\cup} \\
&= T1_{\rightarrow} + T2_{\cup} + T3_{\cup} + T6_{\rightarrow} + (T4_{\cup} + T5_{\cup} + T7_{\cup} + T3_{\cup}) 2T.O.F_{Circumference} \\
&= \mathbf{T1}_{\rightarrow} + \mathbf{T2}_{\cup} + \mathbf{T3}_{\cup} + \mathbf{T6}_{\rightarrow} + \mathbf{2T.O.F}_{Circumference}
\end{aligned}$$

Equation 87

---


$$\begin{aligned}
\mathbf{time}_{3^{rd} \text{ anticlock detection}} &= \mathbf{time}_{2^{nd} \text{ anticlock detection}} + T4_{\cup} + T5_{\cup} + T7_{\cup} + T3_{\cup} \\
&= \mathbf{T1}_{\rightarrow} + \mathbf{T2}_{\cup} + \mathbf{T3}_{\cup} + \mathbf{T6}_{\rightarrow} + \mathbf{4T.O.F}_{Circumference}
\end{aligned}$$

Equation 88

---

---

Therefore if the Lamb wave have enough energy to keep bouncing back and forth, the  $\text{time}_{n^{\text{th}} \text{ anticlock detection}}$  should follow the pattern

$$\text{time}_{1^{\text{st}} \text{ anticlock detection}} = T_{1 \rightarrow} + T_{2 \cup} + T_{3 \cup} + T_{6 \rightarrow}$$

$$\text{time}_{2^{\text{st}} \text{ anticlock detection}} = T_{1 \rightarrow} + T_{2 \cup} + T_{3 \cup} + T_{6 \rightarrow} + 2T \cdot O \cdot F_{\text{Circumference}}$$

$$\text{time}_{3^{\text{rd}} \text{ anticlock detection}} = T_{1 \rightarrow} + T_{2 \cup} + T_{3 \cup} + T_{6 \rightarrow} + 4T \cdot O \cdot F_{\text{Circumference}}$$

$$\therefore \text{time}_{n^{\text{th}} \text{ anticlock detection}} = T_{1 \rightarrow} + T_{2 \cup} + T_{3 \cup} + T_{6 \rightarrow} + 2(n - 1)T \cdot O \cdot F_{\text{Circumference}}$$

Equation 89

---

Based on the conditions in Equation 79,

$$\begin{aligned} T_{2 \cup} &= T_{\text{IUD}} - T_{4 \cup} = T_{\text{IUD}} - (T \cdot O \cdot F_{\text{Circumference}} - T_{3 \cup} T_{\text{D}\cup\text{crack}}) \\ &= T_{\text{IUD}} - T \cdot O \cdot F_{\text{Circumference}} + T_{\text{D}\cup\text{crack}} \end{aligned}$$

Equation 90

---

---


$$\begin{aligned}
\text{time}_{n^{\text{th anticlock detection}}} &= T_{1\rightarrow} + T_{2\cup} + T_{3\cup} + T_{6\rightarrow} + 2(n-1)T.O.F_{\text{Circumference}} \\
&= (T_{1\rightarrow})T_{TX\rightarrow I} + T_{2\cup}(T_{I\cup D} - T.O.F_{\text{Circumference}} + T_{D\cup\text{crack}}) + T_{3\cup}T_{D\cup\text{crack}} \\
&\quad + T_{6\rightarrow}T_{D\rightarrow RX} + 2(n-1)T.O.F_{\text{Circumference}} \\
&= T_{TX\rightarrow I} + T_{I\cup D} - T.O.F_{\text{Circumference}} + T_{D\cup\text{crack}} + T_{D\cup\text{crack}} + T_{D\rightarrow RX} \\
&\quad + 2(n-1)T.O.F_{\text{Circumference}} \\
&= T_{TX\rightarrow I} + T_{I\cup D} - T.O.F_{\text{Circumference}} + 2T_{D\cup\text{crack}} + T_{D\rightarrow RX} \\
&\quad + 2(n-1)T.O.F_{\text{Circumference}} \\
&= \mathbf{T_{TX\rightarrow I} + T_{I\cup D} + T_{D\rightarrow RX} + 2T_{D\cup\text{crack}} + (-3 + 2n)T.O.F_{\text{Circumference}}
\end{aligned}$$

Equation 91

---

To isolate  $T_{D\cup\text{crack}}$  to locate the crack/defect distance from point 'I' in the clockwise direction,

$$\begin{aligned}
\mathbf{time}_{1^{\text{st anticlock detection}}} - \mathbf{time}_{1^{\text{st detection}}} & \\
&= (T_{1\rightarrow} + T_{2\cup} + T_{3\cup} + T_{6\rightarrow}) - (T_{1\rightarrow} + T_{2\cup} + T_{3\cup} + T_{4\cup} + T_{5\cup} + T_{6\rightarrow}) \\
&= -(T_{4\cup} + T_{5\cup}) = \mathbf{-2T_{D\cup\text{crack}}}
\end{aligned}$$

Equation 92

Note: The outcome of this operation is a negative value, this will be useful later in identifying the scenarios from observed data.

---

---

Finally using Equation 92 the absolute distance between point 'D' and the defect/crack can be calculated using,

$$\mathbf{distance}_{D\cup\text{crack}} = V_{gr} \times T_{D\cup\text{crack}} = V_{gr} \times \left( \frac{\mathbf{time}_{1^{st}\text{ anticlock detection}} - \mathbf{time}_{1^{st}\text{ detection}}}{-2} \right) \quad \text{Equation 93}$$

### 6.5.3 Scenario 3: Multiple defects presence after the first RX detection point

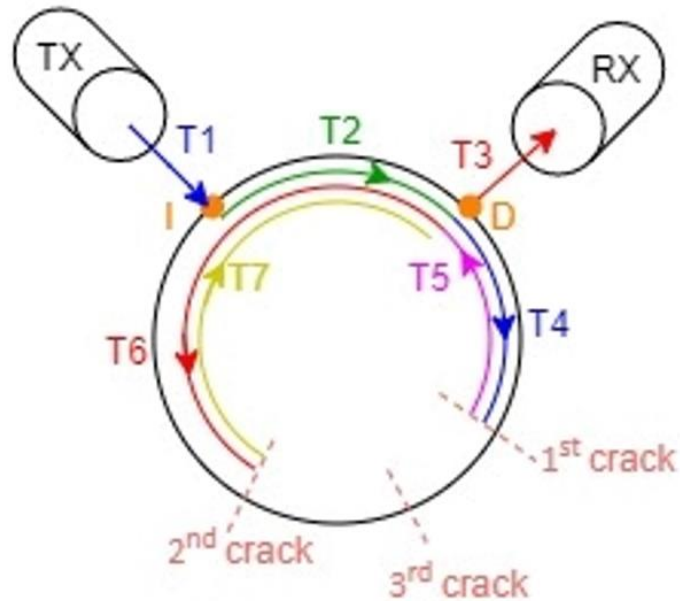


Figure 179: Illustration of wave paths to, from and around the circumference of a cracked/defected drum with 2 or more defects on one side between the TX and RX

<b>TX</b>	Ultrasonic transmitter.
<b>RX</b>	Ultrasonic receiver.
<b>I</b>	Incident point where longitudinal waves induce a Lamb wave into the drum's shell
<b>D</b>	Point where the longitudinal wave detected by the RX were generated from the travelling Lamb waves.
<b>T1→</b>	T.O.F of a longitudinal wave from TX to 'I' through air.
<b><math>T_{TX \rightarrow I}</math></b>	
<b>T2↻</b>	T.O.F of a Lamb wave from 'I' to 'D' along drum circumference
<b><math>T_{I \rightarrow D}</math></b>	
<b>T3→</b>	T.O.F of longitudinal wave from 'D' to RX through air
<b><math>T_{D \rightarrow RX}</math></b>	
<b>T4↻</b>	T.O.F of Lamb wave from point 'D' to the 1 <sup>st</sup> crack
<b>T5↻</b>	T.O.F of the Lamb wave reflected by the 1 <sup>st</sup> crack back to point 'D'
<b>T6↻</b>	T.O.F of the Lamb wave reflected by the 1 <sup>st</sup> crack from point 'D' to the 2 <sup>nd</sup> crack
<b>T7↻</b>	T.O.F of Lamb wave reflected by the 2 <sup>nd</sup> crack back to point 'D'

In the same way of processing the wave detection time in the previous scenarios, the 1<sup>st</sup> wave detection in scenario 3 should occur at

$$\text{Assuming a negligible defect thickness} \begin{cases} T5_{\cup} + T6_{\cup} < T.O.F_{Circumference} \\ T4_{\cup} + T7_{\cup} < T.O.F_{Circumference} \\ T4 = T5 = T_{D\cup crack} \\ T7_{\cup} = T6_{\cup} = T_{D\cup crack} \end{cases} \quad \text{Equation 94}$$

1<sup>st</sup> wave detection should occur at

$$time_{1^{st} detection} = T1_{\rightarrow} + T2_{\cup} + T3_{\rightarrow} \quad \text{Equation 95}$$

and the 2<sup>nd</sup> wave detection should occur at

$$time_{2^{nd} detection} = time_{1^{st} detection} + T4_{\cup} + T5_{\cup} + T6_{\cup} + T7_{\cup} \quad \text{Equation 96}$$

From there, the waves will repeat the same pattern from T4 to T7 as they bounce back and forth by the defect before creating another longitudinal wave towards the RX, and so the 3<sup>rd</sup> wave detection should occur at

$$time_{3^{rd} detection} = time_{2^{nd} detection} + T4_{\cup} + T5_{\cup} + T6_{\cup} + T7_{\cup} \quad \text{Equation 97}$$

And so, the n<sup>th</sup> wave will be at

$$\begin{aligned} \therefore time_{n^{th} detection} &= T1_{\rightarrow} + T2_{\cup} + T3_{\rightarrow} + n(T4_{\cup} + T5_{\cup} + T6_{\cup} + T7_{\cup}) \\ &= \mathbf{T_{TX \rightarrow I} + T_{I \cup D} + T_{D \rightarrow RX} + n(T4_{\cup} + T5_{\cup} + T6_{\cup} + T7_{\cup})} \end{aligned} \quad \text{Equation 98}$$



$T.O.F_{Circumference}$  will not occur in this scenario because the gap between the 1<sup>st</sup> and 2<sup>nd</sup> defect will be a blind zone where the waves do not travel to. This means that the detection times in this scenario cannot be used to isolate the  $T.O.F_{Circumference}$ , and if a 3<sup>rd</sup> defect occurs between in the blind zone between the 1<sup>st</sup> and 2<sup>nd</sup> defect, it will not be detectable in this simplistic scenario.

$$(T4_{\cup} + T5_{\cup} + T6_{\cup} + T7_{\cup}) < 2(T.O.F_{Circumference}) \quad \text{Equation 99}$$

$$\therefore \mathbf{time}_{n^{th} \text{ detection}} = T_{TX \rightarrow I} + T_{I \cup D} + T_{D \rightarrow RX} + n \left( < 2(T.O.F_{Circumference}) \right) \quad \text{Equation 100}$$

Now if the Rx is rotated to face the 171.85° to detect the longitudinal waves from the Lamb wave traveling anticlockwise, the 1<sup>st</sup> peak detection will occur at

$$\mathbf{time}_{1^{st} \text{ anticlock detection}} = T1_{\rightarrow} + T2_{\cup} + T4_{\cup} + T5_{\cup} + T3_{\rightarrow} \quad \text{Equation 101}$$

From there, the wave will follow the same route from  $T6_{\cup}$ ,  $T7_{\cup}$ ,  $T4_{\cup}$  and  $T5_{\cup}$  before getting detected again. So,

$$\mathbf{time}_{2^{nd} \text{ anticlock detection}} = \mathbf{time}_{1^{st} \text{ anticlock detection}} + T6_{\cup} + T7_{\cup} + T4_{\cup} + T5_{\cup} \quad \text{Equation 102}$$

---

Makes the  $n^{\text{th}}$  detection,

$$\begin{aligned} \text{time}_{n^{\text{th}} \text{ anticlock detection}} &= (T_{1 \rightarrow} + T_{2 \cup} + T_{4 \cup} + T_{5 \cup} + T_{3 \rightarrow}) + n(T_{6 \cup} + T_{7 \cup} + T_{4 \cup} + T_{5 \cup}) \\ &= (T_{TX \rightarrow I} + T_{I \cup D} + T_{D \rightarrow RX} + T_{4 \cup} + T_{5 \cup} + 2T_{D \cup \text{crack}}) \\ &\quad + n \left( < 2(T \cdot O \cdot F_{\text{Circumference}}) \right) \\ &= T_{TX \rightarrow I} + T_{I \cup D} + T_{D \rightarrow RX} + 2T_{D \cup \text{crack}} + n \left( < 2(T \cdot O \cdot F_{\text{Circumference}}) \right) \end{aligned} \quad \text{Equation 103}$$

---

To isolate  $T_{D \cup \text{crack}}$ .

$$\begin{aligned} \text{time}_{1^{\text{st}} \text{ anticlock detection}} - \text{time}_{1^{\text{st}} \text{ detection}} & \\ &= (T_{1 \rightarrow} + T_{2 \cup} + T_{4 \cup} + T_{5 \cup} + T_{3 \rightarrow}) - (T_{1 \rightarrow} + T_{2 \cup} + T_{3 \rightarrow}) = T_{4 \cup} + T_{5 \cup} \\ &= 2T_{D \cup \text{crack}} \end{aligned} \quad \text{Equation 104}$$

---

This means that the distance between point 'D' and the first crack/defect in the clockwise direction is,

$$\text{distance}_{D \cup \text{crack}} = V_{gr} \times T_{D \cup \text{crack}} = V_{gr} \times \left( \frac{\text{time}_{1^{\text{st}} \text{ anticlock detection}} - \text{time}_{1^{\text{st}} \text{ detection}}}{2} \right) \quad \text{Equation 105}$$

### 6.5.4 Scenario 4: Multiple defects surrounding the RX detection point

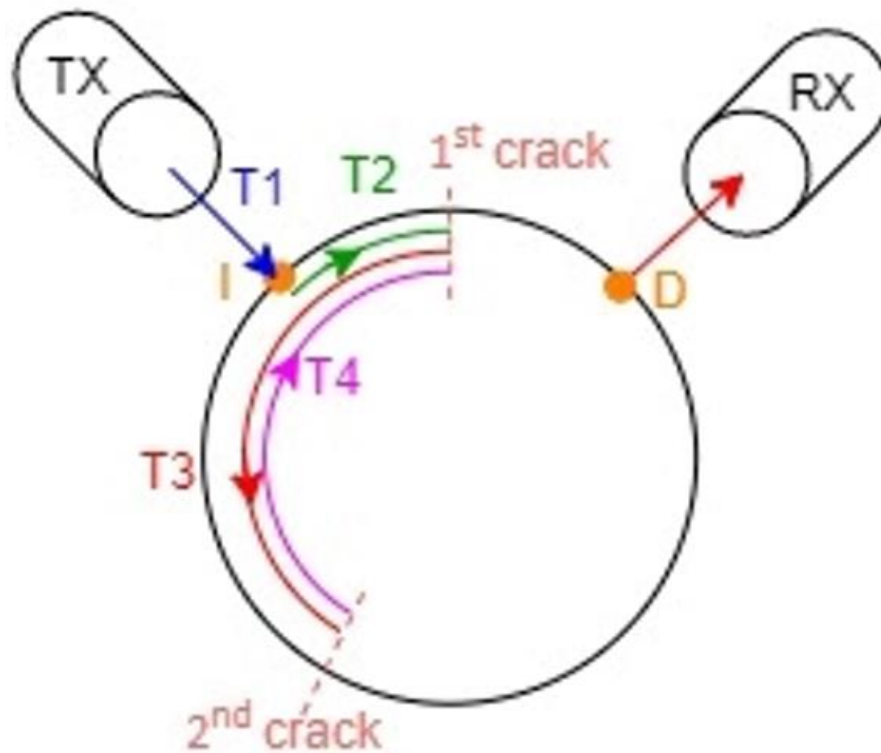


Figure 180: Illustration of wave paths to, and around the circumference of a cracked drum with cracks on both side between the TX an RX

<b>TX</b>	Ultrasonic transmitter.
<b>RX</b>	Ultrasonic receiver.
<b>I</b>	Incident point where longitudinal waves induce a Lamb wave into the drum's shell.
<b>D</b>	Point where the longitudinal wave detected by the RX were generated from the travelling Lamb waves.
<b>T1→</b> <i>T<sub>TX→I</sub></i>	T.O.F of an ultrasonic wave from TX to drum through air.
<b>T2↻</b>	T.O.F of a clockwise Lamb wave from 'I' to the 1 <sup>st</sup> crack along the drum circumference.
<b>T3↻</b>	T.O.F of the Lamb wave reflected by the 1 <sup>st</sup> crack back to the 2 <sup>nd</sup> crack along drum circumference.
<b>T4↻</b>	T.O.F of the Lamb wave reflected by the 2 <sup>nd</sup> crack back to the 1 <sup>st</sup> crack along drum circumference.

In the scenario where there are defects in both directions between the TX and RX, the Lamb waves will bounce back and forth between the two defects and will not reach point 'D' to create longitudinal waves for the RX to detect. Therefore, there will be no expected wave detections to use for circumferential measurements or defect detection.

### 6.5.5 Processing detection patterns

Given that the anticlockwise waves in all the scenarios above are a result of a reflection from defects, it will be safe to assume the presence of any anticlockwise Lamb wave is an indication of the presence of a defect.

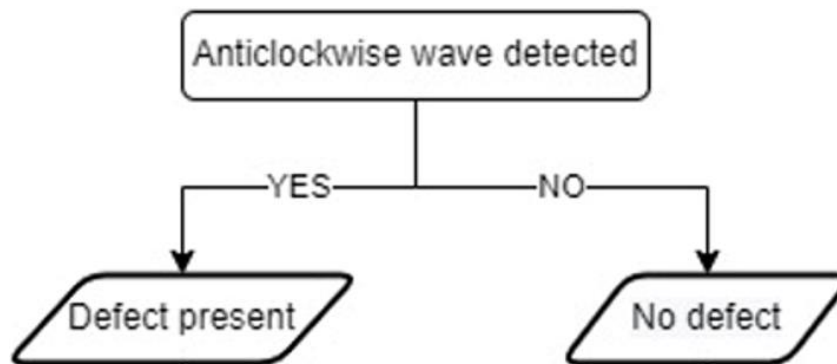


Figure 181: First stage of a flow chart to identify defects along the circumference of an ILW 500 L drum.

In real life, the Lamb waves will disperse as they flow into the medium and not be confined in the thin cross section assumed in the four defect scenarios described so far. If the width of the Lamb waves travelling across the cross section is wider than the defect, a portion of the wave will pass by or next to the defect and keep moving forward around the drum circumference without being reflected creating another detectable set of waves past the defect with a detection time pattern  $time_{n^{th}} \text{ escaped detection}$ .

The escaped waves will act as the normal forward moving waves from Figure 118 with a constant pattern,

$$\begin{aligned} \mathit{time}_{n^{\text{th}} \text{ escaped detection}} &= \mathit{time}_{n^{\text{th}} \text{ detection}} \\ &= T_{TX \rightarrow I} + T_{I \cup D} + T_{D \rightarrow RX} + (n - 1) T.O.F_{\text{Circumference}} \end{aligned} \quad \text{Equation 106}$$

This pattern will overlap with the patterns described in all the scenarios analysed so far, therefore there will always be peak detections at  $\mathit{time}_{1^{\text{st}} \text{ escaped detection}} = T_{TX \rightarrow I} + T_{I \cup D} + T_{D \rightarrow RX}$  followed by a detection every  $T.O.F_{\text{Circumference}}$ .

	$\mathit{time}_{n^{\text{th}} \text{ detection}}$	$\mathit{time}_{1^{\text{st}} \text{ anticlock detection}}$
No defect	$T_{TX \rightarrow I} + T_{I \cup D} + T_{D \rightarrow RX} + (n - 1)T.O.F_{\text{Circumference}}$	0
Scenario 1	$T_{TX \rightarrow I} + T_{I \cup D} + T_{D \rightarrow RX} + 2(n - 1)T.O.F_{\text{Circumference}}$	$T_{TX \rightarrow I} + T_{I \cup D} + T_{D \rightarrow RX} + 2T_{D \cup \text{crack}} + (2n)T.O.F_{\text{Circumference}}$
Scenario 2	$T_{TX \rightarrow I} + T_{I \cup D} + T_{D \rightarrow RX} + (2n - 1)T.O.F_{\text{Circumference}}$	$T_{TX \rightarrow I} + T_{I \cup D} + T_{D \rightarrow RX} + 2T_{D \cup \text{crack}} + (-3 + 2n)T.O.F_{\text{Circumference}}$
Scenario 3	$T_{TX \rightarrow I} + T_{I \cup D} + T_{D \rightarrow RX} + n \left( < 2(T.O.F_{\text{Circumference}}) \right)$	$T_{TX \rightarrow I} + T_{I \cup D} + T_{D \rightarrow RX} + 2T_{D \cup \text{crack}} + n \left( < 2(T.O.F_{\text{Circumference}}) \right)$
Scenario 4	0	0

The clockwise wave patterns ( $time_{n^{th} detection}$ ) in all the scenarios except Scenario 4 start with  $T_{TX \rightarrow I} + T_{I \cup D} + T_{D \rightarrow RX}$  followed by a multiple of  $T.O.F_{Circumference}$ . However, if we consider the escaped waves pattern  $time_{n^{th} escaped detection} = T_{TX \rightarrow I} + T_{I \cup D} + T_{D \rightarrow RX} + (n - 1) T.O.F_{Circumference}$ , which will overlap all 4 defected scenarios patterns. The 1<sup>st</sup> peak detection in both defected and non-defected scenarios will always occur at  $T_{TX \rightarrow I} + T_{I \cup D} + T_{D \rightarrow RX} + T.O.F_{Circumference}$  seconds. This will prevent the use the clockwise detection in defect detection if a portion of the clockwise waves bypass the defect except for Scenario 3, because the multiples in Scenario 3 are  $< 2(T.O.F_{Circumference})$  and not full  $T.O.F_{Circumference}$ . The difference between the  $T.O.F_{Circumference}$  pattern and  $< 2(T.O.F_{Circumference})$  pattern will be observed as a phase shift between the two patterns as described in Figure 182.

Scenario 3		
n	$time_{n^{th} escaped detection}$	$time_{n^{th} detection}$
1	$T_{TX \rightarrow I} + T_{I \cup D} + T_{D \rightarrow RX}$	$T_{TX \rightarrow I} + T_{I \cup D} + T_{D \rightarrow RX} + (< 2(T.O.F_{Circumference}))$
2	$T_{TX \rightarrow I} + T_{I \cup D} + T_{D \rightarrow RX} + T.O.F_{Circumference}$	$T_{TX \rightarrow I} + T_{I \cup D} + T_{D \rightarrow RX} + 2 (< 2(T.O.F_{Circumference}))$
3	$T_{TX \rightarrow I} + T_{I \cup D} + T_{D \rightarrow RX} + 2T.O.F_{Circumference}$	$T_{TX \rightarrow I} + T_{I \cup D} + T_{D \rightarrow RX} + 3 (< 2(T.O.F_{Circumference}))$

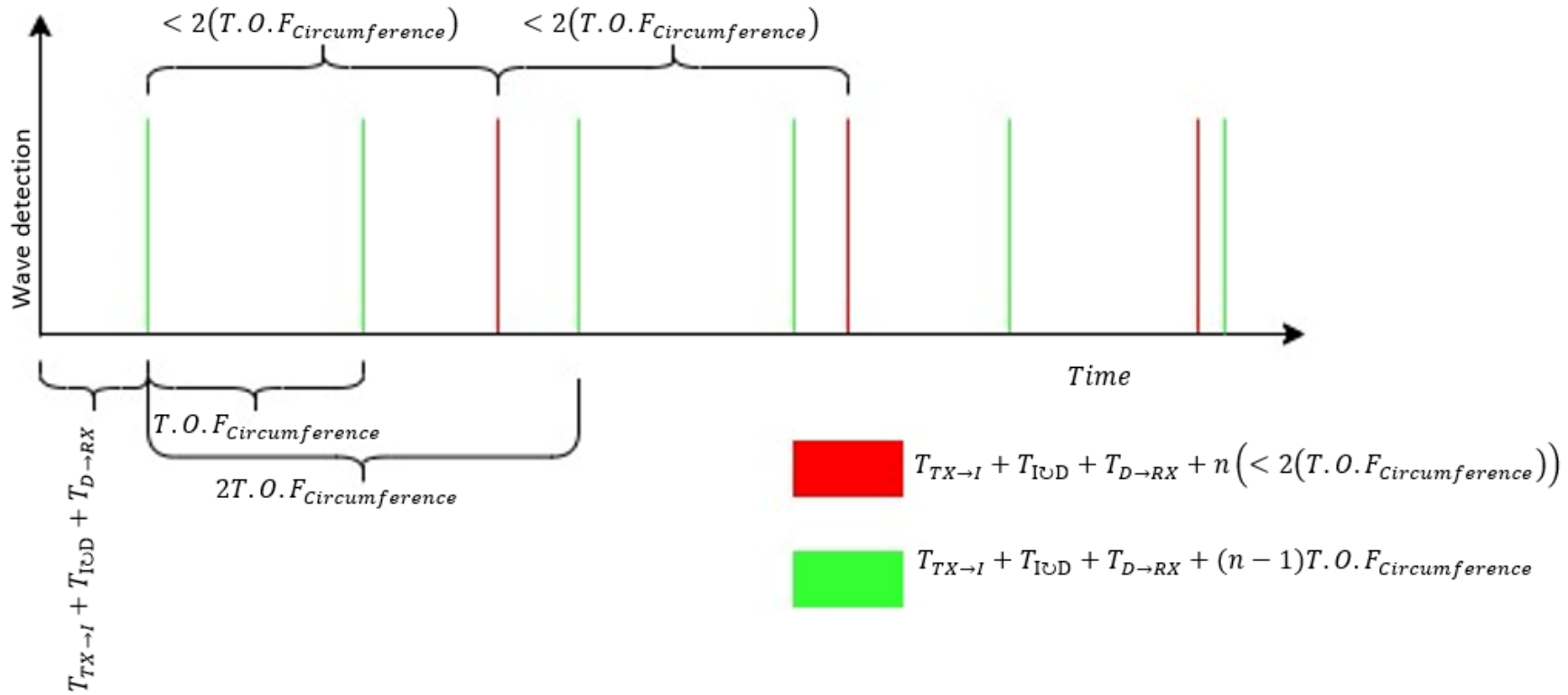


Figure 182: Scenario 3 clockwise wave pater from the initial wave (red) and wave pattern from the  $time_{n^{th}}$  escaped detection waves (green).

Similarly, some of the  $time_{n^{th} \text{ escaped detection}}$  waves in Scenario 4 have a chance of interacting with the defects as they bounce around, they will form multiple patterns of their own, creating different sets of phase shifted patterns like that of Figure 182. Consequently, the presence of phase shifted patterns that do not follow  $T.O.F_{Circumference}$  gaps between the detections will be the identifier for both Scenarios 3 and 4. To observe and validate the phase shifted peaks in Figure 183, a minimum of 5 synchronous  $T.O.F_{Circumference}$  and a pair of phase synchronous peaks will need to be detectable. This will not be the case Scenario 1 and 2  $time_{n^{th} \text{ escaped detection}}$  because the  $time_{n^{th} \text{ escaped detection}}$  will overlap the  $time_{n^{th} \text{ detection}}$ , and thus no phase shifted patterns will be observed.

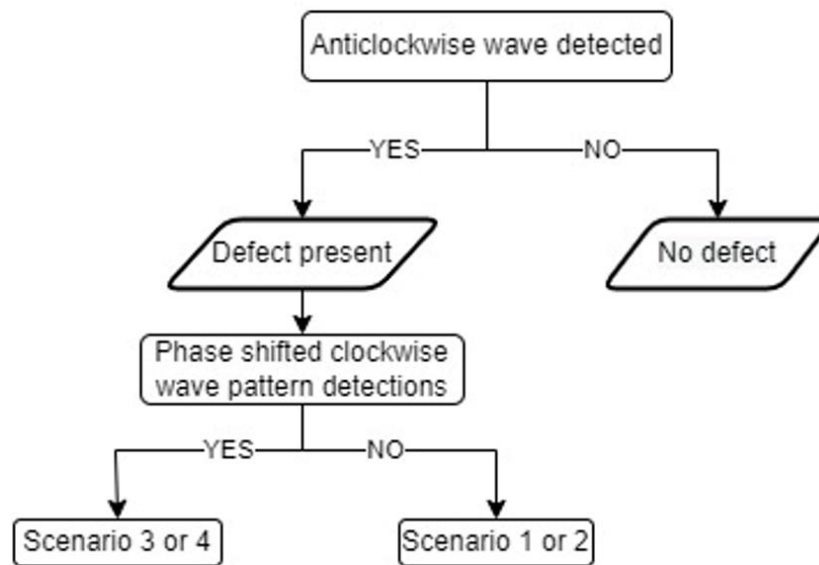


Figure 183: Second stage of a flow chart to identify the defect scenario along the circumference of an ILW 500 L drum.

Measuring the circumference in Scenarios 1 and 2, used the same equation (Equation 72 and Equation 85).

$$Circumference_{ultrasonic} = V_{gr} \times \left( \frac{time_{n^{th} \text{ detection}} - time_{(n-1)^{th} \text{ detection}}}{2} \right) \quad \begin{array}{l} \text{Equation 72} \\ \text{Equation 85} \end{array}$$



This will only be true if there are no  $time_{n^{th} \text{ escaped detection}}$  and the wave is completely reflected, because the  $time_{n^{th} \text{ escaped detection}} = T_{TX \rightarrow I} + T_{I \cup D} + T_{D \rightarrow RX} + (n - 1) T \cdot O \cdot F_{Circumference}$  pattern will overlap the scenarios  $time_{n^{th} \text{ detection}}$  pattern and so the  $Cicumference_{ultrasonic}$  will be the same as the non-defected drum. Since the  $time_{n^{th} \text{ escaped detection}}$  pattern is identical to that of the non-defected drum, the  $Cicumference_{ultrasonic}$  can be calculated using Equation 35,

$$\begin{aligned}
 Cicumference_{ultrasonic} &= V_{gr} \\
 &\times (time_{n^{th} \text{ detection}} - time_{(n-1)^{th} \text{ detection}})
 \end{aligned}
 \tag{Equation 35}$$

Therefore if

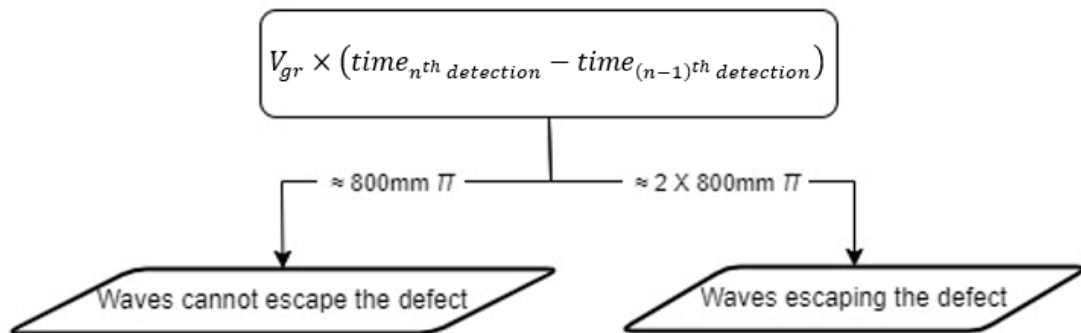


Figure 184: Identifying if the Lamb wave is able to bypasses(escape) through or around the defect.

Defects that are large enough to reflect the wave completely and not allow any defects to pass are likely to be larger and deeper than the defect that let them escape, thus should be flagged as higher risk defect.

In Scenarios 1 and 2, Equation 78 and Equation 93 that were used to calculate the distance from the detection point to the defect ( $distance_{D \cup crack}$ ) were identical except for the polarity of their divider calculated using Equation 35,

Scenario 1:

$$\begin{aligned}
 distance_{D\cup crack} &= V_{gr} \times T_{D\cup crack} \\
 &= V_{gr} \times \left( \frac{time_{1^{st} anticlock detection} - time_{1^{st} detection}}{2} \right)
 \end{aligned}$$

Equation 78

---

Scenario 2:

$$\begin{aligned}
 distance_{D\cup crack} &= V_{gr} \times T_{D\cup crack} \\
 &= V_{gr} \times \left( \frac{time_{1^{st} anticlock detection} - time_{1^{st} detection}}{-2} \right)
 \end{aligned}$$

Equation 93

Therefore  $distance_{crack}$  can be used to identify between Scenarios 1 and 2 based on the result's polarity.

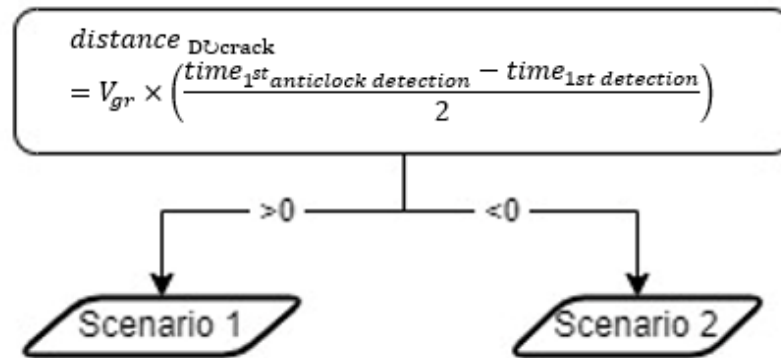


Figure 185: Identifying the difference between Scenario 1 and 2 based on the  $distance_{D\cup crack}$  polarity.

Finally, given that the standard ILW 500 L drum circumference is  $800\pi$  mm,  $Cicumference_{ultrasonic} > 800\pi$  mm should be an indicator of a wasteform expansion stretching out the drum's structure. The overall defect identification chart can be presented as following,

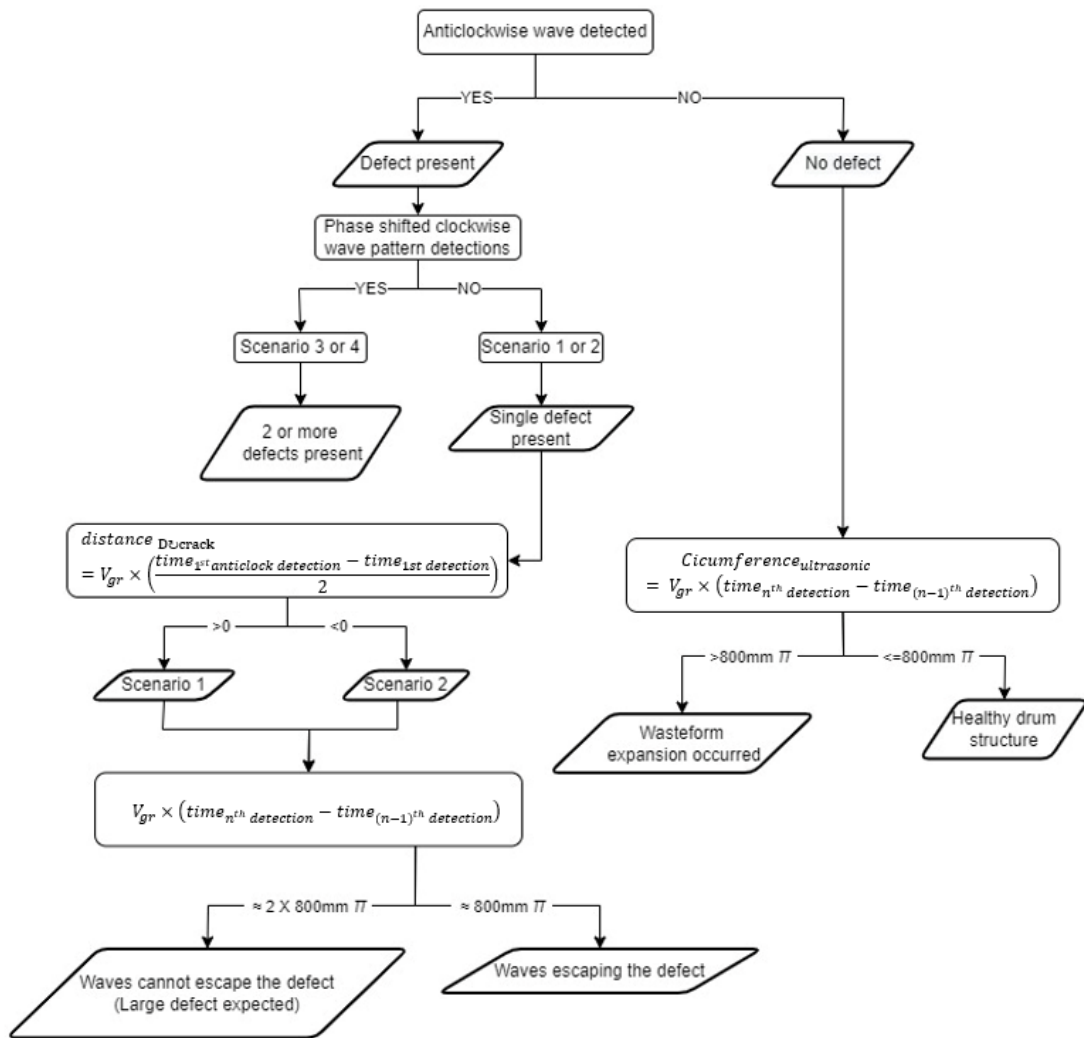


Figure 186: Flow chart to identify the defect scenario along the circumference of an ILW 500 L drum.

### 6.5.6 Reflected wave validation

To validate if the waves reflected by the discontinuity defect can only be detected if the RX angle is opposite to that used in the circumferential measurements as suggested in Figure 177. A test sample was created with an intentional defect to test the defect detection process proposed. The defect was created in the form of a discontinuity in the welding process of the sample as per Figure 187. This was intended to simulate a crack caused by wastefrom expansion, or stress corrosion cracking. The discontinuity was created during the welding process of the rolled sheet, to avoid the use of cutting tools in the creation of the defect, to create the smallest gap possible between the two sides of the discontinuity gap.

If the cylindrical shape was created as per Figure 124 and the discontinuity defect was then introduced using a cutting tool, the discontinuity gap will only be as thin as the cutting tools available.

Moreover, by eliminating the cutting tool thickness, and allowing the two sides of the discontinuity to touch, the Lamb waves may be able to travel from one side of the gap to the other, and not be stopped by the defect. This will validate the theory proposed in 6.5.5 where the wave can by bypass(escape) the defect and not get detected by the system.

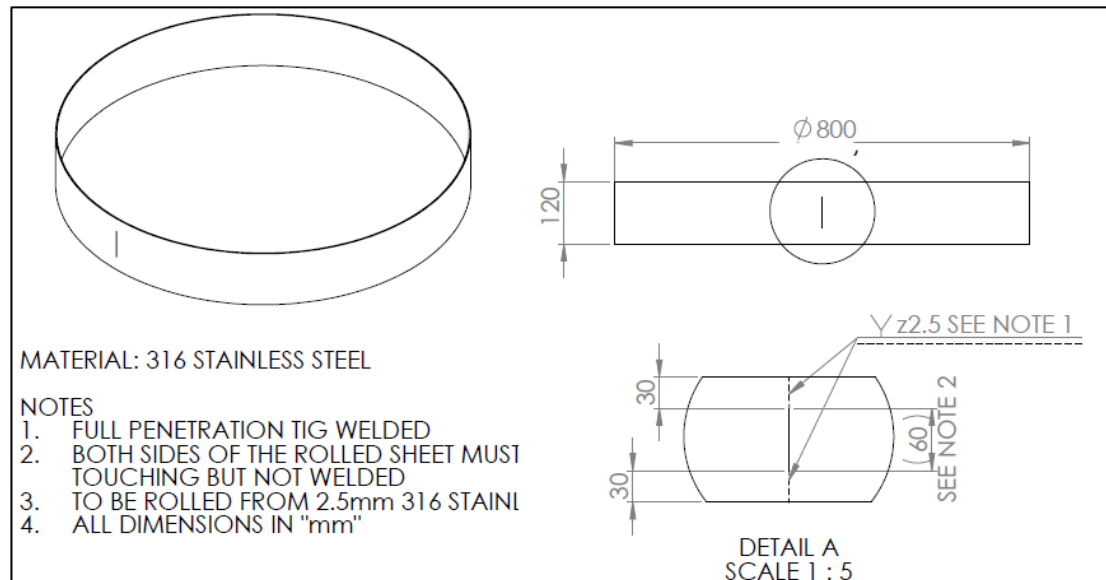


Figure 187: Manufacturing drawing used to fabricate the intentionally defected sample. (Figure is not scale)

**Note:** Despite the discontinuity defect in the test being introduced at the welding stage of fabricating the cylindrical sample, this test was created to validate the discontinuity defect in an aged drum only, and not to detect discontinuity in an unused drums or welds processes. Unused drums' weld seams are expected to be tested by the manufacturer or other parties prior to deployment.

The test used the setup configuration described in Section 5.3 Figure 111 and the new defected sample was used as the workpiece. The TX and RX were place on either side of the defect as per Figure 188.

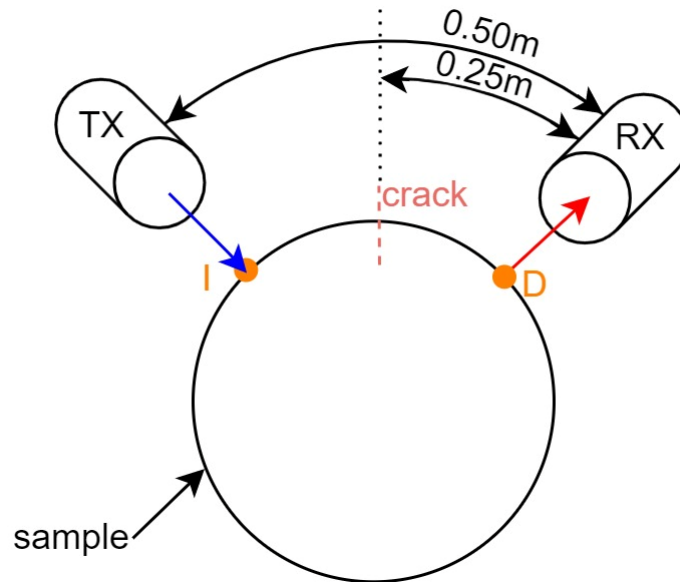


Figure 188: Layout of the ultrasonic transducers TX and RX in relation to the defect.

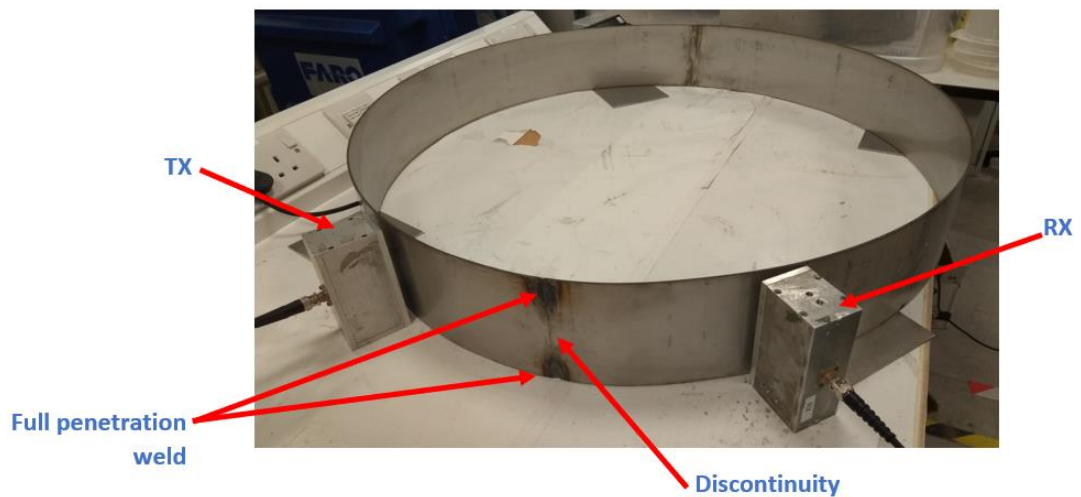


Figure 189: Defected 800m diameter 316L stainless-steel sample being inspected using a pair of air-coupled ultrasonic transducers.

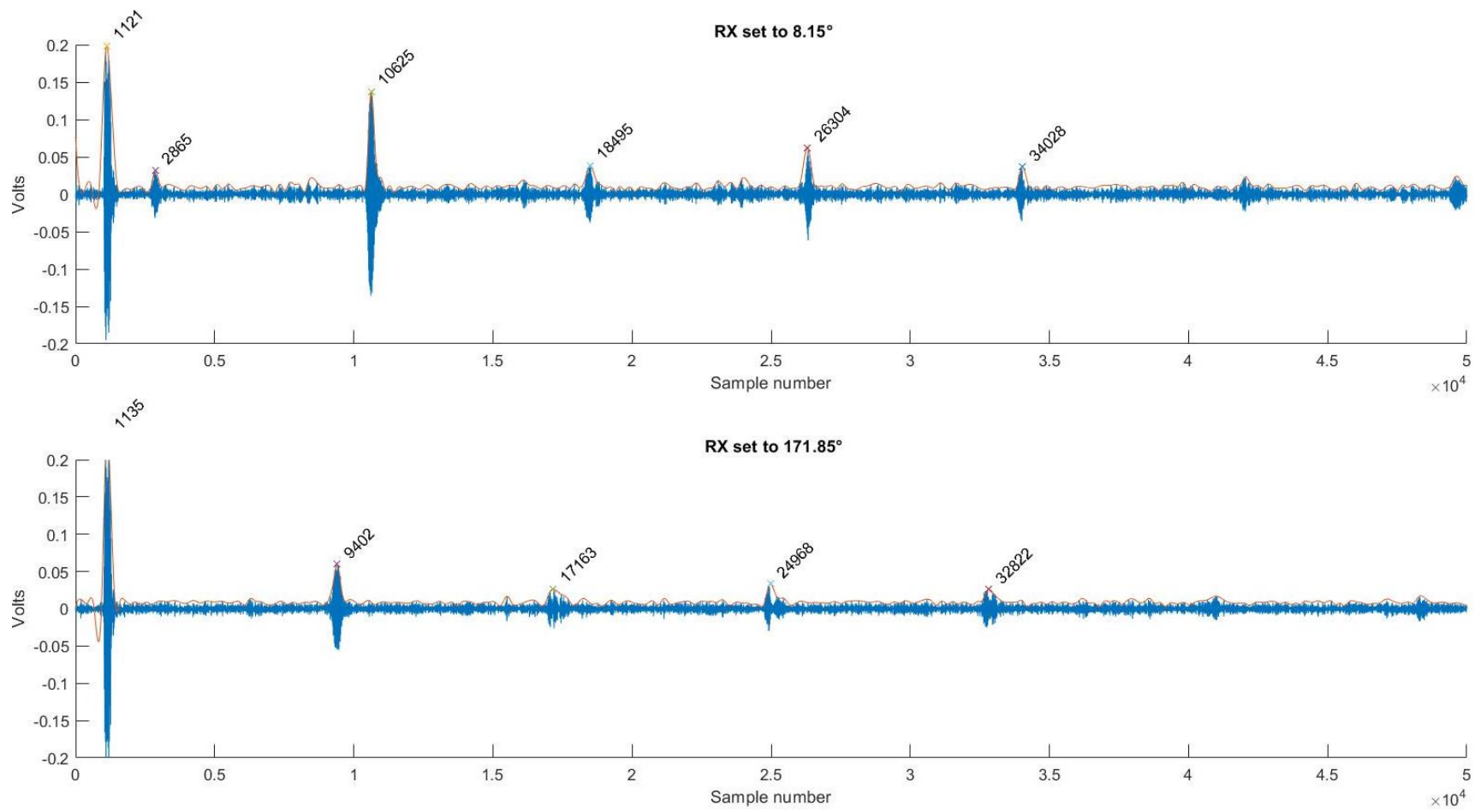


Figure 190: (Top) Lamb wave detections with the transducer RX pointing towards the TX at 8.15 °. (Bottom) Lamb wave detections with the transducer RX pointing towards the reflections at 171.15 °.

The defect was placed between the TX and RX as per Scenario 2 in Section 6.5.2 to give the Lamb wave the least favourable chance of being detected by the RX at 8.15 ° in a single defect scenario. Figure 190 shows that the Lamb wave did bypass the defect and get detected by the RX as normal at 8.15 °. In Scenario 2,

$$\mathit{time}_{n^{\text{th}} \text{ detection}} = T_{TX \rightarrow I} + T_{I \cup D} + T_{D \rightarrow RX} + (2n - 1)T.O.F_{\text{Circumference}} \quad \text{Equation 89}$$

and

$$\mathit{time}_{n^{\text{th}} \text{ escaped detection}} = T_{TX \rightarrow I} + T_{I \cup D} + T_{D \rightarrow RX} + (n - 1)T.O.F_{\text{Circumference}} \quad \text{Equation 106}$$

This means that  $\mathit{time}_{n=1 \text{ escaped detection}}$  will occur first then,  $\mathit{time}_{n=1 \text{ detection}}$  will overlap with  $\mathit{time}_{n=2 \text{ escaped detection}}$  at the second peak. This can be observed in Figure 190 where the amplitudes of the 1<sup>st</sup> and 2<sup>nd</sup> peaks, where the escaped wave occurs first with low amplitude, followed by the overlapping waves causing a higher amplitude in the 2<sup>nd</sup> peak. The patterns also continue with the 3<sup>rd</sup> peak having a smaller amplitude than the 4<sup>th</sup> peak because the 4<sup>th</sup> peak combines both  $\mathit{time}_{n=2 \text{ detection}}$  and  $\mathit{time}_{n=4 \text{ escaped detection}}$ , whereas the 3<sup>rd</sup> peak is  $\mathit{time}_{n=3 \text{ escaped detection}}$  only. Thus, validating the escaped waves theory.

The  $T.O.F_{\text{avg Circumference}}$  of the peaks detected at 8.15 ° is,

$$\begin{aligned} T.O.F_{\text{avg Circumference}} &= \left( \frac{5^{\text{th}} \text{Peak} - 1^{\text{st}} \text{Peak}}{4} \right) \times \left( \frac{\text{horizontal scale} \times 10}{\text{samples}} \right) \\ &= \left( \frac{34028 - 2865}{4} \right) \times \left( \frac{(500 \times 10^{-6} \text{s}) \times 10}{50000} \right) = 7.79 \times 10^{-4} \text{s} = 0.779 \text{ms} \end{aligned} \quad \text{Equation 107}$$

$$V_{gr} = \frac{\text{Circumference}_{\text{measured}}}{T.O.F_{\text{avg Circumference}}} = \frac{2.512\text{m}}{0.779\text{ms}} = 3.22 \text{ m/ms} \quad \text{Equation 108}$$


---

$$\begin{aligned} \text{time}_{n=1 \text{ escaped detection}} &= \\ &= (1^{\text{st}} \text{ peak}_{X \text{ coordinate}} - \text{tigger pulse}_{X \text{ coordinate}}) \\ &\times \left( \frac{\text{oscilloscope horizontal scale} \times 10}{\text{samples}} \right) \\ &= (2865 - 1121) \times \left( \frac{(500 \times 10^{-6}\text{s}) \times 10}{50000} \right) = 1.744 \times 10^{-4}\text{s} = 0.174 \text{ ms} \end{aligned} \quad \text{Equation 109}$$


---

$$\begin{aligned} \text{time}_{n=1 \text{ detection}} &= \\ &= (2^{\text{nd}} \text{ peak}_{X \text{ coordinate}} - \text{tigger pulse}_{X \text{ coordinate}}) \\ &\times \left( \frac{\text{oscilloscope horizontal scale} \times 10}{\text{samples}} \right) \\ &= (10625 - 1121) \times \left( \frac{(500 \times 10^{-6}\text{s}) \times 10}{50000} \right) = 9.504 \times 10^{-4}\text{s} = 0.950 \text{ ms} \end{aligned} \quad \text{Equation 110}$$


---



$$\begin{aligned}
& \mathbf{time}_{n=1 \text{ anticlock detection}} \\
&= (2^{\text{nd}} \text{ peak}_X \text{ coordinate} - \text{tigger pulse}_X \text{ coordinate}) \\
&\times \left( \frac{\text{oscilloscope horizontal scale} \times 10}{\text{samples}} \right) \\
&= (9402 - 1135) \times \left( \frac{(500 \times 10^{-6} \text{s}) \times 10}{50000} \right) = 8.267 \times 10^{-4} \text{s} = 0.827 \text{ ms}
\end{aligned}$$

Equation 111

$$\mathbf{distance}_{D\cup crack} = V_{gr} \times T_{D\cup crack} = V_{gr} \times \left( \frac{\mathbf{time}_{1^{\text{st}} \text{ anticlock detection}} - \mathbf{time}_{1^{\text{st}} \text{ detection}}}{-2} \right)$$

Equation 93

$$\therefore \mathbf{distance}_{D\cup crack} = 3.22 \text{ m/ms} \times \left( \frac{0.827 - 0.95}{-2} \right) = 0.198 \text{ m}$$

Equation 112

The discrepancy between the **distance**  $D\cup crack$  the ultrasonic scan result and the measured value is due to the offset caused by the TX and RX module's geometries, angles, and true point of wave contact with the sample, that was described in Section 5.5 and notated in Equation 40 and Equation 41 as 'c'.

## 6.6 Transducers performance over time

After the prolonged use of the transmitter and receiver setup in all the experiments described so far, the readings quality started to deteriorate, and the amplitude and definition of the Lamb wave detected dropped.

The transducers were analysed by the manufacture, where degradation to the transducer matching layer was detected. After the transducers matching layers were replaced, the peak electric resonance frequencies of the transmitter shifted to  $f_{electric} = 538$  KHz and the receiver's mechanical resonance shifted to  $f_{mechanical} = 655$  KHz.

This shift in resonance frequencies from their original 500 KHz resonance meant that the transmitter's electric to mechanical energy conversion is not optimal at 500 KHz anymore, and the transmitter should operate at 538 KHz for maximum efficiency. Meanwhile the receiver sensitivity to mechanical excitation is optimal at 655 KHz, which is different from the transmitter ideal operational frequency of 538 KHz. This mismatch in resonance created a scenario where the transmitter cannot create Lamb wave efficiently enough at the frequency where the receiver is most sensitive and vice versa, thus reducing the transduction efficiency to a point where it was no longer effective for the required tasks, putting an end to the experimentation using the ultrasonic transducers available.

The degradation of the transducers happened in lab condition after prolonged use at high energy levels, which wore out the transducers' matching layer. In the ILW vaults the environmental elements along with the ionising radiation that would be constantly bombarding the transducers with fast neutron will likely accelerates the rate of electronics and sensor deterioration. This further emphasises that the amplitude of the Lamb waves detected should not be considered in metrological measurements, due to its susceptibility to environmental and alignment factors, and only the time-of-flight based detection patterns should be considered for metrology.

## 6.7 Summary

A system was developed to align ultrasonic transducers to irregular workpieces and transduce ultrasonic Lamb waves for metrological scans.

The system uses a pattern-based algorithm to validate the scan signals and detect wastefrom expansion and defects in 500 L ILW drums. The pattern identification algorithm requires the Lamb waves to travel around the drum circumference at least 5 time.

Increasing the acquisition averaging and signal filtering can significantly improve the wave detection process at the cost of acquisition time. However, the wave detection will be also challenged by the damping effects observed from the pressures applied by the expanding cementitious wastefrom inside the drums.

More experimentation will be required to validate all the pattern recognition scenarios describe in the Section 6.5, and a multi-physic simulation is required to confirm the expected internal pressure of an ILW container that exceeded it yield point due to its solid contents' expansion as described in Section 6.4.

## Chapter 7: Future work and conclusion

### 7.1 Future developments

To raise the technology readiness level (TRL) of the proposed robotic sensor deployment concept and automate the data collection process.

The passive robotic system will benefit from:

- More development work in optimising the cable management needed to deny any chance of the power/control umbilical entanglement, as the robot hops across the stillage tiers.
- Evaluating the stability and rigidity of the slit tubes hanging down in the vertical direction.
- Creating and optimising a manoeuvring pattern to minimise the inspection process time by positioning the sensor gimbals in locations that would provide the maximum amount of data.
- Performing finite element analysis to ensure that the robot's stillage hopping process will not pose any risk to the structural integrity of the stillage lifting arrangement or stacking stability.
- Identify the type of motor (electromagnetic or hydraulic) needed to provide the required forces to manoeuvre the robot while adhering to nuclear storage sites operational regulations.

For the idea of rapid visual inspection using UAVs to mature, more work is required to ,

- Develop a system to manoeuvre and navigate the UAV safely in the tight spaces between the stillages without external positioning sensors.
- Create a stabilisation system to control the UAV's attitude without the axis coupling issues described in Section 4.5.4.
- Test the efficacy of different sensor technologies while being deployed onboard the UAV.

In order to automate the entire ultrasonic inspection process of the ILW 500 L drums,

- Software development is required to validate the Lamb waves detections using the patterns described in Section 6.5.5.

- The software must also be able to communicate with the motion control system of the robot to adjust the angle control gimbals to achieve the optimum wave detection angles and positions, using the process described in Section 6.2 Figure 139.
- Identify the best positions to locate the ultrasonic transducers around the drum while inside the stillages using the passive robot's sensor gimbal's degrees of freedom.
- Identify the ultrasonic lamb wave frequencies that would provide the most reliable circumferential measurements after considering the anomalies described in Section 5.7.

The image and point cloud stitching process required to create the incomplete point clouds and photogrammetry data that will be fused with the ultrasonic data needs to be,

- Optimised to process the monotonous data using the sensor gimbal IMU data as described in Section 3.3.2 and 3.4.2.
- Provide feedback to the robot's controls to position the camera and lighting in locations that reduce the reflections and/or glare caused by the shiny surfaces of the drums and stillages.
- Detect anomalies in the images for defect screening, characterisation, and quantification.
- Provide feedback to the robot to allow it to move the sensors/gimbal to locations from which it can collect any missing data in the scans.

## 7.2 Future research

Given the findings from Section 6.4.2, more investigation in the true cause of the drums structural deformation is needed. If the deformation is indeed caused by the cementitious contents pressure on the drum's shell, then a powerful air coupled transducer will need to be developed to overcome the damping effects observed in Section 6.4.3. Otherwise, if the deformation is caused by the long-term creep effect described in Section 2.7, the dampening effects may not be present, and an ultrasonic inspection system similar to the one used in this project's experimentation would be adequate. To find out which of these scenarios is more likely, a multi-physic simulation that can consider the

time factor and changes in pressure caused by an expanding solid instead of a constant force is required.

More research is required in confirming the possibility of adapting or creating a new EMAT transducer that would be capable of generating Lamb waves into the ILW drums shells and other types of nuclear waste packages. This may eliminate some of the disadvantages of the air coupled piezoelectric transduction associated with the variability in longitudinal wave velocities caused by environmental factors. EMATs may require a strong pulsing electromagnetic field to generate the ultrasonic waves into the drum's shell as described in Section 3.3.4.2.2 and 5.2.1. Therefore, the chemical and physical stability of the radioactive contents during and after exposure to the electromagnetic fields should also be considered to ensure the continued stability and safety of the waste immobilisation process.

Finally, once all the challenges in the point cloud laser scans and ultrasonic inspection are overcome. Data postprocessing algorithms will be needed to fuse the two sets of data and create the estimation of the complete drum shell. Since the results from the fusion processes will involve predictions and estimations, the algorithms should be able to screen the highly unlikely results and provide an evaluation of the uncertainty of each output to assist the users post inspection decisions.

Research into the possibility of adapting or modifying the proposed concepts to CM&I other types of nuclear decommissioning encapsulation containers including the new proposed non-metallic containers [14] and high level nuclear waste "Special Nuclear Material" (SNM) packages, should be conducted. This will be required to adapt the CM&I techniques proposed to the different stacking arrangements and spatial challenges associated with the different nuclear waste storage practices and philosophies.

### 7.3 Final conclusions

The increase in production of nuclear ILW [7] and the observed signs of structural deformation in some of the legacy 500 L drums encapsulating it [6], creates a need for CM&I of the drums during long-term storage, to guarantee their continued safety for geological disposal [2]. This is

challenged by the large quantity [4] and tight storage arrangement of the ILW vaults [5]. To overcome this challenge without compromising the security and safety of the inspection process, two different robotic sensor deployment concepts has been proposed for deploying non-contact sensors for CM&I structural integrity of ILW 500 L drums without the need to move or modify them.

The first proposed system is a UAV capable of flying between the ILW stillage stacks to rapidly collect visual information about the ILW drums while they are in-situ using cameras.

The second robotic system consists of a passive robot that utilises existing features of the ILW stillages and containers to anchor and manoeuvre itself across the containers tiers, to monitor and inspect far and hard to reach containers without the need for overhead cranes. The system is expected to deploy a minimum of three non-contact sensing modalities that can provide both direct and indirect line of sight measurements. This will be in the form of:

- 1- Camera imagery
- 2- Point cloud laser scans
- 3- Ultrasonic dimensional scans

The data from the camera imagery and point cloud laser scans is restricted by the drums' containment stillages, which only allows access to 30 % of the surfaces of interest. The available data can provide information on the overall position and contour of the drum, deformations, and visible surface corrosion on the available 30 % of surface only. Meanwhile ultrasonic inspection can provide circumferential measurements and defect detection using non-contact air coupled transducers.

The ultrasonic inspection utilises the small access gaps in the stillage structure to transduce Lamb waves that can travel around the drum circumference and use the wave's T.O.F to compute the drum's circumference along the horizontal cross section in which the waves are transduced. Lab environment experiments were able to measure cross sectional stainless-steel samples with uncertainties of 3.5 % and an empty ILW drum specimen with an uncertainty of 1.16 %. Further

research also indicated that this uncertainty will significantly increase in real life environment due to the uneven changes in the properties of the ILW drum shells due to the aging effects caused by the drum's environment and contents. Along with circumferential measurements, the Lamb wave detection patterns were also able to detect discontinuity defects caused by mechanical stresses or corrosion.

The experiments performed during this research indicates that the ultrasonic inspection will be challenged by the dampening effects caused by increased contact caused by the expanding cementitious contents of the drum and its shell. However, finite element simulations predict that in order for the expanding content to apply enough contact pressure to stretch the drum by the observed >4 mm expansions, the drum's shell is likely to plastically deform which may cause a drop in the observed contact pressure between the contents and the drum, thus reduce the lamb waves dampening effects.

The ultrasonic circumferential measurements combined with the laser scan point clouds, can potentially be fused together to create a complete image of the ILW 500 L drums, without requiring access to the entire drums' surfaces, to achieve the in-situ metrological inspection goal.



## Chapter 8: Appendix

### 8.1 Java code

```
PVector rotate_around(PVector _vector, PVector _axis, float theta, char axis) {  
    PVector converted_matrix = new PVector(0, 0, 0);  
    converted_matrix = rotate_around(_vector.sub(_axis), theta, axis);  
    converted_matrix.add(_axis);  
    return converted_matrix;  
}
```

```
////////////////////////////////////
```

```
PVector rotate_around(PVector _vector, float theta, char axis) {  
  
    float[][] position_matrix = {{_vector.x}, {_vector.y}, {_vector.z}};  
    PVector converted_matrix = new PVector(0, 0, 0);
```

```
float[][] z_rotation_matrix = { {cos(theta), -sin(theta), 0}, {sin(theta), cos(theta), 0}, {0, 0, 1} }; ///rotation around z matrix
```

```
float[][] y_rotation_matrix = { {cos(theta), 0, sin(theta)}, {0, 1, 0}, {-sin(theta), 0, cos(theta)} }; ///rotation around y matrix
```

```
float[][] x_rotation_matrix = { {1, 0, 0}, {0, cos(theta), -sin(theta)}, {0, sin(theta), cos(theta)} }; ///rotation around x matrix
```

```
float[][] product= new float[3][1];
```

```
if (axis == 'x')
```

```
    product = multiplyMatrices(x_rotation_matrix, position_matrix, 3, 3, 1);
```

```
else if (axis == 'y')
```

```
    product = multiplyMatrices(y_rotation_matrix, position_matrix, 3, 3, 1);
```

```
else if (axis == 'z')
```

```
    product = multiplyMatrices(z_rotation_matrix, position_matrix, 3, 3, 1);
```

```
converted_matrix.x= product[0][0];  
converted_matrix.y= product[1][0];  
converted_matrix.z= product[2][0];  
return converted_matrix
```

## References

- [1] “Nuclear Power in the United Kingdom | UK Nuclear Energy - World Nuclear Association.” [Online]. Available: <https://www.world-nuclear.org/information-library/country-profiles/countries-t-z/united-kingdom.aspx>. [Accessed: 16-May-2021].
- [2] A. Cook *et al.*, “Atmospheric-Induced Stress Corrosion Cracking of Austenitic Stainless Steels Under Limited Chloride Supply,” *Corrosion*, no. May 2014, pp. 1–11, 2011.
- [3] B. T. . Swift *et al.*, “Implications of RWMD 500 Year Waste Container Integrity Target compared with 150 Years for Container Design and Cost,” 2011.
- [4] N. D. Authority, “UK Radioactive Waste Inventory - <https://ukinventory.nda.gov.uk/site/sellafield/> Generated 15/06/2022,” vol. d, 2022.
- [5] C. P. J. F Bate, D Roberts, A R Hoch, “Gas migration calculations on the vault scale Report to Nirex,” *SA/ENV-0932*, no. 3.1, 2012.
- [6] K. Hodgson, “Nexia Solutions Commercial Laser scanning inspection of 12 ILW drums retrieved from Nexia Solutions Commercial Laser scanning inspection of 12 ILW drums retrieved from,” 2007.
- [7] R. Bogue, “Robots in the nuclear industry: A review of technologies and applications,” *Ind. Rob.*, vol. 38, no. 2, pp. 113–118, 2011.
- [8] IAEA, “Nuclear power plant outage optimisation strategy,” no. October, 2002.
- [9] Nuclear Decommissioning Authority, “Interim Storage of Higher Activity Waste Packages – Integrated Approach,” no. 1, 2011.
- [10] United Kingdom Nirex Limited, “Nirex Report Generic Repository Studies Generic post-closure Performance Assessment,” *Nirex Rep. N/080*, no. July, pp. 1–156, 2003.
- [11] N H Edmunds; Shelton P, “Development of Concepts for Geological Repositories,” 2007.
- [12] J. A. Kuo, “Point Cloud Data Post-processing Software Market

Survey Report,” 2014.

- [13] D. G. Bennett and S. M. Wickham, “Review of Waste Immobilisation Matrices,” no. January, 2016.
- [14] S. V. Barlow and J. D. Palmer, “The Packaging of Waste for Safe Long-Term Management,” 2000.
- [15] S. K. BATE and B. D. Daniels, “A Review of Manufacturing Processes Used in Stainless Steel Intermediate Level Waste Containers to Evaluate the Presence of Residual Stresses Report to NDA,” 2009.
- [16] I. Bannister, “Graham Enigneering Ltd.” Graham Engineering LTD.
- [17] C. S. Walker and E. Agency, “Characterisation and solubility behaviour of synthetic calcium silicate hydrates,” no. June 2003, 2017.
- [18] G. F. Sinclair, “Encapsulation of llw Raffinate in the Dounreay Cementation Plant,” pp. 205–209.
- [19] R. W. M. Limited, “Waste Package Specification and Guidance Documentation : Specification for Waste Packages Containing Low Heat Generating Waste : Part D – Container Specific Requirements,” no. June, 2020.
- [20] NDA, “Geological Disposal Guidance on the application of the Waste Package Specifications for unshielded waste packages,” *Wps/701/01*, no. August, p. 47, 2014.
- [21] SCX Special Projects, “SCX Special Projects Wins Dounreay Contract.” [Online]. Available: <http://scxspecialprojects.co.uk/news/scx-special-projects-wins-dounreay-contract/>. [Accessed: 08-Jun-2020].
- [22] “Nuclear Decommissioning Authority WASTE PACKAGE SPECIFICATION AND GUIDANCE DOCUMENTATION WPS/604: Lifting Frame for Stillage and corner lifting variant of 3 cubic metre Box Waste Package: Description and Design Guidelines,” 2008.
- [23] R. W. M. Limited, “Geological Disposal:Guidance on the application of the specification for stillages for use in the transport and disposal of 500 litre drum waste packages,” 2015.
- [24] Nuclear Decommissioning Authority, “ILW vault drop heights in

higher strength rock,” no. 13169795, 2009.

- [25] P. B. Bamforth *et al.*, “Cement materials for use as backfill, sealing and structural materials in geological disposal concepts . A review of current status,” *Serco*, no. SERCO/005125/001 Issue 3, pp. 1–235, 2012.
- [26] “HSS - High stakes lifting.” [Online]. Available: [https://www.hsssearch.co.uk/page\\_677605.asp](https://www.hsssearch.co.uk/page_677605.asp). [Accessed: 08-Jun-2020].
- [27] A. Group, “Higher-activity radioactive waste: implementation strategy - gov.scot,” *STRATEGY/PLAN*. [Online]. Available: <https://www.gov.scot/publications/higher-activity-waste-implementation-strategy/pages/3/>. [Accessed: 08-Jun-2020].
- [28] D. Hilton, “Measurement of ILW Drums, evaluation of a replacement non contact scanner for the Phase Vision system and specification of a Scanning Test Facility,” 2014.
- [29] T. Park, R. Kvarnström, and H. Lampen, “DESIGN AND OPERATION OF A WIDE RANGE SEGMENTED GAMMA,” pp. 1–10.
- [30] N. Estre, D. Eck, J. L. Pettier, E. Payan, C. Roure, and E. Simon, “High-Energy X-Ray Imaging Applied to Nondestructive Characterization of Large Nuclear Waste Drums,” *IEEE Trans. Nucl. Sci.*, vol. 62, no. 6, pp. 3104–3109, 2015.
- [31] V. Moulin, V. Rebuffel, M. Antonakios, Sauze.R.; and J. P. ; Gorius, “X-RAY IMAGING MODALITIES FOR NUCLEAR WASTE DRUMS INSPECTION,” 2004, vol. 16th World.
- [32] Game changers technology, “CHALLENGE : Condition Monitoring and Inspection,” 2009.
- [33] A. B. Cook *et al.*, “Assessing the risk of under-deposit chloride-induced stress corrosion cracking in austenitic stainless steel nuclear waste containers,” *Corros. Eng. Sci. Technol.*, vol. 49, no. 6, pp. 529–534, 2014.
- [34] L. A. Deibler, “Room temperature creep in metals and alloys,” 2014.
- [35] R. P. Reed and R. P. Walsh, “Low-temperature creep of austenitic stainless steels,” *J. Phys. Conf. Ser.*, vol. 897, no. 1, 2017.

- [36] R. G. Wilhelm, R. Hocken, and H. Schwenke, "Task Specific Uncertainty in Coordinate Measurement," *CIRP Ann.*, vol. 50, no. 2, pp. 553–563, Jan. 2001.
- [37] W. Cuypers, N. Van Gestel, A. Voet, J. P. Kruth, J. Mingneau, and P. Bleys, "Optical measurement techniques for mobile and large-scale dimensional metrology," *Opt. Lasers Eng.*, vol. 47, no. 3–4, pp. 292–300, 2009.
- [38] W. B. Penzes, "Time Line for the Definition of the Meter," pp. 1–3, 2002.
- [39] "ISO 10360-2:2009 - Geometrical product specifications (GPS) -- Acceptance and reverification tests for coordinate measuring machines (CMM) -- Part 2: CMMs used for measuring linear dimensions." [Online]. Available: <https://www.iso.org/standard/40954.html>. [Accessed: 26-Mar-2019].
- [40] "ISO10360-2." [Online]. Available: <https://www.renishaw.com/cmmsupport/knowledgebase/en/iso10360-2--22137>. [Accessed: 26-Mar-2019].
- [41] G. H. J. Florussen, F. L. M. Delbressine, M. J. G. Van De Molengraft, and P. H. J. Schellekens, "Assessing geometrical errors of multi-axis machines by three-dimensional length measurements," vol. 30, pp. 241–255, 2001.
- [42] D. M. Weckenmann, A., T. Estler, G. Peggs, "Probing Systems in Dimensional Metrology."
- [43] A. Weckenmann, M. Knauer, and H. Kunzmann, "The Influence of Measurement Strategy on the Uncertainty of CMM-Measurements," *CIRP Ann.*, vol. 47, no. 1, pp. 451–454, 2007.
- [44] S. . Phillips, B. Borchardt, W. . Estler, and J. Buttress, "The estimation of measurement uncertainty of small circular features measured by coordinate measuring machines," *Precis. Eng.*, vol. 22, no. 2, pp. 87–97, 2002.
- [45] R. Edgeworth and R. G. Wilhelm, "Sampling and Measurement Uncertainty in Coordinate Metrology," no. February, 1999.
- [46] D. H. Lee and N. G. Cho, "Assessment of surface profile data

- acquired by a stylus profilometer,” *Meas. Sci. Technol.*, vol. 23, no. 10, 2012.
- [47] D. Gay, “Correctly rounded binary-decimal and decimal-binary conversions,” *Numer. Anal. Manuscr.*, 1990.
- [48] A. American and N. Standard, “An American National Standard IEEE Standard for Radix-Independent Floating-Point Arithmetic,” 1994.
- [49] F. M. M. Chan, T. G. King, and K. J. S, “The influence of sampling strategy on a circular feature in coordinate measurements,” vol. 19, no. 2, pp. 73–81, 1996.
- [50] “circle | Definition of circle in English by Oxford Dictionaries.” [Online]. Available: <https://en.oxforddictionaries.com/definition/circle>. [Accessed: 15-Feb-2019].
- [51] American Society of Mechanical Engineers, *ANSI B89.3.1-1972*. New York, 1972.
- [52] P. Lockhart, “Controlling Roundness,” *quality quick clicks* 407, Jun-2008.
- [53] F. M. M. Chan, T. G. King, and K. J. Stout, “The influence of sampling strategy on a circular feature in coordinate measurements,” *Measurement*, vol. 19, no. 2, pp. 73–81, Oct. 1996.
- [54] S. I. Gass, C. Witzgall, and H. H. Harary, “Fitting Circles and Spheres to Coordinate Measuring Machine Data,” *Int. J. Flex. Manuf. Syst.*, vol. 10, no. 1, pp. 5–25, 1998.
- [55] N. A. T. P.A.H. Fennell, N.R. Smart, M. Izzo, “Characterisation of environmental conditions in an ILW store,” 2012.
- [56] H.-D. Jacoby, *Entwicklung und Merkmale eines Dreikoordinaten-Messgeraets, Zeitschrift fuer industrielle Fertigung*. 1979.
- [57] A. J. Lewis, *A fully traceable miniature CMM with sub-micrometre uncertainty, Proceedings of SPIE Conference*. 2003.
- [58] P. Ka, M. Dovica, S. Slosar, and J. Ková, “Comparision of contact and contactless measuring methods for form evaluation,” vol. 48, pp. 273–279, 2012.
- [59] D. Zhang, J. Cao, G. Dobie, and C. MacLeod, “A Framework of Using



- Customized LIDAR to Localize Robot for Nuclear Reactor Inspections,” *IEEE Sens. J.*, vol. XX, no. XX, pp. 1–8, 2021.
- [60] C. N. Macleod, R. Summan, G. Dobie, and S. G. Pierce, “Quantifying and improving laser range data when scanning industrial materials,” *IEEE Sens. J.*, vol. 16, no. 22, pp. 7999–8009, 2016.
- [61] R. A. Clark *et al.*, “3D model generation using an airborne swarm,” *AIP Conf. Proc.*, vol. 1650, pp. 1460–1467, 2015.
- [62] K. Morishima *et al.*, “Discovery of a big void in Khufu’s Pyramid by observation of cosmic-ray muons,” *Nature*, vol. 552, no. 7685, pp. 386–390, 2017.
- [63] R. Kaiser, “Muography: Overview and future directions,” *Philos. Trans. R. Soc. A Math. Phys. Eng. Sci.*, vol. 377, no. 2137, 2019.
- [64] D. Mahon *et al.*, “First-of-a-kind muography for nuclear waste characterization,” *Philos. Trans. R. Soc. A Math. Phys. Eng. Sci.*, vol. 377, no. 2137, 2019.
- [65] D. Koodalil and K. Balasubramaniam, “Inspection of Hidden and Curved Regions in Composite Structures using Non-contact Guided Ultrasonic Waves,” *19th World Conf. Non-Destructive Test. 2016*, no. January, pp. 1–7, 2016.
- [66] M. LORENZ and S. LEWANDOWSKI, “Ultrasonic Multi-Skip Inspection at Clamped Saddle Supports,” *18th World Conf. NDT*, no. April, p. 206, 2012.
- [67] M. Tabatabaeipour *et al.*, “A Feasibility Study on Guided Wave-Based Robotic Mapping,” *IEEE Int. Ultrason. Symp. IUS*, vol. 2019-Octob, pp. 1567–1570, 2019.
- [68] K. K. Shung and M. J. Zipparo, “Ultrasonic transducers and arrays,” *IEEE Eng. Med. Biol. Mag.*, vol. 15, no. 6, pp. 20–30, 1996.
- [69] R. E. Green, “Non-contact ultrasonic techniques,” *Ultrasonics*, vol. 42, no. 1–9, pp. 9–16, 2004.
- [70] Kemu Studio, “ACOUSTIC IMPEDANCE OF VARIOUS MATERIALS TABLE.” [Online]. Available: [https://calculla.com/acoustic\\_impedance](https://calculla.com/acoustic_impedance). [Accessed: 26-Feb-2023].

- [71] W. A. Grandia and C. M. Fortunko, "NDE applications of air-coupled ultrasonic transducers," *Proc. IEEE Ultrason. Symp.*, vol. 1, pp. 697–709, 1995.
- [72] T. Piotrowski, M. Mazgaj, A. Zak, and J. Skubalski, "Importance of atomic composition and moisture content of cement based composites in neutron radiation shielding," *Procedia Eng.*, vol. 108, pp. 616–623, 2015.
- [73] N. Bohr and J. A. Wheeler, "The mechanism of nuclear fission," *Phys. Rev.*, vol. 56, no. 5, pp. 426–450, 1939.
- [74] N. Bhadwal, M. T. Milani, T. Coyle, and A. Sinclair, "Dry coupling of ultrasonic transducer components for high temperature applications," *Sensors (Switzerland)*, vol. 19, no. 24, 2019.
- [75] X. Jian, S. Dixon, and R. S. Edwards, "Ultrasonic generation and optimization for EMAT," *AIP Conf. Proc.*, vol. 760, no. 2005, pp. 1041–1046, 2005.
- [76] L. Cheng, M. Kogia, A. Mohimi, V. Kappatos, C. Selcuk, and T. H. Gan, "Crack characterisation using invariable feature extraction in stainless steel specimen used for absorber tubes of CSP applications via EMAT," *Renew. Energy*, vol. 101, no. 2017, pp. 771–781, 2017.
- [77] "Are 304 & 316 Stainless Steels Magnetic? | Meyer Tool & Mfg. - Meyer Tool & Mfg." [Online]. Available: <https://www.mtm-inc.com/ac-20110117-how-nonmagnetic-are-304-and-316-stainless-steels.html>. [Accessed: 16-Feb-2019].
- [78] D. Rifai, A. N. Abdalla, K. Ali, and R. Razali, "Giant magnetoresistance sensors: A review on structures and non-destructive eddy current testing applications," *Sensors (Switzerland)*, vol. 16, no. 3, 2016.
- [79] "EMAT Technology: What is EMAT and how it works." [Online]. Available: <https://www.innerspec.com/emat-technology>. [Accessed: 06-Feb-2022].
- [80] H. Gao, S. Ali, and B. Lopez, "Austenitic Weld Inspection with EMAT Phased Array," no. February, pp. 1–10, 2019.
- [81] G. Dobie, "Ultrasonic Sensor Platforms for Non-Destructive

Evaluation,” 2010.

- [82] I. A. Viktorov., *Rayleigh and Lamb waves: Physical theory and applications*. Plenum Press, 1967.
- [83] G. Jiang, R. M. Voyles, and J. J. Choi, “Precision Fully-Actuated UAV for Visual and Physical Inspection of Structures for Nuclear Decommissioning and Search and Rescue,” *2018 IEEE Int. Symp. Safety, Secur. Rescue Robot. SSRR 2018*, pp. 1–7, 2018.
- [84] C. Li, L. Yu, and S. Fei, “Large-Scale, Real-Time 3D Scene Reconstruction Using Visual and IMU Sensors; Large-Scale, Real-Time 3D Scene Reconstruction Using Visual and IMU Sensors,” *IEEE Sens. J.*, vol. 20, no. 10, 2020.
- [85] K. Shivaraj, K. Balasubramaniam, C. V. Krishnamurthy, and R. Wadhwan, “Ultrasonic Circumferential Guided Wave for Pitting-Type Corrosion Imaging at Inaccessible Pipe-Support Locations,” *J. Press. Vessel Technol.*, vol. 130, no. 2, p. 021502, 2008.
- [86] M. Tabatabaeipour *et al.*, “Application of ultrasonic guided waves to robotic occupancy grid mapping,” *Mech. Syst. Signal Process.*, vol. 163, no. May 2021, p. 108151, 2022.
- [87] G. Andrew, M. Gryniewski, and T. Campbell, “AARM: A robot arm for internal operations in nuclear reactors,” *2010 1st Int. Conf. Appl. Robot. Power Ind. CARPI 2010*, pp. 1–5, 2010.
- [88] N. Marturi *et al.*, “Towards advanced robotic manipulation for nuclear decommissioning: A pilot study on tele-operation and autonomy,” *Int. Conf. Robot. Autom. Humanit. Appl. RAHA 2016 - Conf. Proc.*, 2017.
- [89] L. Gargiulo *et al.*, “Development of an ITER relevant inspection robot,” *Fusion Eng. Des.*, vol. 83, no. 10–12, pp. 1833–1836, 2008.
- [90] R. Bloss, “Snake-like robots ‘reach’ into many types of applications,” *Ind. Rob.*, vol. 39, no. 5, pp. 436–440, 2012.
- [91] R. Buckingham, “Snake arm robots,” *Ind. Rob.*, vol. 29, no. 3, pp. 242–245, 2002.
- [92] N. Takesue, G. Zhang, J. Furusho, and M. Sakaguchi, “Precise Position Control of Robot Arms Using a Homogeneous ER Fluid,” no. April, pp. 55–61, 1999.

- [93] S. Voisembert, A. Riwan, N. Mechbal, and A. Barraco, "A novel inflatable robot with constant and continuous volume," *Proc. - IEEE Int. Conf. Robot. Autom.*, pp. 5843–5848, 2011.
- [94] R. Fernández-Rodríguez, V. Feliu, and A. González-Rodríguez, "A proposed wall climbing robot for oil tank inspection," *Adv. Mob. Robot. - Proc. 11th Int. Conf. Climbing Walk. Robot. Support Technol. Mob. Mach. CLAWAR 2008*, pp. 597–604, 2008.
- [95] O. Unver and M. Sitti, "A miniature ceiling walking robot with flat tacky elastomeric footpads," *Proc. - IEEE Int. Conf. Robot. Autom.*, pp. 2276–2281, 2009.
- [96] D. W. Hong, "Biologically Inspired Locomotion Strategies : Novel Ground Mobile Robots at RoMeLa," *3rd Int. Conf. Ubiquitous Robot. Ambient Intell.*, no. Urai, 2006.
- [97] I. Virgala, M. Dovica, M. Kelemen, E. Prada, and Z. Bobovský, "Snake robot movement in the pipe using concertina locomotion," *Appl. Mech. Mater.*, vol. 611, pp. 121–129, 2014.
- [98] B. C. Jayne, "What defines different modes of snake locomotion?," *Integr. Comp. Biol.*, vol. 60, no. 1, pp. 156–170, 2020.
- [99] S. Kim, C. Laschi, and B. Trimmer, "Soft robotics: A bioinspired evolution in robotics," *Trends Biotechnol.*, vol. 31, no. 5, pp. 287–294, 2013.
- [100] J. Z. Ge, A. A. Calderón, and N. O. Pérez-Arancibia, "An earthworm-inspired soft crawling robot controlled by friction," *2017 IEEE Int. Conf. Robot. Biomimetics, ROBIO 2017*, vol. 2018-Janua, pp. 834–841, 2017.
- [101] E. W. Hawkes, L. H. Blumenschein, J. D. Greer, and A. M. Okamura, "A soft robot that navigates its environment through growth," *Sci. Robot.*, vol. 2, no. 8, pp. 1–8, 2017.
- [102] D. Trivedi, C. D. Rahn, W. M. Kier, and I. D. Walker, "Soft robotics: Biological inspiration, state of the art, and future research," *Appl. Bionics Biomech.*, vol. 5, no. 3, pp. 99–117, 2008.
- [103] L. Stadelmann, T. Sandy, A. Thoma, and J. Buchli, "End-Effector Pose Correction for Versatile Large-Scale Multi-Robotic Systems," *IEEE Robot. Autom. Lett.*, vol. 4, no. 2, pp. 546–553, 2019.

- [104] S. G. Pierce *et al.*, “Visual asset inspection using precision UAV techniques,” *8th Eur. Work. Struct. Heal. Monit.*, pp. 1–10, 2016.
- [105] R. W. Deters, G. K. Ananda, and M. S. Selig, “Reynolds number effects on the performance of small-scale propellers,” *32nd AIAA Appl. Aerodyn. Conf.*, no. June, pp. 1–43, 2014.
- [106] M. M. N. \* R. N. \*\* E. Garone, “Taut Cable Control of a Tethered UAV,” *Int. Fed. Autom. Control*, 2014.
- [107] H. Xu and J. Wu, “Metal mine underground safety monitoring system based on WSN,” *Proc. 2012 9th IEEE Int. Conf. Networking, Sens. Control. ICNSC 2012*, pp. 244–249, 2012.
- [108] M. Robotics, “Marvelmind Indoor Navigation System Operating Manual.” Marvelmind, 2019.
- [109] O. S. Andrew J. Davison, Ian D. Reid, Nicholas D. Molton, “MonoSLAM: Real-Time Single Camera SLAM,” *IEEE Trans. Pattern Anal. Mach. Intell.*, vol. 29, no. 6, 2007.
- [110] D. M. Cole and P. M. Newman, “Using laser range data for 3D SLAM in outdoor environments,” *Proc. - IEEE Int. Conf. Robot. Autom.*, no. October, pp. 1556–1563, 2003.
- [111] X. Yuan and J. Zhu, “Inverse dynamic modeling and analysis of a coaxial helicopter’s swashplate mechanism,” *Mech. Mach. Theory*, vol. 113, pp. 208–230, 2017.
- [112] “Lithium polymer battery pack, Lithium polymer cell, Li Po battery pack, protection circuit.” [Online]. Available: [http://www.ibtpower.com/Battery\\_packs/Li\\_Polymer/Lithium\\_polymer\\_cells.html](http://www.ibtpower.com/Battery_packs/Li_Polymer/Lithium_polymer_cells.html). [Accessed: 08-Feb-2022].
- [113] S. D. Levy, “Robustness Through Simplicity: A Minimalist Gateway to Neurorobotic Flight,” *Front. Neurobot.*, vol. 14, Mar. 2020.
- [114] Q. Zhang, Z. Liu, J. Zhao, and S. Zhang, “Modeling and attitude control of Bi-copter,” *AUS 2016 - 2016 IEEE/CSAA Int. Conf. Aircr. Util. Syst.*, vol. 100191, pp. 172–176, 2016.
- [115] Space Technology Mission Directorate, “Simplified High-Performance Roll Out Composite Magnetometer Boom , Phase I,” *TechPort*, 2017.

- [116] D. A. Galletly and S. D. Guest, "Bistable composite slit tubes. I. A beam model," *Int. J. Solids Struct.*, vol. 41, no. 16–17, pp. 4517–4533, 2004.
- [117] B. Davis and D. Arias, "High Strain Composite Deployable Booms for Cubesats ROCCOR Mission & Approach," in *13th Annual Cubesat Developers' Workshop*, 2016.
- [118] G. Knott and A. Viquerat, "Curved Bistable Composite Slit Tubes with Positive Gaussian Curvature," *AIAA J.*, vol. 56, no. 4, pp. 1679–1688, 2018.
- [119] G. Knott and A. Viquerat, "Helical bistable composite slit tubes," *Compos. Struct.*, vol. 207, no. September 2018, pp. 711–726, 2019.
- [120] M. R. Jongerden and B. R. Haverkort, "Battery aging, battery charging and the kinetic battery model: A first exploration," *Lect. Notes Comput. Sci. (including Subser. Lect. Notes Artif. Intell. Lect. Notes Bioinformatics)*, vol. 10503 LNCS, pp. 88–103, 2017.
- [121] H. T. Roman, P. O. Box, and W. R. Sigrist, "Pipe crawling inspection robots: an overview," *October*, vol. 8, no. 3, pp. 576–583, 1993.
- [122] C. N. MacLeod, "Considerations for automated NDE applications," University of Strathclyde, 2014.
- [123] C. Pei, T. Liu, H. Chen, and Z. Chen, "Inspection of delamination defect in first wall with a flexible EMAT-scanning system," *Fusion Eng. Des.*, vol. 136, no. September 2017, pp. 549–553, 2018.
- [124] X. Sun *et al.*, "Interaction of lamb wave modes with weak material nonlinearity: Generation of symmetric zero-frequency mode," *Sensors (Switzerland)*, vol. 18, no. 8, pp. 1–19, 2018.
- [125] W. Luo, X. Zhao, and J. L. Rose, "A guided wave plate experiment for a pipe," *J. Press. Vessel Technol. Trans. ASME*, vol. 127, no. 3, pp. 345–350, 2005.
- [126] R. Wille and H. Fernholz, "Report on the first European Mechanics Colloquium, on the Coanda effect," *J. Fluid Mech.*, vol. 23, no. 4, pp. 801–819, 1965.
- [127] J. S. Coetsee, G. J. Van den Berg, and P. Van der Merwe, "Effect of workhardening and residual stresses due to cold work of forming on the strength of cold-formed stainless steel lipped channel

- sections," *Int. Spec. Conf. Cold-Formed Steel Struct.*, pp. 505–523, 1990.
- [128] Q. Auzoux, L. Allais, C. Caës, I. Monnet, A. F. Gourgues, and A. Pineau, "Effect of pre-strain on creep of three AISI 316 austenitic stainless steels in relation to reheat cracking of weld-affected zones," *J. Nucl. Mater.*, vol. 400, no. 2, pp. 127–137, 2010.
- [129] C. Pokor, X. Averty, Y. Bréchet, P. Dubuisson, and J. P. Massoud, "Effect of irradiation defects on the work hardening behavior," *Scr. Mater.*, vol. 50, no. 5, pp. 597–600, 2004.
- [130] J. WOODCOCK, "WPEP Drum Body Details.pdf," RILEY WARRINGTON CHESHIRE, 1997.
- [131] C. Ye, W. Kan, Y. Li, and H. Pan, "Experimental study of hydrogen embrittlement on AISI 304 stainless steels and Rayleigh wave characterization," *Eng. Fail. Anal.*, vol. 34, pp. 228–234, 2013.
- [132] IEAE, "Interim Storage of Radioactive Waste Packages," *Tech. REPORTS Ser. No. 390*, vol. 390, 1998.
- [133] J. D. Hawthorne, "Cementitious Grouts for ILW Encapsulation – Composition, Hydration and Performance," *Civ. Eng.*, vol. PhD, no. September, p. 188, 2016.
- [134] J. D. N. Cheeke, X. Li, and Z. Wang, "Observation of flexural Lamb waves (A0 mode) on water-filled cylindrical shells," *J. Acoust. Soc. Am.*, vol. 104, no. 6, pp. 3678–3680, 1998.
- [135] "End of Average - Education Elements." [Online]. Available: <https://www.edelements.com/blog/end-of-average>. [Accessed: 25-May-2022].
- [136] "Lt. Gilbert S. Daniels and the myth of averages - Arbital," *Duncan Sabien*, 2016. [Online]. Available: <https://arbital.com/p/5n1/>. [Accessed: 25-May-2022].
- [137] W. H. B. Parker, "Electromagnetic : Interference : A Tutorial," pp. 177–186, 1996.
- [138] S. Zhenfei, S. Donglin, and X. Shuguo, "Detecting the number of EMI sources based on higher order statistics," *Proc. 20th Int. Zurich Symp. Electromagn. Compat. EMC Zurich 2009*, pp. 465–468, 2009.

- [139] D. Roylance, "Pressure vessels," *Massachusetts Institute of Technology Cambridge, MA 02139*. 2001.
- [140] O. Ifayefunmi and D. D. Ibrahim, "The effect of material discontinuity on the flanges of axially compressed steel cones," *Int. J. Mech. Eng. Technol.*, vol. 9, no. 6, pp. 32–41, 2018.
- [141] "Coefficient of Friction Equation and Table Chart." [Online]. Available:  
[https://www.engineersedge.com/coefficients\\_of\\_friction.htm](https://www.engineersedge.com/coefficients_of_friction.htm).  
[Accessed: 26-May-2022].
- [142] B. G. Rabbat and H. G. Russell, "Friction Coefficient of Steel on Concrete or Grout," *J. Struct. Eng.*, vol. 111, no. 3, pp. 505–515, 1985.
- [143] K. Dasgupta, "Dry Friction Licture notes." Indian Institute Of Technology–Guwahati.
- [144] A. Ryu and Y. Saidpour, "Stress Analysis of Thin-Walled Pressure Vessels," *Mod-ern Mech. Eng.*, vol. 5, pp. 1–9, 2015.
- [145] A. Chakraborty, "The effect of surface stress on the propagation of Lamb waves," *Ultrasonics*, vol. 50, no. 7, pp. 645–649, 2010.
- [146] Y. Yu *et al.*, "Acceptance angle measurement of CMUTs and PZT ultrasonic transducers," *2016 IEEE Int. Conf. Consum. Electron. ICCE-China 2016*, pp. 3–6, 2017.